Guidewire-mounted thermal sensors to assess coronary hemodynamics

Citation for published version (APA):
Horst, van der, A. (2012). *Guidewire-mounted thermal sensors to assess coronary hemodynamics*. [Phd Thesis 1 (Research TU/e / Graduation TU/e), Biomedical Engineering]. Technische Universiteit Eindhoven. https://doi.org/10.6100/IR732530

DOI:
10.6100/IR732530

Document status and date:
Published: 01/01/2012

Document Version:
Publisher's PDF, also known as Version of Record (includes final page, issue and volume numbers)

Guidewire-mounted thermal sensors to assess coronary hemodynamics

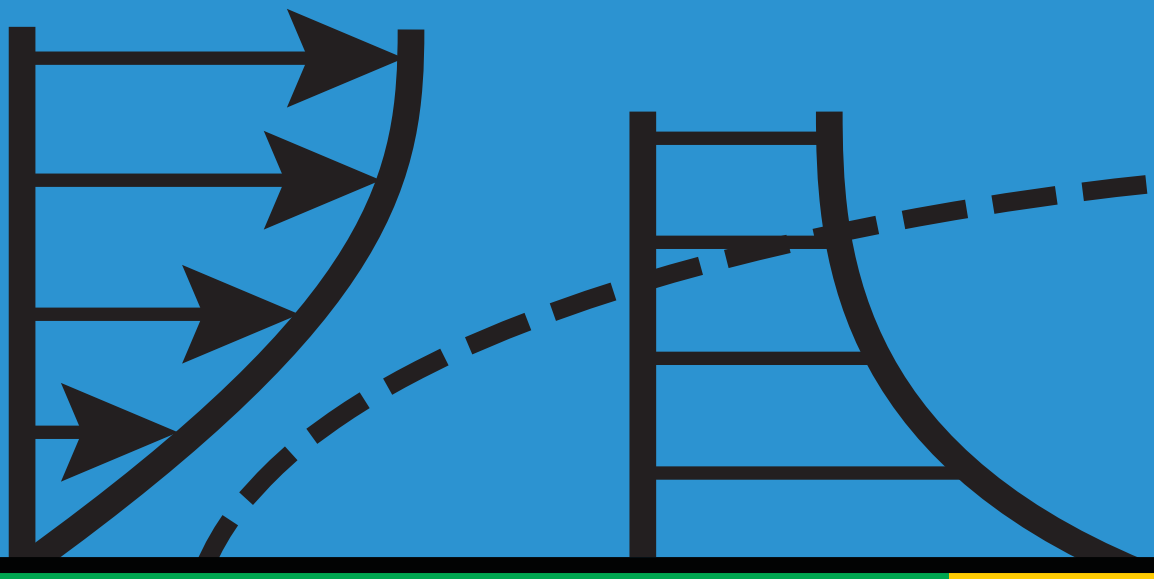

Arjen van der Horst

Guidewire-mounted thermal sensors to assess coronary hemodynamics

A catalogue record is available from the Eindhoven University of Technology Library

ISBN: 978-90-386-3142-4

Cover design by Arjen van der Horst, Tilburg, The Netherlands
After the idea of Hanneke Gelderblom, Enschede, The Netherlands

Printed by PrintPartners Ipskamp B.V. Enschede, The Netherlands

The research described in this thesis is supported by the Dutch Technology Foundation STW, which is part of the Netherlands Organisation for Scientific Research (NWO) and partly funded by the Ministry of Economic Affairs, Agriculture and Innovation (project number: SmartSiP 10046)

Guidewire-mounted thermal sensors to assess coronary hemodynamics

PROEFSCHRIFT

ter verkrijging van de graad van doctor aan de
Technische Universiteit Eindhoven, op gezag van de
rector magnificus, prof.dr.ir. C.J. van Duijn, voor een
commissie aangewezen door het College voor
Promoties in het openbaar te verdedigen
op donderdag 31 mei 2012 om 16.00 uur

door

Arjen van der Horst

geboren te Tilburg

Dit proefschrift is goedgekeurd door de promotoren:

prof.dr.ir. F.N. van de Vosse
en
prof.dr. N.H.J. Pijls

Copromotor:
dr.ir. M.C.M. Rutten

Summary

Guidewire-mounted thermal sensors to assess coronary hemodynamics

The vessels of the coronary circulation are prone to arteriosclerotic disease, which can lead to the development of obstructions to blood flow. The conventional way to diagnose the severity of this type of disease is by coronary angiography. This method, however, only provides insight into the morphology of the coronary vessels, whereas for an accurate diagnosis a measure for the actual flow impediment is needed. To perform these measurements, sensor-tipped guidewires have been developed to measure intra-coronary pressure and blood flow velocity. Diagnosis of coronary disease based on the time-average of these measurements have been shown to improve the clinical outcome of treatment significantly. However, since the coronary vessels are embedded in the (contracting) cardiac muscle, the interpretation of these indices is complicated and can be improved by simultaneously assessing the dynamics of coronary pressure and flow. The research described in this thesis therefore focusses on the one hand on developing devices for the simultaneous assessment of coronary pressure and flow dynamics and on the other hand on modeling the heart and coronary vessels to support the interpretation of these dynamic measurements.

In the development of a device which can measure both coronary pressure and flow, two different strategies have been chosen. In the first strategy, a method has been developed to operate an already clinically used pressure sensor-tipped guidewire (pressure wire) as a thermal anemometer to also measure flow. In an *in-vitro* model it has been demonstrated that the power required to electrically heat the sensor is a measure for the shear rate at the sensor surface and that the method can be used to assess coronary flow reserve (CFR). By slightly adapting the method and combining it with a continuous thermodilution method, it has also been shown that the dynamics of both pressure and volumetric flow can be measured simultaneously in physiological representative *in-vitro* and *ex-vivo* experiments. The main drawbacks of this thermal method with a pressure wire are the relatively high sensor temperature required and the inability to detect flow reversal.

In the second strategy, a new flow sensor, embedded in a flexible polyimide chip, has been specially designed to be mounted on a guidewire. The flow sensing element consists of a heater, operated at constant power, and thermocouples measuring the

temperature difference up- and downstream from the heater. To gain insight into the working principle and the importance of the different design parameters, an analytical model has been developed. Experiments where upscaled sensors have been subjected to steady and pulsatile flow, indicate that the model is able to reproduce the experimental results fairly well but that the sensitivity to shear rate is rather limited in the physiological range. This sensitivity to shear rate can possibly be improved by operating the heater at constant temperature, which has been investigated with *in-vitro* experiments with upscaled sensors and a finite element analysis of the real, small size sensor. These studies have demonstrated that constant temperature operation of the heater is beneficial over constant power operation and that the dynamics of physiological coronary shear rate, including retrograde flow, can be assessed at an overheat temperature of only 5 K. From these characterization studies a new design of the sensor has been proposed, which is currently being manufactured to be tested in both *in-vitro* and *ex-vivo* experiments.

To support the interpretation of the dynamic pressure and flow measurements, a numerical model of the heart and coronary circulation has been developed. The model is based on the coupling of four interacting parts: A model for the left ventricle which is based on the mechanics of a single myofiber, a 1D wave propagation model for the large epicardial coronary arteries, a stenosis element, and a Windkessel representation of the coronary micro-vessels. Comparison of the results obtained with the model with experimental observations described in literature has shown that the model is able to simulate the effect of different types of disease on coronary hemodynamics. After further validation, the model can be used as a tool to study the effect of combinations of epicardial and/or microcirculatory disease on pressure- and flow-based indices.

To model the relation between the pressure and flow waves in the coronary arteries correctly, as well as to assist in the decision-making regarding the mechanical treatment of coronary stenoses, the mechanical behaviour of the coronary arterial wall is required. Therefore, a mixed numerical-experimental method has been employed to fit a micro-structurally based constitutive model to *in-situ* extension-inflation experiments on porcine coronary arteries. It has been demonstrated that the model can accurately describe the experimental data and, additionally, it has been found that the most influential parameter, describing the collagen fiber orientation, can be considered constant at physiological loading. In further research, this can be used to tackle over-parameterization issues inherent to fitting similar constitutive models to data obtained in a clinical setting.

In this thesis, a computational model of the coronary circulation is presented and methods for simultaneous pressure and flow assessment are introduced. By operating an already clinically used pressure wire as a thermal anemometer, a methodology was developed which is close to clinical application, while a new sensor was designed to be more accurate in different flow conditions.

Contents

Chapter 1

General introduction

1.1 Coronary circulatory disease

The coronary circulation is prone to the development of arteriosclerotic disease. This type of disease can manifest itself as an atherosclerotic plaque, which can result in a local narrowing or stenosis, and/or a more diffusively distributed thickening of the arterial wall. The entire coronary circulation, from the large epicardial arteries to the microvasculature, can be affected. The main effect of this narrowing/stiffening is an increased resistance to blood flow and a decrease in the perfusion pressure distal to the diseased location. As a consequence, the myocardial tissue can get deprived from the required blood with oxygen, resulting in myocardial ischemia. While initially symptoms indicating this disease occur during exercise, when the demand of oxygen is greatest, further progression may lead to irreversible myocardial damage or infarction.

Treatment of a stenosis is usually focussed on reopening of the artery to restore blood flow. The most common minimally invasive method to accomplish this is percutaneous coronary intervention or PCI. This is a catheter-based approach, in which a balloon catheter is advanced over a guidewire to the location of the atherosclerotic plaque. At the position of the stenosis the balloon is inflated, with or without a stent, pushing the plaque material into the wall and thus restoring the normal lumen area. Disease in the microvasculature cannot be treated with PCI and can only be ameliorated with specific drugs. Treatment itself is also not without risk, e.g., due to possible restenosis at the location of a stent. Therefore, it is paramount to base treatment on an adequate diagnosis to improve the clinical outcome.

The currently most used methodology to diagnose a stenosis in the catheterization laboratory is coronary angiography, which has been already available since the 1960's (Sones and Shirey, 1962). Here, two-dimensional projections of the lumen of the coronary vessels are made using X-ray fluoroscopy. A clear drawback of this method is that it only gives information regarding the stenosis morphology and not the actual impediment of blood flow. For this reason, sensor-tipped guidewires have been

developed to assess coronary pressure and flow. Due to the availability of these hemodynamical measurements, several indices based on average pressure and/or flow measurements have been developed to quantify epicardial and microvascular disease (Kern et al., 2006). Besides average values of coronary pressure and flow, recent research indicates that the dynamics of coronary pressure and flow is also valuable in quantifying and discerning between different types of arterial (Mancini et al., 1989), microvascular (Hirsch et al., 2008; Escaned et al., 2009; Okcular et al., 2010), and cardiac (Davies et al., 2006a) disease.

While pressure measurement in the coronary arteries is relatively easy, flow is more difficult to obtain. The most commonly used method to assess coronary flow in the catheterization laboratory is by a Doppler-crystal mounted guidewire, which measures the blood velocity (Siebes et al., 2004). A drawback of this method is that the luminal area is required to estimate the flow rate and, due to the radial dependence of the blood velocity, adequate Doppler-derived velocity signals can be difficult to obtain, resulting in a poor Doppler signal in 10%-19% of all patients (Kern et al., 2006; Ganz and Hsue, 2009).

The main objective of the studies described in this thesis is to develop devices and methods for the simultaneous assessment of the dynamics of coronary pressure and flow. Additionally, to improve the interpretation of the hemodynamical measurements for the detection different types of disease, a numerical model of the heart and coronary circulation is developed. This introductory chapter covers the basic features of the anatomy and physiology of the coronary circulation, the available diagnostic techniques for the detection of coronary circulatory disease, and the conceptual models to describe coronary hemodynamics. Finally, the outline of this thesis is given, introducing the different chapters.

1.2 The coronary circulation

The function of the human cardiovascular system is to transport blood with nutrients and waste products between the different organs. The driving force of this system is the contraction of the heart. The heart is a four chambered muscle, which propels blood from the venous system, through the pulmonary circulation, to the systemic arterial system.

The coronary arteries supply the heart itself with blood and originate just distal from the aortic valve (Fig. 1.1). The coronary circulation consists of a network of different serial compartments. Epicardial arteries, with a typical diameter ($\varnothing$) of 4-2.5 mm, branch via smaller arteries and arterioles, into a capillary network where the exchange of oxygen, metabolic waste, and nutrients takes place. Compared to the microcirculation ($\varnothing < 200$ μm), the resistance to blood flow in the large conductive vessels ($\varnothing > 400$ μm) is negligible (Aarnoudse et al., 2004a). As part of the microcirculation, the arteriolar vessels ($\varnothing < 100$ μm) constitute the largest resistance to flow and can regulate their vascular tone to match the blood flow to the myocardial demand. In response to exercise, this autoregulatory mechanism can increase the blood flow four- to six-fold. The capillary bed forms a network

of interconnected vessels of similar diameters ($\varnothing \approx 5\ \mu$m), with approximately one capillary per myofiber. During hyperaemia, when the arteriolar vascular tone is relaxed, the capillaries offer the most resistance to blood flow. After passing the capillary bed, the blood collects in the coronary veins and flows back into the right atrium via the coronary sinus. Besides this serial network there are also collateral vessels interconnecting different coronary arteries. These collaterals are only functional in the presence of possible obstructions in the coronary arteries and can function as a natural bypass.

Due to the unique location of the coronary arteries, being embedded in the cardiac muscle, the flow in the coronary arteries is highly influenced by the beating heart. Scaramucci already hypothesized in 1689 (Porter, 1898) that coronary flow is impeded in the period the heart contracts. Due to this contraction and the resulting high ventricular pressure, the pressure in the myocardium increases, impeding the arterial flow and augmenting venous outflow. Compared to systole, this results in a relatively high flow in diastole. In section 1.4, this mechanism is explained further.

The mechanical properties of the coronary arterial wall are an important factor in both the mechanical treatment of atherosclerosis and describing the relation between the pressure and flow waves in the coronary arteries. Therefore, the morphology and mechanical behaviour of the coronary arterial wall is described in the next section.

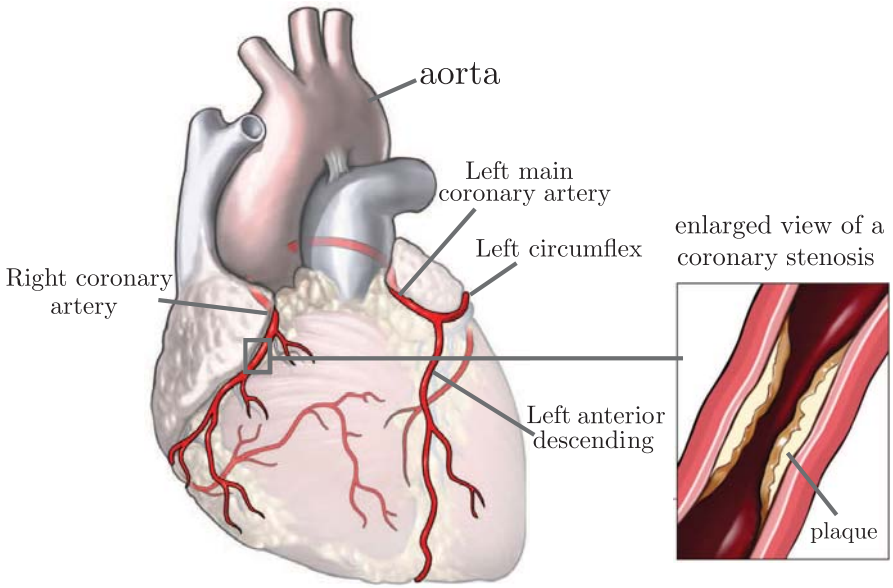

Figure 1.1: *The heart and the main coronary arteries, including a schematic representation of a stenosis in the right coronary artery. (Medical Illustrations copyright ©2012 Nucleus Medical Art, Inc. All Rights Reserved. www.nucleusinc.com)*

1.2.1 The coronary arterial wall

The wall of the coronary arteries is composed of three main layers, each with its own structure and cell type. The inner layer, or intima, is in contact with the blood and consists of an endothelial monolayer and the internal elastic lamina. The media consists of layers of nearly circumferentially oriented smooth muscle cells (Clark and Glagov, 1985) and collagenous and elastin bundles. The outermost layer, or adventitia, mainly consists of collagen fibers (Rhodin, 1980).

The mechanical behaviour of the arterial wall depends on the composition and orientation of the different components, which are constantly remodeling to adapt to their environment (Humphrey et al., 2009). Figure 1.2a shows the typical mechanical behaviour of a (passive) coronary artery. The pressure-diameter relation of coronary arteries clearly demonstrates a highly non-linear behaviour, with increased stiffness at high pressures. Experiments with removal of either elastin or collagen (Roach and Burton, 1957) indicated that this non-linear stiffening is the result of gradual straightening of a distribution of initially wavy collagen fibers (Lanir, 1979). Besides the non-linear pressure-diameter relation, arteries also display a characteristic behaviour in the axial direction (Fig. 1.2b). At high axial stretches the axial force increases with increasing pressure, while the axial force decreases at low axial stretch. At a certain transition axial stretch the axial force is invariant to variations in the pressure. This transition stretch was first indicated by van Loon (1977) and Weizsäcker et al. (1983) as the physiological axial pre-stretch of an artery, which was confirmed in later studies (Humphrey et al., 2009). For porcine coronary arteries this transition stretch was investigated by Van den Broek (2010), which showed that the magnitude of this transition stretch based on axial force measurement was similar to the stretch determined on an isolated beating heart. The transition stretch found was 1.37 ± 0.02, which was comparable to other studies that determined the coronary axial stretch (Kassab et al., 2002; Carboni et al., 2007).

The different models explaining this mechanical behaviour are discussed in section 1.4.2.

1.3 Diagnosis of coronary circulatory disease

1.3.1 Anatomic assessment of coronary artery disease

The most commonly used method to determine the severity of a coronary stenosis is coronary angiography. Here, a contrast agent is infused into the coronary arteries and using X-ray imaging a projection of the lumen of the arteries is made. A stenosis then shows as a narrowing of this lumen (Figure 1.3a). There are several limitations in using angiography to quantify the severity of coronary circulatory disease. The shape of a stenosis can be over- or underestimated, since two-dimensional (2D) projections are made of a three-dimensional (3D) geometry (Isner et al., 1981) (see Fig. 1.3b). Furthermore, the shape of the stenosis, being highly irregular or more smooth, is important for the actual flow impediment. With intravascular ultrasound (IVUS) or optical coherence tomography (OCT) a very accurate image can be made

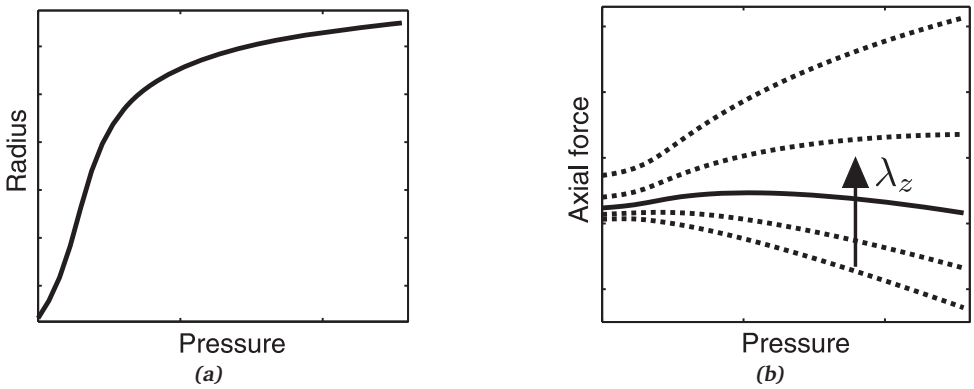

Figure 1.2: a) *An example of the pressure-radius relation of a coronary artery.*
b) *An example of the pressure-axial force relation of a coronary artery at different axial stretches (λ_z). The solid line represents the physiological axial stretch.*

of the coronary lumen, showing the exact shape of the stenosis. However, even with the exact geometry known, the functional significance of a stenosis can still not be assessed, because the pressure and flow also depends on the presence of collaterals, size of the perfusion area, and microvascular resistance. Another disadvantage of angiography is that the microvessels cannot be visualized, limiting its use to the large epicardial arteries.

1.3.2 Assessment of coronary circulatory disease via hemodynamic measurements

Advancements in sensor-tipped guidewires enabled the assessment of coronary pressure and flow. This resulted in several indices based on pressure and/or flow measurements to quantify and distinguish between different types of disease. In this section the different indices are discussed.

Coronary flow reserve (CFR) was the first index developed based on intracoronary measurements (Gould et al., 1990). It is defined as the ratio of hyperaemic to resting flow and is therefore a measure for the capacity of the resistive vessels to augment blood flow, e.g. in response to an increased metabolic demand. Without the presence of disease the maximum CFR is approximately five. In case of a flow impeding disease, the autoregulatory mechanism will already lower the arteriolar resistance in resting conditions to compensate for the increased resistance. A CFR below two is generally considered to be the value below which treatment is required. There are several limitations associated with the concept of CFR. It is unable to discriminate between an epicardial stenosis and microvascular disease and age, heart rate, and mean arterial pressure all affect CFR, due to its dependency on the resting flow.

To overcome the limitations of CFR in assessing the severity of a stenosis, the index of fractional flow reserve (FFR) was developed (Pijls et al., 1996). FFR is defined as the average hyperaemic flow in the presence of a stenosis ($\bar{Q}^S_{hyp}$) relative to the

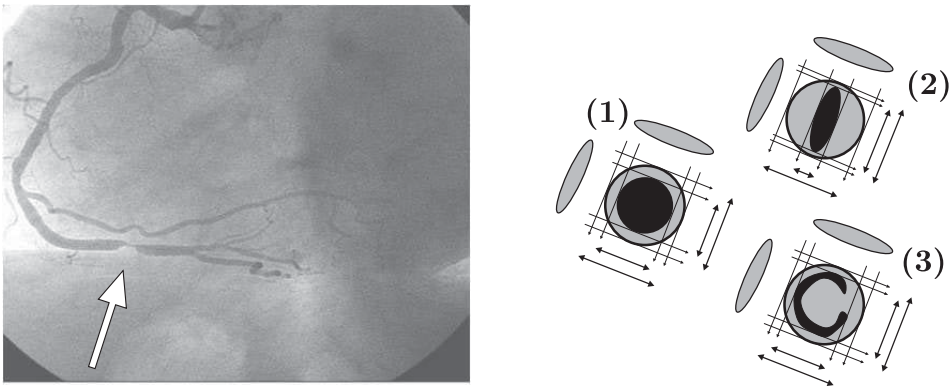

(a) *(b)*

Figure 1.3: a) *An angiogram showing a stenosis (indicated by the white arrow) in one of the coronary arteries.* ***b)*** *Schematic representation of the x-ray projections of different types of stenoses showing that the 2D projections can be misleading in the assessment of the geometry of a stenosis. The black area represent the lumen with blood (and contrast fluid). For the artery without stenosis (**1**) the projection from both sides is equal. One of the projections of the oval shaped lumen (**2**) appears normal, while the other appears severely narrowed. The severely narrowed vessel shown in (**3**) even appears normal in both projections. Adapted from Van 't Veer (2008).*

average hyperaemic flow if there were no stenosis present ($\bar{Q}^N_{hyp}$). If it is assumed that the myocardial resistance (R_{myo}) is minimal and constant and the central venous pressure is negligibly small compared to the perfusion pressure ($P_v \ll P_d$) the FFR can be described by the ratio of average pressures (see Fig. 1.4):

$$FFR = \frac{\bar{Q}^S_{hyp}}{\bar{Q}^N_{hyp}} \simeq \frac{(\bar{P}_d - \bar{P}_v)/R_{myo}}{(\bar{P}_a - \bar{P}_v)/R_{myo}} \simeq \frac{\bar{P}_d}{\bar{P}_a}, \tag{1.1}$$

Here, P_a and P_d are the aortic pressure and pressure distal to a stenosis, respectively. While CFR only indicates that disease is present somewhere in the coronary circulation, FFR quantifies the severity of a specific coronary stenosis. Especially, with multiple stenoses or in combination of microvascular disease FFR can interrogate whether an individual stenosis should be treated or not. The cut-off value below which treatment is required currently is 0.8 (Tonino et al., 2009). Although some of the assumptions that are made are subject to controversy in literature (Meuwissen et al., 2002b; Spaan et al., 2006), it was demonstrated by Tonino et al. (2009) that compared to angiography-based treatment, FFR-based treatment greatly reduces major adverse cardiac events after PCI.

Based on both pressure and velocity measurements the hyperaemic stenosis resistance index (h-SRv) was developed as a direct measure of the resistance of a stenosis (Meuwissen et al., 2002a). h-SRv is defined as the ratio of the average pressure gradient over a stenosis and the average peak velocity. Above a cut-off value

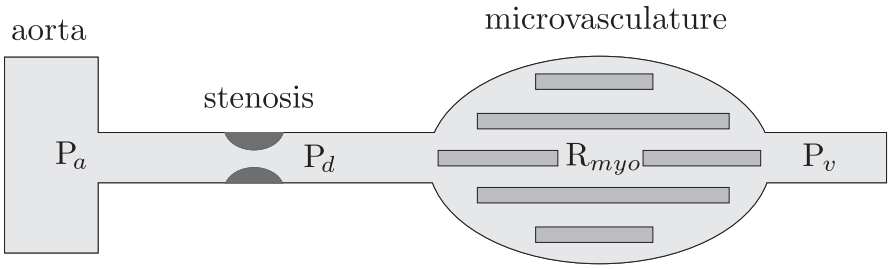

Figure 1.4: *Schematic representation of the coronary circulation with a stenosis in an epicardial artery.*

of 0.8 mmHg s cm^{-1} a stenosis is considered severe and should be treated. The main advantage, compared to FFR, is that no assumptions regarding the microvasculature are required. Meuwissen et al. (2002a) also showed that h-SRv is a better indicator of the functional significance of intermediate size stenoses. The disadvantage of this method compared to FFR is that coronary flow velocity is required, which is, as discussed before, more difficult to obtain than pressure.

A similar index, based on pressure and flow velocity measurements, was proposed to determine the resistance of the microvasculature. The hyperaemic microvascular resistance (h-MRv) is defined as the ratio of the average perfusion pressure and the average peak velocity. Although so far it is mainly used to determine changes in microvascular resistance resulting from PCI (Meuwissen et al., 2002a; Verhoeff et al., 2005), recently Kitabata et al. (2009) showed that h-MRv was a useful predictor of the transmural extent of an infarction.

Another index specific for the coronary microvasculature is the index of microvascular resistance (IMR), which is also defined as the ratio of the perfusion pressure and myocardial flow (Fearon et al., 2003). The flow is determined with a bolus injection thermodilution method, where the inverse of the mean transit time of this bolus is a measure for the flow. *In-vitro* (Aarnoudse et al., 2004b), animal (Fearon et al., 2004), and human (Aarnoudse et al., 2004a) studies indicated that, if the average pressure at zero flow (or wedge pressure) is taken into account, IMR is a good measure for the myocardial resistance.

All previous indices are based on time-averaged values of pressure and flow to determine an direct or indirect measure for the average resistance value. The coronary circulation, however, is a dynamic system which is greatly influenced by the contraction of the cardiac muscle. Figure 1.5 shows the characteristic shape of the pressure and flow signals in the left main coronary artery, with flow predominantly occurring in diastole. Several indices have been developed to utilize the time-dependent behaviour of coronary pressure and/or flow to quantify different types of disease. For example, the deceleration time of diastolic flow velocity (DDT) has been shown to be a measure for the compliance of the myocardial tissue. Among others, Hozumi et al. (2003) and Okcular et al. (2010) have shown that DDT is a good predictor for the recovery of myocardial viability after an acute myocardial infarction.

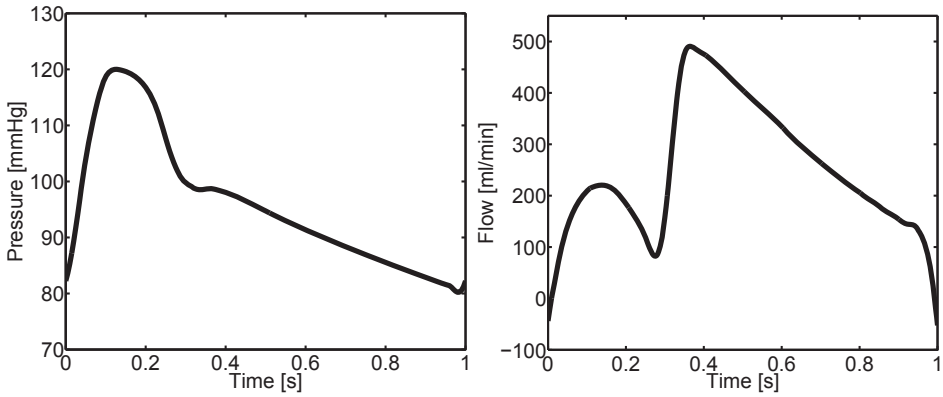

(a) *(b)*

Figure 1.5: *A typical example of the dynamics of coronary pressure* ***(a)*** *and flow* ***(b)****.*

Another index that makes use of the time-dependent pressure flow relation is the instantaneous hyperaemic diastolic velocity-pressure slope (IHDVPS), which is defined as the conductance of the flow velocity-pressure relation during diastole (Mancini et al., 1989). It was shown that this index, compared to CFR, is useful for quantification of coronary stenoses, with minimal hemodynamic dependency (Mancini et al., 1989; Di Mario et al., 1994). Escaned et al. (2009) applied this index for the assessment of coronary microvascular disease and found it to be superior to CFR in detecting structural microcirculatory changes. Based on this diastolic conductance index, Krams et al. (2004) developed a relative index: diastolic coronary vascular reserve (DCVR), which is defined as the ratio of hyperaemic over resting diastolic conductance. Compared to CFR, DVCR is less sensitive to systolic extravascular compression and may therefore be more useful for studying microcirculatory changes in human disease states where, e.g., ventricular hypertrophy is present.

Wave intensity analysis (WIA) is a time-domain method developed by Parker and Jones (1990), to characterize the traveling waves in the arterial system. It is based on the method of characteristics and states that every wave can be reconstructed by the superposition of infinitesimal wavefronts. An advantage of this method, compared to frequency-domain methods, is that no assumptions need to be made regarding the periodicity or linearity of the system. By simultaneous pressure and flow (velocity) measurements it is possible to separate the forward and backward components that make up the pulse waveforms, if the pulse wave velocity is known. These forward and backward traveling compression and expansion waves can provide valuable information on the conditions of the system upstream and downstream of the measuring site (Parker, 2009). WIA was applied to the coronary arteries to study the origin of the coronary waveform characteristics (Sun et al., 2000; Davies et al., 2006a; Hadjiloizou et al., 2008). The clinical applicability, however, was questioned by Kolyva et al. (2008), due to difficulties determining the wave speed in coronary arteries.

1.4 Modeling coronary hemodynamics

Figure 1.5 demonstrates the characteristic dynamics of coronary pressure and flow. The pressure is similar to the aortic pressure, with high pressure in systole, while the flow is markedly diastolic dominated. There are basically four conceptually different mathematical models proposed in literature describing coronary-cardiac interaction to explain the mechanism that governs this hemodynamic behaviour.

The systolic extravascular resistance model was proposed by Gregg and Green (1940). The model was based on the assumption that during systole the coronary resistance is higher than in diastole. The mechanism responsible for this increase in resistance was, however, not elucidated. Several phenomena cannot be explained by this model, including the out-of-phase behaviour of arterial and venous flow and the occurrence of retrograde flow.

Downey and Kirk (1975) introduced the vascular waterfall model, in which the vessels are assumed to collapse when the intramyocardial tissue pressure exceeds the pressure in the intramyocardial veins. Since the intramyocardial pressure varied from ventricular pressure at the endocardium to zero at the epicardium, it could explain the increased flow impediment in the subendocardium. However, as with the systolic extravascular resistance model, it was unable to explain retrograde flow and out of phase behaviour of arterial and venous flow.

The compliance of the intramural vessels was taken into account in the intramyocardial pump model (Spaan, 1985). In this model, the ventricular cavity pressure serves as the extravascular pressure on the compliant vessels. In systole, the ventricular cavity pressure squeezes blood out of the compliant coronary vessels, impeding arterial inflow. In diastole the vessels recoil, augmenting arterial inflow and decreasing venous outflow. Bruinsma et al. (1988) later adjusted the model to incorporate varying resistances based on the diameters of the vessels.

The time-varying elastance model was first proposed by Suga et al. (1973) and applied to explain coronary hemodynamics by Krams et al. (1989). This model is basically similar to the intramyocardial pump model, except that the pump action is generated by the varying elastance of the myocardium instead of transmission of the ventricular pressure. This concept is inspired by the observation that the systolic coronary flow is also impeded in empty isolated beating hearts where no ventricular cavity pressure is generated. However, without taking the ventricular pressure into account, the differences between subendocardial and epicardial flow cannot be explained.

A more elaborate model incorporating the active myofiber mechanics, perfusion, and mass transport was developed by Zinemanas et al. (1994). Although with increasing complexity more experimental observations could be replicated, the number of model parameters also increased, making it more difficult to determine critical model parameters pin-pointing different types of disease. A less complex model, which relates the mechanics of myofibers to global left ventricular mechanics was developed by Bovendeerd et al. (2006). With this model, most systemic and coronary hemodynamical features could be replicated with a limited number of parameters.

1.4.1 Computational modeling of arterial hemodynamics

The most accurate way to model the pressure and flow in large arteries is by full 3D analysis with appropriate fluid-structure interactions. Using this 3D approach, detailed information can be obtained regarding pressure gradients and velocity fields. This is especially of interest at regions where secondary flow is expected, e.g., at the aortic valve leaflets, bifurcations, stenoses, or aneurysms. These 3D simulations are, however, computationally very expensive and consequently can only be applied to small segments of the arterial system. Simplified models describing the cardiovascular system are then required to serve as boundary conditions proximal and distal to the 3D segment. These models can be either lumped Windkessel models or distributed electrical transmission line or wave propagation models. Windkessel models consist of elements analog to electrical resistors, capacitors, and inductors. While these models have proven to be very useful in describing the behaviour of the entire systemic tree, distributed electrical transmission line and 1D wave propagation models are more suitable to describe pressure and flow waves in the individual arteries. Compared to transmission line theory, wave propagation models based on the 1D balance of mass and momentum equations (Hughes and Lubliner, 1973) are able to describe non-linear phenomena better with a limited number of segments. To solve the wave propagation equations, assumptions are required to describe the pressure dependency of vessel distension. Furthermore, a choice has to be made for the radial distribution of the blood velocity. Often simple parabolic profiles (Huo and Kassab, 2007) or flat profiles (Formaggia et al., 2006) are assumed. More realistic profiles that take into account both inertial and viscous forces in the fluid include Womersley (Womersley, 1957; Reymond et al., 2009) or approximate velocity profiles (Bessems et al., 2007). The main advantage of the model by Bessems et al. (2007) is that it does not require frequency analysis, while providing proper estimates of the non-linear and friction terms in the momentum equation.

1D wave propagation models of the coronary epicardial arteries have been reported in several studies. Smith et al. (2002) and Huo and Kassab (2007) applied 1D models to vessels representing the coronary arterial anatomy. In these studies, however, the interaction with the cardiac muscle was not taken into account. This interaction with the cardiac muscle was taken into account in the 1D model of Mynard and Nithiarasu (2008), where the vessels were loaded with an approximated left ventricular pressure. Recently, as part full systemic arterial tree, Reymond et al. (2009) coupled a 1D model to a time-varying elastance model to describe the relation between ventricular pressure and volume and to model coronary hemodynamics.

In **chapter 3**, a model is presented and validated that couples a 1D wave propagation model (Bessems et al., 2007), to the single-fiber heart contraction model by Bovendeerd et al. (2006). The main advantage of combining these models is that this heart model, compared to more phenomenological models, is based on microstructural material and macrostructural geometrical properties. This enables the simulation of cardiac disease with physiology-based parameter changes, while the 1D vessel representation allows for both the coupling to a more detailed 3D model and the investigation of the global dynamics of the coronary pressure and flow in health and disease.

1.4.2 Modeling of the coronary arterial wall

Several models have been proposed to model the coronary arterial wall. In the first phenomenological models, exponential (Fung et al., 1979), polynomial (Vaishnav et al., 1973), and logarithmic (Takamizawa and Hayashi, 1987) strain-energy functions have been used to model the mechanical behaviour of the arterial wall. A disadvantage of these models is that they require many parameters to capture experimental observations and, additionally, the material constants do not have a direct physical meaning. More recently, models were developed which do take the microstructure into account. Holzapfel et al. (2000) modeled the arterial wall as a fiber reinforced material with the fibers, representing collagen, oriented as a cross-ply (Fig. 1.6a). To include fiber dispersity, Driessen et al. (2005) added an angular fiber distribution function to this model. Based on the ideas of Lanir (1979), the non-linear, anisotropic behaviour was modeled by Zulliger et al. (2004a), describing the recruitment of the wavy collagen fibers.

While it has been demonstrated that the parameters of these micro-structure-based models can be fitted accurately to experimental data obtained *in-vitro* or *in-situ*, clinically available data essentially lack information regarding the stress-free geometry, which is required in the procedure of fitting the model parameters. Van den Broek et al. (2011) showed that using a model similar to Driessen et al. (2005), with a generic material parameter set, the mechanical behaviour of different porcine coronary arteries could be described accurately. The only information required was a radius measurement at physiological loading and the corresponding pressure. While this generic approach can be very useful, e.g. in the development of PTCA catheters, this approach may not be applicable for individualized diagnosis and treatment, since large variations in the material behaviour are expected due to aging or disease. A way to make fitting of a constitutive model to clinical measurements in individual arteries possible without over-parameterization issues, is by putting appropriate constraints on the fitting procedure (Stålhand and Klarbring, 2005). In **chapter 2** the model developed by Holzapfel et al. (2000), was fitted to measurements described in Van den Broek et al. (2011) to investigate whether it is possible to put constraints to the most important parameter of the model; the collagen fiber orientation.

1.5 Devices to measure coronary pressure and flow

The most commonly used method to measure pressure in the coronary arteries is using a guidewire with a pressure sensor mounted at its tip. These pressure wires are very thin (∅ 0.36 mm) and are normally inserted percutaneously via the femoral or radial artery. Using these pressure wires the dynamics of pressure in the coronary arteries can measured very accurately and reliably.

Flow measurement in arteries is more challenging, mainly due to the radial dependence of the blood velocity profile. For invasive flow assessment, three types of techniques are available: Indicator-dilution methods, Doppler methods, and thermal-convection methods. The indicator-dilution technique can be based on either rapid bolus injection or continuous infusion of the infusate. The rapid bolus injection

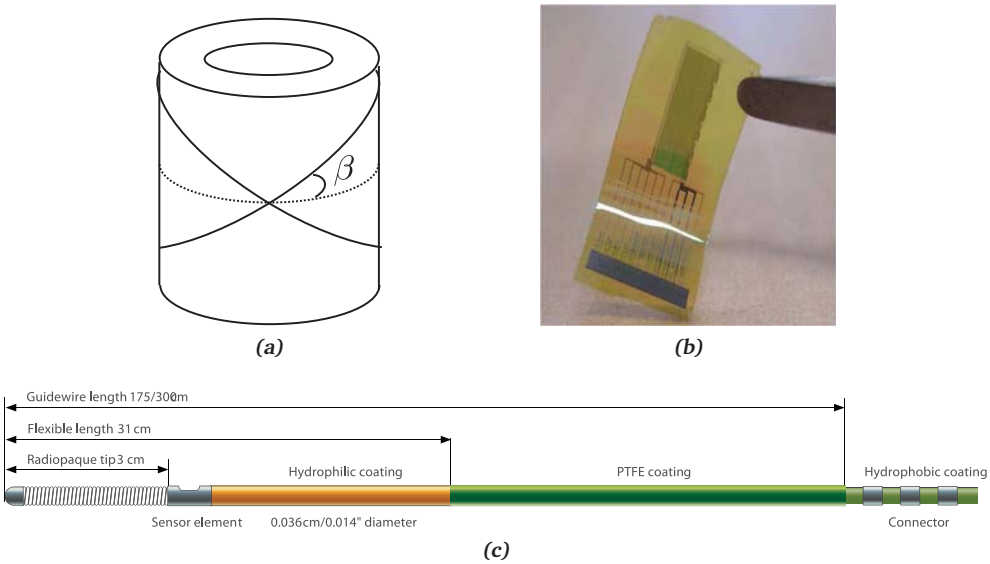

Figure 1.6: ***a)*** *Schematic representation of the arterial wall with embedded fibers oriented as a cross-ply .* ***b)*** *An image of the flexible thermal flow sensor developed by Haartsen (2007).* ***c)*** *The PressureWire Certus^{TM}. Adapted from St. Jude Medical (St. Paul, MN) (www.sjmprofessional.com).*

technique has been applied to the coronary circulation among others by Pijls et al. (2002) and Barbato et al. (2004), where a bolus injection of cold saline solution was given through a guiding catheter at the coronary ostium. The mean transit time or shape of the temperature curve was then recorded with temperature measurements downstream in a coronary artery by a pressure-temperature sensor-tipped guidewire (PressureWire Certus, St. Jude Medical, St. Paul, MN)[1]. Although it was found that this method was reliable for the assessment of CFR, it was not suitable for absolute flow rate detection. A continuous thermodilution method was developed by Van 't Veer et al. (2009) to measure absolute coronary flow. A specially designed infusion catheter was manufactured to provide proper mixing of the continuously infused colder infusate with the blood. By measuring the temperature at a certain distance distal to the infusion catheter, absolute flow could be assessed. While this method has been successfully applied in the clinic (Aarnoudse et al., 2007), a disadvantage of this method is that it requires extra, time-consuming, steps in the catheterization procedure and is only suitable for assessing the average flow.

Invasive assessment of coronary blood velocity can be performed with a guidewire with a Doppler-crystal at the tip. This method uses the Doppler effect to detect the velocity of red blood cells. A guidewire that combines a Doppler-crystal with a pressure sensor for simultaneous pressure and blood velocity assessment is available (ComboWireXT, Volcano, San Diego, CA). While compared to the other flow measurement techniques, this method is used most in the clinic, adequate Doppler-

[1]Formerly: Radi Medical Systems AB, Uppsala, Sweden

derived velocity signals can be difficult to obtain (Kern et al., 2006; Ganz and Hsue, 2009). Furthermore, to be able to relate the measured signal to flow, both the cross-sectional area of the artery and the velocity profile are required.

The thermoconvective method has been used already four decades ago for blood flow velocity measurements (Seed and Wood, 1970a,b, 1972; Clark, 1974; Nerem et al., 1976; Paulsen, 1980a,b). A thin film mounted on a probe was held at a constant temperature, a few degrees above blood temperature. The probe (typically L-shaped with a diameter of 1 mm), was introduced into a vessel by puncturing the vessel wall. The supplied electrical power could be related to the blood flow using calibration methods based on models describing the heat transfer between the film and the blood (Bellhouse and Rasmussen, 1968; Pedley, 1972a,b, 1976a). At that time, the main drawback of this method was the size of the probe, influencing blood flow in small arteries, and the necessity to insert the probe through the vessel wall at the location of measurement. Although the principle of hot-film anemometry is still widely used in fluid dynamics, the technique was abandoned for clinical applications. Nowadays, due to the miniaturization of sensors on guidewires this technique might be applicable for coronary flow assessment. Therefore, in **chapter 4** we investigate whether it is possible to use a pressure wire, similar to the one depicted in Figure 1.6c, as a thermal anemometer to assess CFR. In **chapter 5** this technique is combined with the continuous thermodilution method to investigate the feasibility of this combined methodology to assess the dynamics of volumetric flow.

Haartsen (2007) developed a thermal sensor on a flexible chip, based on the CIRCONFLEX technology (Dekker et al., 2005), to measure local flow rates. This sensor, depicted in Figure 1.6b, consists of two thermopiles and a heating element embedded in a polyimide film. The heating element is operated at constant power and the temperature differences measured by the thermopiles are a measure for the flow at the sensor surface. Due to the flexibility of the chip, this sensor device can potentially be mounted on a guidewire. Compared to the anemometric method with the pressure wire, where an existing devices is operated in a alternative way, the sensor on the chip can be specially designed for coronary flow assessment. Furthermore, by measuring the temperature difference between a proximal and distal location of the heater, flow reversal, which is not uncommon in coronary arteries, can be determined. To be able to optimize this sensor for coronary flow assessment, this type of sensor is further investigated by analytical, numerical, and experimental characterization in **chapters 6** and **7**.

1.6 Aim and outline of this thesis

The general aim of the work described in this thesis is to develop guidewire-mounted sensors capable of measuring the dynamics of coronary pressure and flow. To accomplish this, two different pathways were chosen. In the first, an already clinically used pressure-sensing guidewire is operated in such a way that flow could also be assessed. This approach had some drawbacks inherent to the fact the device originally was not designed for flow measurement. Therefore, in collaboration with the Flexible and Stretchable Electronics group of the Delft University of Technology,

also a new thermal sensor was developed, specially designed to be mounted onto a guidewire. The basic design of the flow sensor element consisted of a heater and thermocouples measuring the temperature difference up- and downstream from the heater, embedded in a flexible polyimide substrate.

Since the guidewire-mounted sensors are only able to directly measure the pressure and flow waves in relatively large epicardial arteries, an appropriate model is required to detect microvascular or cardiac disease from hemodynamical measurements. For that reason, a model is constructed to describe the effect of different combinations of coronary and cardiac pathologies on pressure and flow waves in the epicardial arteries. As part of that model, the mechanical properties of the coronary arterial wall are required.

In **chapter 2**, it is described how a fiber-reinforced hyperelastic model of the arterial wall was fitted to inflation-extension experiments on porcine and human coronary arteries. The fiber orientation at physiological loading, determined with the model, was studied to improve the feasibility of fitting the model to clinically obtained patient-specific data. The obtained results were simplified to be incorporated into the model of the coronary circulation, which is presented in **chapter 3**. The model comprises a heart contraction model, a 1D description of the aorta and epicardial coronary arteries, a stenosis element, and Windkessel elements to model the combined contribution of the all other arterial and microvascular vessels. Via experimental observations described in literature the model was validated for coronary and cardiac disease.

In **chapter 4** it is explained how the pressure-sensing guidewire was operated as a thermal anemometer to assess local flow rate. In an *in-vitro* set-up it was investigated whether this method was able to reliably determine CFR. The method is enhanced in **chapter 5**, to enable simultaneous assessment of pressure and flow, instead of sequential measurements. In this chapter the feasibility of combining this anemometric method with a continuous thermodilution method, to assess volumetric flow dynamics, was determined.

In the process of the design of the new flow sensor, an analytical model was developed to determine the importance of the different design parameters. In **chapter 6**, this analytical model is presented and validated with *in-vitro* measurements. Towards a final design of the sensor, a finite element model was used to investigate whether the sensor should be operated at constant power or constant temperature. This is described in **chapter 7** and a final geometry was proposed to be tested in further research.

Finally, in **chapter 8** the main findings of the aforementioned chapters are discussed and put in broader perspective. General conclusions are drawn and recommendations are provided for further research.

Chapter 2

The fiber orientation in the coronary arterial wall at physiological loading evaluated with a two-fiber constitutive model

A patient-specific mechanical description of the coronary arterial wall is indispensable for individualized diagnosis and treatment of coronary artery disease. A way to determine the artery's mechanical properties is to fit the parameters of a constitutive model to patient-specific experimental data. Clinical data, however, essentially lack information about the stress-free geometry of an artery, which is necessary for constitutive modeling. In previous research, it has been shown that a way to circumvent this problem is to impose extra modeling constraints on the parameter estimation procedure. In this study, we propose a new modeling constraint concerning the in-situ fiber orientation (β_{phys}). β_{phys}, which is a major contributor to the arterial stress-strain behaviour, was determined for porcine and human coronary arteries using a mixed numerical-experimental method. The in-situ situation was mimicked using in-vitro experiments at a physiological axial pre-stretch, in which pressure-radius and pressure-axial force were measured. A single layered, hyperelastic, thick-walled, two-fiber material model was accurately fitted to the experimental data, enabling the computation of stress, strain, and fiber orientation. β_{phys} was found to be almost equal for all vessels measured (36.4 ± 0.3)$^\circ$, which theoretically can be explained using netting analysis. In further research, this finding can be used as an extra modeling constraint in parameter estimation from clinical data.

The contents of this chapter are based on Arjen van der Horst, Chantal N. van den Broek, Frans N. van de Vosse, and Marcel C.M. Rutten, The fiber orientation in the coronary arterial wall at physiological loading evaluated with a two-fiber constitutive model. *Biomech Mod Mechanobiol*, **11**; 533–542, 2012.*

* *Parts also printed in C.N. van den Broek, PhD thesis (2010), chapter 5.*

2.1 Introduction

Insight into the mechanical properties of the coronary arterial wall can give valuable information concerning the genesis and progress of atherosclerosis, wall remodeling, and the prediction of the effects of medical intervention, e.g., balloon angioplasty (Holzapfel et al., 2000; Humphrey et al., 2009).

A widely used approach to characterize the mechanical properties of arteries is based on a mixed experimental-numerical method, in which parameters of a constitutive model are fitted to experimental stress-strain data. In a previous study, it was shown that using a generic material parameter set, with average morphologic parameters, the mechanical behaviour of different porcine coronary arteries could be described accurately (van den Broek et al., 2011). The only information needed then was a radius measurement at physiological loading and the corresponding pressure. This generic approach can be very useful, e.g., in the development of PTCA catheters, intended to be used in a patient population, from which the specific arterial properties are unknown a priori. However, for individualized diagnosis and treatment, this approach may not be applicable, since large variations in the material behaviour are expected due to aging or disease.

Other studies adopted a patient-specific modeling approach to assess the elastic modulus or distensibility from a clinically obtained pressure-radius relation (Hansen et al., 1995; Vavuranakis et al., 1999). More recently, constitutive models that take the microstructure into account, were fitted to patient data (Masson et al., 2008; Stålhand, 2009). This had the advantage that pathologies could be related to the parameters associated with different tissue components. An obvious challenge in the parameter estimation based on clinical data, is the limited amount of information in the measured signals. For example, they do not provide any information regarding the axial strain, the radial deformations in the low pressure range, and the stress-free geometry. Including all these extra unknown parameters in the estimation procedure can easily result in over-parameterization. To overcome this problem, extra optimization constraints can be incorporated into the fitting protocol. From *in-vitro* studies, it is well known that at physiological axial strain, the external axial force is independent of the internal pressure (van Loon, 1977; Weizsäcker et al., 1983). Several studies used this pressure-invariant axial force constraint to fit models to clinical data. Stålhand and Klarbring (2005) incorporated it as a loose constraint into the estimation procedure in combination with a thick-walled, Fung type, material model and successfully validated it with *in-vivo* data from a human aorta. Furthermore, making use of a methodology that was first proposed and successfully applied by Schulze-Bauer and Holzapfel (2003), Stålhand (2009) was even able to fit a more microstructurally based, thin-walled, two-fiber constitutive model (Holzapfel et al., 2000), to clinical data obtained from human aortas. Besides the pressure-invariant axial force constraint, this methodology comprises a second constraint, which prescribes the ratio of axial to circumferential stress at a certain characteristic pressure. The combination of the two constraints avoided over-parameterization, thus rendering a unique set of parameters. A drawback of this approach is that the value of the stress-ratio constraint was adopted from *in-vitro* animal experiments

(Fung et al., 1979), which may not directly apply to (pathological) human arteries. Since a thin-walled approach was used, residual stresses were not taken into account. Furthermore, in the studies mentioned, no validation with respect to the axial force and radius in the low pressure range was reported.

Stålhand et al. (2004) also used the two-fiber model but in combination with a thick-walled approach and without the extra constraints. The parameters of the model, including residual stresses, were successfully estimated from *in-vivo* human aortic data. However, to avoid over-parameterization, the parameter that accounts for the orientation of the collagen fibers in the stress-free configuration had to be prescribed. Since collagen is the main load-bearing structure in arteries at physiological load levels, it is evident that prescribing this parameter will highly influence the estimation results. There are several stress- or strain-based hypotheses that could explain the fiber organization in fibrous tissues (Baaijens et al., 2010). These hypotheses, however, do not provide a clear and unambiguous procedure how to tackle over-parameterization.

This study therefore aims to gain more insight into the fiber orientation at physiological loading conditions and to describe this with a relatively simple two-fiber constitutive model.

Hereto, *in-vitro* measurements were performed on porcine and human coronary arteries, at physiological axial pre-stretch. The inner radius and reduced axial force were measured, while the artery was loaded with a dynamic pressure. Taking into account that the results should be applicable to clinical data, a constitutive model with a limited number of parameters is preferable. Therefore, a thick-walled, 1D, single-layered, fiber-reinforced model, of which the constitutive equations were developed by Holzapfel et al. (2000) and used for parameter estimation from clinical data (Stålhand et al., 2004; Stålhand, 2009), was used in this study. Residual stresses were incorporated into the model by minimizing the circumferential stress gradients at physiological pressure by introducing a stress-free geometry with an opening angle (Chuong and Fung, 1986; Takamizawa and Hayashi, 1987). An estimation procedure was employed to fit the parameters of the model to the experimental data over the entire pressure range. The model was then used to compute the stress, strain, and global morphological parameters at physiological loading.

2.2 Materials and methods

2.2.1 Experimental procedure

Since the experimental set-up used has already been described in detail in Van den Broek et al. (2011), only a short summary of the experimental procedure is presented here. Porcine hearts ($n = 7$) were obtained from a local slaughterhouse. Human coronary artery segments ($n = 2$) were obtained from explanted hearts from patients with heart failure receiving a donor heart at the Herz- und Diabeteszentrum Nordrhein-Westfalen (HDZ-NRW, Bad Oeynhausen, Germany). The study was approved by the local medical ethics committee. Patient details can be found in Table 2.1.

Table 2.1: *Patient data, and the measured $\lambda_{z,phys}$. m, male; dTGA, dextro-Transposition of the great arteries; lTGA, levo-Transposition of the great arteries; Minor IT, Minor intimal thickening.*

	Sex	Age (yrs)	Heart disease	Status LAD	$\lambda_{z,phys}$
1	m	26	dTGA	Minor IT	1.3
2	m	41	lTGA	Minor IT	1.15

A proximal segment of the left anterior descending coronary artery (LAD) was excised from the heart and cannulae were sutured to the proximal and distal ends of the segment. The length between the sutures was measured, representing the unstretched length (l_0). Side branches, about 5-6 per arterial segment, were closed using small stainless steel arterial clips (Ligaclip® Extra, Ethicon Endo-Surgery Inc., Cincinnati, OH). The vessel was placed in an organ bath (Fig. 2.1), containing a Kreb's solution, which was kept at a temperature of 37°C and 38°C for the human and porcine arteries, respectively. The vessel was mounted to the set-up by connecting the cannulae to silicone rubber tubes, making it part of a closed circuit. A pressure pump, which was driven by a pneumatic proportional valve (Festo, The Netherlands), was used to create a pulsatile pressure (p), which was measured with a pressure transducer (P10EZ, BD, USA). The length of the vessel could be controlled with a linear actuator and controller (235.5 DG and C843, Physik Instrumente, Germany), which was connected to the proximal cannula. The axial force (F_z) was measured with a force transducer (J&M Instruments, The Netherlands), which was connected

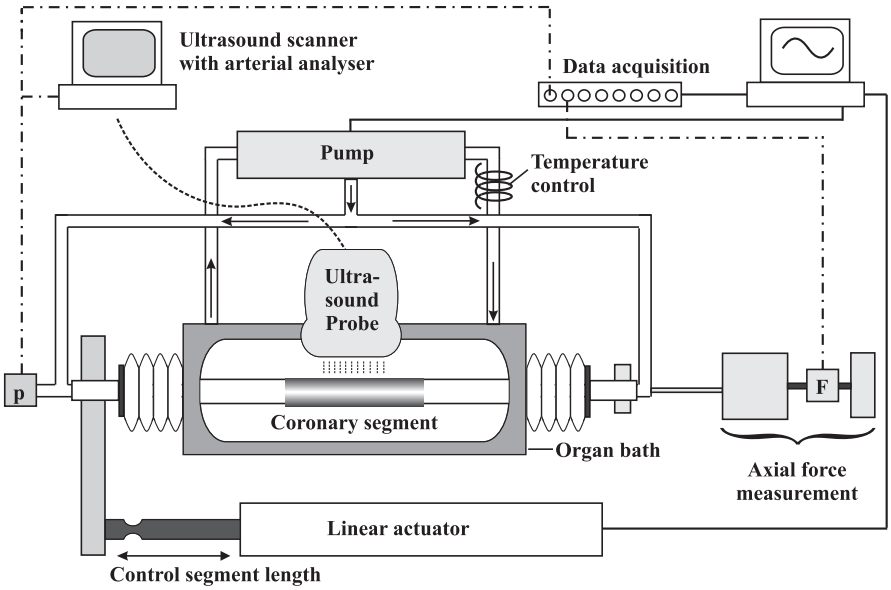

Figure 2.1: *Schematic representation of the experimental set-up. Adapted from Van den Broek et al. (2011).*

to the distal cannula. An ultrasound scanner with a linear probe (8MHz, Esaote Europe, The Netherlands), combined with an arterial analyzer (Art.Lab, Esaote Europe, The Netherlands), operated at 32 lines cm^{-1} in B-mode (30 frames s^{-1}), was used to measure the inner diameter ($D_i = 2r_i$, with r_i the inner radius), which was recorded simultaneously with the pressure. The linear actuator, the pressure-axial force acquisition, and the valve controlling the pressure were controlled using Labview software (National Instruments, USA).

Test protocol

The arterial segments were kept in the Kreb's solution for 30 min, after which papaverine (10^{-4} M) was added to induce vasorelaxation. After 15 min, the vessel was loaded with a cyclic pressure and stretched axially at a strain rate of 0.01 s^{-1} until the amplitude of the measured axial force signal was minimal. Several studies (van Loon, 1977; Weizsäcker et al., 1983) have shown that this axial stretch (λ_z) is equal to the physiological axial pre-stretch ($\lambda_{z,phys}$) for the large elastic arteries. We assume a similar behaviour for coronary arteries. At this $\lambda_{z,phys}$, the vessel was pressurized with a sinusoidal function with a mean and amplitude of 8 kPa. After reproducible signals were measured, the p-r_i and p-F_z signal were recorded for one pressure cycle. The change in axial force during a pressure cycle (ΔF_z) was obtained by subtracting the axial force at $p = 0$. As some hysteresis was present, the p-r_i and p-ΔF_z relations at increasing pressure load were averaged with the corresponding relations at decreasing pressure load. The resulting p-r_i and p-ΔF_z relations were used in the estimation procedure described in section 2.2.3. After the mechanical testing, a small ring was cut from the middle of the arterial segment and fixed in a 10% formalin solution in PBS. By measuring the inner and outer circumference of a stained ring section, the cross-sectional area of the unloaded segment (A_0) was determined. Previous research has shown that obtaining the unloaded inner and outer diameter from histology has a measuring inaccuracy of about 5-6% (Choy et al., 2005). While modeling the arteries, these possible inaccuracies were not taken into account.

2.2.2 Constitutive model

Considering the applicability to clinical data, a relatively simple constitutive model with a limited amount of parameters is used in this study. We therefore chose not to include smooth muscle activity (Zulliger et al., 2004b), a layered structure (Wang et al., 2006), and more realistic fiber distributions (Gasser et al., 2006). Following Holzapfel et al. (2000), the artery is modeled as an incompressible, thick-walled, fiber-reinforced cylinder. The collagen fibers are modeled one-dimensionally, exerting only stress in the fiber direction ($\vec{e}_f^{\,i}$). The Cauchy stress σ is defined as:

$$\sigma = -p_h \mathbf{I} + \hat{\tau} + \sum_{i=1}^{2} \tau_f^i \, \vec{e}_f^{\,i} \, \vec{e}_f^{\,i} \ , \tag{2.1}$$

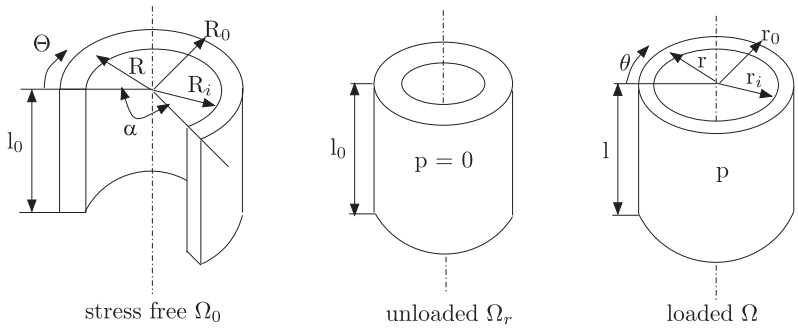

Figure 2.2: *The stress-free reference configuration Ω_0, the unloaded configuration Ω_r, and the loaded configuration Ω. Adapted from Van Oijen (2003).*

with p_h the hydrostatic pressure, $\mathbf{I}$ the unity tensor, $\hat{\tau}$ the isotropic matrix stress, and τ_f^i the fiber stress of fiber i. τ_f represents the contribution of all fibrous material and $\hat{\tau}$ of all other (isotropic) tissue components. The isotropic matrix is described as a neo-Hookean material by

$$\hat{\tau} = G(\mathbf{B} - \mathbf{I}) \ , \tag{2.2}$$

with G the shear modulus and $\mathbf{B}$ the Finger tensor. $\mathbf{B}$ is defined as $\mathbf{B} = \mathbf{F} \cdot \mathbf{F}^T$, with $\mathbf{F}$ the deformation gradient tensor (see (2.9)). The fibers can only exert force in tension with the fiber stress defined as:

$$\begin{array}{ll} \tau_f = k_1 {\lambda_f}^2 ({\lambda_f}^2 - 1) e^{k_2 ({\lambda_f}^2 - 1)^2} & \text{if } \lambda_f \geq 1 \\ \tau_f = 0 & \text{if } \lambda_f < 1 \ . \end{array} \tag{2.3}$$

Here, k_1 and k_2 are constants determining the stress-strain relation of the collagen fibers, and λ_f is the fiber stretch. The fiber stretch can be calculated from the right Cauchy-Green tensor ($\mathbf{C} = \mathbf{F}^T \cdot \mathbf{F}$) and the undeformed fiber direction ($\vec{e}_{f_0}$):

$$\lambda_f = \sqrt{\vec{e}_{f_0} \cdot \mathbf{C} \cdot \vec{e}_{f_0}} \ . \tag{2.4}$$

$\vec{e}_{f_0}$ of fiber i ($i = 1, 2$) can be described in matrix notation:

$$\vec{e}^{\,i}_{f_0} = [0 \quad \cos(\beta_0) \quad (-1)^i \sin(\beta_0)]^T \ , \tag{2.5}$$

with β_0 the angle of the fiber relative to the circumferential direction.
To take the residual stresses in the unloaded configuration (Ω_r) into account, we assume an open configuration (Ω_0) as the stress-free reference configuration (Fig. 2.2). In cylindrical coordinates (R,Θ,Z) the geometry of Ω_0 is then defined as:

$$R_i \leq R \leq R_o, \qquad 0 \leq \Theta \leq (2\pi - \alpha), \qquad 0 \leq Z \leq l_0 \ , \tag{2.6}$$

with R_i and R_o, the inner and outer radius, respectively, α the opening angle, and l_0 the length of the undeformed tube. The geometry of the loaded configuration (Ω) is defined in cylindrical coordinates (r,θ,z) by:

$$r_i \leq r \leq r_o, \qquad 0 \leq \theta \leq 2\pi, \qquad 0 \leq z \leq l \ . \tag{2.7}$$

Here, r_i, r_o, and l represent the inner and outer radius, and the length of the deformed tube, respectively.

When assuming isochoric deformation without torsion, the cylindrical coordinates (r,θ,z) can be written as:

$$r = \sqrt{\frac{R^2 - {R_i}^2}{k\lambda_z} + {r_i}^2}, \qquad \theta = k\Theta, \qquad z = \lambda_z Z \ , \tag{2.8}$$

with $k = 2\pi/(2\pi - \alpha)$. The deformation gradient $\mathbf{F}$ is given by:

$$\mathbf{F} = \lambda_r \, \vec{e}_r \, \vec{e}_R + \lambda_\theta \, \vec{e}_\theta \, \vec{e}_\Theta + \lambda_z \, \vec{e}_z \, \vec{e}_Z \ , \tag{2.9}$$

with $\vec{e}_R$, $\vec{e}_\Theta$, $\vec{e}_Z$ the unit base vectors of (R,Θ,Z), and the following stretch ratios:

$$\lambda_r = \frac{\partial r}{\partial R} = \frac{R}{rk\lambda_z}, \qquad \lambda_\theta = \frac{r}{R}\frac{\partial \theta}{\partial \Theta} = \frac{kr}{R}, \qquad \lambda_z = \frac{l}{l_0} \ . \tag{2.10}$$

Balance equations

Neglecting body forces, inertia, and viscoelastic behaviour, the conservation of momentum equation reads

$$\vec{\nabla} \cdot \sigma = \vec{0} \ . \tag{2.11}$$

Assuming axisymmetry and neglecting edge effects, only the radial component of (2.11) is relevant:

$$\frac{\partial \sigma_{rr}}{\partial r} + \frac{\sigma_{rr} - \sigma_{\theta\theta}}{r} = 0 \ . \tag{2.12}$$

Using the boundary conditions, $\sigma_{rr}(r = r_o) = 0$ and $\sigma_{rr}(r = r_i) = -p$, together with $\tau = \sigma + p_h \mathbf{I}$ we obtain an expression for the internal pressure:

$$p = \int_{r_i}^{r_o} (\tau_{\theta\theta} - \tau_{rr}) \frac{dr}{r} = 0 \ . \tag{2.13}$$

The deformation resulting from axial extension and an internal pressure is found by solving (2.13). Since, in general, (2.13) cannot be solved analytically, a numerical technique is used. We define the circumferential stretch at the inner surface as: $\lambda_{\theta_i} = \frac{kr_i}{R_i}$. For a given α and λ_z, the extra stress can be written as a function of λ_{θ_i} and r. (2.13) can then be written as:

$$\int_{r_i}^{r_o} f(\lambda_{\theta_i}, r) \frac{dr}{r} - p = 0, \qquad \text{with } f(\lambda_{\theta_i}, r) = (\tau_{\theta\theta} - \tau_{rr}) \ . \tag{2.14}$$

A Newton iteration scheme was employed to linearize (2.14) with respect to λ_{θ_i}. The linearized equations were then solved by dividing the wall into 10 subdomains and performing piecewise quadratic Newton-Cotes integration. After solving (2.14), the reduced axial force could be computed using:

$$F_z = 2\pi \int_{r_i}^{r_o} \sigma_{zz} r dr - p\pi r_i^2 \ . \tag{2.15}$$

2.2.3 Estimation procedure

The main idea of the estimation procedure is to minimize the difference between the experiments, consisting of the p-r_i and p-ΔF_z data, and the same signals computed with the model, by optimizing the model parameters. Keeping the clinical applicability in mind, we assumed here that ΔF_z is zero over the measured pressure range, since it is impossible to measure the axial force *in-vivo*.

First, to have an equal contribution over the pressure range, the data were re-sampled from time-equidistant to pressure-equidistant over the pressure range of $0 - 16$ kPa with 25 samples. The difference between the experiment and model was minimized by optimizing the four material parameters (G, k_1, k_2, β_0) and one geometrical parameter, for which the inner radius in the unloaded configuration ($r_{i_{\Omega_r}}$) was chosen. To quantify the difference between the experiment and the model the objective function ψ is defined as:

$$\psi(\Upsilon) = \frac{1}{N_s} \sum_{j=1}^{N_s} \left(\left(r_{i,M}(j) - r_{i,E}(j)\right)^2 + \varepsilon_F \left(\Delta F_{z,M}(j)\right)^2 \right) . \tag{2.16}$$

Here, Υ consists of the five parameters ($\Upsilon = \{G, k_1, k_2, \beta_0, r_{i_{\Omega_r}}\}$), $N_s = 25$ is the number of samples, $\varepsilon_F = 0.01$ is a scaling parameter for ΔF_z, and subscript M and E represent the model and experiment, respectively. To introduce residual stresses in the unloaded configuration, we make use of the general idea that the arterial wall is able to remodel its microstructure towards a preferred biomechanical state. More specifically, the hypothesis that the circumferential stress gradient is minimal at physiological pressure ($p = 13.3$ kPa) and axial pre-stretch (Chuong and Fung, 1986; Takamizawa and Hayashi, 1987; Hayashi and Naiki, 2009), was translated into a second objective function $\vartheta(\alpha)$:

$$\vartheta(\alpha) = \frac{1}{N_d} \sum_{m=1}^{N_d} \left(\Delta\sigma_{\theta\theta}(m)\right)^2 , \tag{2.17}$$

with $\Delta\sigma_{\theta\theta} = \sigma_{\theta\theta} - \sigma_{\theta\theta}(r_i)$, and $N_d = 10$ the number of subdomains that make up the wall. It is assumed that the stretches in the unloaded configuration are small, which means that the fiber contribution is small as well. It can therefore be considered as a simple homogeneous bending problem, which means that the mid-wall circumferential stretch does not change between the stress-free and unloaded configuration. This, together with the incompressibility condition, means that the wall thickness does not change between the stress-free and the unloaded configuration (Taber and Eggers, 1996). R_i and R_o can therefore be expressed in terms of $r_{i_{\Omega_r}}$ and the measured unloaded cross-sectional area A_0:

$$\begin{aligned} h_{\Omega_r} = \sqrt{r_{i_{\Omega_r}}^2 + \tfrac{A_0}{\pi}} - r_{i_{\Omega_r}} &= H , \\ R_i = k\left(r_{i_{\Omega_r}} + \tfrac{h_{\Omega_r}}{2}\right) - \tfrac{H}{2} &= k r_{i_{\Omega_r}} + \tfrac{h_{\Omega_r}}{2}(k-1) , \\ R_o = R_i + H &= k r_{i_{\Omega_r}} + \tfrac{h_{\Omega_r}}{2}(k+1) . \end{aligned} \tag{2.18}$$

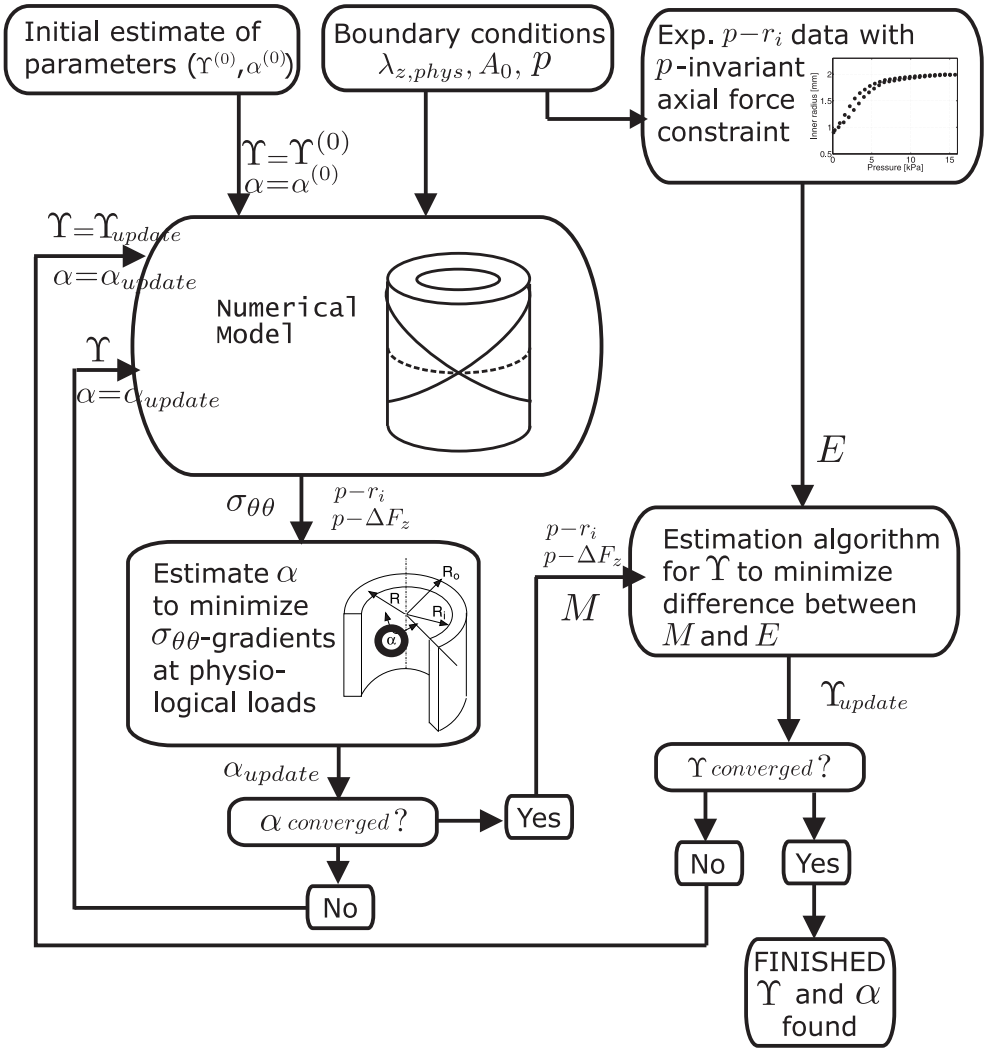

Figure 2.3: *A schematic representation of the procedure to estimate* $\Upsilon = \{G, k_1, k_2, \beta_0, r_{i_{\Omega_r}}\}$ *by minimizing the difference between the experiments* (E) *and model* (M)*, while keeping the circumferential stress gradients minimal by optimizing* α*.*

H and h_{Ω_r} are the wall thickness of the stress-free and unloaded configuration, respectively.

The estimation procedure (Fig. 2.3) started with the input for the model; the axial pre-stretch ($\lambda_{z,phys}$), the unloaded cross-sectional area (A_0), and the pressure (p), obtained from the experiments, and an initial estimate of Υ ($\Upsilon^{(0)}$) and α ($\alpha^{(0)}$). Subsequently, ϑ was minimized (using Levenberg-Marquardt), leading to a new

estimate of α. This continued until ϑ was minimized, resulting in an estimate of α for a certain Υ. This procedure of minimizing ϑ was repeated every time one of the five parameters was changed, even while determining the Jacobian. The objective function ψ was minimized using the Levenberg-Marquardt algorithm, as implemented in the *lsqnonlin*-subroutine in Matlab (R2010a, The Mathworks, Natick, MA). To prevent convergence issues in solving (2.14), the upper and lower bounds of Υ were {5 kPa, 0.1 kPa, 0.1, 10°, 0.5 mm} and {500 kPa, 50 kPa, 100, 50°, 2 mm}, respectively. This resulted in an Υ and α, for which the model described the experimental data and which meets the uniform stress/strain hypothesis. To test whether a global minimum of ψ was found, the estimation procedure was repeated with three different initial parameter sets; $\Upsilon_1^{(0)}$ = {30 kPa ,3 kPa, 3, 30°, 1 mm}, $\Upsilon_2^{(0)}$ = {20 kPa ,20 kPa, 10, 20°, 1.5 mm}, $\Upsilon_3^{(0)}$ = {200 kPa ,1 kPa, 15, 45°, 1.7 mm}. Furthermore, the eigenvalues of the Hessian at the converged solution were computed to assess if any over-parameterization existed. This estimation procedure was also repeated without the optimization of the opening angle ($\alpha = 0$), to gain insight into the effect of estimating the opening angle based on the uniform stress/strain hypothesis.

2.2.4 Data analysis

The variation of the parameters (R_i, α, G, k_1, k_2, β_0) between the different LADs were analyzed by determining the mean and standard deviation of each parameter. For each LAD, the quality of the p-r_i relation obtained with the model was quantified by determining the mean relative difference between the model and the experiment:

$$\delta_r = \frac{1}{N_s} \sum_{j=1}^{N_s} \left| \frac{r_{i,M}(j) - r_{i,E}(j)}{r_{i,E}(j)} \right| . \tag{2.19}$$

The deviation of ΔF_z from zero was quantified according to:

$$\delta_F = \frac{1}{N_s} \sum_{j=1}^{N_s} |\Delta F_{z,M}(j)| . \tag{2.20}$$

The effect of including the opening angle in the optimization scheme on the estimated material parameters, was quantified for each LAD by:

$$\delta_\alpha = \frac{\Upsilon - \Upsilon_{\alpha=0}}{\Upsilon_{\alpha=0}} . \tag{2.21}$$

Since the aim of the current study was to investigate the fiber orientation, the mean fiber orientation and different stress components as a function of pressure were determined for each artery.

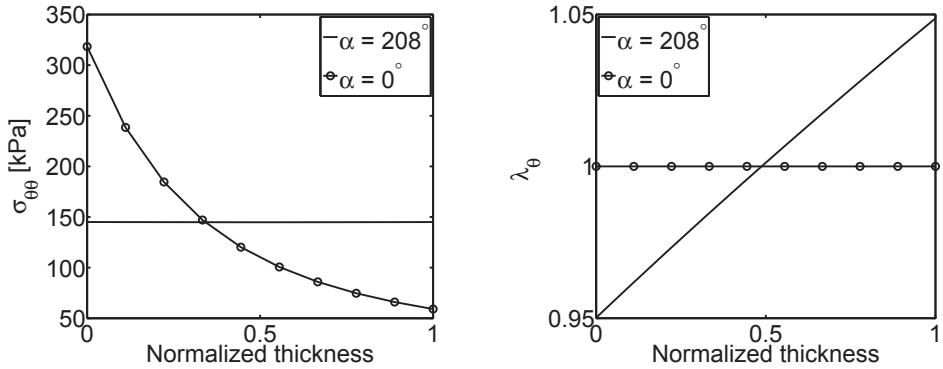

Figure 2.4: a) *Example of the circumferential Cauchy stress at mean physiological pressure (p=13.3 kPa) without ($\alpha = 0°$) and with (α=208°) opening angle, through the arterial wall thickness (0-1=r_i-r_o).* ***b)*** *The circumferential residual stretch in the unloaded configuration without (α=0°) and with (α=208°) opening angle through the arterial wall thickness (0-1=r_i-r_o).*

2.3 Results

In Table 2.2 the geometric parameters obtained from the experiments ($\lambda_{z,phys}$ and A_0) and the optimization procedure (R_i, H and α) are shown for all 9 LADs. The two human LADs are represented by numbers 8 and 9. The unloaded arterial cross-sectional area A_0, obtained from histology, was (3.0 ± 0.7) mm^2. The average physiological pre-stretch $\lambda_{z,phys}$ was 1.35 ± 0.09. The other three geometrical parameters, R_i, H, and α, were derived using the fitting procedure described in (2.16)-(2.18) and are also shown in Table 2.2. The minimization of the stress-gradients at $p = 13.3$ kPa, resulting in an estimate of α, was successful, as the circumferential stress gradient through the wall was close to zero at physiological pressure when residual strain was included (Fig. 2.4a). The resulting residual circumferential stretch in the unloaded configuration Ω_r was approximately $\pm 5\%$ (Fig. 2.4b). A typical result, in this case of one of the human arteries, of the p-r_i and p-ΔF_z relations from the experiment and the fitted model is shown in Figure 2.5. For all measured porcine and human segments, the p-r_i and p-ΔF_z relations could be fitted accurately. The average relative deviation of p-r_i (δ_r) and the average deviation of ΔF_z from zero (δ_F) were therefore also very small; 0.6% (or 10 μm) and 0.4 mN, respectively (Table 2.3).

The estimated material parameters are shown in Table 2.3 and Figure 2.6. The maximal relative difference between parameters obtained with the three initial parameter sets ($\Upsilon^{(0)}_{1-3}$) was less than 0.3%. This indicates that a global minimum of the objective function (ψ) was found. Furthermore, the eigenvalues of the Hessian of the converged solutions were all greater than zero, indicating that the Hessian is convex near the solution and no over-parameterization existed. The parameters of the human arteries (represented with $\bigtriangledown$, $\diamondsuit$) were not very different from the porcine

Table 2.2: *Geometric parameter values of porcine LAD 1-7 and human LAD 8-9 and their means and standard deviations (SD); $\lambda_{z,phys}$, the physiological axial pre-stretch; A_0 the cross sectional area of the unloaded artery; R_i, H, and α, the final estimate of the stress-free inner radius, wall thickness, and opening angle from the estimation procedure.*

LAD	$\lambda_{z,phys}$	A_0 (mm^2)	R_i (mm)	H (mm)	α (°)
Porcine					
1	1.36	3.0	3.3	0.32	208
2	1.49	4.2	4.1	0.38	211
3	1.39	2.3	3.1	0.29	216
4	1.41	2.9	2.7	0.33	184
5	1.34	2.9	3.0	0.30	183
6	1.38	2.3	4.1	0.29	255
7	1.36	3.0	2.7	0.32	171
Human					
8	1.30	4.0	3.3	0.29	135
9	1.15	2.3	2.4	0.27	167
Mean	1.35	3.0	3.2	0.31	192
SD	0.09	0.7	0.6	0.03	35

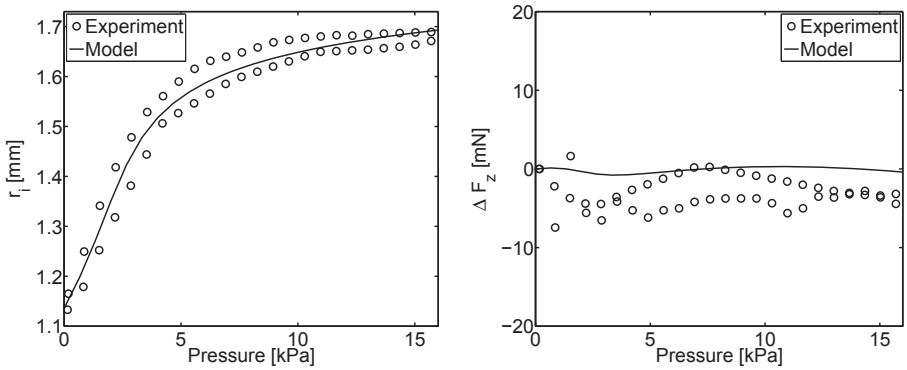

(a) ***(b)***

Figure 2.5: *Typical example of the model fit (solid line) of the experimental (circles) p-r_i* ***(a)*** *and p-ΔF_z* ***(b)*** *relations. The artery shown is LAD 9 (human) represented in Figure 2.6 with $\diamondsuit$.*

arteries, apart from k_2, which was much larger for LAD 8 ($\bigtriangledown$). While this might be an indication that the overall waviness of the collagen fibers of this vessel is less, we do not have an explanation for this feature.

The effect of including the opening angle on the parameters is shown in Table 2.4. The relative difference in the material parameters found was small, indicating that the relative influence of the opening angle on the p-r_i and p-ΔF_z relations is also small. Furthermore, the small relative difference in δ_r and δ_F show that including

Table 2.3: *Mean and standard deviation (SD) of the fitted material parameter values and the deviations in r_i and ΔF_z, of LAD 1-9.*

	G (kPa)	k_1 (kPa)	k_2 (-)	β_0 (°)	δ_r ($\times 10^{-3}$)	δ_F (mN)
Mean	21	2	8	36	6	0.4
SD	4	0.5	9	3	3	0.1

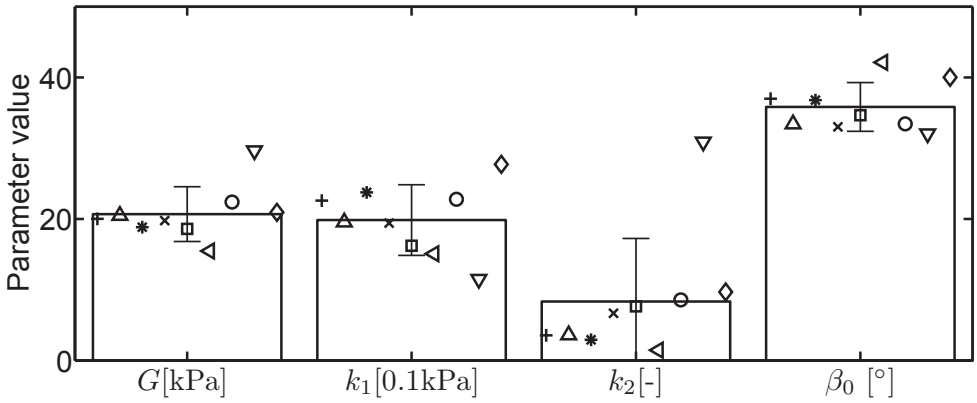

Figure 2.6: *The fitted material properties of all measured arteries. Each marker represents one LAD, human LADs 8 and 9 are represented by $\triangledown$ and $\diamondsuit$. The errorbars represent the standard deviations of the parameters of all the LADs.*

the opening angle, via the homogeneous stress/strain hypothesis, does not have a negative impact on the quality of the fit.

Figure 2.7a clearly shows that the collagen fibers are the main load bearing structure at physiological pressure. Compared to the matrix, the fiber contribution to the extra stress is approximately 5× and 10× higher in the axial and circumferential direction, respectively. Hence, when using a highly orthotropic model, the fiber orientation is very important in determining the stress-strain behaviour. Figure 2.7b shows the fiber angle β for all vessels as a function of p. While the variation between the vessels is high at $p = 0$ ($\bar{\beta} = (48 \pm 4)°$), at physiological pressure, β is almost equal for all vessels; $(36.4 \pm 0.3)°$ at $p = 13.3$ kPa.

Table 2.4: *Mean and standard deviation (SD) of δ_α of LAD 1-9; the relative difference between the material parameters found with and without including the opening angle in the estimation scheme.*

	ΔG (%)	Δk_1 (%)	Δk_2 (%)	$\Delta\beta_0$ (%)	$\Delta\delta_r$ (%)	$\Delta\delta_F$ (%)
Mean	-4	-0.4	8	-1	8	-7
SD	1	1	1	0.3	6	5

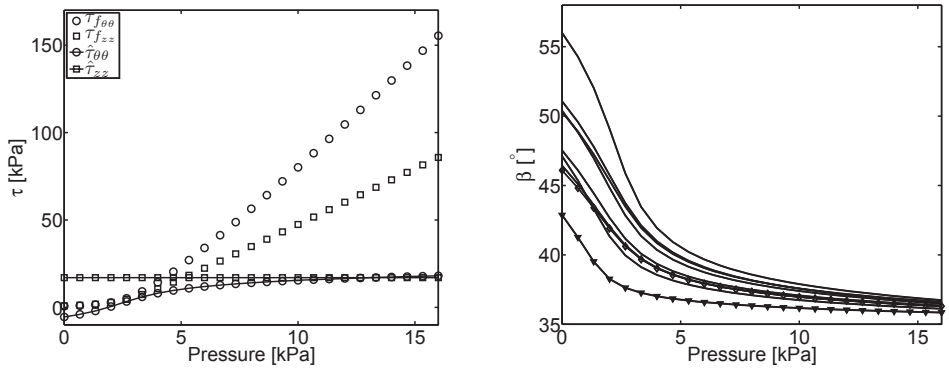

(a) *(b)*

Figure 2.7: a) *The average fiber (τ_f) and matrix ($\hat{\tau}$) contributions to the extra stress τ in the circumferential and axial direction.* ***b)*** *The average fiber orientation β as a function of p at $\lambda_{z,phys}$. Solid lines represent the porcine LADs, solid lines with $\bigtriangledown$ and $\diamondsuit$ represent human LADs 8 and 9, respectively.*

2.4 Discussion

In this study, we used *in-vitro* inflation and extension experiments on porcine and human coronary arteries to investigate the fiber orientation, as represented by a widely used two-fiber model (Holzapfel et al., 2000), at physiological loading conditions and was found to be very similar for all arteries measured. The experiments mimicked the *in-vivo* situation by stretching the arterial segments to $\lambda_{z,phys}$, but also enabled investigation of the mechanical behaviour at the low pressure range. A microstructure-based constitutive model was successfully fitted to the experimental data, enabling the computation of the stresses and strains.

As already discussed in Van den Broek et al. (2011), the main advantage of the adopted experimental approach is that the measurements are performed in a physiological environment. The structural integrity of the arterial segment is maintained and damage is prevented by not exceeding the physiological pressure values. The measurements were performed at an approximation of the physiological axial pre-stretch. Since measurements were performed on the epicardial coronary arteries, we assumed that the extravascular pressure due to the cardiac contraction, was negligible. This also means that caution should be exercised when applying the current results to coronary arteries closer to the endocardium.

The main advantage of the single-layer model used is that there are a limited number of material parameters to be estimated, while the microstructure of the arterial wall is globally taken into account. It is, however, well known that the arterial wall consists of three layers, with different constituents and related material parameters. Furthermore, it has been shown that a model with a fiber distribution is better able to capture observations from *in-vitro* studies (Gasser et al., 2006). Although adopting a model with a more realistic morphology, i.e. more layers, constituents, and fiber distributions, will yield a more accurate description of the

mechanics of the arterial wall, including all these extra parameters in the estimation procedure will result in over-parameterization of the objective function, especially with the limited amount of information available in clinical data.

By adopting a thick-walled model, residual stresses could be taken into account. We chose a relatively easy way to implement the residual stresses, via the opening angle method as formulated by Taber and Eggers (1996). An approach based on an optimization law was chosen instead of experimentally determining the opening angles of the arteries. As already discussed in other papers (e.g., Rachev and Greenwald (2003)), experimentally obtained open-sector geometries do not resemble a perfect circle with an uniform wall thickness. Considering that the method should be applicable clinically, we believe, that the adopted approach is preferable. By introducing a second objective function, to minimize the circumferential stress gradient in the wall at physiological pressure and axial pre-stretch, a measure for the opening angle α was found. While other, more sophisticated, methods to incorporate residual stresses are available (VanDyke and Hoger, 2002; Olsson et al., 2006), the current method proved be relatively easy to implement and sufficient to minimize the stress gradients at physiological loading. A prerequisite for this method of inversely estimating α to work, is that the p-r_i and p-ΔF_z relations are relatively insensitive to small changes in α. This was confirmed by the small differences between the material parameters found with and without including the estimation scheme for α. Including the residual stress/strain this way did also not negatively influence the quality of fit, as was shown by the small differences in δ_r and δ_F (Table 2.4). The average value of α was $(192 \pm 35)^\circ$, which corresponds to experimental values found by Guo and Kassab (2004) and Wang and Gleason (2010) for porcine coronary arteries and by Valenta et al. (1999) for human coronary arteries. Note, that due to the minimization of the circumferential stress gradients, and therefore the strain gradients, the fibers throughout the wall thickness are all oriented in the same direction at $p = 13.3$ kPa.

A limitation of this study is that only circumferential residual strains are taken into account. Recent studies have clearly shown that (layer-specific) axial residual strains exists and that they can have a significant effect on the stress distribution in the arterial wall (Holzapfel et al., 2007; Wang and Gleason, 2010). Including these residual axial strains resulted in a decrease in circumferential stress gradients, while the axial stress gradients increased. In further research it would be very interesting to included these residual axial strains into the optimization procedure. However, to be able do this for patient-specific, intact arteries requires an optimization rule which captures these effects.

The model was able to fit the measured p-r_i and p-ΔF_z relations accurately, represented by an average deviation of only 10 μm ($\bar{\delta}_r$ = 0.006) and 0.4 mN ($\bar{\delta}_F$) from the experimental data. Multiple initial parameter sets resulted in the same optimal parameter set Υ, indicating that a global minimum of the objective function (ψ) was found. An important parameter to fit both p-r_i and p-ΔF_z relations accurately is the scaling parameter ε_F. ε_F was chosen in such a way that the contribution of the radius and axial force to the objective function was approximately equal. By altering ε_F either the radius or axial force data will therefore start to dominate the objective function and a different global minimum will be found. If ε_F is chosen very

high, which means a very strict axial force constraint, the solution space is likely to be restricted so much that it is unlikely that the constitutive equations are able to describe the found p-r_i relations.

The relative variation in Υ between the different vessels is quite large, especially for the parameter k_2. The relative variation in the parameter representing the global fiber orientation β_0 is quite small, but, since the main load is taken by the fibers (Fig. 2.7a), the p-r_i and p-ΔF_z relations are most sensitive to changes in β_0. The value of β_0 corresponds to the average fiber angle of the adventitia of the human aorta as found by Holzapfel et al. (2002). Besides the value of k_2 of LAD 8 ($\bigtriangledown$), the material parameters of the human arteries were consistent with those of the tested porcine arteries. A clear limitation of this study is that we were able to only include two human specimens. Therefore, further research is needed to confidently translate the obtained results to human coronary arteries. The two human specimens, however, do contribute to the findings regarding the fiber orientation at physiological loading, while their axial pre-stretch was significantly lower.

With the experimental set-up, only the changes in axial force (ΔF_z) could be measured accurately, while other studies (Zulliger et al., 2004a; Rezakhaniha and Stergiopulos, 2008) reported problems with fitting both p-r_i and p-F_z relations with similar fiber-reinforced models. Rezakhaniha and Stergiopulos (2008) proposed a model which included anisotropic elastin, which increased the axial stress, enabling fitting of both the radius and absolute axial force data. It would be interesting to use a model which incorporates anisotropic elastin in future studies. It should be noted, however, that increasing the number of material parameters will likely result in over-parameterization. Furthermore, since clinically obtained data lack absolute force information, it is unlikely that this anisotropic elastin parameter can be fitted, and should therefore be prescribed.

As mentioned before, in the physiological pressure range the fibers bear almost all the load (Fig. 2.7a). The fiber orientation (β) is therefore the main determinant of the stress-strain behaviour at those pressures, especially in this two-fiber model. Note, that β is determined by the axial and circumferential strain, and the value of β in the stress-free configuration (β_0). For all vessels measured, the fiber orientation at physiological loading β_{phys} was almost equal being $(36.4 \pm 0.3)^\circ$, as indicated by a standard deviation of only 1%. An explanation for this particular fiber orientation can be found by applying netting analysis. In filament-wound composite theory (Gay et al., 2003), netting analysis is often used to describe the behaviour of fiber-reinforced composite materials. The main assumption in netting analysis is that all loads are supported by the fibers only. Since we model the arterial wall as a filament-wound tube, netting analysis can be used to approximate the fiber orientation in the high pressure range. As described in several papers (Spencer et al., 1974; Wild and Vickers, 1997; Xia et al., 2001) an optimal fiber angle exists for which the fibers take all the load due to the internal pressure. This optimal winding angle is approximately 35° relative to the circumferential direction. This behaviour is exactly what we see in our results; for high pressures β approaches 35° (Fig. 2.7b). The derived angle aligns between the largest principal stress directions, which is in agreement with the theory proposed by Hariton et al. (2007), which hypothesized that the collagen remodeling

is modulated by the magnitude of the principal stresses.

It must be stressed, that the fiber orientation found must not be viewed as the actual fiber morphology in the arterial wall but just as the net result of all fibrous material as described with the two-fiber model. The findings in this study are therefore mainly of interest as extra modeling constraints or for reducing the number of parameters, with similar, highly orthotropic, models.

2.5 Conclusion

Porcine and human coronary arteries were subjected to inflation-extension experiments at physiological axial conditions and a pressure range of $0 - 16$ kPa. The main finding was that the fiber orientation at physiological loading, as described with the two-fiber model (Holzapfel et al., 2000), is almost equal for all arteries measured, which could be physically interpreted using netting analysis and may result from arterial remodeling. In future studies, which use similar, highly orthotropic, models to estimate material parameters from clinical data, this may prove to be useful in reducing the number of parameters or as an extra modeling constraint.

Acknowledgements

We thank Dr. Milting and Dr. Morshuis (HDZ-NRW, Bad Oeynhausen, Germany) for providing the human coronary arteries.

Author contributions

The research presented in this chapter was performed in close collaboration with Chantal van den Broek, which performed the inflation-extension experiments on the porcine and human coronary arteries. Parts of this chapter were also printed in C.N. van den Broek, PhD thesis (2010), chapter 5.

Performed experiments: C.N. van den Broek, A. van der Horst
Data analysis: A. van der Horst, C.N. van den Broek
Interpretation of results: all
Prepared figures: A. van der Horst, C.N. van den Broek
Drafted manuscript: A. van der Horst
Edited and revised manuscript: all
Approved final version of manuscript: all

Chapter 3

A wave propagation model of the coronary circulation

An appropriate model describing the primary relations between the cardiac muscle and coronary circulation might be useful for interpreting coronary hemodynamics in combinations of coronary circulatory disease. The main contribution of the present study is the coupling of a microstructure-based heart contraction model with a 1D wave propagation model. The 1D representation of the vessels enables patient-specific modeling of the coronary circulation and/or can serve as boundary conditions for detailed 3D models, while the heart model enables the simulation of cardiac disease, with physiology-based parameter changes. Here, the different components of the model are explained and the ability of the model to describe coronary hemodynamics in health and disease is validated. Two disease types are modeled: coronary epicardial stenoses and left ventricular hypertrophy with an aortic valve stenosis.
In all simulations (healthy and diseased), the dynamics of pressure and flow qualitatively agreed with experimental observations described in literature. We conclude that the model is a suitable tool for the investigation and diagnosis of combinations of different disease types by their influence on coronary pressure and flow waves.

The contents of this chapter are based on Arjen van der Horst, Frits L. Boogaard, Marcel van 't Veer, Marcel C.M. Rutten, Nico H.J. Pijls, and Frans N. van de Vosse, A wave propagation model of the coronary circulation, *To be submitted.*

3.1 Introduction

Diagnosis of coronary circulatory disease based on coronary pressure and/or flow has been shown to improve the clinical outcome of treatment (Kern et al., 2006). The direct measurement of coronary hemodynamics, however, is still limited to the large epicardial vessels, which means that microvascular disease can only be determined from upstream measurements using an appropriate model of the vessels and their interaction with the cardiac muscle (Waters et al., 2011).

Due to location of the coronary arteries, being embedded into the myocardium, the contraction of the heart influences coronary hemodynamics. This results in the unique feature that blood is mainly supplied during diastole, while coronary epicardial pressure is high in systole. Several mathematical models have been proposed to model the effect of cardiac contraction on the coronary vessels. Downey and Kirk (1975) proposed the vascular waterfall mechanism, which explained the increased resistance to blood flow by vascular collapse when the intramyocardial pressure, determined by ventricular cavity pressure, exceeds the lumen pressure. Spaan et al. (1981) introduced the intramyocardial pump model, which accounted for the role of vascular compliance. The intramyocardial pressure, determined by the ventricular cavity pressure, served as the extravascular pressure. The time-varying elastance concept (Suga et al., 1973) was applied to the coronary circulation by Krams et al. (1989), in which flow is impeded due to a varying stiffness of the cardiac wall. Other, more elaborate, models also include the effect of the coronary vessels on the cardiac contraction (e.g., Zinemanas et al. (1994)).

One-dimensional (1D) wave propagation models are potentially very useful tools in the interpretation of arterial hemodynamics (van de Vosse and Stergiopulos, 2011; Waters et al., 2011). They can provide better insight into the effect of combinations of epicardial and microvascular disease on clinically used indices. Furthermore, a 1D representation of the coronary arteries also enables the application of wave intensity analysis (Parker and Jones, 1990; Parker, 2009) to elucidate the effects of different kinds of disease on the pressure and flow waves. Using this technique the pressure and flow waves are separated into forward and backward running compressive and decompressive waves, providing insight into the conditions up- and downstream of the measurement location. Wave intensity analysis has been applied to study coronary hemodynamics and its interaction with the cardiac muscle by Sun et al. (2000), Davies et al. (2006a), and Hadjiloizou et al. (2008).

Application of 1D wave propagation models to the coronary circulation is reported in several studies. Smith et al. (2002) and Huo and Kassab (2007) applied 1D models to vessels representing the coronary arterial anatomy. However, in these studies the interaction with the cardiac muscle was not taken into account. The effect of the cardiac contraction was taken into account in the 1D models of Mynard and Nithiarasu (2008), where the coronary vessels were loaded with an approximated left ventricular pressure. Recently, as part of an elaborate arterial tree, Reymond et al. (2009) coupled a 1D model to a time-varying elastance model to describe the relation between ventricular pressure, volume, and coronary hemodynamics.

In this study, a model is presented which couples a 1D wave propagation

model (Bessems et al., 2007) to the single-fiber heart contraction model, which was introduced by Arts et al. (1991) and further developed by Bovendeerd et al. (2006). The coronary and systemic microvasculature is modeled using three-element Windkessels. The aorta and its main branches, including the epicardial coronary arteries, are modeled with the 1D wave propagation elements and stenoses are modeled according to the 1D stenosis element developed by Bessems (2007). The main advantage of combining these models is that the heart model, compared to more phenomenological models, is based on microstructural material and macrostructural geometrical properties, allowing the simulation of cardiac disease with physiology-based parameter changes, while the 1D vessel model gives a continuous representation of the epicardial vessels and enables investigation of the coronary pressure and flow waves. This combination makes it possible to validate the effect of epicardial and/or microcirculatory disease on pressure- and flow-based indices already used in the clinic and to investigate new indices based on epicardial hemodynamics alone. Furthermore, the 1D representation of the arteries can serve as boundary conditions for more detailed 3D models, describing a specific part of the coronary arteries.

Here, the different components of the model are explained and the ability of the model to describe both normal and pathological coronary pressure and flow dynamics is evaluated via comparison with experimental observations described in literature. Two disease types are modeled: coronary stenoses located in the epicardial vessels and left ventricular hypertrophy with an aortic valve stenosis, affecting the coronary microvasculature.

3.2 Materials and Methods

The model consists of three main elements: A heart contraction model, a wave propagation model for the large arteries, and Windkessel elements to model the coronary and systemic microcirculation. As part of the wave propagation model, Bessems (2007) developed an element that can describe the effect of a stenosis on the local hemodynamics. Since the wave propagation model and heart model have already been described in Bessems et al. (2007) and Bovendeerd et al. (2006), respectively, only a short description of the models is given below.

3.2.1 Heart contraction model

Similar to Bovendeerd et al. (2006), the left ventricle is modeled as thick-walled sphere, consisting of nested spherical shells. When assuming rotational symmetry and homogeneity of mechanical load, the relation between tissue stress and ventricular pressure (p_{lv}), cavity volume(V_{lv}), and wall volume (V_w) can be described as:

$$p_{lv} = \frac{1}{3}(\sigma_{f_m} - 2\bar{\sigma}_{r_m})\ln\left(1 + \frac{V_w}{V_{lv}}\right) . \tag{3.1}$$

Here, σ_{f_m} is the fiber stress and $\bar{\sigma}_{r_m}$ is the radial wall stress at $r_{lv} = \bar{r_{lv}}$, the shell located at one third of the ventricular wall. This representative shell was chosen

because the strain at this location is similar to the fiber strain (Bovendeerd et al., 2006). At this location, assuming incompressibility of the myocardial tissue, the fiber stretch (λ_{f_m}) and radial stretch (λ_{r_m}) can be related to the ventricular geometry by (Arts et al., 1991):

$$\frac{l_s}{l_{s,0}} = \lambda_{f_m} = \lambda_r^{-\frac{1}{2}} = \left(\frac{V_{lv} + \frac{1}{3}V_w}{V_{lv,0} + \frac{1}{3}V_w} \right)^{\frac{1}{3}} , \tag{3.2}$$

with l_s the instantaneous sarcomere length and l_{s0} the sarcomere length at $V_{lv,0}$; the cavity volume at zero transmural pressure.

The myofibers are modeled one-dimensionally, exerting only stress in the fiber direction. The fiber stress consists of an active (σ_a) and passive (σ_p) stress component, where σ_p only depends on the sarcomere length (l_s), while σ_a also depends on the sarcomere shortening velocity (v_s) and time elapsed since activation (t_a).

$$\sigma_f = \sigma_p(l_s) + \sigma_a(l_s, v_s, t_a) . \tag{3.3}$$

The active stress is modeled according to Kerckhoffs et al. (2003), which describes a combination of the contractility (c) and three functions:

$$\sigma_a(l_s, v_s, t_a) = c g_1(l_s) g_2(l_s, t_a) g_3(v_s) . \tag{3.4}$$

g_1 relates the active stress to the sarcomere length and is given by:

$$g_1(l_s) \quad = \quad \begin{cases} 0 & l_s \leq l_{sa0} \\ \sigma_{a0} \tanh^2(c_a(l_s - l_{sa0})) & l_s > l_{sa0} \end{cases} \tag{3.5}$$

Where it is assumed that the fibers can only exert stress in tension. σ_{a0} and c_a are a scaling and curvature parameter, respectively. l_{sa0} is the sarcomere length at which the stress is zero. The time dependent activation function g_2 is defined as:

$$g_2(l_s, t_a) \quad = \quad \begin{cases} 0 & t_a < 0 \\ \tanh^2\left(\frac{t_a}{t_r}\right) \tanh^2\left(\frac{t_{max} - t_a}{t_d}\right) & 0 \leq t_a < t_{max} \\ 0 & t_a \geq t_{max} \end{cases} \tag{3.6}$$

Here, t_{max} is the activation duration and t_r and t_d are the activation rise and decay time constant, respectively.

The dependency of the active stress on the sarcomere shortening velocity is modeled hyperbolically:

$$g_3(v_s) = \frac{v_{s0} - v_s}{v_{s0} + c_v v_s} \text{ with } v_s(t) = -\frac{dl_s(t)}{dt} , \tag{3.7}$$

with v_{s0} the unloaded shortening velocity and c_v the curvature of the hyperbolic relation.

The passive stress in the fiber (σ_p) and radial (σ_r) direction are modeled in a similar way:

$$\sigma_p(l_s) = \begin{cases} 0 & l_s \leq l_{s,0} \\ \sigma_{p0}(e^{c_p(\lambda_f - 1)} - 1) & l_s > l_{s,0} \end{cases} \tag{3.8}$$

$$\sigma_r(l_s) = \begin{cases} 0 & l_s \leq l_{s,0} \\ \sigma_{r0}(e^{c_r(\lambda_r - 1)} - 1) & l_s > l_{s,0} \end{cases} \tag{3.9}$$

The passive stress-length relation is determined by the scaling parameters σ_{p0} and σ_{r0} and the curvature parameters c_p and c_r, respectively.

The intramyocardial pressure (p_{im}) is used as the extravascular pressure on the coronary circulation and is assumed to be linearly dependent on the radial position in the wall. The shell at $r_{lv} = \bar{r_{lv}}$ is also considered representative for p_{im}:

$$\bar{p}_{im} = p_{im}(\bar{r_{lv}}) = \bar{\sigma}_{r_{lv}} + \frac{r_{o,lv} - \bar{r_{lv}}}{r_{o,lv} - r_{i,lv}} p_{lv} \ , \tag{3.10}$$

with $r_{i,lv}$ and $r_{o,lv}$ the inner and outer radius of the ventricle, respectively.

Valves

The mitral valve is modeled as an ideal diode, where the pressure gradient over the mitral valve (Δp_{mv}) is determined by Ohm's law:

$$\Delta p_{mv} = Q_{mv} R_{mv} \ , \tag{3.11}$$

with R_{mv} defined as:

$$R_{mv} = \begin{cases} R_{mv,o} & \text{if } \Delta p_{mv} \geq 0 \ , \\ R_{mv,c} & \text{if } \Delta p_{mv} < 0 \ . \end{cases} \tag{3.12}$$

For the aortic valve the inertia is taken into account and opens due to a positive pressure gradient (Δp_{av}) and closes when the flow through the valve (Q_{av}) becomes negative. The differential equation relating Δp_{av} to Q_{av} is defined as:

$$\Delta p_{av} = L_{av} \frac{dQ_{av}}{dt} + R_{av} Q_{av} \ . \tag{3.13}$$

Here, R_{av} is the resistance and L_{av} the inertia of the valve. L_{av} is determined by the cross-sectional area A_v, the effective valvular length l_{av}, and blood density ρ; $L_{av} = \rho l_{av}/A_{av}$. The value of the resistance parameter R_{av} is determined by the state of the valve:

$$R_{av} = \begin{cases} R_{av,o} & \text{if the valve is open} \\ R_{av,c} & \text{if the valve is closed} \ . \end{cases} \tag{3.14}$$

The values of the different parameters are listed in Table 3.2.

3.2.2 Wave propagation model

The governing equations describing the one-dimensional propagation of pressure and flow waves of a Newtonian incompressible fluid are derived from the conservation of mass and momentum and were taken from Bessems et al. (2007). The conservation of mass is derived as:

$$\frac{\partial A}{\partial t} + \frac{\partial Q}{\partial z} + \psi = 0 \ , \tag{3.15}$$

with z and t representing the axial direction and time, A is the local arterial lumen area, Q is the volumetric flow rate, and ψ the flow per unit length distributed to small side-branches that are not separately modeled by vascular segments. As described by Bessems et al. (2007), an appropriate velocity profile function is assumed that describes the frictional forces and non-linear terms in the balance of momentum equation (see Fig. 3.1):

$$\frac{\partial Q}{\partial t} + \frac{\partial}{\partial z}\left(\delta \frac{Q^2}{A}\right) + \frac{A}{\rho}\frac{\partial p}{\partial z} = A f_z + \frac{2\pi r_i}{\rho}\tau_w + \frac{\eta}{\rho}\frac{\partial^2 Q}{\partial z^2} \ . \tag{3.16}$$

Here, p is the transmural pressure, f_z is the body force in the axial direction, and η and ρ are the dynamic viscosity and density of the fluid, respectively. The wall shear stress is given by:

$$\tau_w = -\frac{2\eta}{(1-\zeta_c)r_i}\frac{Q}{A} + \frac{r_i}{4}(1-\zeta_c)\frac{\partial p}{\partial z} \ , \tag{3.17}$$

with $\zeta_c = \max[0, (1-\sqrt{2}/\alpha)]^2$ representing the relation between the radius of the inertia dominated core and the thickness of the Stokes layer. α is the Womersley parameter according to $\alpha = r_i\sqrt{\frac{2\pi\rho f}{\eta}}$, with f the heart rate. The ζ_c parameter also determines the δ parameter of the convective term in (3.16):

$$\delta = \frac{2 - 2\zeta_c(1-\ln\zeta_c)}{(1-\zeta_c)^2} \ . \tag{3.18}$$

Arterial wall model

To solve (3.15) and (3.16) a constitutive relation between p and A is required. In chapter 2 (van der Horst et al., 2012), it was demonstrated that a model based on the two-fiber constitutive model developed by Holzapfel et al. (2000) was able to accurately capture the radius-pressure relations of porcine and human coronary arteries. In that model the arterial wall was modeled as a cross-ply of helically wound fibers embedded in a cylinder composed of hyperelastic material. The stress (σ) - stretch (λ) behaviour is determined by:

$$\sigma = -p_h\mathbf{I} + G(\mathbf{B} - \mathbf{I}) + \sum_{i=1}^{2} \tau_f^i \, \vec{e}_f^{\,i} \, \vec{e}_f^{\,i} \ , \tag{3.19}$$

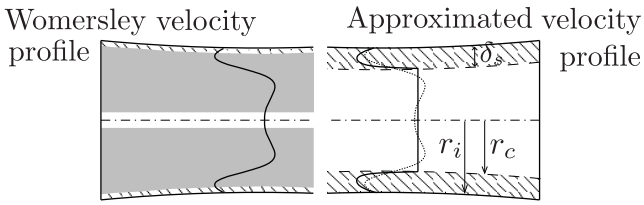

Figure 3.1: *A schematic representation of the exact velocity profile (left) and the approximation (right). r_c is the approximated core radius and δ_s the viscous layer. Adapted from Bessems (2007).*

with p_h the hydrostatic pressure, $\mathbf{I}$ the unity tensor, G the shear modulus, $\mathbf{B}$ the Finger tensor, and τ_f^i the fiber stress of fiber i. $\vec{e}_f^{\,i}$ is the fiber orientation, which is represented by the angle β with the circumference (see Fig. 3.2a). The fiber can only exert stress in tension, with τ_f defined as:

$$\begin{aligned} \tau_f &= k_1 \lambda_f^2 (\lambda_f^2 - 1) e^{k_2 (\lambda_f^2 - 1)^2} && \text{if } \lambda_f \geq 1 \\ \tau_f &= 0 && \text{if } \lambda_f < 1 \ . \end{aligned} \tag{3.20}$$

Here, λ_f is the collagen fiber stretch and k_1 and k_2 are constants determining the stress-stretch relation of the collagen fibers. For coronary arteries the value of these four parameters have been determined in chapter 2 (Fig. 2.6). With removal of the outliers, the median of the four parameters are: G = 19.3 kPa, k_1 = 2.01 kPa, k_2 = 5.10, β_0 = 34.6°.

The stress-free geometry is determined by the opening angle parameter and the axial stretch λ_z (see Fig. 2.2), which are both estimated according to optimization rules explained in chapter 2. The first rule states that at physiological loading the circumferential stress gradients across the wall are minimal. The opening angle parameter is optimized to comply with this rule. The second rule emerges from the finding that the fiber orientation at physiological loading (β_{phys}) is almost constant for all arteries characterized in chapter 2. Using this rule, λ_z can be directly related to the circumferential stretch at p = 13.3 kPa, via two constants: β_0 and β_{phys}=36.4°.

The balance equations resulting from this two-fiber model are solved using numerical integration. Since a numerical integration scheme is also employed to solve (3.15) and (3.16), the direct implementation of this two-fiber model will be computationally very expensive. Therefore, as an intermediate step, a phenomenological model described by Langewouters et al. (1984) is used to analytically relate the compliance (C) to the pressure (p):

$$C = C_0 + \frac{C_1}{1 + \left(\frac{p - p_{max}}{p_w}\right)^2} \ . \tag{3.21}$$

Here, C_0, C_1, p_{max}, and p_w determine the C-p relation. To relate this analytical model to the two-fiber model, it is assumed that these four parameters depend on the only clinically measurable quantities: the radius ($r_{i,p}$) and wall-thickness (h_p) at

physiological axial stretch and pressure (p = 13.3 kPa). First, the C-p relation was determined with the two-fiber model (including the optimization rules) for different combinations of $r_{i,p}$ and h_p. $r_{i,p}$ and h_p ranged from 0.25 to 3 mm and from 0.025 to 0.3 mm, respectively. Then, for each combination of $r_{i,p}$ and h_p within the range 0.05<κ<0.15 ($\kappa = \frac{h_p}{r_{i,p}}$), the four parameters of the Langewouters model were fitted with the Gauss-Newton algorithm as implemented in Matlab (R2010a, The Mathworks, Natick, MA). Using the *multiple regression* function in Statgraphics (Centurion XVI, statpoint technologies, inc. Warrenton, VA) a polynomial was extracted based on the best R^2-adjusted value:

$$\begin{aligned} C_0(r_{i,p}, h_p) &= A_p C_{0,1}(1 + C_{0,2}\kappa^2 + C_{0,3}\kappa) \ , & R^2 &= 0.999 \ , \\ C_1(r_{i,p}, h_p) &= A_p C_{1,1}(1 + C_{1,2}\kappa^2 + C_{1,3}\kappa) \ , & R^2 &= 0.999 \ , \\ p_{max}(r_{i,p}, h_p) &= p_{max,1} + p_{max,2}\tfrac{1}{\kappa} + p_{max,3}\kappa \ , & R^2 &= 0.996 \ , \\ p_w(r_{i,p}, h_p) &= p_{w,1} + p_{w,2}\tfrac{1}{\kappa} + p_{w,3}\kappa \ , & R^2 &= 0.999 \ . \end{aligned} \tag{3.22}$$

The parameters are determined by $A_p = \pi r_{i,p}^2$ and κ and the correlation is good, as indicated by the R^2 values. With these relations, the compliance of the coronary arteries as function of the instantaneous diameter could be determined and used in the wave propagation model.

For the systemic arterial walls we use a simple linear elastic model:

$$C = \frac{2\pi(1-\mu^2)r_i^3}{hE} \ . \tag{3.23}$$

Here, E is the Young's modulus and μ is Poisson's ratio. For all systemic arteries, incompressibility is assumed (μ =0.5) and E = 0.4 MPa (Stergiopulos et al., 1992).

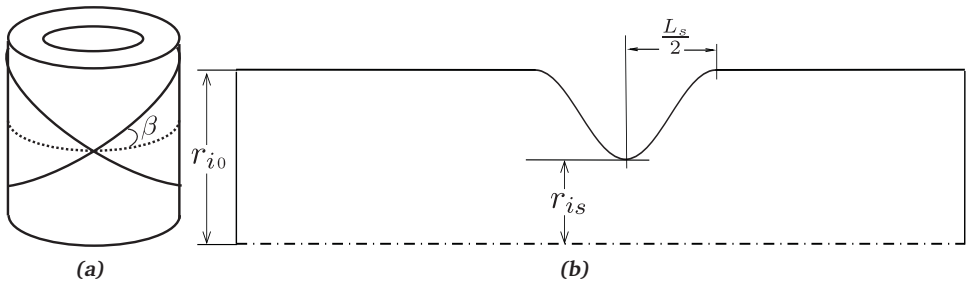

Figure 3.2: ***a)*** *A schematic representation of the model of coronary arterial wall (Holzapfel et al., 2000). The fiber orientation is determined by angle β.* ***b)*** *A two-dimensional representation of the stenosis element. L_s is the length of the stenosis, r_{is} the radius of the vessel at the neck of the stenosis, and r_{i0} the radius of the vessel proximal to the stenosis. Adapted from Bessems (2007).*

Stenosis element

While one-dimensional theory is suitable to model the pressure and flow waves in relatively straight arteries, it may yield unrealistic results in pathological regions

like aneurysms and stenoses. In the derivation of the one-dimensional model it is assumed that variations in the cross-sectional area of the vessels is relatively small, so the radial and circumferential blood velocity is negligibly small with respect to the axial component. Considering that epicardial coronary arteries are prone to the development of stenoses, it is necessary to use a specific element that can be incorporated into to the 1D model.

Bessems (2007) developed a 1D stenosis element, based on the semi-empirical relations obtained by Young and Tsai (1973a,b) but with an improved contribution of the viscous and unsteady components, to calculate the pressure-drop over an axisymmetric narrowing. The parameters of this model are based on two-dimensional axisymmetrical finite element simulations of stenotic hemodynamics. The axisymmetric stenosis geometry is depicted in Figure 3.2b.

For oscillatory flow simulations Bessems (2007) derived the following relation for the pressure drop over a stenosis (Δp_s):

$$\Delta p_s = K_v(\alpha) R_{st} Q + \frac{\rho K_t}{2A_0^2}\left(\frac{A_0}{A_s} - 1\right)^2 |Q|Q + K_u(\alpha) L_u \frac{\partial Q}{\partial t} + K_c(\alpha)\bar{Q} \ . \quad (3.24)$$

The parameter, A_0 and A_s are the cross-sectional areas of the vessel proximal to and at the neck of the stenosis, respectively. $\bar{Q}$ is the average flow, and K_v, K_t, K_u, and K_c are empirically determined constants obtained by Bessems (2007). They are given by:

$$K_v = 1 + 0.053\frac{A_s}{A_0}\alpha \ , \ K_t = 0.95 \ , \ K_u = 1.2 \ , \ K_c = 0.0018\alpha^2 \ . \quad (3.25)$$

R_{st} is the resistance and L_u is inertia across the stenosis:

$$R_{st} = \frac{8\eta}{\pi r_{i0}^4}\int_{L_s} \frac{r_{i0}^4}{r_{is}^4(z)} dz \text{ and } L_u = \frac{\rho}{\pi r_{i0}^2}\int_{L_s} \frac{r_{i0}^2}{r_{is}^2(z)} dz \ . \quad (3.26)$$

r_{i0} is the radius of the vessel proximal of the stenosis and $r_{is}(z)$ the varying radius of the vessel at the site of the stenosis. When assuming that the pressure drop develops linearly over the length of the stenosis, (3.24) can be written in the following differential form:

$$\frac{\partial Q}{\partial t} + \frac{K_v R_{st}}{K_u L_u} Q + \frac{\rho K_t}{2A_0^2 K_u L_u}\left(\frac{A_0}{A_s} - 1\right)^2 |Q|Q + \frac{L_s}{K_u L_u}\frac{\partial p}{\partial z} + \frac{K_c R_{st}}{K_u L_u}\bar{Q} = 0 \ . \quad (3.27)$$

The conservation of mass in the stenosis is given by (3.15), for which the compliance is assumed to be negligible.

3.2.3 Lumped elements

The contribution of the peripheral vasculature at each end-point of the 1D model is lumped with three-element Windkessel elements (see Westerhof et al. (1969)). The relation between the pressure and flow for these elements can be written as:

$$C_w \frac{\partial p}{\partial t} + R_{tot} p = Q \ . \quad (3.28)$$

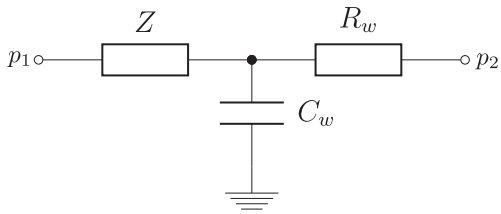

Figure 3.3: *A Windkessel element with parameters Z, R_w, and C_w.*

Here, C_w is the compliance and R_{tot} is the sum of resistance R_w and wave impedance Z, representing the total compliance and resistance of the distal vascular bed, respectively (see Fig. 3.3). The wave impedance is given by:

$$Z = \sqrt{\frac{\rho}{\bar{A}\bar{C}}}\,, \tag{3.29}$$

with $\bar{A}$ and $\bar{C}$ the average cross-sectional area and compliance of the connecting vessel. The total resistance R_{tot} was determined from the average flow ($\bar{Q}$) and pressure drop ($\bar{\Delta p}$) over the Windkessel element:

$$R_t = \frac{\bar{Q}}{\bar{\Delta p}}\,, \tag{3.30}$$

Note that R_t does not have to be the resistance in one Windkessel but may be distributed over several Windkessel elements. Finally, C_w is the compliance of the artery defined by a time constant $\tau = R_w C_w$, with $\tau = 2$ s.

3.2.4 The total model

The model of all 1D vessels and lumped elements is shown in Figure 3.4. The pulmonary venous pressure (1200 Pa $\approx$ 9 mmHg) serves as the input for the left ventricle (LV) in diastole. The contraction sequence described in section 3.2.1 increases the left ventricular pressure (p_{lv}), closing the mitral valve and, if the pressure exceeds the aortic pressure (p_{ao}), opening the aortic valve. From the resulting pressure gradient the flow over the aortic valve is calculated using (3.13) and serves as the input for the aortic wave propagation elements.

To include the effect of the systemic wave reflections, the aorta is modeled with all major side branches, with at each distal end a terminal impedance that is prescribed using the three-element Windkessel element. The geometrical data are taken from Stergiopulos et al. (1992) and are listed in Table 3.1.

A hypothetical anatomy of the main coronary branches is assumed. The left main coronary artery (LMCA) and right coronary artery (RCA) originate 5 mm distal from the aortic valve. The LMCA splits in the left anterior descending (LAD) and circumflex (LCx) arteries. The LAD has total length of 7.5 cm with four side branches (representing the diagonal and septal side branches), while the LCx has a length of 6 cm with three side branches (marginal and posteriorlateral branches). The geometry

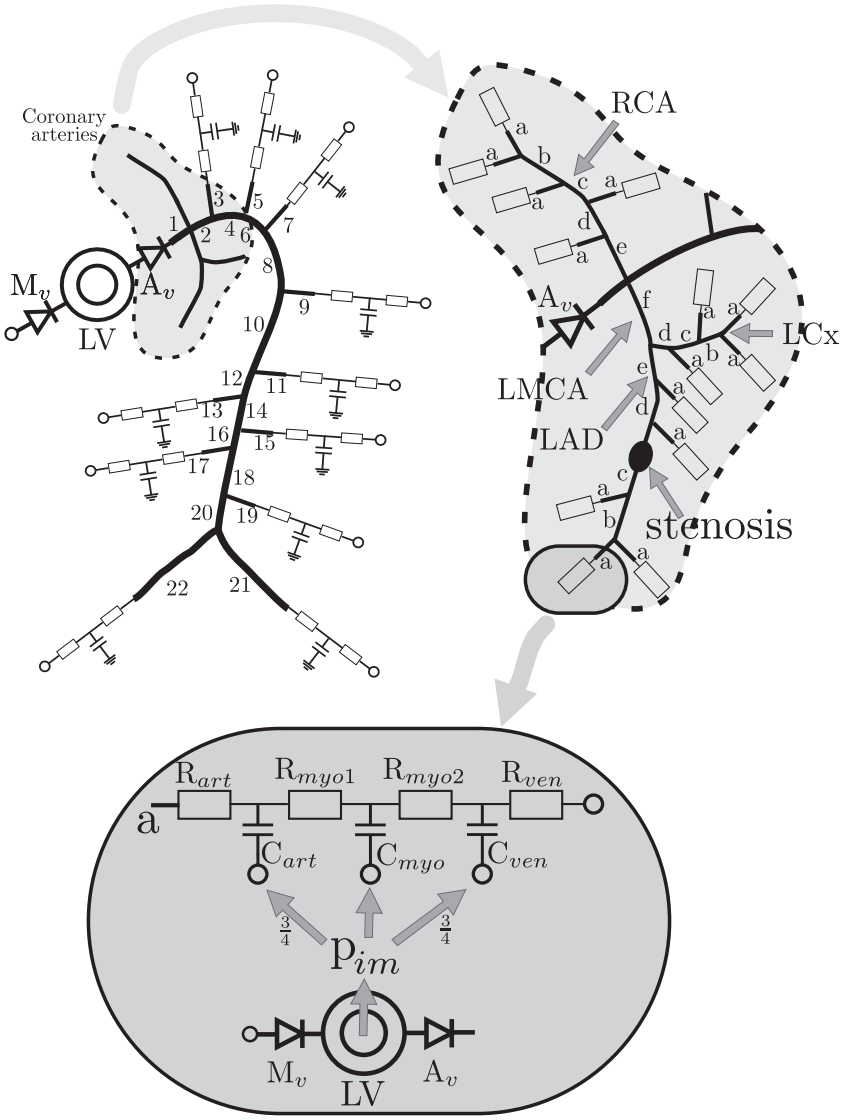

Figure 3.4: *The total model consisting of the left ventricle (LV), with the mitral (M_v) and aortic valve (A_v), the aorta, and the coronary circulation. The aorta and its main branches are numbered according to Table 3.1. The LMCA has a length of 5 mm and splits into the LAD and the LCx, with a length 7.5 cm and 6 cm, respectively. Side branches are modeled at intervals of 1.5 cm. Each coronary segment is represented by the characters a - f. The radius of segment a is 1 mm and Murray's law is used to determine the radius of segments b-f. All a-segments are connected to the three Windkessel elements representing the coronary microvessels. The intramyocardial pressure (p_{im}) acts on the three capacitors that represent the vessel compliance. When a stenosis is modeled, it is incorporated into the c-segment of the LAD.*

of the RCA is equal to the LAD and it is assumed that it supplies both the left and right ventricle (RV), with a ratio of 0.4. Since the RV is not modeled here, it is assumed that the intramyocardial pressure (p_{im}) of the RV is smaller by a factor proportional to the ratio of maximum pressure in the two ventricles ($p_{im,RV} = 0.2p_{im,LV}$). For all terminal coronary 1D vessels (14 in total) a radius of 1 mm was prescribed and for each bifurcation Murray's law (Murray, 1926) determines the ratio of the mother and daughter vessels. Based on Van den Broek et al. (2011), it is assumed that for all coronary vessels the wall thickness is equal to 10% of the radius ($\kappa = 0.1$).

The microvasculature is modeled with three serial Windkessel elements. The total resistance (R_t) is determined using Ohm's law by assuming an average pressure of 100 mmHg and prescribing a flow of approximately 20 ml/min through every terminal branch. Following Bovendeerd et al. (2006), R_t is distributed over the four resistances according to: $R_{art} = \frac{7}{27}R_t$, $R_{myo1,2} = \frac{9}{27}R_t$, and $R_{ven} = \frac{2}{27}R_t$. The values of the three capacitors are based on measurements by Spaan (1985): $C_{art} = 0.2$ mm^{3}Pa^{-1}, $C_{myo} = 0.53$ mm^{3}Pa^{-1}, and $C_{ven} = 0.65$ mm^{3}Pa^{-1}. The intramyocardial (p_{im}) pressure that is generated by the heart contraction model is connected to the three capacitors to model the extravascular pressure on the coronary vessels. Since the circulation is not closed, a constant venous pressure of 700 Pa ($\pm$ 5 mmHg) is prescribed at the output of the model.

Solution procedure

As described in Kroon et al. (2012), the 1D and 0D pressure and flow relations are solved fully coupled by writing the differential equations in the same form. Here, only a short description of the solution procedure is given. For a full description of the solution procedure the reader is referred to Kroon et al. (2012). For each subelement of the Windkessel element two nodal point pressures and flows are defined. The two nodal flows are directed inwards for each subelement. (3.28) can then be written as:

$$\underset{\sim}{C}_e \frac{\partial \underset{\sim}{p}_e}{\partial t} + \underset{\sim}{R}_e \underset{\sim}{p}_e = \underset{\sim}{Q}_e \ . \tag{3.31}$$

The matrix $\underset{\sim}{R}_e$ contains the reciprocals of the wave impedance Z and peripheral resistance R_w and $\underset{\sim}{C}_e$ contains the compliance C_w. The nodal point pressures and flows are in columns $\underset{\sim}{p}_e$ and $\underset{\sim}{Q}_e$, respectively. Temporal discretization, with time step Δt, is performed using the Euler implicit integration scheme resulting in:

$$\underset{\sim}{K}_e^{0D} \underset{\sim}{p}_e^{t+\Delta t} = \underset{\sim}{f}_e^{0D} + \underset{\sim}{q}_e^{t+\Delta t} \ , \tag{3.32}$$

with,

$$\begin{aligned} \underset{\sim}{K}_e^{0D} &= \tfrac{1}{\Delta t}\underset{\sim}{C}_e + R_e \ , \\ \underset{\sim}{f}_e^{0D} &= \tfrac{1}{\Delta t}\underset{\sim}{C}_e \underset{\sim}{p}_e^{t} \ . \end{aligned} \tag{3.33}$$

To be able to fully couple the differential equations in (3.15) and (3.16), they have to be written in the same form as the Windkessel elements. First, the equations are linearized with the area, compliance, wall shear stress, and convective acceleration

Table 3.1: *Geometric and physiological parameters of the arterial vessels. The length (L), proximal radius (r_{ip}), distal radius (r_{id}), and wall thickness (h) of the systemic arteries are based on Stergiopulos et al. (1992). The parameters of the Windkessel elements (Z,R_w, and C_w; see Fig. 3.3) were determined as described in section 3.2.3. The numbers of the different vessels correspond to the numbers shown in Figure 3.4.*

Nr.	name	L mm	r_{ip} mm	r_{id} mm	h mm	Z MPa s m^{-3}	R_w GPa s m^{-3}	C_w mm^3 Pa^{-1}
1	ascending aorta A	5.0	14.7	14.7	1.63			
2	ascending aorta B	35	14.7	14.4	1.63			
3	innominate	30	6.20	6.20	0.80	52.2	0.36	4.125
4	aortic arch A	20	11.2	11.2	1.26			
5	left carotid	30	3.70	3.70	0.63	161	1.80	0.835
6	aortic arch B	39	10.7	10.7	1.15			
7	left subclavian	30	4.23	4.23	0.66	118	1.19	1.259
8	thoracic aorta A	52	9.99	9.99	1.10			
9	intercostals	30	2.00	2.00	0.49	659	11.7	0.128
10	thoracic aorta B	104	6.75	6.75	1.00			
11	celiac	30	3.00	3.00	0.64	273	3.40	0.442
12	abdominal aorta A	53	6.10	6.10	0.90			
13	sup. mesenteric	30	4.35	4.35	0.69	112	1.09	1.374
14	abdominal aorta B	10	5.90	5.90	0.80			
15	left renal	30	2.60	2.60	0.53	356	5.28	0.284
16	abdominal aorta C	10	5.90	5.90	0.80			
17	right renal	30	2.60	2.60	0.53	356	5.28	0.284
18	abdominal aorta D	106	5.80	5.48	0.75			
19	inf. mesenteric	30	1.60	1.60	0.43	108	23.1	0.065
20	abdominal aorta E	10	5.20	5.20	0.65			
21	l. common iliac	30	3.68	3.68	0.60	15.9	1.83	0.820
22	r. common iliac	30	3.68	3.68	0.60	15.9	1.83	0.820

from the previous time step. The 1D vessels are divided into a number of non-overlapping elements (of 2.5 mm) with two nodes. The Gaussian quadrature rule is used to spatially integrate the element equations. The temporal integration is also performed with the Euler implicit scheme resulting in:

$$\underline{K}_e^{1D} \underset{\sim}{p}_e^{t+\Delta t} = \underset{\sim}{f}_e^{1D} + \underset{\sim}{Q}_e^{t+\Delta t} \ . \tag{3.34}$$

The flow of the subelements is again defined inwards, which automatically implicates that during the assembly process, the pressure at the boundary of connecting elements is equal and that the inflow is equal to the outflow. The large system of equations, resulting from the relations at element level, can be written as:

$$\underline{K} \underset{\sim}{p} = \underset{\sim}{f} + \underset{\sim}{Q} \ . \tag{3.35}$$

The column $\underset{\sim}{Q}$ is the external nodal flow column, which contains all zeros except for the nodes where the external flow is prescribed. By prescribing the pressures at the distal nodal point of the Windkessel elements, (3.35) is iteratively solved at each time step. When the pressures are known, the flow at each nodal point can be extracted using (3.32) and (3.34).

Table 3.2: *The parameters describing the heart, blood, and arterial wall. The values between brackets represent the parameters used to model LVH-AVS before and after AVR, respectively.*

Parameter	Value	Unit	Parameter	Value	Unit
$V_{LV,0}$	60 (60,60)	10^{-6}m^3	A_{av}	679	10^{-6}m^2
V_w	200 (250,200)	10^{-6}m^3	$R_{av,o}$	1 (3·10^7,1)	Pa s m^{-3}
$l_{s,0}$	1.9	10^{-6}m	$R_{av,c}$	1·10^{12}	Pa s m^{-3}
$l_{s,a0}$	1.5	10^{-6}m	$R_{mv,o}$	4·10^6	Pa s m^{-3}
c	1 (1.4,1)	-	$R_{mv,c}$	1·10^{12}	Pa s m^{-3}
σ_{a0}	90	10^3Pa	ρ	1050	kg m^{-3}
c_a	2.4	10^6m	η	0.004	kg m^{-1}s^{-1}
t_a	75	10^{-3}s	ψ	0	10^{-6}m^3 s
t_d	75	10^{-3}s	f_z	0	kg m s^{-2}
t_{max}	0.4	s	$C_{0,1}$	284	10^{-9}m^2 Pa^{-1}
$v_{s,0}$	10	10^{-6}m s^{-1}	$C_{0,2}$	12.1	-
c_v	1	-	$C_{0,3}$	-3.59	-
$v_{s,0}$	10	10^{-6}m s^{-1}	$C_{1,1}$	1.09	10^{-9}m^2 Pa^{-1}
c_v	1	-	$C_{1,2}$	34.7	-
$v_{s,0}$	10	10^{-6}m s^{-1}	$C_{1,3}$	-9.85	-
c_v	1	-	$p_{max,1}$	646	Pa
$\sigma_{p,0}$	0.9	10^3Pa	$p_{max,2}$	-17.0	Pa
c_p	12	-	$p_{max,3}$	15.9	10^3Pa
$\sigma_{r,0}$	0.2	10^3Pa	$p_{w,1}$	708	Pa
c_r	9	-	$p_{w,2}$	-14.8	Pa
l_{av}	10	10^{-3}m	$p_{w,3}$	12.9	10^3Pa

The final set of equations is solved using a direct profile solver (Segal, 1993), as implemented in the finite element package Sepran (Ingenieursbureau SEPRA, Leidschendam, The Netherlands).

Simulations and data analysis

To test whether the model is able to describe coronary hemodynamics in both normal and pathological situations, three different simulations are performed. The normal, healthy, situations is modeled with the parameters listed in Tables 3.1 and 3.2. The pressure, flow, and volumes of the heart and aorta obtained with the model are qualitatively compared to similar signals described by Van de Vosse and Stergiopulos (2011). The modeled coronary pressure and flow in the LMCA and RCA are compared to pressure and velocity measurements performed simultaneously in the LMCA and RCA by Hadjiloizou et al. (2008). Two types of pathological situations are modeled: a stenosis in the LAD (see Fig. 3.4) and left ventricular hypertrophy due to an aortic valve stenosis (LVH-AVS).

Dynamic pressure measurements proximal and distal to a mild (50% diameter, length 2.65 mm) and severe (70% diameter, length 7.48 mm) stenosis, performed in the catheterization laboratory of the Catharina hospital (Eindhoven, The Netherlands), are used to validate the stenosis element. Since the flow through the stenotic vessels was not measured, quantitative comparison is difficult. Therefore, the dynamics of the measured and modeled pressure signals is only compared qualitatively. Since the pressure measurements are performed during hyperaemia, the

flow in the model was increased five-fold, by decreasing the coronary microvascular resistances. Furthermore, the most clinically used index to quantify coronary stenoses, fractional flow reserve (FFR), which is defined as the ratio of the pressure distal and proximal to a stenosis (see chapter 1), is determined with both the model and the measurements.

The ability of the model to describe coronary hemodynamics when LVH-AVS is present is validated with clinical measurements performed by Hildick-Smith and Shapiro (2000). With transthoracic Doppler echocardiography, they measured the dynamics of flow in the LAD in LVH-AVS patients before and six months after aortic valve replacement (AVR). While the average left ventricular cavity volume was constant before and six months after AVR, the measured average ventricular mass decreased significantly: from 271 to 226 g. The average aortic valve pressure gradient before AVR was 93 mmHg. The two situations before and after AVR are modeled with ventricular wall volumes based on the measured ventricular wall mass, assuming a mass density of 1.1 kg/l. The contractility and aortic valve resistance are increased such that the pressure gradient across the aortic valve is approximately 93 mmHg, while the average aortic pressure remains normal. The model parameters of the heart contraction model and valves are listed in Table 3.2. The main features of the dynamics of the modeled flow in the LAD are qualitatively compared to the measurements by Hildick-Smith and Shapiro (2000).

As it is expected that the difference between the used coronary arterial wall model and a simple linear elastic model is largest in the low pressure range, the difference between the two models is investigated both proximal and distal to the severe stenosis described above. The relative differences between the pressure, flow, cross-sectional area, compliance, and wall shear stress calculated with the model are quantified according to:

$$\delta_y = 100 * \frac{y - y_{lin}}{\bar{y}/2 + \bar{y}_{lin}/2} \ . \tag{3.36}$$

Here, y is the signal obtained with the used coronary arterial model and y_{lin} is the signal obtained with the linear elastic model with a Young's modulus of 1.5 MPa and a Poisson ratio of 0.5.

3.3 Results

3.3.1 Normal hemodynamics

Figure 3.5 shows that the heart and systemic pressures, flows, and volumes obtained with the model, qualitatively agree with values found in literature (van de Vosse and Stergiopulos, 2011). With a stroke volume of 70 ml/min, a mean aortic flow of 4.8 l/min, and an aortic mean and pulse pressure of 93 and 47, respectively, the main clinically relevant parameters are within the normal physiological range. The dynamics of the different signals are also similar, except the time-dependent behaviour of the mitral flow, especially at late diastole (Fig. 3.5c and 3.5f). This is obviously due to the lack of the atrial contraction in the model.

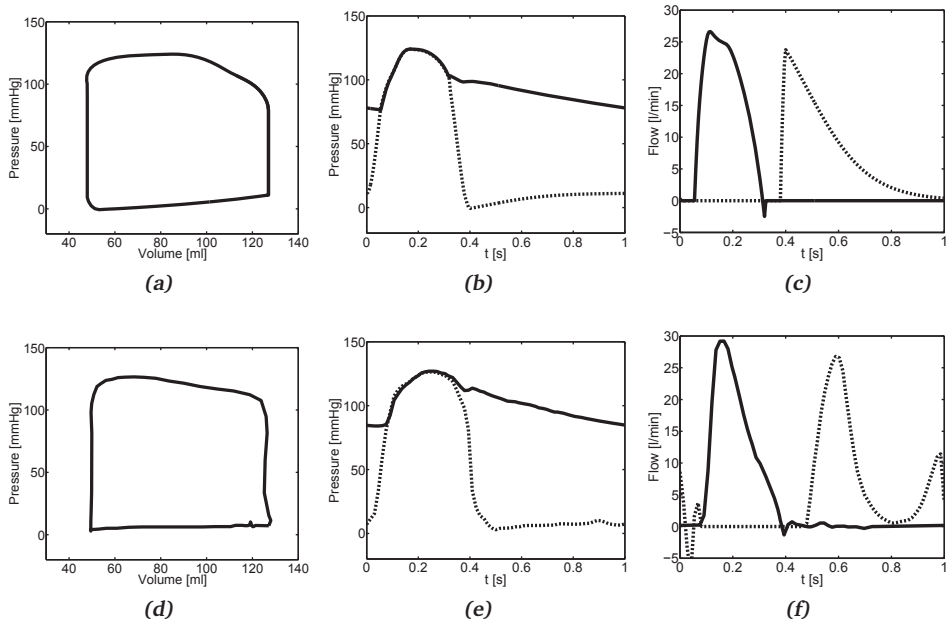

Figure 3.5: Top: *The left ventricular pressure-volume loop* ***(a)****, the left ventricular pressure (- -) and aortic (-) pressure* ***(b)****, and the flow through the aortic (-) and mitral (- -) valve* ***(c)****, obtained with the model.* ***Bottom:*** *Similar signals representing human hemodynamics, adapted from Van de Vosse and Stergiopulos (2011, Fig. 3). The pressure-volume loop in* ***(d)*** *is determined from the data in* ***(e)*** *and* ***(f)*** *with the end-systolic volume assumed to be 45 ml.*

The modeled pressure and flow in the left main (LMCA) and proximal right (RCA) coronary artery are depicted in Figure 3.6. The data are compared to pressure and blood velocity measurements acquired simultaneously in a human LMCA and RCA (Hadjiloizou et al., 2008). It should be noted that the mean and pulse pressure measured by Hadjiloizou et al. (2008) were relatively high and there was a small offset between the pressure measured in the RCA and LMCA (Fig. 3.6d). Although these pressures are not considered representative for non-diseased vessels, the data do enable the qualitative comparison between the flow velocities in both the LMCA and RCA and the pressure-flow relation. The modeled pressures in the LMCA and RCA were almost identical and are determined by the aortic pressure. The flow in the LMCA was diastolic dominated, with the typical flow impediment during early systole. Although it depends to what degree the RCA supplies blood to the left or right ventricle, the flow in the RCA was markedly less dominant in diastole, compared to the LMCA. This demonstrates the influence of the intramyocardial pressure on the coronary flow. The pressure-flow relations for both the LMCA and RCA are depicted in Figure 3.6c and qualitatively agree with the measurements presented by Hadjiloizou et al. (2008) (Fig. 3.6f).

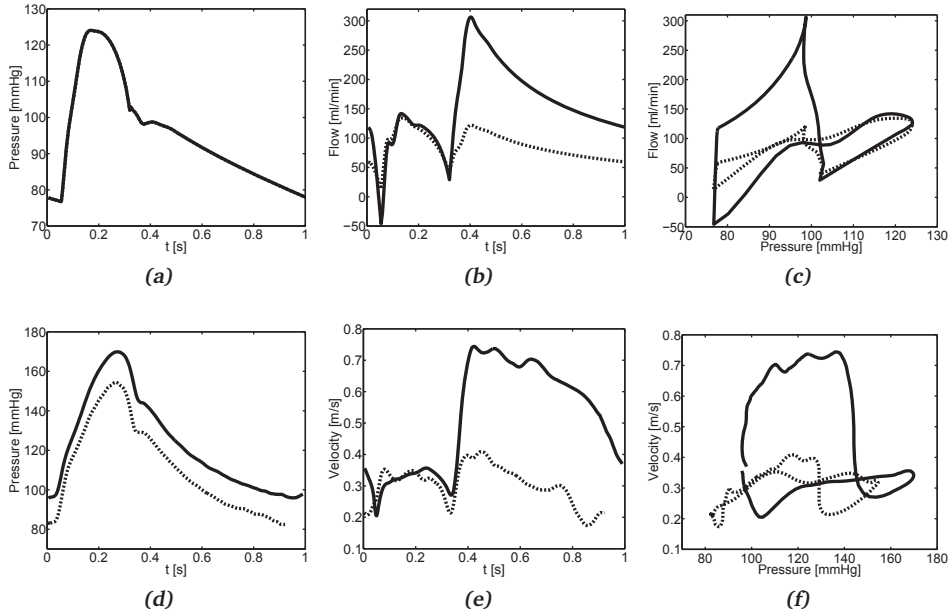

Figure 3.6: Top: *The left main (-) and right (- -) coronary pressure* ***(a)****, flow* ***(b)****, and pressure-flow relation* ***(c)****, obtained with the model.* ***Bottom:*** *Similar signals representing human coronary hemodynamics, data obtained from Hadjiloizou et al. (2008, Fig. 1).*

3.3.2 Stenosis

The pressure measurements depicted in Figure 3.7c and 3.7d demonstrate the effect of a mild (50% diameter) and severe (70% diameter) stenosis, respectively. It is apparent that the pressure gradient was much larger for the severe stenosis, especially in diastole when the flow was highest. The pressures determined with the model showed the same behaviour as the measurements, with the largest pressure gradient in diastole (Fig. 3.7a and 3.7b). For the modeled mild stenosis this pressure gradient variation between systole and diastole is larger than in the experimental data. A possible explanation for this discrepancy is a less distinct difference between systolic and diastolic flow in that measurement. The FFR's determined with the measurements were 0.93 and 0.57 for the mild and severe stenosis, respectively, whereas the FFR's determined with the model were 0.96 and 0.61.

3.3.3 Left ventricular hypertrophy with an aortic valve stenosis

In Figure 3.8 the effect of LVH-AVS on the coronary flow is shown and compared to transthoracic Doppler echocardiography measurements by Hildick-Smith and Shapiro (2000, Fig. 3a and Fig. 4a), before and six month after AVR. The normal characteristic flow dynamics, with a small positive systolic and large diastole component, was found

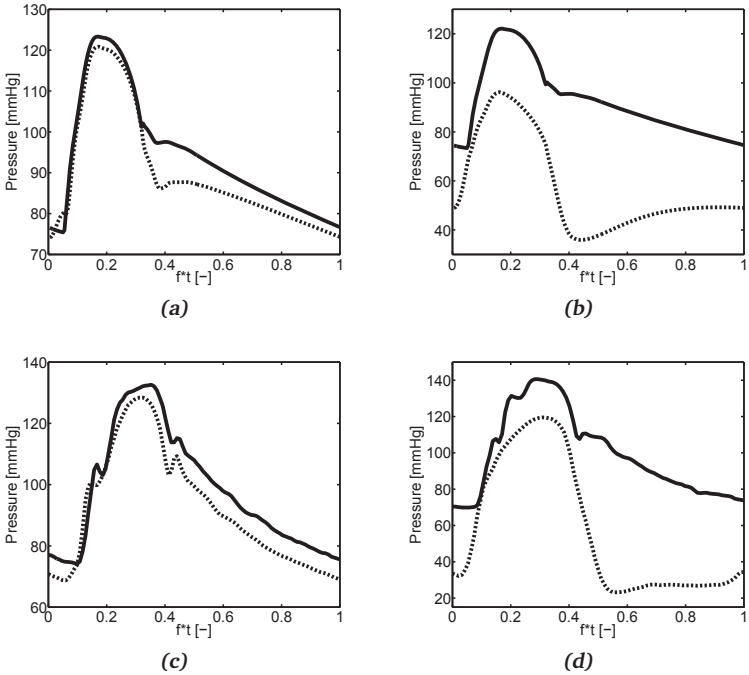

Figure 3.7: *The pressure proximal (-) and distal (- -) to a 50% diameter stenosis with a length of 2.65 mm* ***(a,c)*** *and a 70% diameter stenosis with a length of 7.48 mm* ***(b,d)****, determined with the model* ***(a,b)*** *and measured in human coronary arteries* ***(c,d)*** *at the Catharina Hospital, Eindhoven, The Netherlands. Written informed consent was given by each patient.*

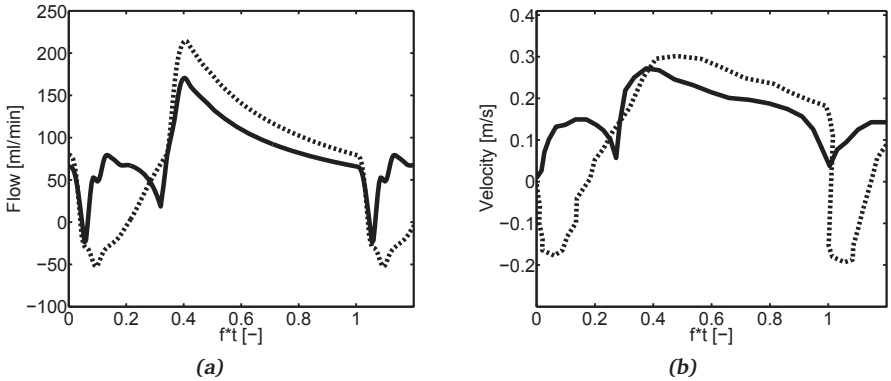

Figure 3.8: *Flow in the LAD of LVH-AVS patients before (- -) and six months after (-) AVR determined with the model* ***(a)*** *and measured in a human LAD with transthoracic Doppler echocardiography by Hildick-Smith and Shapiro (2000)* ***(b)****.*

after AVR, in both the measurements and the simulations. Before the AVR, so when the LVH-AVS is present, the measurements reveal that the small positive systolic flow component was replaced by a period of negative flow. This feature was also captured by the model, demonstrating the influence of the increased intramyocardial pressure on the coronary flow dynamics.

3.3.4 Arterial wall model

The effect of using the arterial wall model proposed by Langewouters et al. (1984) compared to a linear elastic model will be most apparent in the low pressure range. Therefore, the difference between the two arterial wall models was determined both proximal and distal to the 70% diameter stenosis. In Figure 3.9 the relative difference between the two models, as defined by (3.36), on the pressure (p), flow (Q), cross-sectional (A), compliance (C), and wall shear stress (τ_w) are shown. Proximal to the stenosis, the difference between the two models was small. The maximal δ_C was 34% but this did not results in major difference in the other quantities. Distal to the stenosis, the maximal δ_C was 210%. While the effect on the pressure (max $\delta_p = 5\%$), flow (max $\delta_Q = 2\%$), and cross-sectional area (max $\delta_A = 8\%$) was rather limited, the wall shear stress changed significantly (max $\delta_{\tau_w} = 17\%$).

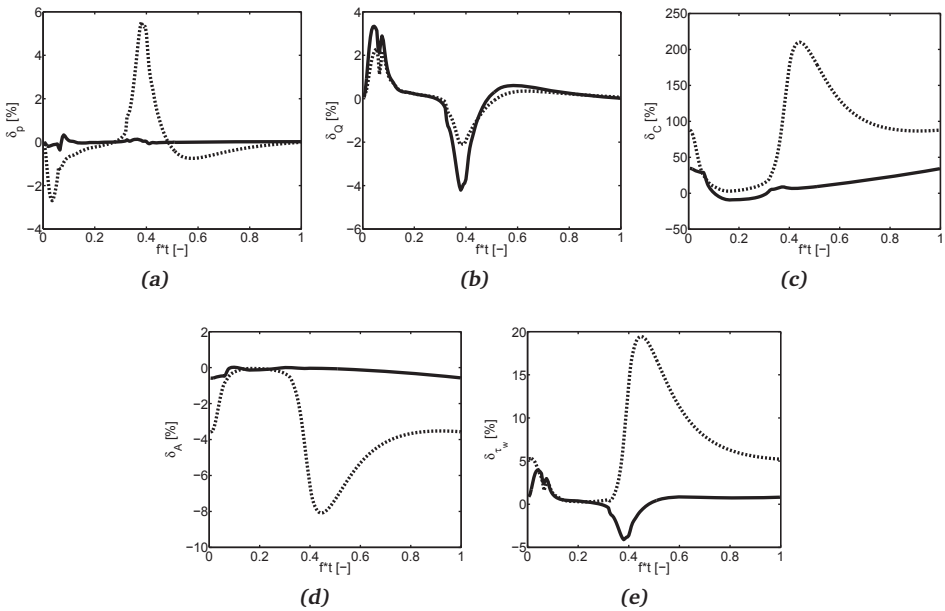

Figure 3.9: *The difference between the results obtained the Langewouters model and linear elastic model, as described in (3.36). The pressure (p), flow (Q), cross-sectional (A), compliance (C), and wall shear stress (τ_w) are shown proximal (-) and distal (- -) to the 70% diameter stenosis.*

3.4 Discussion

In the present study, previously published models of the heart and vessels have been combined to create a model capable of describing coronary hemodynamics in health and disease. By coupling a heart model to a 1D wave propagation model, the effect of heart disease on both the coronary microvessels and the aortic perfusion pressure could be related to coronary epicardial hemodynamics. With the combination of models, stable solutions were obtained and the waveforms found with the model featured the main characteristics of both systemic and epicardial coronary pressure and flow dynamics. Additionally, by changing a limited amount of parameters a coronary stenosis and left ventricular hypertrophy with an aortic valve stenosis (LVH-AVS) could be modeled and produced specific hemodynamical features that qualitatively agreed with experimental observations described in literature.

The heart mechanics is governed by the single-fiber contraction model developed by Bovendeerd et al. (2006). The main advantage of this particular model is that it is based on microstructural material and macrostructural (global) geometrical properties, enabling the simulation of cardiac disease with physiology-based parameter changes, as was demonstrated by simulating LVH-AVS. Obviously, being modeled as a sphere with myofibers oriented in the same direction in each shell, the heart model is a simplified representation of the cardiac muscle. Although the validity of this model should be evaluated for each type of cardiac disease, this simplified representation is also the strength of model, since it is able to produce physiological hemodynamics with a limited amount of parameters. Due to the use of a representative intramyocardial pressure, and average values for the coronary compliances and resistances, the coronary flow in the model should be regarded as a mean flow over the myocardium. It therefore cannot describe radial layer-specific differences in coronary perfusion, which can be clinically relevant in relation to ischemia. These spatial differences, however, can be incorporated by modeling branches at different layers in the myocardium. Then, at each layer a specific (non-)linear compliance can be prescribed (see Algranati et al. (2011)). The contraction of the left atrium was not modeled, which was clearly reflected in the mitral valve flow. This, however, did not result in an unrealistic pressure-volume relation in the left ventricle. The right ventricle was also not incorporated into the model, with the right ventricular intramyocardial pressure ($p_{im,RV}$) approximated by a factor (0.2) proportional to the left ventricular intramyocardial pressure ($p_{im,LV}$). To get a more realistic measure of $p_{im,RV}$, the right ventricle can also be modeled with a similar heart contraction model as was demonstrated by Cox et al. (2009).

The systemic large epicardial coronary arteries are modeled one-dimensionally, which enables the investigation of the propagating pressure and flow waves as was validated by Bessems et al. (2007). This specific model has the advantage that it is time domain-based and has a velocity profile that approximates the actual Womersley profiles. This is especially important when the 1D model is used as the boundary condition for a more detailed 3D model.

The described solution procedure by Kroon et al. (2012), enables easy coupling between the 1D and lumped elements. This is particulary convenient in case of

bifurcations and the coupling to the Windkessel elements. A limitation of the current solution procedure is that it incorporates only wave elements with two nodes, whereas higher order elements (e.g. spectral elements) might provide more accurate results. However, as shown by Kroon et al. (2012), this limitation has little influence, as element size appeared of minor importance.

A three-element Windkessel element was chosen to represent the coronary microvasculature. While this representation did result in physiological coronary hemodynamics, a four element Windkessel element (Stergiopulos et al., 1998) might improve the signal, particulary at the large increase in flow during early diastole where the inertia of the blood will play a role. Furthermore, it was found that the parameters of the first Windkessel element have a very large influence on the dynamics of the coronary flow. A proper sensitivity analysis of the model parameters may be helpful in the correct parameter choice for patient-specific modeling.

The compliance of the arterial wall of the coronary vessels was modeled with the analytical model of Langewouters et al. (1984). The parameters of the model were fitted to the model described in chapter 2. For different radii and wall thicknesses an accurate, polynomial description was found for each parameter of the Langewouters model. The main advantage of this approach is that the analytical description enables easy implementation into the model, at low additional computational cost, while the microstructural properties are taken into account. By comparing the pressure and flow waves obtained with this wall model with a linear elastic model, it was found that the differences where very small, even distal to a severe stenosis where the change in compliance are the largest. The wall shear stress, however, did change significantly (17%) distal to this stenosis. This might be of clinical interest, since the wall shear stress has been indicated as a factor involved in the development and destabilization of plaques (Slager et al., 2005).

The stenosis element has been shown to be compatible with the wave propagation elements and agrees qualitatively with pressure measurements from the clinic. The flow in these stenotic vessels was, however, not measured, which makes a proper quantitative comparison impossible. The stenosis is modeled as being smooth and axisymmetric, whereas in clinical practice stenoses are irregular. This might also be the reason why the measured FFR values where lower than the ones obtained with the model. Although 3D modeling (Shanmugavelayudam et al., 2010) is required to investigate to what extent the stenosis element is capable of describing the hemodynamics of irregular stenoses, it is likely that in most cases the stenosis element cannot adequately describe stenoses found in the clinic. The stenosis element used is therefore less suitable for patient-specific modeling and should be viewed as a tool to investigate the global effect of stenoses in combination with other disease types on coronary hemodynamics.

The simulated LVH-AVS also qualitatively agreed with the data described in literature, indicating that model is able to capture the global effect of LVH-AVS on coronary flow. However, for a proper validation of the model, simultaneous measurements of left ventricular pressure and volume and coronary pressure and flow should be performed in both non-diseased and LVH-AVS hearts.

For a proper validation of the model, a number of case studies should also

be performed, in which the effect of for different disease types on coronary hemodynamics is measured under well controlled conditions. An isolated beating heart set-up (de Hart et al., 2011) might be a suitable platform for these studies.

The next step in improving the model would be to include autoregulatory mechanisms. The baroreflex mechanism could be included to regulate the heart rate, as was already incorporated into a similar heart contraction model by Cox et al. (2009). Furthermore, by including the coronary autoregulation, the difference between resting and hyperaemic flow can be simulated (Kim et al., 2010). This is valuable since it enables the determination of clinical indices based on the difference between resting and hyperaemic hemodynamics, e.g. coronary flow reserve (Gould et al., 1990) or diastolic coronary vascular reserve (Krams et al., 2004). This heart contraction model is suitable to include this mechanism, since the work performed by the heart can be used as a parameter in the autoregulation mechanism.

Besides application of this model to enhance the diagnosis in case of combinations of multiple disease types, the model can also be used to investigate the global effect of an intervention, bypass surgery, or collaterals on coronary epicardial hemodynamics. To be able to use the model for patient-specific modeling of the (diseased) coronary circulation, model parameters need to be fitted to hemodynamical measurements. Besides adequate measuring devices for coronary pressure and flow (and lumen area), this will require a proper parameter sensitivity analysis of the model.

3.5 Conclusion

It was demonstrated that the model developed is capable of describing coronary epicardial pressure and flow waves in health and disease and can therefore serve a the basis for further research to improve and validate the model. It can then be used as a tool to study the effect of combinations of epicardial and/or microcirculatory disease on pressure- and flow-based indices and can serve, due to the 1D representation of the arteries, as boundary conditions for more detailed 3D models.

Author contributions

Performed experiments: A. van der Horst, F.L. Boogaard
Data analysis: A. van der Horst, M. van ’t Veer
Interpretation of results: all
Prepared figures: A. van der Horst
Drafted manuscript: A. van der Horst
Edited and revised manuscript: A. van der Horst, M. van ’t Veer, M.C.M. Rutten, F.N. van de Vosse
Approved final version of manuscript: A. van der Horst, M. van ’t Veer, M.C.M. Rutten, F.N. van de Vosse

Chapter 4

Thermal anemometric assessment of coronary flow reserve with a pressure-sensing guidewire: an *in-vitro* evaluation

Assessment of coronary flow reserve (CFR) with a commercially available pressure-sensor-tipped guidewire using the principle of thermal anemometry could provide major clinical benefits both in determining and in distinguishing between epicardial and microvascular coronary artery disease. In constant-temperature anemometry, the electrical power required to maintain an element at a constant temperature is a measure for the local shear rate. Here, the feasibility of applying this thermal anemometric method to a pressure-sensing guidewire is investigated using an in-vitro model.

A theoretical relation between electrical power and steady shear rate based on boundary layer theory was derived and evaluated in an experimental set-up. In steady flow, a reproducible relation between electrical power and shear rate was obtained with an overheat temperature of 20 K, which was in good agreement with theory. The relation between shear rate and flow, however, depends on the geometry of the artery and position of the guidewire inside the vessel. Although this means that this thermal anemometric method is less useful for absolute flow measurements, CFR could be assessed even for unsteady flow using the steady calibration curve with a mean relative difference of (3 ± 5)% compared to CFR derived from the golden standard; an ultrasonic flow measurement device.

The contents of this chapter are based on Arjen van der Horst, Maartje C.F. Geven, Marcel C.M. Rutten, Nico H.J. Pijls, and Frans N. van de Vosse, Thermal anemometric assessment of coronary flow reserve with a pressure-sensing guide wire: an *in-vitro* evaluation. *Med Eng Phys*, **33**; 684–691, 2011.*

* *Parts also printed in M.C.F. Geven, PhD thesis (2007), chapter 5.*

4.1 Introduction

While coronary angiography plays a pivotal role in decision-making regarding the diagnosis and treatment of coronary artery disease (CAD), it has well recognized limitations concerning the assessment of the functional significance of CAD (Isner et al., 1981; Kern et al., 1997). This has led to the development of sensor-tipped guidewires, enabling the quantification of CAD by direct hemodynamic measurements. The most widely used physiology-based index to quantify an epicardial stenosis is fractional flow reserve (FFR); the ratio of hyperaemic blood flow in a stenotic artery to normal hyperaemic flow. FFR can clinically be obtained with intracoronary pressure measurements (Pijls et al., 1996). A recent study, by Tonino et al. (2009), has demonstrated that FFR-guided treatment significantly reduces major adverse events after percutaneous coronary interventions (PCI). The vasodilatory reserve of the coronary arteries can be characterized with coronary flow reserve (CFR), which is defined as the ratio of hyperaemic to resting flow. CFR is influenced by both the epicardial and the microvascular condition of the coronary system.

Although indices like FFR and CFR have proven to be valuable tools in quantifying the significance of CAD, the combination of both FFR and CFR is required to be able to discriminate between epicardial and microvascular disease and should ideally be measured using a single guidewire (Bruyne et al., 1996; Meuwissen et al., 2002b). A wire combining pressure and flow velocity assessment is available (Siebes et al., 2004), where the blood velocity is measured with a Doppler-crystal. Adequate Doppler-derived velocity signals can, however, be difficult to obtain, resulting in a poor Doppler signal in 10%-19% of all patients (Kern et al., 2006; Ganz and Hsue, 2009).

Recently, another method, which uses the commercially available pressure-temperature sensor-tipped PressureWire (St. Jude Medical, St. Paul, MN) in a thermodilution application, was introduced and evaluated (Bruyne et al., 2001; Pijls et al., 2002; Aarnoudse et al., 2007; van 't Veer et al., 2009). This methodology enables both the assessment of CFR, using a bolus injection method (Bruyne et al., 2001; Pijls et al., 2002), and volumetric flow, by applying continuous infusion (Aarnoudse et al., 2007; van 't Veer et al., 2009). Clinical application, however, involves the use of additional equipment (e.g. infusion catheter, infusion pump) and time-consuming steps during catheterization. Furthermore, only the mean coronary flow is measured, while assessment of the phasic pattern has also been indicated to be valuable in the clinical setting (Kern, 1992; Kern et al., 1994). In this study, a novel approach for flow assessment with the PressureWire, based on the principle of hot-film anemometry, is investigated.

Four decades ago, the method of hot-film anemometry was already investigated for blood flow velocity measurements (Seed and Wood, 1970a,b, 1972; Clark, 1974; Nerem et al., 1976; Paulsen, 1980a,b). A thin film mounted on a probe was held at a constant temperature, a few degrees above blood temperature. The probe (typically L-shaped with a diameter of 1 mm), was introduced into a vessel by puncturing the vessel wall. The supplied electrical power could be related to the blood flow using

calibration methods based on models describing the heat transfer between the film and the blood (Bellhouse and Rasmussen, 1968; Pedley, 1972a,b, 1976a). The main drawback of this method at that time was the size of the probe, influencing blood flow in small arteries, and the necessity to insert the probe through the vessel wall at the location of measurement. Although the principle of hot-film anemometry is still widely used in fluid dynamics (Bruun, 1996; Pfeifer and Schubert, 2008; Uchiyama and Ide, 2009), the technique was abandoned for clinical applications. An exception is the TruCCOMS^{TM} system (Aortech, Glasgow, Scotland), where this technique is applied to determine the cardiac output (Segers et al., 2003; Leather et al., 2004; Claessens et al., 2009).

In this study, this thermoconvection-based flow measurement principle is re-applied using a commercially available pressure-sensor-tipped guidewire. Besides FFR assessment, which the sensor was originally designed for, this will give extra information concerning blood flow during standard catheterization procedures. Compared to the guidewires with Doppler-derived blood velocity measurements, this methodology might be more suitable for getting accurate measurements. Furthermore, it is cost-effective since it adds extra functionality to an existing device. Compared to the thermodilution method, less additional equipment and time-consuming steps are required.

Here, the feasibility of this novel method for CFR measurements has been evaluated using an *in-vitro* model. An approximate relationship between shear rate and power supplied to the sensor is derived and an experimental set-up, including the electronic circuit to keep the sensor at constant temperature, is described. To obtain the optimal sensor temperature, measurements in water flow have been performed at different sensor temperatures. Furthermore, the sensor response has been determined with different geometrical boundary conditions to test whether the assumptions made in the derived relationship hold and the sensor actually is sensitive to the local shear rate. Finally, CFR obtained with the sensor in a flow similar to coronary flow is compared to CFR measured with a reference flow meter.

4.2 Materials and methods

The PressureWire 5 (St. Jude Medical, St. Paul, MN) consists of a pressure-temperature sensor incorporated in a 0.36 mm diameter guidewire with a length of 175 cm. The sensor is located at 3 cm from the tip, and consists of a chip with two equally temperature-dependent resistors. The resistors are connected by three microcables to a proximal connector, which enables connection to an external data acquisition device. As shown in Figure 4.1, the chip is oriented at a small angle θ to the surrounding metal casing, leaving the chip exposed to the fluid. One of the resistors is the pressure sensor (strain gauge), mounted on a deformable membrane. The other resistor is used as a temperature compensator.

To use the PressureWire as a constant temperature anemometer the temperature compensator resistor has been incorporated into a feedback controlled Wheatstone bridge (Fig. 4.3), which enables the control of the resistance, and therefore the temperature, of this resistor. To relate the electrical power, required to keep the

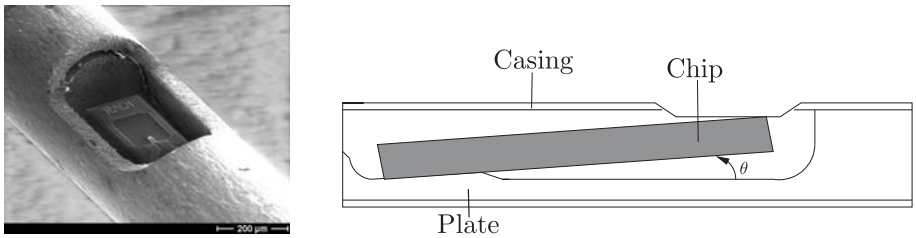

(a) *(b)*

Figure 4.1: *An image* ***(a)*** *and schematic representation* ***(b)*** *of the sensor of the PressureWire. The chip is glued on the plate and protected by a casing with an opening to expose the sensor to the fluid. The image has been acquired from St. Jude Medical (St. Paul, MN).*

temperature of the resistor constant, to the flow rate, an analytical expression is derived in the next section.

4.2.1 Analytical description: general hot-film models

From boundary layer theory (Schlichting and Gersten, 2000), relations between the heat transfer (q) from the sensor to the fluid and the shear rate (S) on the sensor surface can be derived. If the sensor is assumed to be a partially heated flat plate at constant temperature in steady flow (see Fig. 4.2) and the thermal boundary layer thickness is small compared to the thickness of the viscous boundary layer, the relation between heat transfer and shear rate at the sensor is:

$$q \sim \frac{k}{(\alpha L)^{\frac{1}{3}}} \Delta T S^{\frac{1}{3}} \ . \tag{4.1}$$

Here k and α are the thermal conductivity and diffusivity of the fluid, respectively. L is a characteristic length scale in the x direction (e.g., the length of the heated part) and ΔT is the difference between the sensor and ambient temperature. If the thermal properties of the fluid, overheat temperature, and sensor length are assumed to be constant, the heat transfer is only a function of the shear rate. The source of the heat transfer from the sensor to the fluid is the electrical power (P) supplied to the resistor. Hence, by measuring the voltage over the resistor, the electrical power can be determined, representing the convective heat flux, which depends on the local shear rate:

$$P \sim q \sim S^{\frac{1}{3}} \ . \tag{4.2}$$

Deviations from the steady boundary layer theory are expected when the measurement principle is applied in coronary flow. The viscous and thermal boundary layers and hence the relations between heat transfer, shear rate, and flow vary in time in non-stationary flow. Capacitive effects of the sensor material may come into play, which means that storage and release of heat in the sensor material will affect

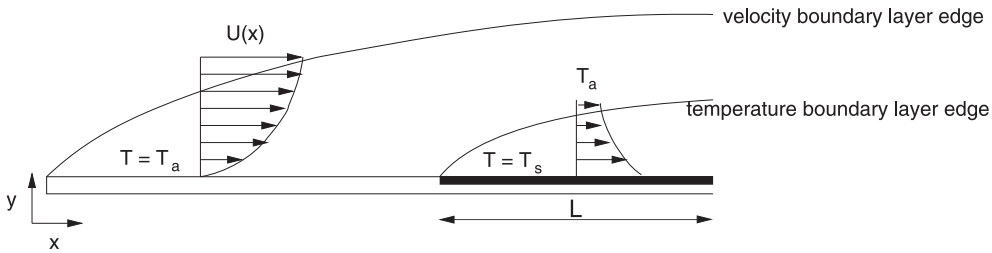

Figure 4.2: *Schematic representation of the developing viscous and thermal boundary layers for flow over a partially heated flat plate.*

the instantaneous heat transfer from the sensor itself. Furthermore, the complex geometry of the PressureWire, with the resistor placed at the bottom of a cavity, may lead to complex flow patterns and additional capacitive effects.

Since the effects described above will alter the relations between the heat transfer and shear rate, as stated in (4.2), a general form of a calibration function for heat transfer to stationary flow is assumed:

$$P = P_0 + (P_1 - P_0)\left[\frac{S}{S_1}\right]^n . \tag{4.3}$$

In this expression, P is the absolute measured electrical power and P_0 is the absolute power at zero flow; the heat loss due to diffusion. S_1 is a scaling parameter for the shear rate:

$$S_1 = c\frac{4\bar{Q}_{rest}}{\pi R^3} . \tag{4.4}$$

P_1 (the power at $S = S_1$) and n are constants, depending on the overheat of the sensor to the blood, the geometry of the probe, and the thermodynamic properties of the blood (Clark, 1974). $\bar{Q}_{rest}$ is 50 ml/min, the approximate mean coronary resting flow, R is 1.5 mm, the radius of the vessel, and c a parameter depending on the radial position of the wire. When the sensor is located near the vessel wall c is approximately one, which increases by a factor three when the sensor is located at the center of the vessel (Tsangaris, 1984).

4.2.2 Experimental characterization

For the characterization of the relationship between the heat flux from the sensor and fluid flowing over the wire, it is very important to create an environment in which both the flow through, and the temperature inside, a tube can be controlled very accurately.

A glass tube with an inner diameter of 3 mm, similar to that of a coronary artery, was placed in a temperature-controlled water bath (F34-HL, Julabo Labortechnik GmbH, Seelbach, Germany) with a temperature accuracy of ± 0.01 K. The flow through the tube was driven by a piston pump, operated by a computer-controlled

linear motor (ETB32, Parker). At the distal end of the tube the flow was registered by an ultrasonic flowmeter (4PSB, Transonic Systems Inc, Ithaca, NY). The PressureWire was introduced into the glass tube, and connected to an electronic circuit. To avoid variation of the cable resistance R_c due to temperature changes, the PressureWire was entirely submerged in the thermal bath. The signals from the flow meter and multimeter were simultaneously recorded via an acquisition board (PCI-6024, National Instruments, Austin, TX) to a computer at a sampling frequency of 50 Hz.

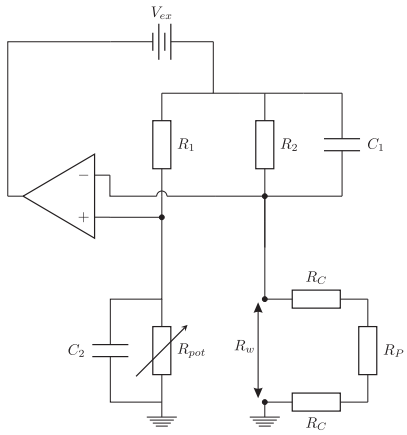

Component	value	unit
R_a	2.0 - 3.7 $\cdot 10^3$	[Ω]
R_p	2.0 - 3.7 $\cdot 10^3$	[Ω]
R_c	4.0 $\cdot 10^1$	[Ω]
C_1	1.0 $\cdot 10^{-7}$	[F]
C_2	1.0 $\cdot 10^{-7}$	[F]
R_1	2.6967 $\cdot 10^3$	[Ω]
R_2	2.6870 $\cdot 10^3$	[Ω]
R_{pot}	3.0320 - 3.1365 $\cdot 10^3$	[Ω]

Figure 4.3: *Schematic representation of the Wheatstone bridge used to control the temperature of R_w (combination of the resistor on the chip R_p and microcable resistances R_c) The bridge consists of a potentiometer R_{pot}, which is used to fix R_w, and two temperature invariant resistors R_1 and R_2. The Op-amp balances the bridge via negative feedback. The values of the different components are listed in the table.*

Electronic circuit

Figure 4.3 depicts the electronic circuit that is used to set and maintain the resistance (R_w) and therefore the temperature of the passive resistor of the PressureWire. R_w equals the sum of the resistance of the cables (R_c), connecting the PressureWire sensor with the connector end, and the resistor itself (R_p). The circuit consists of a Wheatstone bridge, with a feedback operational amplifier (LM324AN, National Semiconductor, Santa Clara, CA), in which R_w is incorporated. The other components of the bridge are two fixed resistors (R_1, R_2), a potentiometer (R_{pot}), two capacitors (C_1, C_2) and two power supplies (ES 030-5, Delta Elektronika B.V., Zierikzee, The Netherlands): V_{op-amp} and V_{ex}. The values of all the components are listed the table (Fig. 4.3, right). The two capacitors are incorporated to stabilize the bridge. By manually adjusting the value of R_{pot}, the value of R_w for which the bridge is balanced is set and the power dissipated by the bridge is controlled by the operational amplifier. The voltage over R_w is measured by a digital multimeter (DMM 199, Keithley Instruments Inc, Cleveland, OH).

4.2.3 Characterization of the relation between shear rate and electrical power

To gain more insight into the relation between the electrical power dissipated in the sensor and the reference flow, the non-linear calibration curve has to be derived for different sensor temperatures. Therefore calibration curves were determined at temperatures 5 K, 10 K, 20 K, and 35 K above the ambient temperature, 310 K (37°C). A simplification of coronary flow, a sinusoidal flow with an amplitude equal to the mean flow $\bar{Q}$ and a frequency f of 1 Hz was applied:

$$Q = \bar{Q}\left(1 + \cos(2\pi f t)\right) \ . \tag{4.5}$$

A mean flow of 0, 12, 25, 50, 100, 150, 200, 250, and 300 ml/min was applied. Similar to S_1, the mean shear rate $\bar{S}$ is then approximated according to:

$$\bar{S} = c\frac{4\bar{Q}}{\pi R^3} \ , \tag{4.6}$$

with $\bar{Q}$ the mean flow, R the vessel radius, and c a constant depending on the radial position of the wire.

To determine the stationary relation between electrical power and shear rate, a steady flow of 0, 50, 100, 150, 200, and 250 ml/min was applied. The shear rate was calculated with (4.6) and the measured electrical power was fitted to the power law model (4.3).

All the measurements were performed with the PressureWire located near the vessel wall and the cavity oriented towards the center of the tube. To investigate whether the heat flux from the sensor is really determined by the shear rate, the sensor was also subjected to equal flows in a tube with a diameter of 4 mm. Compared to the 3 mm tube, this will result in a decreased shear rate in the 4 mm vessel and therefore a decreased sensor response at equal flow rates. Since the sensor is located inside a cavity, the orientation of this cavity might influence the sensor response. Therefore, the sensor response was measured with the cavity oriented towards the tube wall and compared to the situation where the sensor was oriented towards the center of the tube.

The shear rate at the sensor surface depends on both the vessel radius and radial position. Since *in-vivo* the radial position is very hard to determine, the conversion from shear rate to flow is impossible. A relative index like CFR might therefore be more suitable for *in-vivo* application, since for a given vessel diameter and radial position, the average shear rate is proportional to the average flow (see (4.6)). CFR is defined as the ratio of the mean hyperaemic to mean resting flow:

$$\text{CFR} = \frac{\bar{Q}_{hyp}}{\bar{Q}_{rest}} \tag{4.7}$$

To test whether it is possible to estimate CFR from the measurements, a flow resembling the flow of a left anterior descending (LAD) coronary artery was created with the piston pump. As the resting flow a mean flow of 50 ml/min was chosen.

Flows with a mean of 50, 100, 150, 200, and 250 ml/min were chosen to represent the hyperaemic conditions, resulting in a CFR range of 1-5. The time-averaged values of electrical power were measured and converted to shear rate according to the obtained steady calibration curve. The estimated CFR (CFR_e) was then determined according to:

$$\mathrm{CFR}_e = \frac{\bar{S}_{e_{hyp}}}{\bar{S}_{e_{rest}}} \tag{4.8}$$

and compared to the flow based CFR. The accuracy of the estimated CFR was determined using a Bland-Altman representation (Bland and Altman, 1986) of the relative difference between estimated and reference CFR.

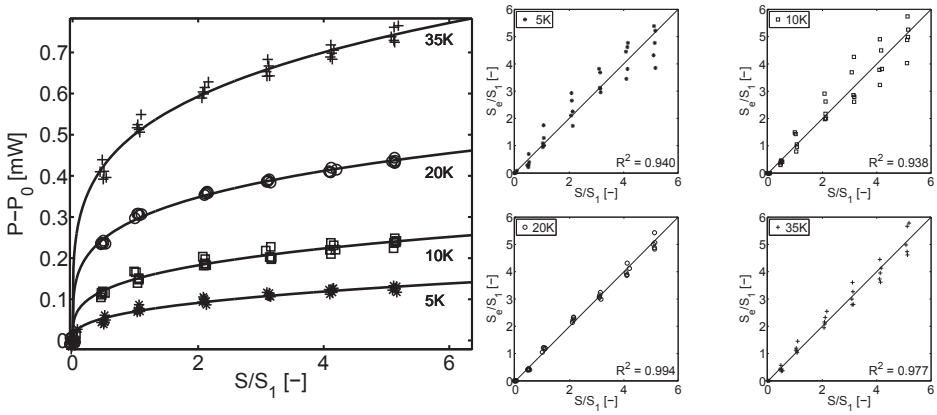

Figure 4.4: Left: *The mean measured electrical power versus the dimensionless shear rate for the four different sensor temperatures (5 K, 10 K, 20 K, and 35 K above ambient temperature).* ***Right:*** *The dimensionless shear rate, calculated with the obtained calibration curves for the four overheat temperatures, versus the reference values, showing that the error is the smallest for the measurements at the overheat temperature of 20 K.*

4.3 Results

4.3.1 Sensor temperature

The mean electrical power relative to the value at zero flow (P-P_0) for the different overheats is depicted in Figure 4.4. It can be clearly seen that the sensitivity of the sensor to shear rate, represented by the slope of the fitted calibration curves, increases for increasing sensor temperatures. The reproducibility, however, is decreased when comparing the 35 K to the 20 K measurements. The right side of Figure 4.4 shows that when the calibration curves are used to calculate the shear rate from the power

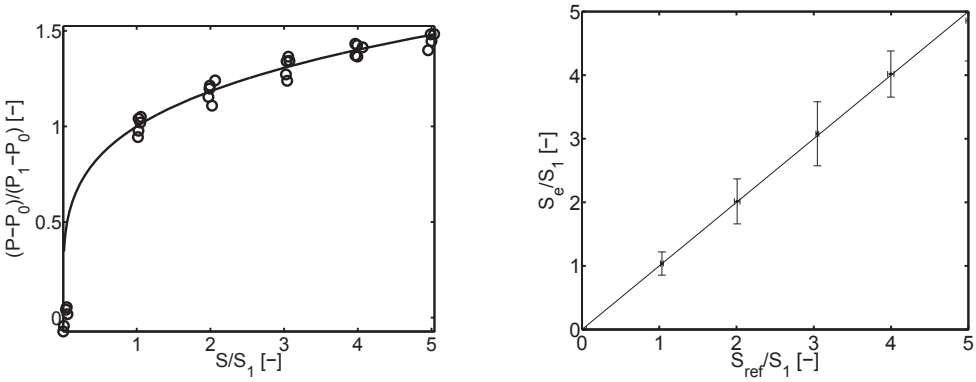

(a) *(b)*

Figure 4.5: ***a)*** *The dimensionless electrical power versus dimensionless shear rate in stationary conditions with an overheat of 20 K.* ***b)*** *The estimated versus reference dimensionless shear rate.*

measurements, the difference between the calculated and reference shear rate is the smallest at the overheat temperature of 20 K. The mean absolute error of the dimensionless shear rate (S/S_1) is 0.11 for the measurements at 20 K, which is smaller than for the measurements at 5 K, 10 K, and 35 K which are 0.31, 0.32, and 0.20, respectively. Therefore, an overheat of 20 K was used in all further experiments.

4.3.2 Stationary calibration

The relation between applied shear rate and electrical power was determined between 0 and 5 S/S_1. The sensor was located near the vessel wall, so S_1 = 314 s^{-1}, which means a maximum shear rate of approximately 1600 s^{-1}. The theoretical relation between electrical power and flow (see (4.3)) could be fitted accurately to the electrical power as measured under steady flow conditions (Fig. 4.5, $P_0 = 9.2$ mW, $P_1 = 9.5$ mW, $n = 0.24$; $R^2 = 0.99$). The value of R^2 is close to 1, which indicates that the theoretical relation is appropriate to describe the sensor response in steady shear rate. The estimated shear rate S_e was derived using the fitted calibration curve and is shown in (Fig. 4.5b). The mean absolute difference between the reference and calculated dimensionless shear rate was 0.3 $\pm$ 0.2.

4.3.3 Shear rate dependence: vessel diameter and sensor orientation

When the same flow is applied to a tube with a diameter of 4 mm instead of 3 mm, the shear rate at the location of the sensor will decrease according to (4.6). Figure 4.6a shows that the calibration curve obtained with the 3 mm tube (Fig. 4.5) could also describe the sensor response measured in the 4 mm tube. This is a clear indication that the sensor response is determined by the shear rate.

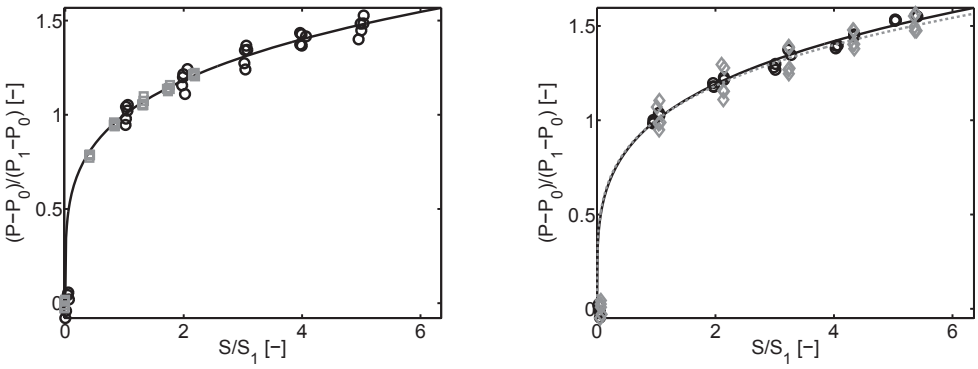

Figure 4.6: a) *The sensor response for a tube diameter of 3 mm (○) and 4 mm (□) with the cavity facing the center.* ***b)*** *The sensor response when the cavity is facing the wall (◇, regression curve −−) and center (○, regression curve –) of the tube. In both experiments the guidewire was located on bottom of the vessel.*

In Figure 4.6b the mean electrical power versus the reference shear rate is depicted for 3 series of 3 measurements at the two orientations: with the cavity facing either the wall, or the center of the tube. While the reproducibility of the measurements was less when the cavity was facing the wall, the mean electrical power response was equal for both situations.

4.3.4 CFR

Since the experiments with different vessel diameters clearly showed that the sensor measures the local flow rate, which can be described using the shear rate, the sensor response depends on the radial position of the wire. A relative index like CFR might therefore be more suitable for *in-vivo* application. The estimated CFR (CFR_e) was determined with the steady calibration curve obtained in the tube with a diameter of 3 mm and was calculated according to (4.8). Hyperaemic flows of 50, 100, 150, 200, and 250 ml/min, with a resting flow of 50 ml/min, were chosen, representing a CFR range of 1-5. Figure 4.7 shows the applied flow resembling coronary flow and the corresponding electrical power. Interestingly, this shows that, except for the shoulder region near the peak of the power-curve and an average time difference between the applied flow and measured power of approximately 0.07 s, the power signal seems to be a good representation of the flow. The time-average of these signals was used to determine CFR_e and the flow based CFR (CFR_{ref}; see (4.7)). Fig. 4.8 demonstrates that the difference between CFR_e and CFR_{ref} (represented by deviation from the line of identity) was relatively small, especially for the clinically important small CFR values. A small offset of $(3 \pm 5)\%$ compared to the reference CFR was found. This corresponds to a mean absolute difference between estimated and reference CFR of 0.2 ± 0.2 on the entire range.

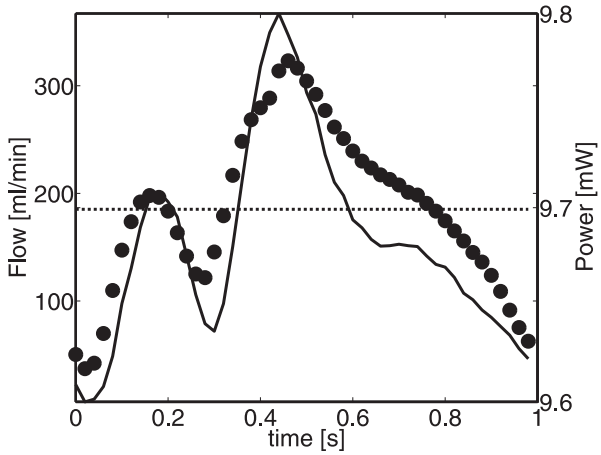

Figure 4.7: *The applied flow (-), resembling coronary flow, and the measured electrical power (•) with its time-average (- -) used to estimate the CFR-values in Figure 4.8.*

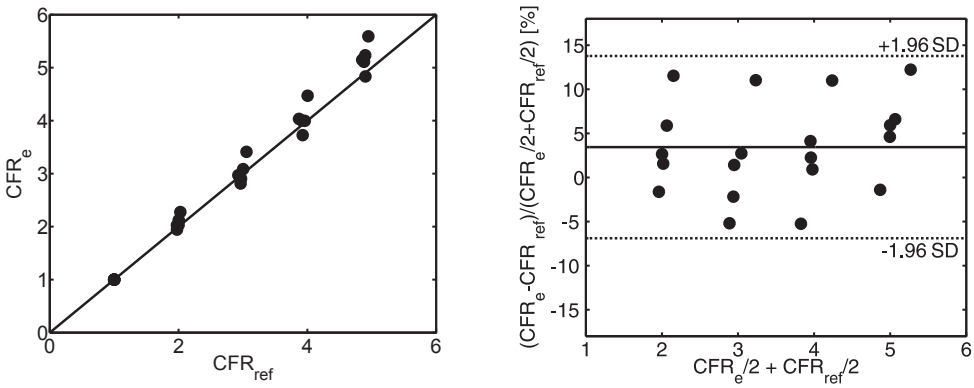

(a) ***(b)***

Figure 4.8: a) *CFR determined with a flow resembling a coronary flow (•).* ***b)*** *Bland Altman plot showing the relative difference between CFR_e and the flow based CFR. The average (-) and 95 % confidence interval (- -) are also included. The sensor overheat was 20 K and the stationary calibration at that temperature (Fig. 4.5) was used to convert the measured power via shear rate to CFR.*

4.4 Discussion

The aim of this study was to investigate the feasibility of using a pressure-sensing guidewire as a thermal anemometer for CFR assessment. An electronic circuit was developed to regulate the temperature of the sensor and experiments were performed to characterize the sensor for different temperatures, geometrical boundary conditions, stationary, and non-stationary flows.

Calibration with different sensor overheat temperatures (5 K, 10 K, 20 K, and 35 K) showed that, although the sensitivity to flow increased for increasing overheat, an overheat of 20 K seemed to be optimal due to a decrease in the reproducibility of the measurements performed at an overheat of 35 K. Since relatively large temperature increments were taken, an optimal overheat might be found between 10 K and 35 K. Small changes in ambient temperature had a significant effect on the measured signal. This might be overcome by obtaining the fluid temperature (with the same thermistor on the wire) and correcting the sensor temperature accordingly. Then it is still important that during one measurement the ambient temperature remains constant. An additional drawback, not presented here, is that although reproducible calibration curves were obtained for multiple wires, each individual wire showed differences in both diffusive, represented by parameter P_0, and convective heat transfer, represented by P_1 and n. Every wire should therefore be calibrated separately which can be performed at the manufacturers' of the PressureWire, where they are calibrated for pressure as well.

In the case of stationary flow, the theoretical relation between electrical power and shear rate could be fitted accurately. This suggests that the flat plate with small thermal boundary layer thickness assumption is appropriate to describe the sensor behaviour in stationary flow.

The finding that the orientation of the wire had little influence on the mean heat transfer indicates that not only the resistor but also the surrounding material was heated. This means that the effective sensor size was larger than the resistor alone and included the surrounding material.

Another important issue, apparent from the measurements in different vessel diameters, is that, as expected, the heat transfer from the sensor depends on the shear rate and not the absolute flow. This means that information about both the radial position and the vessel diameter is required to make the conversion from shear rate to flow. Since coronary flow is obviously not steady, non-stationary effects will also come into play. Especially damping of the measured signal in combination with the non-linear behaviour will complicate the conversion from electrical power to shear rate. Damping of the signal is related to the capacitive effect of both the surrounding material and the capacitors in the electronic circuit and the developing boundary layer. A transfer function between the heat transfer and shear rate, e.g. as described by Bellhouse and Rasmussen (Bellhouse and Rasmussen, 1968), might be useful in the clarification of this matter.

The dynamics of the applied coronary flow could be clearly recognized in the measured electrical power signal (see Figure 4.7). The shoulder region near the peak of the power curve might be explained by the occurrence of flow instabilities

in the high flow region, increasing the heat transfer from the sensor. Although this behaviour requires further investigation, including a proper calibration for flow rates with different frequencies and amplitudes, this thermoconvection-based method might also be suitable for dynamic shear rate assessment.

The results obtained in this study are in general in concordance with Claessens et al. (2009), which studied the operation principles of the TruCCOMS™ system (Aortech, Glasgow, Scotland). In this system, the flow in the pulmonary arteries is determined by measuring the power necessary to keep the temperature of a thermistor constant at 2 K above blood temperature. The main advantage of this system is that the overheat temperature is much lower than for our sensor. This is probably possible due to the large size of the sensor, which is mounted on a 7 F catheter, making this system unsuitable for coronary flow assessment.

Being a mean flow-based relative index, CFR is less sensitive to the issues described above. It was shown that, when using the steady calibration curve, CFR could be estimated for unsteady flow, resembling coronary flow. To be able to measure CFR reliably, the radial position of the wire should not change between the measurements in rest and hyperaemia. It should be noted that a radial position closer to the center of the tube will result in a higher local flow velocity at the sensor surface, which means a higher shear rate. Due to the non-linear relation between shear rate and power, this means a lower signal-to-noise ratio compared to a sensor which is closer to the vessel wall. In principle, the sensor is not able to distinguish between positive and negative local flow rates. Although the applied coronary-like flows already had phases of negative flow velocity at the sensor surface, the exact effect of flow reversal on the determination of CFR needs clarification in further research. Furthermore, the effect of curvature and/or bifurcation of the vessels, resulting in e.g. secondary flows, on the CFR measured via this thermal anemometric method still has to be investigated.

4.4.1 *In-vivo* application

All measurements described in this paper have been performed with water in a controlled environment. Before this method can be used for CFR measurements in a clinical setting, several issues have to be investigated. An overheat of 20 K may induce problems in *in-vivo* application, concerning damage to both blood cells and the vessel wall and fibrin deposition on the probe (Seed and Wood, 1972). However, when the measurement time is less than 100 s, no significant thermal damage is reported for red blood cells and arterial tissue for temperatures up to 60°C (an overheat of 23 K) (Agah et al., 1994; Pfefer et al., 2000). Furthermore, the resistor is very small in size and the absolute power dissipated is very limited. Finally, using more sophisticated electronic circuitry and signal processing methods, sufficient sensitivity and signal-to-noise ratio might also be reached at a lower overheat

Since the deviations in blood temperature during one measurement are expected to be small, this is not likely to affect the convective part of the calibration relation. To correct for absolute blood temperature this temperature should be measured, by obtaining the resistance of R_p, before starting a measurement and setting the

overheat accordingly. Finally, although for both water and blood a similar shape of the calibration curve was found in previous studies (Seed and Wood, 1972; Clark, 1974), a proper investigation of the sensor response in blood should be performed.

4.5 Conclusion

Although additional research is needed before this method can be used in the catheterization laboratory, this study clearly indicates that it is feasible to use a commercially available pressure-sensing guidewire as thermal anemometer. Besides FFR measurements, which was already possible with the PressureWire, this will potentially enhance the PressureWire with a relatively easy way to obtain CFR, based on shear rate measurements.

Author contributions

The experimental work described in this chapter was performed as part of the author's MSc-project, which was financially supported by the Dutch Technology Foundation STW (project number: EPG.5454) and supervised by Maartje Geven. The experimental data also served as the basis of the research described in M.C.F. Geven, PhD thesis (2007), chapter 5.

Performed experiments: A. van der Horst
Data analysis: A. van der Horst, M.C.F. Geven
Interpretation of results: all
Prepared figures: A. van der Horst, M.C.F. Geven
Drafted manuscript: A. van der Horst
Edited and revised manuscript: all
Approved final version of manuscript: all

Chapter 5

A combination of thermal methods to assess coronary pressure and flow dynamics with a pressure-sensing guidewire

Measurement of coronary pressure and absolute flow dynamics have shown great potential in discerning different types of coronary circulatory disease. In the present study, the feasibility of assessing pressure and flow dynamics with a combination of two thermal methods, developed in combination with a pressure-sensor-tipped guidewire, has been evaluated in an in-vitro coronary model. A continuous infusion thermodilution method was employed to determine the average flow, whereas a thermal anemometric method was utilized to assess the pressure and flow dynamics simultaneously. In the latter method, the electrical power supplied to an element, kept at constant temperature above ambient temperature, was used as a measure for the shear rate.
It was found that the method was able to assess coronary pressure and flow dynamics for different flow amplitudes, heart rates, and different pressure wires, using a single calibration function. However, due to the fact that the thermal anemometric method cannot detect local shear rate reversal, the method was unable to reliably measure flow dynamics close to zero. Nevertheless, the combined methodology was able to reliably assess diastolic hemodynamics. The diastolic peak flow and average diastolic resistance could be determined with a small relative error of (8±7)% and (7±5)%, respectively.

The contents of this chapter are based on Arjen van der Horst, Marcel van 't Veer, Robin A.M. van der Sligte, Marcel C.M. Rutten, Nico H.J. Pijls, and Frans N. van de Vosse. A combination of thermal methods to assess coronary pressure and flow dynamics with a pressure-sensing guide wire, *submitted to Med Eng Phys*.

5.1 Introduction

Due to the recent developments in guidewire mounted sensors, the dynamics of coronary pressure and flow has become of interest to elucidate the complex interaction between the coronary circulation and the myocardium (Siebes et al., 2009; Waters et al., 2011). It has shown great potential in discerning different types of arterial (Mancini et al., 1989), microvascular (Hirsch et al., 2008; Escaned et al., 2009; Okcular et al., 2010), and cardiac (Davies et al., 2006a) disease based on abnormal hemodynamics. The current diagnostic approaches used are based on pressure and/or flow in a specific part of the cardiac cycle, e.g. via wave intensity analysis (Parker and Jones, 1990; Sun et al., 2000). Ideally, pressure and flow should be measured simultaneously with a single guidewire. In clinical practice, a sensor-tipped guidewire (ComboWireXT, Volcano, San Diego, CA) is available that combines pressure and flow velocity assessment (Siebes et al., 2004), of which the latter is measured with a Doppler-crystal. Adequate Doppler-derived velocity signals can be difficult to obtain, however, resulting in a poor Doppler signal in 10%- 19% of all patients (Kern et al., 2006; Ganz and Hsue, 2009). Additionally, blood velocity is measured instead of flow, which means that the obtained signal depends on both the size of the vessel and radial position of the guidewire.

The aim of present work is to develop a method able to simultaneously assess the dynamics of coronary pressure and volumetric flow. The proposed methodology consists of a combination of a thermal anemometric and a thermodilution-based method with a pressure and temperature sensor-tipped guidewire (PressureWire Certus, St. Jude Medical, St. Paul, MN), originally designed to measure coronary pressure for the determination of fractional flow reserve (FFR), see e.g. Tonino et al. (2009).

In previous research it was shown that the PressureWire could be operated as a thermal anemometer (chapter 4; van der Horst et al. (2011)). By measuring the power required to keep an element on the tip of the PressureWire at constant temperature, coronary flow reserve (CFR) could be determined accurately. Additionally, a clear relation between the dynamics of the applied flow and the measured electrical power was found. Similar to measurements with the guidewire-mounted Doppler-crystal, this method could not directly assess the dynamics of volumetric flow, since the sensor response was only determined by the shear rate at the sensor surface.

Another method to assess flow, developed in combination with the PressureWire, utilized the principle of thermodilution and was investigated by Van 't Veer et al. (2009) and successfully applied in the clinic by Aarnoudse et al. (2007). In these studies it was demonstrated that absolute volumetric flow rate could be measured, by continuously infusing a saline solution at room temperature and measuring the temperatures of the blood, infusate, and the mixture distal to the infusion site. With this method, however, only the mean flow could be measured.

In this study, a methodology is developed in which the continuous thermodilution method is used to calibrate the dynamic signals obtained with the thermal anemometric method for assessing the dynamics of volumetric flow. In addition, the thermal anemometric method is improved, to enable simultaneous assessment of flow

and pressure, instead of sequential measurements. In *in-vitro* experiments with a physiologically representative model of the coronary circulation (Geven et al., 2004) the methods are evaluated under well-controlled conditions. The method is tested with different PressureWires, vessels diameters, heart rate, and flow amplitudes. To demonstrate the clinical relevance of the combined methodology, the diastolic peak flow and average diastolic resistance obtained with the method are compared to the values obtained with reference flow and pressure measurements. Besides the *in-vitro* measurements, as a proof of principle in genuine physiological conditions, a single series of measurements is performed in an isolated beating pig heart set-up (de Hart et al., 2011).

5.2 Materials and methods

5.2.1 Sequential pressure and local flow rate assessment

The PressureWire Certus (St. Jude Medical, St. Paul, MN), is a guidewire with a pressure-temperature sensor on a chip, inside a cavity, 3 cm from its tip (see Fig. 1.6c). Located on the chip are a piezo-resistive pressure sensor R_A and a temperature compensation resistor R_P, having the same temperature characteristics. Three microcables (each with resistance R_C) run through the guidewire to connect the two resistors, via a proximal connector, to an appropriate interface (RADI Analyzer, Uppsala, Sweden) to record and process the signals. Figure 5.1a shows the electrical circuit (Wheatstone bridge) used to measure pressure, where the resistors R_{BP}, R_{BA}, and an operational amplifier are inside the interface and V_{Pres} is a measure for the pressure.

In chapter 4, resistor R_P was incorporated into a feedback controlled Wheatstone bridge to be able to control its temperature (see Figure 5.1b). By adjusting the potentiometer R_T, R_P can be set to a fixed value and therefore a fixed temperature.

$$R_P = R_T \frac{R_{B_P}}{R_{B_T}} - 2R_C \ . \tag{5.1}$$

By measuring the electrical power required to keep R_P constant, a measure for the shear rate (S) at the sensor surface, can be obtained. The time-averaged power ($\bar{P}$) can be related to the time-averaged shear rate ($\bar{S}$) via a power law:

$$\bar{P} = P_0 + (P_1 - P_0) \left[\frac{\bar{S}}{S_1} \right]^n \ . \tag{5.2}$$

Here, the constants P_0, the power dissipation related to diffusion, P_1, the power at $S = S_1$, and n depend on the overheat of the sensor, the geometry of the probe, and the thermodynamic properties of the blood (Clark, 1974). S_1 is a scaling parameter for the shear rate:

$$S_1 \sim \frac{\bar{Q}_{rest}}{R^3} \ , \tag{5.3}$$

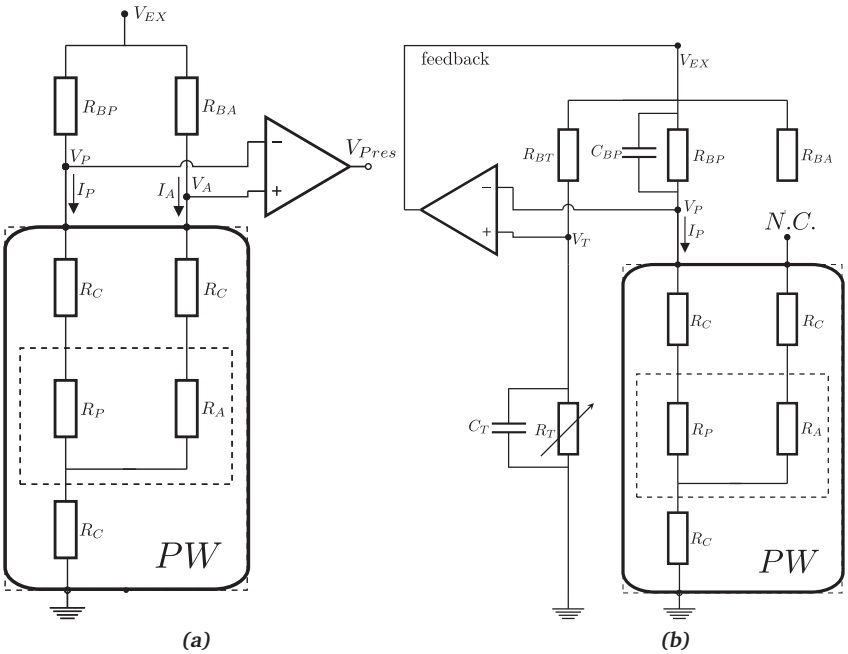

Figure 5.1: a) *Schematic representation of the electrical circuit to measure pressure with the PressureWire (PW). The difference V_A-V_P is a measure for the pressure.* ***b)*** *The feedback-controlled Wheatstone bridge to heat R_P to a constant temperature above ambient temperature. R_T is a potentiometer used to set the temperature of R_P. The capacitors C_{BP} and C_{BA} are incorporated to stabilize the bridge. The branch with the pressure sensitive resistor R_A is not connected (N.C.). The electrical power to the passive branch (R_P + 2R_C) is a measure for the heat transferred to the flow and therefore a measure for the local flow rate.*

with $\bar{Q}_{rest}$ the approximated average resting flow and R the vessel radius.

With this method pressure and a measure for the shear rate could be assessed sequentially. In the next section this method is adapted to enable simultaneous assessment of pressure and local flow.

5.2.2 Simultaneous assessment of pressure and local flow rate

Figure 5.2 shows the proposed electrical circuit to operate the PressureWire as a thermal anemometer while simultaneously measuring pressure. The essential difference compared to the circuit shown in Figure 5.1b is that the branch with the pressure sensitive resistor (R_A) is reconnected to the excitation voltage (V_{EX}). This means that both resistors are being heated, instead of only R_P. A prerequisite for this to work without interference of the pressure on the flow measurement, is the resistance of R_A to be more sensitive to changes in temperature than to changes in pressure. From preliminary research, the estimated interference of a 100 mmHg

pressure difference on the electrical power signal range was approximately 0.3%. We therefore assume that this interference is negligible. The relation between R_T and R_P and R_A and can be expressed as follows:

$$R_T = \frac{R_{B_T}}{R_{B_P}} \left(R_P + R_C \left(2 + \frac{R_{B_P} + R_P + R_C}{R_{B_A} + R_A + R_C} \right) \right) , \tag{5.4}$$

which is similar to the R_P-R_T relation in (5.1), except for the last term. If it is assumed that R_C is equal for the three microcables, R_C, R_A, and R_P can be determined from measuring $R_{P_{tot}} = 2R_C + R_P$, $R_{A_{tot}} = 2R_C + R_A$, and $R_{P,A_{tot}} = 2R_C + R_P + R_A$. Using a predetermined temperature-resistance calibration relation for R_A, R_P, and R_C, the appropriate temperature of R_A and R_P can be set using (5.4).

When the resistors are heated to a constant temperature, the heat flux from the heated chip is equal to the electrical power dissipated in both resistors on the chip:

$$P_{tot} = P_{R_P} + P_{R_A} , \tag{5.5}$$

$$P_{R_P} = \left(\frac{V_{EX} - V_P}{R_{B_P}} \right)^2 R_P , \tag{5.6}$$

$$P_{R_A} = \left(\frac{V_{EX} - V_A}{R_{B_A}} \right)^2 R_A . \tag{5.7}$$

The pressure signal (V_{pres}), as shown in Figure 5.1a, linearly depends on V_{EX}, which is not constant, due to the positive feedback. Therefore, V_{pres}/V_{EX} was chosen as a measure for the pressure.

Since the dissipated heat is influenced by the local flow rate at the sensor surface, instead of the volumetric flow rate, extra information regarding the volumetric flow rate is required. The only clinically available method to measure absolute volumetric flow rate is continuous infusion thermodilution and therefore this method is used to scale the above presented thermal anemometric method. In the next section only the basics of this thermodilution method are explained. Van 't Veer et al. (2009) describes this thermodilution method in detail.

5.2.3 Continuous infusion thermodilution

The continuous infusion thermodilution method is based on the conservation of energy, while infusing a colder fluid into the bloodstream. The hyperaemic average blood flow ($\bar{Q}$) can be calculated by measuring the blood temperature (T_b), temperature of the infusate (T_i), the temperature of the mixture (T), and the infusion rate (Q_i).

$$\bar{Q} = \frac{\rho_i c_{p,i}}{\rho_b c_{p,b}} \left[\frac{T_b - T_i}{T_b - T} \right] Q_i . \tag{5.8}$$

Here, $\rho_{i,b}$ and $c_{p,i,b}$ are the density and the specific heat of the blood (b) and infusate (i), respectively. It is assumed that there is optimal mixing between the blood

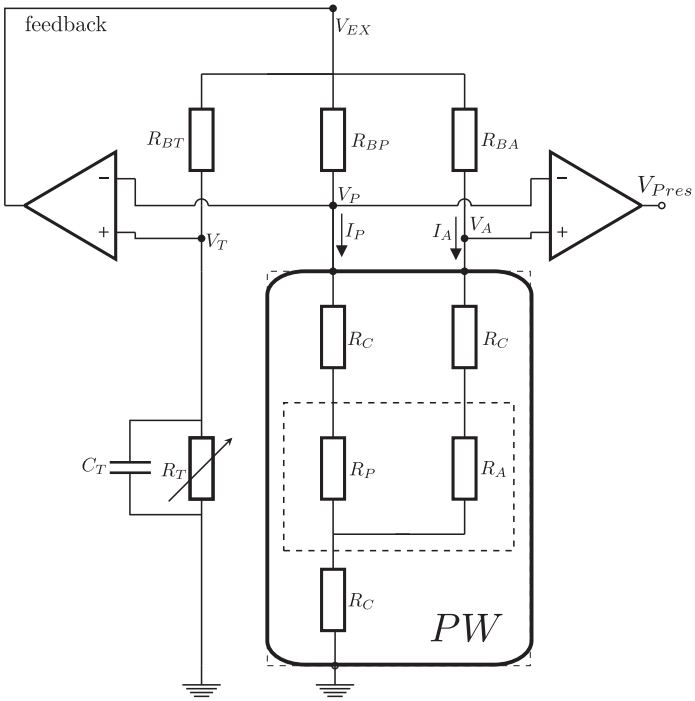

Figure 5.2: *Schematic representation of the electrical circuit to measure pressure and local flow simultaneously. Compared to Figure 5.1b, C_{BP} is removed and the active branch is reconnected to enable pressure measurements. The electrical power to both the passive and active branch is a measure for the local flow rate.*

and the infusate and that the infusate replaces the blood during injection. The temperatures are measured with the PressureWire in combination with the RADI Analyzer (Radi Medical Systems AB, Uppsala, Sweden) and the mixing is obtained with a specially designed infusion catheter (Carac catheter, AMT, Herk-de-Stad, Belgium). To accurately measure T_i and T an additional measurement needs to be performed, to correct for changes in microcable resistance due to the infusion of the colder fluid. For this additional measurement, the infusion catheter is pulled back into the aorta, while the PressureWire remains in the coronary vessel. This prevents transportation of the infusate into the coronary vessel, while the microcables are still cooled due to the continuing infusion. The measured temperature (T_{mc}), during infusion in the aorta, is then only related to changes in the microcable resistance and can be used to correct the already measured infusate $T_{i,m}$ and mixture T_m temperature: $T_i = T_{i,m}$-T_{mc} and $T = T_m$-T_{mc}. Van 't Veer et al. (2009) showed that the region 5-8 cm from the tip of the infusion catheter, was optimal to measure the temperature of the mixture (T) at an infusion rate of 15-25 ml/min. A study in animals and humans (Aarnoudse et al., 2007) confirmed this and showed that the method was reproducible, safe, and accurate in an *in-vivo* environment.

5.2.4 The methodology to combine the thermal anemometric and thermodilution methods

Similar to (5.2), a first order approximation for the relation between the local shear rate at the sensor surface (S) and the volumetric flow is assumed and made dimensionless according to:

$$S^* = \frac{S}{S_1} = \frac{\frac{Q}{a^3}}{S_1} \ . \tag{5.9}$$

Here S^* is the dimensionless shear rate, a is the radius of the measured vessel minus the radius of the guidewire, and S_1 is the scaling parameter introduced in (5.3), with $\bar{Q}_{rest}$ = 50 ml/min and R = 1.5 mm. Furthermore, the electrical power is made dimensionless using the parameters in P_0 and P_1 of (5.2):

$$P^* = \frac{P - P_0}{P_1 - P_0} \ . \tag{5.10}$$

The proposed methodology to assess the dynamics of volumetric flow is based on two key observations. The first observation is that the time-averaged power ($\bar{P}$) is relatively invariant to non-stationary effects (chapter 4). The second observation is presented in the results section of this study (Fig. 5.5) and shows that in the physiological frequency range the power-flow relation is approximately piecewise linear for the whole period of a heart beat, with the gain equal to the slope of the $\bar{P}^*$-$\bar{S}^*$ relation, at the average S^*. Utilizing these observations, the following relation between the measured electrical power and shear rate can be derived:

$$S^* = (P^* - \bar{P}^*)\frac{\Delta S^*}{\Delta P^*} + \bar{S}^* \ , \ \frac{\Delta S^*}{\Delta P^*} = \frac{\bar{S}^*}{n\bar{S}^{*^n}} \tag{5.11}$$

In the last equation, $\bar{S}^*$ has to be determined with the continuous thermodilution method and the estimated vessel radius (similar to (5.9)). The dynamics of the volumetric flow can then be determined via (5.9) from the calculated S^*.

To scale the pressure-representing signal V_{pres}/V_{EX}, the pressure measured during the thermodilution measurement is used. It is assumed that the pressure signal does not change between the measurements and that the relation between the V_{pres}/V_{EX} and the pressure is linear. The offset and gain of this linear relation are thus fitted to convert the V_{pres}/V_{EX} signal to the actual pressure.

5.2.5 Experimental validation

In-vitro set-up

The proposed methodology was tested in an *in-vitro* model (Fig. 5.3), able to describe pressure and flow dynamics of the epicardial arteries. As a full description of this model is already described by Geven et al. (2004), here only a short description will be given. The model, basically, consisted of three parts: the left ventricle, the systemic, and the coronary circulation. The left ventricle was modeled with a

piston pump and two valves. The systemic circulation consisted of a polyurethane tube, representing the aorta, and a system of resistances and a compliance. A polyurethane tube, representing a coronary artery, branched off the aorta and bifurcated in an epicardial and a sub-endocardial branch. The sub-endocardial branch passes through the chamber representing the left ventricle and can collapse due the left ventricle pressure. Using three resistances, a typical physiologic coronary pressure and flow signals could be created. To be able to perform the continuous thermodilution measurements, the total model was submerged in water, kept at a constant temperature of 37.0 $\pm$ 0.05 °C by an external thermal bath and circulator (F34-HL, Julabo Labortechnik GmbH, Seelbach, Germany).

The set-up was instrumented with a guiding catheter, the orifice of which was positioned near the coronary ostium. Two PressureWires were advanced through the guiding catheter and inserted into the main coronary branch. One was connected to the RADI Interface (Radi Medical Systems AB, Uppsala, Sweden) to serve as a reference for the pressure. The other was connected to the electric circuit (Fig. 5.2) to heat the resistors on the chip of the PressureWire and measure the pressure and the power supplied. An infusion catheter (Carac catheter, AMT, Herk-de-Stad, Belgium) was advanced over the latter PressureWire and connected to an infusion pump (Mark V ProVis, MEDRAD inc., Indianola, PA) to enable the continuous thermodilution method. When performing the thermodilution measurements, the PressureWire was connected to the RADI Analyzer (Radi Medical Systems AB, Uppsala, Sweden) to measure the temperatures. As a reference for the coronary flow, a perivascular ultrasound flow probe (4PSB,Transonic Systems Inc, Ithaca, NY) was placed around the main coronary branch, distal to the PressureWires. A computer-mounted acquisition adapter (PCI-6024, National Instruments, Austin, TX) simultaneously recorded all signals for each 10 s measurement, at a rate of 1kHz per channel.

Ex-vivo set-up

An *ex-vivo* platform, to simulate cardiac physiology, was used to test the method with blood in an actual beating heart. This platform was thoroughly discussed in De Hart et al. (2011), we therefore only discuss the extra instrumentation required for the measurements. Basically, the instrumentation was similar to the *in-vitro* set-up, except that the thermodilution measurements were not performed. This decision is motivated by the fact that the method was already tested in animal experiments (Aarnoudse et al., 2007) and it would require x-ray imaging to be able to advance the infusion catheter and PressureWire to the correct locations. Two PressureWires were placed into the left circumflex coronary artery (LCx) via a guiding catheter and connected to the RADI Analyzer (Radi Medical Systems AB, Uppsala, Sweden) and the electrical circuit, respectively. A perivascular flow probe (4PSB,Transonic Systems Inc, Ithaca, NY) was placed around the LCx, proximal to the place of measurement, to measure the reference flow. The time-averaged value of this flow was used as the substitute for the thermodilution method. With a string, placed distal to the PressureWires, the LCx could be ligated to control the average flow. Similar as the *in-vitro* experiments, all signals were recorded simultaneously at a sampling frequency of 1 kHz.

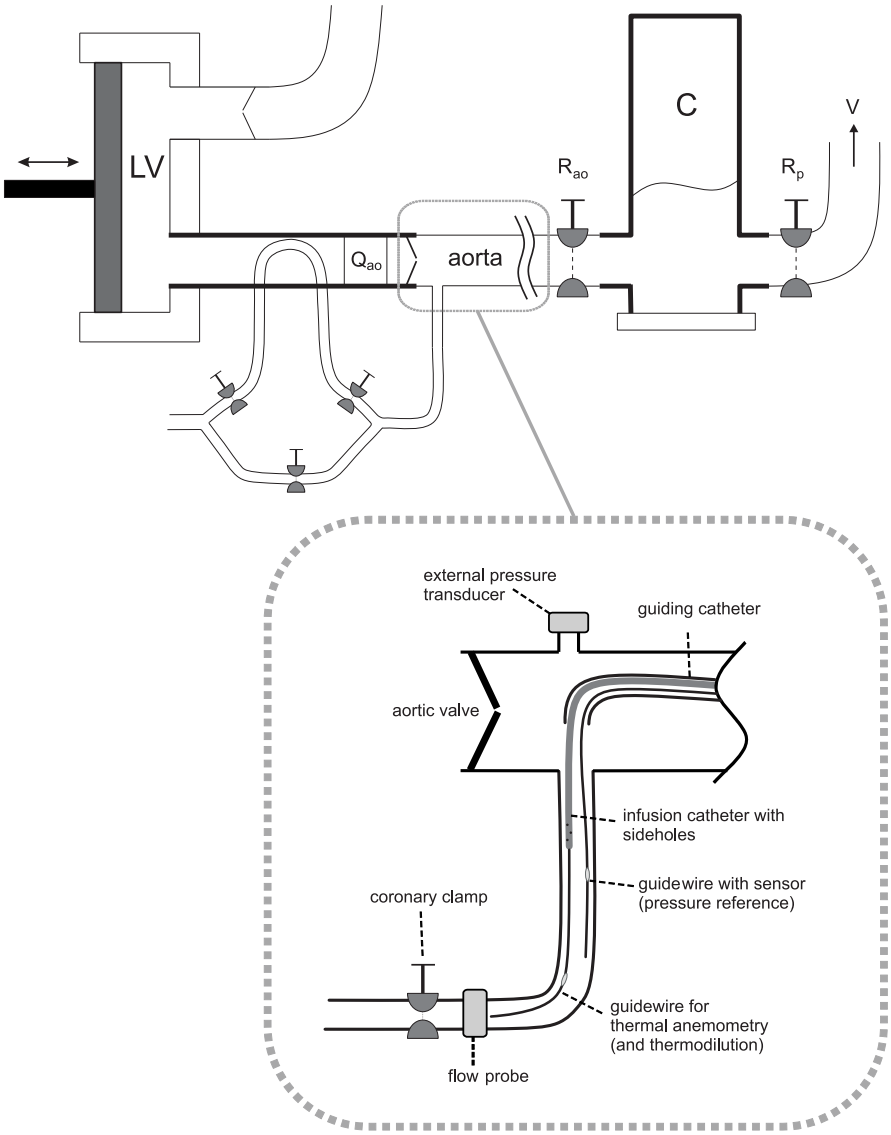

Figure 5.3: *Physiologic representative model for the coronary circulation (Geven et al. (2004)). Adapted from Van 't Veer et al. (2009).*

5.2.6 Experiments and data analysis

To gain more insight into the validity of the method, experiments were performed in which a PressureWire (PW_1) was tested, at an overheat of 20 K, for different types of flow and vessel diameters. The measured electrical power, V_{pres}/V_{EX}, and the reference pressure were filtered with a zero-phase filter as implemented in the *filtfilt-*

subroutine in Matlab (R2010a, The Mathworks, Natick, MA). From these signals eight complete periods were extracted, which were used for further analysis.

First, the mean electrical power-flow relation was derived in vessels with a diameter of 3 and 4 mm. In both vessels the sensor was subjected to three series of five flows; $\bar{Q} = \{50, 100, 150, 200, 250\}$ ml/min. The calibration function as described in (5.2) was fitted to the time-averaged electrical power and dimensionless shear rate using the Gauss-Newton algorithm, resulting in values for the constants P_0, P_1, and n. The predictive value of the fitted relation was quantified by the mean relative error, graphically represented via a Bland-Altman plot (Bland and Altman, 1986). These parameters could then be used to calculate the volumetric flow dynamics, estimated from the measured electrical power and the average flow via (5.11). The phase delay between the estimated and reference flow was determined using cross-correlation. Since the mean shear rate, from the thermodilution measurements, was the only known flow parameter, a simple linear relation between the phase delay and average shear rate was assumed. The parameters of this linear relation were fitted using the Gauss-Newton algorithm. In all other experiments, these relations were then used as the calibration function to estimate the flow from the measured electrical power.

To investigate the influence of variations in flow on the sensor response, experiments were conducted in which the flow amplitude and heart rate were varied for flows with a mean of 50, 150, and 250 ml/min. The heart rate was varied within the physiological range of 60, 75, and 90 beats per minute. The sensor was tested for flows with two different amplitudes: approximately 50% and 100% of the mean flow. Furthermore, two other PressureWires (PW_2 and PW_3) were tested for the same flows as PW_1; $\bar{Q} = \{50, 100, 150, 200, 250\}$ ml/min. For the conversion from electrical power to flow, the constants (P_0, P_1, and n) obtained for PW_1 were used and the eight periods were averaged to get a single waveform used for the comparison. For all experiments, the differences between the estimated and reference flow were quantified with the correlation coefficient (r), mean absolute error (MAE), and mean absolute percentage error (MAPE).

The V_{pres}/V_{EX}-signal was converted to an actual pressure by fitting it to the reference pressure via the Gauss-Newton algorithm, assuming a linear relation. The correlation between the two signals was quantified with the correlation coefficient.

For practical reasons, only one series of measurements has been performed in combination with actual thermodilution measurements. The effect of infusing the cold fluid over the guidewire was investigated by performing the thermodilution method before or after the thermal anemometric measurement. Furthermore, the accuracy of the continuous thermodilution method was evaluated via a Bland-Altman plot.

To demonstrate the clinical relevance of the methodology proposed, the diastolic peak flow (DPF) and the average resistance in diastole were determined and compared to the ones obtained with the reference measurements. The diastolic part of the coronary cycle was determined visually from the typical coronary flow signal for both the estimated and reference flow.

As a proof of principle, a single *ex-vivo* experiment was performed with PW_1 to show that the method can be applied in a genuine physiological environment.

Due to suboptimal performance of the heart in the isolated beating heart set-up the maximum average flow that could be obtained was approximately 125 ml/min. The heart rate was kept constant at approximately 90 BPM with a pacing device (5375 demand pulse generator, Metronic, Minneapolis, MN) and the sensor was subjected to three series of five flows; $\bar{Q} = \{25, 50, 75, 100, 125\}$ ml/min. Although difficult to determine, it was estimated that the vessel diameter was approximately 3 mm. The calibration relation of PW_1, with the constants P_0, P_1, and n and the phase delay determined in the *in-vitro* experiments, was used for the conversion from the electrical power to flow. The difference between the estimated and reference flow was again quantified with r, MAE, and MAPE.

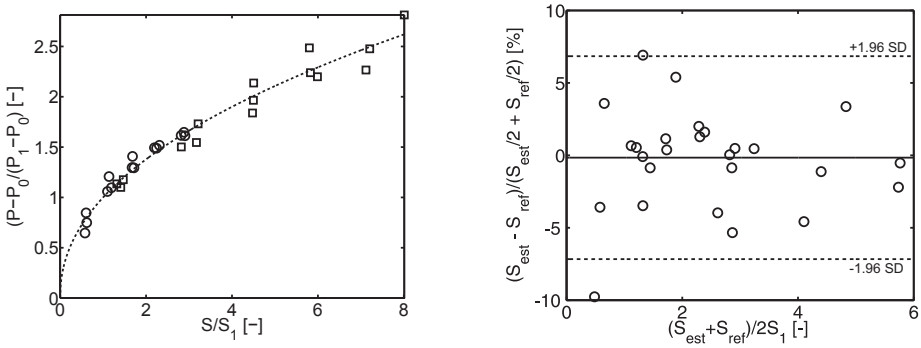

Figure 5.4: a) *The average dimensionless power and shear rate relation for the 3 mm (□) and 4 mm (◯) vessel. The dashed line is the calibration function described in (5.2) with the parameters in Table 5.1.* ***b)*** *Bland-Altman representation showing the relative difference between the estimated and reference dimensionless shear rate.*

5.3 Results

5.3.1 Power-flow relation

Figure 5.4a shows the relation between the average dimensionless shear rate and power. The power law in (5.2) could be accurately fitted (R^2 = 0.97) to the data; the parameters are shown in Table 5.1. The MAE and MAPE between the reference and estimate $\bar{S}/S_1$ were 0.3 and 10%, respectively. The Bland-Altman representation depicted in Figure 5.4b shows that the 95% confidence bounds are at approximately $\pm 7\%$. After a correction for the phase delay the power-flow relation was approximately piecewise linear (Fig. 5.5). As already discussed in section 5.2.2, the proposed methodology makes use of this observation. The time delay (ϕ) between the estimated and reference flow could be approximated by a (weak) linear relation (R^2 = 0.55) depending on the shear rate:

$$\phi = \max(\phi_0 - \phi_1 \bar{S}^*, 0) \ . \tag{5.12}$$

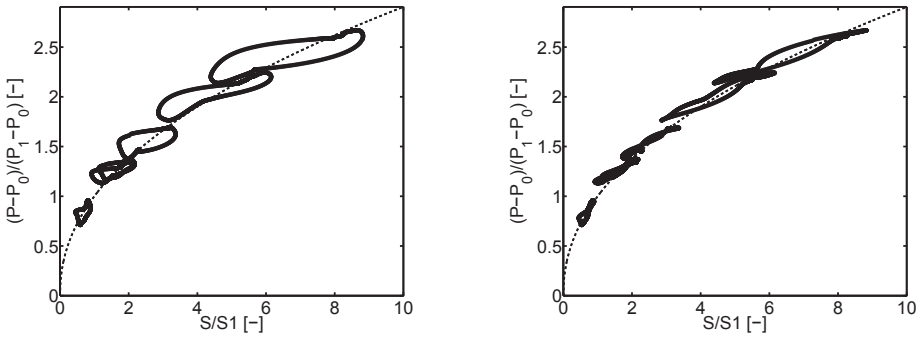

Figure 5.5: *The dimensionless power and dimensionless shear rate relation without* ***(a)*** *and with* ***(b)*** *the correction for the phase-delay. The dashed line is the calibration function described in (5.2) with the parameters in Table 5.1.*

Table 5.1: *The average and standard deviation of the parameters of the power-shear rate relation ($\bar{P} = P_0 + (P_1 - P_0)(\bar{S}/S_1)^n$) and the parameters describing the phase delay ϕ (5.12).*

	P_0 [mW]	P_1 [mW]	n [-]	ϕ_0 [ms]	ϕ_1 [ms]
average	9.95	10.2	0.46	40	6
standard deviation	0.09	0.1	0.1	4	1

The values of the parameters ϕ_0 and ϕ_1 are shown in Table 5.1.

Making use of (5.11), the absolute flow was determined from the measured electrical power and mean absolute flow. The overall correlation between the signals was good, indicated by the average and standard deviation of the parameters quantifying the error between the estimated and reference flow: r = 0.97±0.02 , MAPE = (9±4)%, MAE = (10±6) ml/min. In Figure 5.6 the resulting estimated flows are shown for applied flows with a mean of 50 ml/min and 250 ml/min in both the 3 mm and 4 mm vessel. It shows that the main dynamics of the flow could be determined, however, for flows near zero the correlation between the estimated and reference flow is not so good. A possible explanation for this is related to the conversion from the local to global flow. An approximation of the shear rate based on Womersley's theory (Womersley, 1955), indicates the occurrence of negative shear rates at the sensor surface. Since the sensor cannot distinguish between positive and negative shear rates, these negative shear rates are detected as positive.

Amplitude, frequency, and pressure wire dependence

In Table 5.2, a general overview is presented, showing the effect of using different pressure wires and variations in flow amplitude and frequency, on the deviation between the reference and estimated flow. It shows that in all cases the r value was close to 1, indicating that the overall dynamics of the flow were captured.

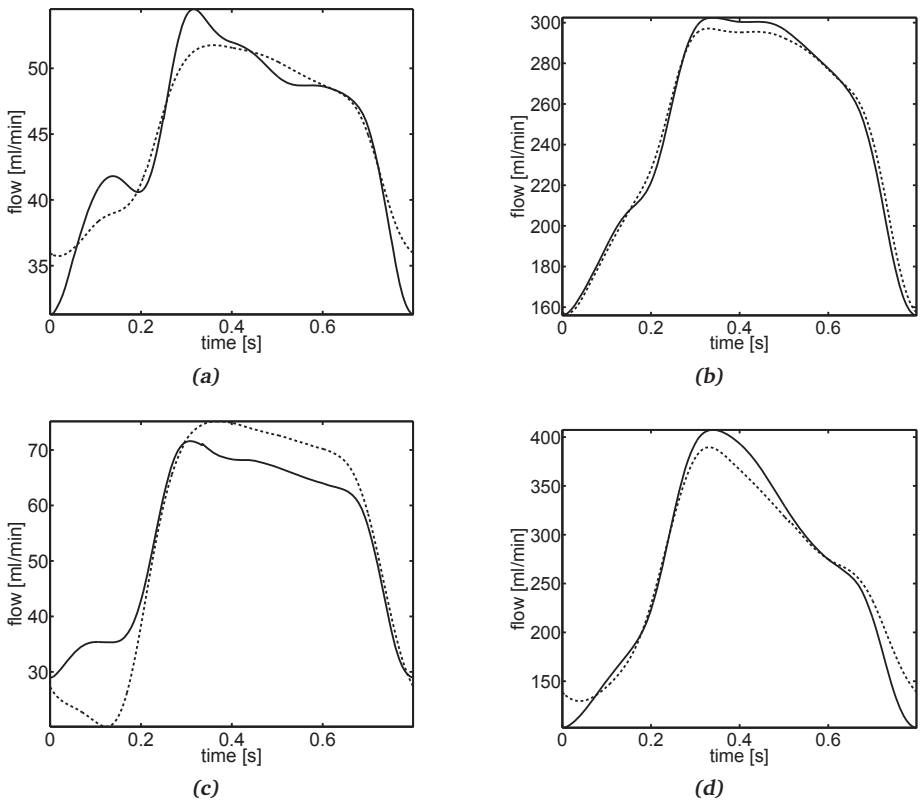

Figure 5.6: *Typical example of the reference flow (−) and flow estimated from the measured electrical power (−−), at low* ***(a,c)*** *and high* ***(b,d)*** *flow in the 3 mm* ***(a,b)*** *and 4 mm vessel* ***(c,d)****. The parameters quantifying the correlation are:* ***a)*** r *= 0.96, MAPE = 3%, MAE =1 ml/min,* ***b)*** r *= 0.99, MAPE = 2%, MAE = 4 ml/min,* ***c)*** r *= 0.98, MAPE = 12%, MAE = 6 ml/min,* ***d)*** r *= 0.99, MAPE = 8%, MAE =14 ml/min.*

Furthermore, the MAPE and MAE were all less than 9% and 12 ml/min, respectively, except for the case where the flow amplitude was equal to the average (AMPL = 100%). In that case, the average MAE was 16 ml/min, while the MAPE was especially high (25%). An obvious explanation for these large errors is an exacerbation of the problem detecting negative shear rates, as explained before.

5.3.2 Pressure measurements

Due to a small leakage in the aortic valve the pressures developed in the set-up deviated from physiological pressures, especially in the diastolic phase (Fig. 5.8). The generated pressures were, however, still suitable to test whether the pressure signal measured during the anemometric method was equal to reference pressure. Figure 5.8a shows that the signal representing the pressure (V_{pres}/V_{EX}), measured while the resistors were being heated, was similar to the reference pressure. The V_{pres}/V_{EX}-

Table 5.2: *The average (avg) and standard deviation (SD) of the three parameters (r, MAPE, and MAE) indicating the error between the estimated and reference flow for the three PressureWires (PW_1, PW_2, PW_3), two amplitudes (AMPL) of flow (50% and 100% of the mean flow), and heart rates (HR) of 60, 75, and 90 beats per minute (BPM).*

	r		MAPE [%]		MAE [ml/min]	
	avg	SD	avg	SD	avg	SD
PW_1	0.97	0.02	9	4	10	6
PW_2	0.96	0.03	5	2	8	5
PW_3	0.96	0.03	8	3	12	8
AMPL = 50 [%]	0.98	0.02	8	1	9	5
AMPL = 100 [%]	0.98	0.02	25	9	16	10
HR = 60 [BPM]	0.98	0.01	5	2	5	2
HR = 75 [BPM]	0.97	0.01	6	3	6	2
HR = 90 [BPM]	0.95	0.02	6	1	7	3

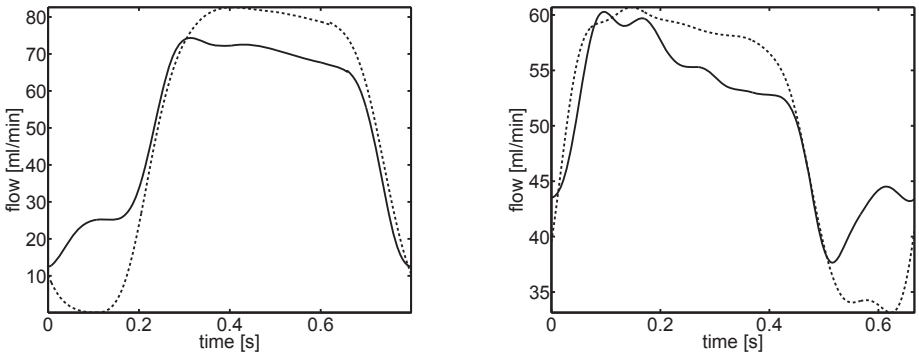

Figure 5.7: *Example of the estimated flow (−−) and reference flow (−) for a flow with a large amplitude* ***(a)*** *and a heart rate of 90 BPM* ***(b)****. The parameters quantifying the correlation are r = 0.97, MAPE = 30%, MAE =10 ml/min and r = 0.93, MAPE = 8%, MAE = 4 ml/min, respectively.*

signal pressure was very small but it could reliably be converted to a pressure via the reference pressure. The correlation between the V_{pres}/V_{EX}-signal and the reference pressure was excellent, expressed by an $r > 0.99$. The reference pressure signal was delayed with an average of 45±4 ms compared to the V_{pres}/V_{EX}-signal, even though it was located 3 cm proximal to the heated sensor. A possible explanation for this may be a filtering step performed by the reference pressure processing device (RADI Analyzer), causing an unknown phase lag in this signal.

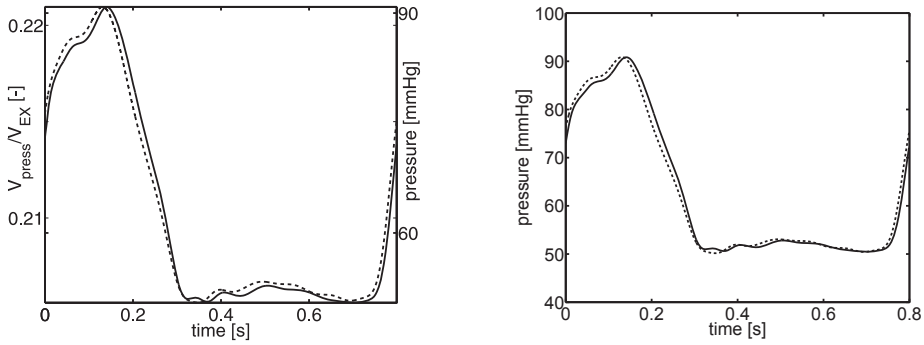

(a) *(b)*

Figure 5.8: a) *The V_{pres}/V_{EX}-signal (−−) and the reference pressure (−) in time.* ***b)*** *The pressure estimated from the V_{pres}/V_{EX}-signal scaled with the reference pressure (−−) and the reference pressure (−).*

5.3.3 Continuous thermodilution

The accuracy of the mean absolute flow measured with the continuous thermodilution method was determined by quantifying the difference between measurements and the line of identity, as depicted in Figure 5.9a. The errors represented by the MAPE (7%) and MAE (11 ml/min) were small. Furthermore, as shown in the Bland-Altman plot (Fig. 5.9b), compared to the reference flow, the estimated flow was slightly overestimated (3%) with 95% confidence bounds of 17%. This was similar to the results reported by Van 't Veer et al. (2009).

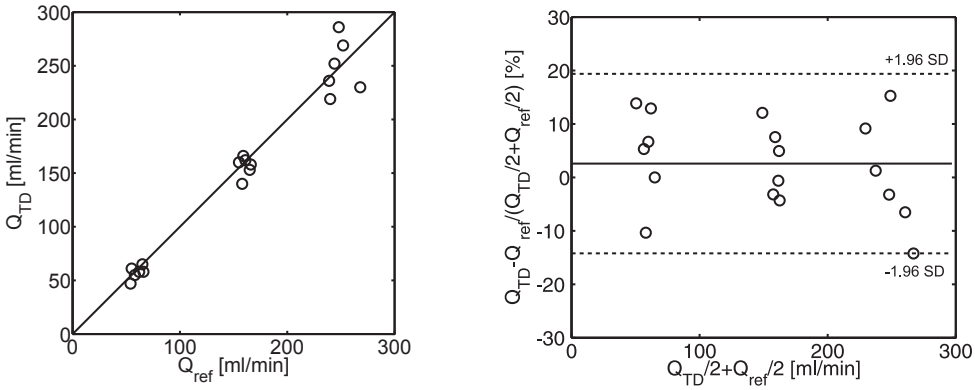

(a) *(b)*

Figure 5.9: a) *Comparison of the average flow calculated from the continuous thermodilution method (Q_{TD}) and the reference flow measurement (Q_{ref}).* ***b)*** *Bland-Altman representation showing the relative difference between Q_{TD} and Q_{ref}.*

Table 5.3: *The average (avg) and standard deviation (SD) of the three parameters (r, MAPE, and MAE), indicating the error between the estimated and reference flow, in case the mean flow ($\bar{Q}$) was determined from the continuous thermodilution (C-TD) or from the reference flow measurement.*

	r		MAPE [%]		MAE [ml/min]	
	avg	SD	avg	SD	avg	SD
with Q from ref	0.96	0.05	7	4	8	7
with $\bar{Q}$ from C-TD	0.92	0.05	11	6	13	8

5.3.4 The combination of continuous thermodilution and thermal anemometry

The influence of the thermodilution method on the thermal anemometric measurements was investigated by conducting the thermodilution protocol before and after the thermal anemometric measurements. It was found that the absolute electrical power required was higher when the thermodilution measurement was conducted first, due to a decrease in the microcable resistance. The sensitivity of the electrical power to changes in shear rate, however, was equal in both situations. Since the combined methodology involves scaling with the average flow, the order of measurement had no influence on the estimated flow.

Furthermore, Table 5.3 shows that the additional error on the estimated flow is limited, when the average flow as determined by the thermodilution is used.

Diastolic physiologic indices

From the presented results it can be concluded that this method is unable to reliably determine the dynamics of the flow close to zero due to the inability of detecting local shear rate reversal. In clinical practice, this means that coronary flow in the left coronary arteries can only be determined in the diastolic phase. Therefore, the accuracy of the proposed methodology was tested for two diastolic indices, which are both an indication of an impaired coronary microvasculature: the diastolic peak flow (DPF) and the microvascular resistance in diastole. To include the errors due to the thermodilution method, the data from the actual combined measurements (Table 5.3) were used.

The results for the difference between the estimated and reference DPF are depicted in Figure 5.10. The errors represented by the MAE and MAPE of the estimated DPF were (14±16) ml/min and (8±7)%, respectively.

The average resistance in diastole could also be determined accurately, indicated by the small deviation from the line of identity (Fig. 5.11). This small error is supported by a MAE of (0.04±0.06) mmHg min/ml and a MAPE of (7±5)%.

5.3.5 *Ex-vivo* validation

Figure 5.12 shows the results obtained in the isolated beating heart set-up. The main dynamics of the applied flow could be clearly recognized in the flow determined from

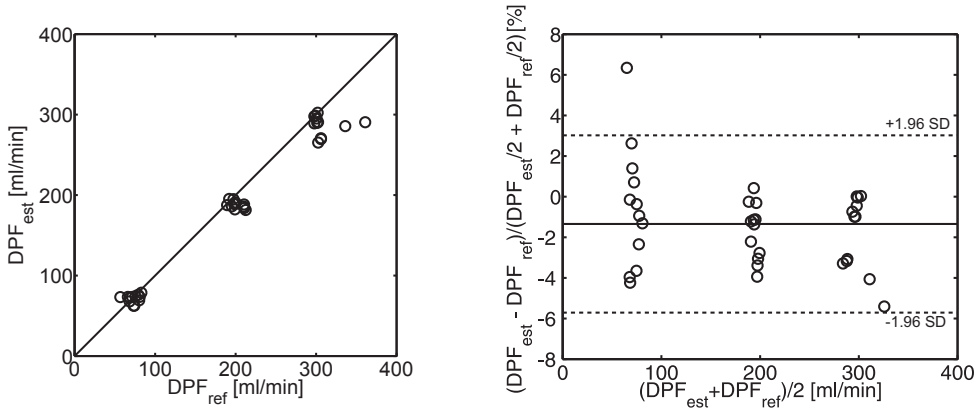

(a) *(b)*

Figure 5.10: ***a)*** *Comparison of the estimated diastolic peak flow (DPF_{est}) and the reference diastolic peak flow (DPF_{ref}).* ***b)*** *Bland-Altman representation showing the relative difference between the estimated and reference diastolic diastolic peak flow.*

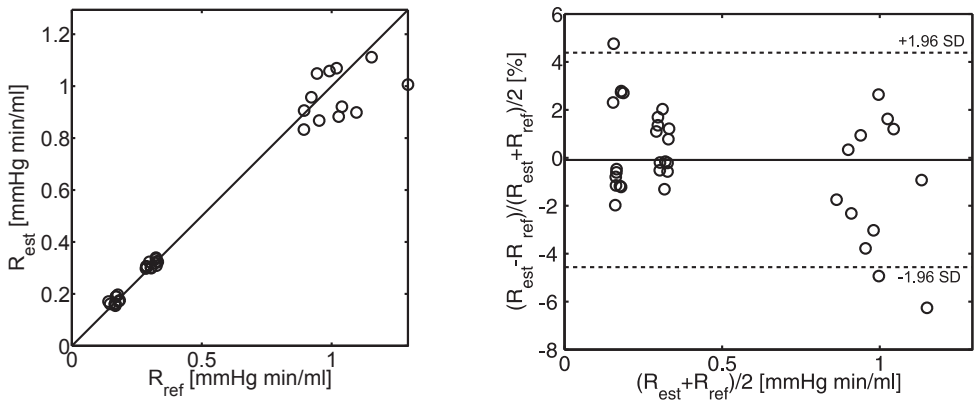

(a) *(b)*

Figure 5.11: ***a)*** *Comparison of the diastolic resistance determined from the estimated (R_{est}) and reference (R_{ref}) flow and pressure signals.* ***b)*** *Bland-Altman representation showing the relative difference between R_{est} and R_{ref}.*

the measured power in both relatively low (Fig. 5.12a) and high flow (Fig.5.12c). It is clear that at high flow the correlation between the estimated and reference flow was better. The overall difference between the applied and estimated flow for the three series of five flows, represented by the average and standard deviation of r, MAE, and MAPE, was 0.93±0.07, (9±5) ml/min and (5±1)%, respectively.

As in the *in-vitro* experiments, the correlation between the pressure estimated from the V_{pres}/V_{EX}-signal and the reference pressure was good, expressed by an average r of 0.99.

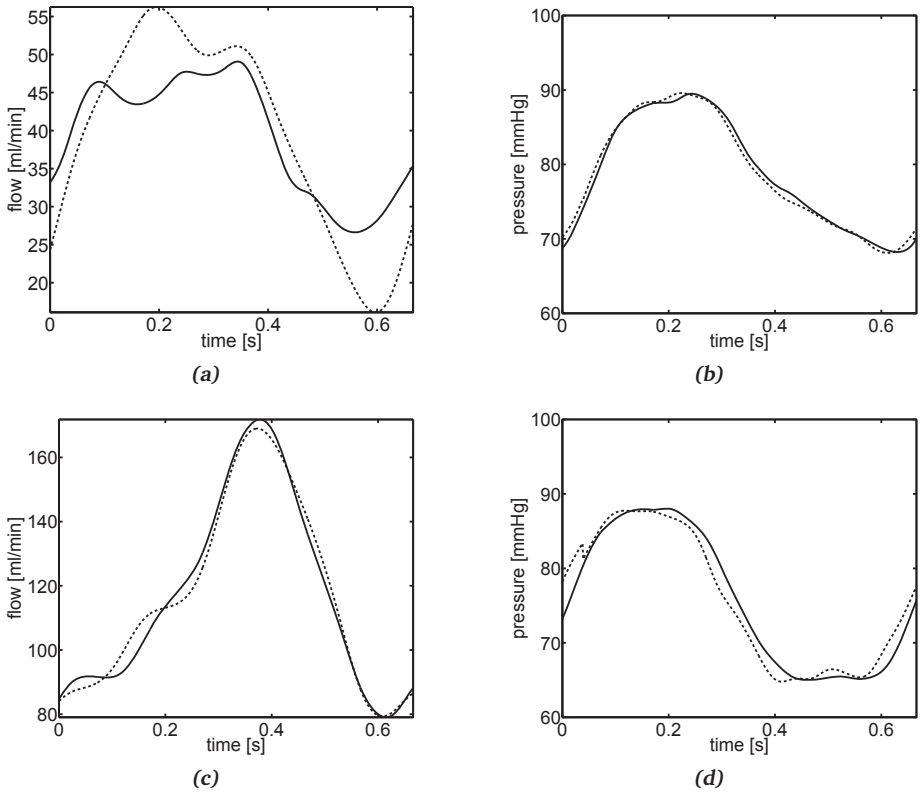

Figure 5.12: *Typical example of the reference flow (−) and flow estimated from the measured electrical power (−−) determined in the isolated beating pig heart set-up at an average flow of 40 ml/min* ***(a)*** *and 132 ml/min* ***(c)****. The reference pressure (−) and the pressure estimated from the* V_{pres}/V_{EX}*-signal (−−) measured simultaneously with these flow measurements are shown in* ***(b)*** *and* ***(d)****, respectively.*

5.4 Discussion

A novel methodology, combining two thermal methods applied to a commercially available pressure-sensing guidewire (PressureWire), was developed to assess coronary pressure and flow, simultaneously, and evaluated in an *in-vitro* model of the coronary circulation. The dynamics of the flow were assessed with a thermal anemometric method, while a continuous infusion thermodilution method was used to determined the average flow. The thermal anemometric method, reported in chapter 4, was shown to be promising in the assessment of coronary flow reserve (CFR) via shear rate measurements. Because the pressure functionality of the PressureWire was retained, this enabled sequential measurement of pressure and shear rate. Although not further investigated, the sequential method was also found to be capable of assessing the dynamics of the shear rate, which motivated this research.

First, the anemometric method was altered to enable simultaneous assessment of pressure and shear rate. This was achieved by adapting the electrical circuit, so a pressure signal could be measured while both the resistors on the chip of the PressureWire were kept at a constant overheat temperature. A good correlation was found between the measured pressure signal and the reference pressure. Within one series of measurements, the parameters of the linear relation between the pressure signal and its reference could be determined reliably. A disadvantage was that the pressure signal was very dependent on the overheat temperature of the sensor. Slight temperature changes of the sensor, e.g. due to variations in microcable resistance, already had a great influence on the scaling parameters. The pressure signal, therefore, needed to be scaled with a reference pressure for each series of measurement. The reference signal, however, can easily be obtained by operating the sensor in its original configuration.

Using the methodology combining the two methods, the absolute volumetric physiological flow dynamics could be determined quite accurately. Nevertheless, it is paramount to realize that the proposed method is based on coarsely simplified relations between electrical power, heat transfer, shear rate, and flow. The relation between the electrical power and shear rate was approximated via a simple, linear, relation. Likewise, the phase delay between the electrical power and shear rate was also assumed to be linear and dependent on the average flow alone. Furthermore, a quasi-steady approach was taken to convert the volumetric flow to a measure for the local flow rate at the sensor surface. There are several phenomena that complicate the relation between electrical power and flow. From Womersley's theory (Womersley, 1955) it is clear that a phase delay exists between the flow and local shear rate, which scales with the Womersley number. For shear rates close to zero, diffusive, and not only advective heat transfer, will play a role. During shear rate reversal the sensor's thermal wake will be carried back over the heated sensor. The casing surrounding the heated chip will act as a heat capacitor, causing storage and release of heat in de- or acceleration of the shear rate. The chip is located inside a cavity, which may result in the development and washing out of eddies inside the cavity. Finally, the radial position of the sensor inside the possibly curved vessel is unknown. Considering all these unknown complicating factors, a very simplified approach was chosen based on the only known flow parameter: the mean absolute flow determined with the continuous thermodilution method. While this simple approach does have its limitations, it performs surprisingly well for physiological flows.

It was shown that a single calibration curve, characterizing the relation between the time-averaged power and shear rate, could be determined for vessels with different diameters. The slope of this calibration curve at the mean shear rate (as determined with the thermodilution method) was then used to convert the measured electrical power to volumetric flow. The overall correlation between the flow dynamics, estimated from the electrical power, and the reference flow was good (r = 0.97, MAPE = 9%, and MAE = 10 ml/min). However, for flow rates approaching zero the correlation is less than desired. This is likely to be caused by local shear rate reversal. Since it is physically impossible to measure shear rate reversal with this thermal anemometric method, the dynamics of the flow close to zero cannot be

assessed.

Conveniently, it was shown that this single calibration relation was also applicable to other PressureWires, which practically means that each PressureWire does not need to be characterized individually. Furthermore, although the heart rate was only varied within the physiological range of a patient in the catheterization laboratory, it seemed to have little effect on the quality of the estimated flows. The large amplitude experiments did show large deviation between the estimated and reference flow. This could also be explained by an exacerbation of the problems regarding the inability of the sensor to distinguish between forward and backward flow.

In the isolated beating heart experiment, the correlation between the applied and estimated flow in the LCx was comparable to the measurements in the *in-vitro* set-up. This is a clear indication that the method is also feasible in blood at genuine physiological conditions. Furthermore, the calibration curve obtained from the *in-vitro* measurements was used to convert the measured power to flow, suggesting that a separate characterization in blood is not required. It must be mentioned that the diameter of the vessel was visually estimated to be 3 mm. An error in the estimate will obviously influence the conversion from shear rate to flow. This was a preliminary study consisting of only one series of measurement. Therefore, further research should be performed in blood under physiological conditions with a proper assessment of the vessel diameter at the measurement site.

The continuous thermodilution method is the only clinically available method to measure the average absolute volumetric coronary flow (Aarnoudse et al., 2007; van 't Veer et al., 2009). Compared to standard catheterization protocols, however, it does require additional equipment (infusion catheter and pump) and extra steps in the protocol. An additional drawback is that the method is only applicable in hyperaemia, due to the dilution of the blood. When combining the anemometric and thermodilution method it was found that the order in which the measurements were performed did not influence the advective heat transfer (represented by the slope of the power shear rate relation). There was a relatively large increase in the diffusive heat transfer when the thermodilution measurement was performed first. The infusion of the cold fluid over the guidewire decreased the resistance of the microcables, which effectively means that the sensor temperature was increased. Hence, the required absolute power was larger. However, due to the scaling with the average flow, obtained with the thermodilution method, this did not affect the calculated absolute flow rate. The additional error, due to inaccuracies of the continuous thermodilution method were also limited. Regarding the clinical applicability of the combination of methods, it was found that the total time of the protocol was not increased much, compared to the thermodilution method alone.

The overheat temperature of 20 K can be argued as a limitation for *in-vivo* application, concerning blood and vessel damage. However, as already discussed in chapter 4, due to the limited time of measurement and the small size of the sensor, it is expected that the amount of damage will be negligible. This issue, however, does require additional research.

The electrical circuit developed to keep the on-chip resistances temperature of the PressureWire constant, was sensitive to disturbances from the outside. By improving

the electrical circuit itself and its shielding, the signal-to-noise ratio is likely to be improved significantly, enabling real time assessment, instead of filtering by averaging eight periods. With this improved signal-to-noise ratio the overheat temperature might also be decreased, while retaining the same level of accuracy.

To be able to take the method to the clinic, it should be incorporated into an already clinically used medical device (e.g. RADI Analyzer). This will prevent dis- and reconnecting the PressureWire to multiple devices. Some parts of the protocol, e.g., the setting of the sensor temperature and the calibration of the pressure signal, can then also be automated to shorten the procedure time.

It was shown that with the proposed methodology the diastolic peak flow (DPF) and average diastolic resistance could be determined quite accurately. High diastolic peak flow is, together with a short diastolic deceleration time and systolic retrograde flow, associated with microvascular obstruction during reperfusion following percutaneous coronary interventions (Hirsch et al., 2008; Okcular et al., 2010). The average diastolic microvascular resistance is a measure for the state of the coronary microvasculature, without the effect of myocardial contraction. A good index to assess coronary microvascular disease is the instantaneous hyperaemic diastolic velocity-pressure slope (IHDVPS) as described by Escaned et al. (2009). This index, however, could not be assessed due to the unphysiological pressures in diastole. Nevertheless, the proposed methodology will likely be able to determine IHDVPS, based on volumetric flow measurements instead of velocity.

Finally, another promising application of both thermal methods is the determination of the absolute flow in resting conditions. The resting average microvascular resistance, CFR, and diastolic coronary vascular reserve (Krams et al., 2004) can then be assessed based on absolute flow measurements. Both measurements should then be performed in hyperaemia, to find the absolute value of the flow and the scaling factor for the anemometric method, while only the anemometric method is applied to determine the resting flow.

5.5 Conclusion

A novel promising methodology was developed to assess coronary pressure and volumetric flow dynamics. Although the method is unsuitable to assess flow dynamics close to zero, with only a few minor additional steps in the standard continuous thermodilution protocol and without altering the hardware of the PressureWire itself, extra information regarding the dynamics of pressure and flow during diastole can be obtained.

Author contributions

Performed experiments: A. van der Horst, M. van ’t Veer, R.A.M van der Sligte
Data analysis: A. van der Horst, M. van ’t Veer, R.A.M van der Sligte
Interpretation of results: all
Prepared figures: A. van der Horst, M. van ’t Veer, R.A.M van der Sligte
Drafted manuscript: A. van der Horst
Edited and revised manuscript: all
Approved final version of manuscript: all

Chapter 6

Analytical and experimental characterization of a miniature calorimetric sensor in pulsatile flow

The behaviour of a miniature calorimetric sensor, which is under consideration for catheter-based coronary artery flow assessment, is investigated in both steady and pulsatile tube flow. The sensor is composed of a heating element operated at constant power, and two thermopiles that measure flow-induced temperature differences over the sensor surface. An analytical sensor model is developed, which includes axial heat conduction in the fluid and a simple representation of the solid wall, assuming a quasi-steady sensor response to the pulsatile flow. To reduce the mathematical problem, described by a two-dimensional advection-diffusion equation, a spectral method is applied. A Fourier transform is then used to solve the resulting set of ordinary differential equations and an analytical expression for the fluid temperature is found. To validate the analytical model, experiments with the sensor mounted into a tube have been performed in steady and pulsatile water flow with various amplitudes and Strouhal numbers. Experimental results are generally in good agreement with theory and show a quasi-steady sensor response in the coronary flow regime. The model can therefore be used to optimize the sensor design for coronary flow assessment.

The contents of this chapter are based on Hanneke Gelderblom, Arjen van der Horst, Jaap Haartsen, Marcel C.M. Rutten, Alfons A.F. van de Ven, and Frans N. van de Vosse, Analytical and experimental characterization of a miniature calorimetric sensor in pulsatile flow, *J Fluid Mech*, **666**, 428–444, 2011.

6.1 Introduction

Flow sensors based on forced convective heat-transfer, such as hot-film anemometers, can be used for the assessment of arterial blood flow (Seed and Wood, 1970a; Clark, 1974; Nerem et al., 1976). In a recent study, Tonino et al. (2009) showed that if the treatment of patients with coronary artery disease is based on an indirect measure for coronary flow (derived from coronary pressure measurements), the clinical outcome improves significantly. Clearly, direct flow assessment by miniature sensors that can be introduced into the coronary arteries would provide even more information about the condition of these arteries (van 't Veer et al., 2009). In this study, we aim to characterize the behaviour of such a miniature convective heat-transfer sensor in steady and pulsatile tube flow, through both an analytical and an experimental approach. The sensor is based on a calorimetric flow measurement principle and it consists of a small aluminium heating element of width b=140 μm, operated at constant power, and two polysilicon thermopiles that measure flow-induced temperature differences over the sensor surface. These sensor elements are embedded in a flexible polyimide substrate having a thickness of 10 μm; see Figure 6.1 (a). In order to use it for coronary flow assessment, the flexible device is bent around a guidewire, which can be inserted into the coronary arteries. In our characterization study however, the device is mounted at the inner wall of a tube, to be able to subject it to a well-defined flow regime. The length l of the device is equal to approximately half the circumference of the inner tube wall; see Figure 6.1 (b). The temperature difference between two positions 100 μm downstream and 100 μm upstream from the heater center (T_d-T_u) is measured, as well as the heater temperature T_h with respect to the ambient fluid temperature T_f far upstream (2000 μm from the heater center). In absence of flow, heat transfer from the sensor to the fluid occurs solely through conduction, resulting in a symmetric temperature distribution over the sensor surface. If a certain fluid flow exists, the advective heat-transfer leads to an asymmetric temperature distribution. The resulting temperature differences are a measure for the flow (Elwenspoek, 1999). Flow reversal will lead to a sign change in T_d-T_u, and hence can be detected, which is an advantage compared to the conventional hot-film anemometers (van Oudheusden and Huijsing, 1989).

Two important dimensionless parameters that appear in the study of thermal sensors in time-dependent flow are the Péclet number *Pe*, and the Strouhal number *Sr*. Here, *Pe* is a measure for the importance of advective compared to conductive heat-transfer, *Sr* for the importance of unsteady compared to advective temperature variations. Formal expressions for *Sr* and *Pe* are given further on (see (6.8) and (6.13), respectively).

Many experimental and analytical studies of hot-film anemometers have been reported in the literature. Experiments with these kinds of probes have been performed by, among others, Seed and Wood (1970a), Clark (1974), Ackerberg et al. (1978), and Van Steenhoven and van de Beucken (1991). Liepmann and Skinner (1954) derived a theoretical relation between the amount of convective heat loss from a hot surface and the local steady shear rate. Pedley (1972a, 1976b) and Menendez and Ramaprian (1985) extended this work to include unsteady, pulsatile flows.

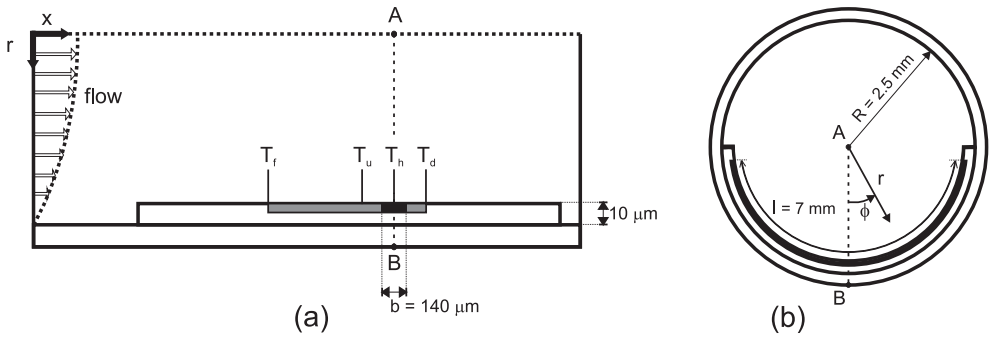

Figure 6.1: *Schematic view of the calorimetric sensor mounted on the inside of the tube wall (not drawn to scale); heater in black, thermopiles in grey, r representing the radial, x the axial, and ϕ the circumferential direction.* ***a)*** *Side-view showing the placement of the sensor elements (heater and thermopiles measuring T_h-T_f and T_d-T_u) with respect to the fluid flow.* ***b)*** *Cross-section showing the positioning of the flexible device inside the tube.*

For miniature flow sensors like the one presented here, the theory developed for hot-film anemometers is not applicable. First of all, because in a thermal sensor with small dimensions, generally operated at small *Pe*, heat conduction in the flow direction cannot be neglected, as is done in the usual boundary-layer approximation. In numerical studies, Tardu and Pham (2005) and Rebay et al. (2007) showed that this axial conduction has a considerable influence on the response of small hot-film gauges. Ackerberg et al. (1978) derived an analytical solution for the heat transfer from a finite strip for $Pe \to 0$, in steady flow. Ma and Gerner (1993) examined the leading and trailing edge of a micro-sensor in steady flow separately to obtain an analytical solution for the entire sensor surface, in analogy to the method used by Springer and Pedley (1973) and Springer (1974).

Second, most analytical studies consider the problem of a uniform surface temperature on the heated element, while our sensor is operated at constant power, which is better described by a heat-flux boundary condition. Liu et al. (1994) and Rebay et al. (2007) used a constant heat-flux boundary condition on the surface of a heated element embedded in an adiabatic wall. However, the thermopiles of our sensor consist of conductive polysilicon, and therefore heat will not only be transferred from the heater to the fluid directly, but also via the surrounding material. In that case, we end up with a conjugate heat-transfer problem, where the heat source is known, but the interface temperature and heat flux to the fluid are unknown; Tardu and Pham (2005) studied this problem numerically. Stein et al. (2002) derived an analytical solution downstream of a flush-mounted heat source in steady flow. Cole (2008) considered conjugate heat-transfer from a steady-periodic heated film, also in steady flow. To the authors' knowledge, only a few analytical models specific for calorimetric sensors exist. Lammerink et al. (1993) described an experimental study and a relatively simple analytical model of such a sensor, but in steady flow and with a different sensor geometry. Calorimetric sensors on highly conductive

silicon wafers are described by Van Oudheusden (1991), also in steady flow and with very small on-sensor temperature differences compared to the sensor overheat. Experimental studies with calorimetric flow sensors in steady flow have been reported by Lammerink et al. (1993) and Nguyen and Kiehnscherf (1995). However, no data on unsteady flow experiments with this type of sensor are available.

Our analysis of the calorimetric flow sensor focuses on the derivation of a new analytical model for the temperature distribution in a pulsatile fluid flow over a small heated element operated at constant power. Experiments with the sensor in steady and pulsatile water flow with Strouhal numbers and amplitudes in the expected physiological flow range are carried out to verify our theoretical predictions. In section 6.2 the mathematical formulation of our problem is given in terms of a two-dimensional advection-diffusion equation. We circumvent the coupling of the heat-transfer problems in the fluid and the substrate by approximating the heat flux from the sensor to the fluid, and use this approximation as a boundary condition for the fluid compartment. The axial conduction term is retained, and therefore our solution holds for all *Pe*-values. Since the heat flux at the boundary is approximated by a continuous function, the leading and trailing edge of the heater do not have to be treated separately (Ma and Gerner, 1993), resulting in one solution for the complete domain. When applied in coronary flow, our sensor will be operated at small Strouhal numbers, therefore a quasi-steady sensor response to the pulsatile flow is assumed. As described in section 6.3, a spectral method is applied to reduce the mathematical problem to one dimension. Then, a Fourier transform is used to solve the resulting set of ordinary differential equations. The experimental technique is described in section 6.4. In section 6.5, the experimental results are compared to the theoretical predictions, and found to be in good agreement. The model developed not only leads to theoretical understanding of the operating principle of the sensor, but it can also be used to optimize the sensor design, as is demonstrated in section 6.5.

6.2 Mathematical problem formulation

In order to formulate an analytical model for the sensor in a pulsatile tube flow (see Figure 6.1), a cylindrical coordinate system (r, ϕ, x) is adopted, where the main flow is in axial or x-direction, r is the radial, and ϕ the circumferential coordinate. The origin of this system is chosen such that $x = 0$ at the heater center. The pulsatile fluid flow is assumed to be fully developed and, because the temperature difference between the heater and the oncoming fluid is relatively small, temperature independent. The typical buoyancy-driven radial velocity can be estimated from the momentum equation in the radial direction using the Boussinesq approximation. For our configuration, the ratio of radial to axial velocity is of order 10^{-2}, hence free convection can be neglected.

The basic problem is thus reduced to that of finding the temperature distribution $T(x, r, \phi, t)$, with t the time, in a prescribed pulsatile fluid flow in a tube of radius R, which is heated by a time-constant prescribed heat influx in a small region of length l and width b around the tube wall; the remaining part of the wall is thermally

insulated. The equation governing the temperature distribution in the fluid is the thermal energy equation in the tube ($x \in \mathbb{R}, 0 \leq r \leq R, -\pi \leq \phi \leq \pi$)

$$\frac{\partial T}{\partial t} + u(r,t)\frac{\partial T}{\partial x} = \alpha \left[\frac{\partial^2 T}{\partial x^2} + \frac{1}{r}\frac{\partial}{\partial r}\left(r\frac{\partial T}{\partial r}\right) + \frac{1}{r^2}\frac{\partial^2 T}{\partial \phi^2}\right], \tag{6.1}$$

together with the boundary condition at the tube wall, $r=R$, describing the prescribed heat influx,

$$\begin{aligned} k\frac{\partial T}{\partial r}(x,R,\phi,t) &= q(x), \text{ if } \frac{-l}{2R} < \phi < \frac{l}{2R}, \\ &= 0, \text{ if } |\phi| > \frac{l}{2R}. \end{aligned} \tag{6.2}$$

Here, u is the velocity in x-direction, α the thermal diffusivity, and k the thermal conductivity. Heat influx q is in Wm^{-2}, such that the power supplied to the heater in W is given by

$$P = l\int_{-\infty}^{\infty} q(x)dx. \tag{6.3}$$

Considering the case that $u > 0$, i.e. the fluid is flowing in the positive x-direction, we state that T must go to T_o, the initial fluid temperature, for $x \to -\infty$, but that T for $x \to +\infty$ must tend to a value $T_\infty > T_o$ for a quasi-steady solution to exist. In that case the total heat-transfer rate P into the fluid is balanced by the advective heat outflow in positive x-direction, equal to $\rho c D(T_\infty - T_o)$, with ρ the density, c the specific heat, and $D = 2\pi\int_0^R u(r,t)rdr$, the total volumetric flow rate at time t.

To emphasize the effect of the two different length scales that arise in the problem, i.e. heater width b and tube radius R, we introduce the following dimensionless variables

$$\hat{x} = \frac{x}{b}, \quad \hat{r} = \frac{r}{R}, \quad \hat{u} = \frac{u}{V}, \quad \hat{t} = \frac{t}{t_c}, \quad \hat{T} = \frac{T - T_o}{T_c}, \tag{6.4}$$

with V the typical axial velocity, t_c the time scale for temperature variations, and T_c the typical temperature scale. The characteristic parameter values can be found in Table 6.1, appropriate choices for t_c and T_c are explained below. Note that the heater width is used as the characteristic length scale in x-direction, implying that we will look for changes in temperature T in the direct axial vicinity of the heater, which is where T_d and T_u are measured. By substituting (6.4) into (6.1), we obtain

$$\frac{b}{t_c V}\frac{\partial \hat{T}}{\partial \hat{t}} + \hat{u}(\hat{r},\hat{t})\frac{\partial \hat{T}}{\partial \hat{x}} = \frac{\alpha}{bV}\frac{\partial^2 \hat{T}}{\partial \hat{x}^2} + \epsilon^2\left[\frac{1}{\hat{r}}\frac{\partial}{\partial \hat{r}}\left(\hat{r}\frac{\partial \hat{T}}{\partial \hat{r}}\right) + \frac{1}{\hat{r}^2}\frac{\partial^2 \hat{T}}{\partial \phi^2}\right], \tag{6.5}$$

with $\epsilon = \sqrt{(\alpha b/V)}/R = 0.006 \ll 1$. Since, in (6.5), the small number ϵ^2 appears in front of the highest derivative with respect to $\hat{r}$, one can expect a boundary layer to develop at the tube wall; i.e. at $\hat{r} = 1$. The outer solution at leading order, with $\epsilon = 0$,

Table 6.1: *The parameter values used in the analytical model, based on the experimental set-up.*

Parameter	value	unit	description
T_o	20	°C	outer flow temperature
T_c	11.7	°C	temperature scale
P	80	mW	heater power
x_h	0	μm	heater center
x_d	100	μm	position where T_d is measured
x_u	-100	μm	position where T_u is measured
x_f	-2000	μm	position where T_f is measured
b	140	μm	heater width
l	7000	μm	heater length
σ	70	μm	standard deviation of the assumed boundary heat-flux distribution
R	2.5	mm	inner tube radius
V	0.1	ms^{-1}	typical axial velocity
S_0	115	s^{-1}	mean shear rate
α	$1.44 \cdot 10^{-7}$	$\mathrm{m}^2\mathrm{s}^{-1}$	thermal diffusivity [b]
k	0.606	$\mathrm{Wm}^{-1}\mathrm{K}^{-1}$	thermal conductivity [b]
ν	$1 \cdot 10^{-6}$	$\mathrm{m}^2\mathrm{s}^{-1}$	kinematic viscosity [b]
ω	2π	rad s^{-1}	angular frequency

[b] (see Incropera et al., 2007, p. 860)

is the trivial solution $\hat{T} = 0$. The temperature problem is thus confined to a small region close to the sensor surface: the thermal boundary layer of thickness δ_T.

Our sensor measures the temperature difference T_d-T_u at distances in the order of magnitude of b up- and downstream of the heater center for $|\phi| < l/2R$. Hence, in the region of interest for our sensor $|x| = O(b)$ and $\delta_T \ll R$. Within this region, the problem is independent of the ϕ-coordinate. The characteristic length-scale for conduction in the ϕ-direction, heater length $l = O(R)$, is much larger than the length scale for conduction in the axial direction, heater width b. For our sensor $b/l = 0.02$; hence conduction in the ϕ-direction and edge effects occurring at $\phi = \pm l/2R$ can be neglected.

Since the thermal boundary layer thickness δ_T is much smaller than the tube radius, the tube wall in a b-environment of the heater can be considered flat. We therefore adopt a spatial rectilinear coordinate system $(\hat{x}, \hat{y})$, where $\hat{x}$ is the surface coordinate in the flow direction, and $\hat{y}$ is the stretched coordinate normal to the surface, defined as $\hat{y} = (R/\delta_T)(1 - \hat{r})$; see Figure 6.2. As a further approximation, we confine the domain for the inner solution to a strip of finite height h. At the upper boundary of the strip, $y = h$ (with $y = \delta_T \hat{y}$), we then require that $\hat{T} = 0$, to match the inner solution to the outer one; see Figure 6.2. How to choose h such that the solution in a b-environment of the heater, where the thermal boundary layer is still thin, is not influenced by the finite size of the domain in y-direction will be explained

further on in this section; see (6.11).

Further downstream (for $x > b$, hence outside our region of interest) the thermal boundary layer widens, due to radial conduction. Both curvature and ϕ-dependence will enter the problem again, while axial conduction will become negligible. Even further downstream ($\hat{x} > R/b$), the fluid temperature will become uniform in each cross-section, with $T \to T_\infty = T_0 + P/\rho c D$. It is therefore important to note that, given the simplifications described above, our method will only yield the correct solution in an b-environment of the heater, i.e. the region of interest for our sensor.

As a further approximation, we assume that the shear rate is the only flow parameter that influences the heat transfer from the sensor surface, implying that the velocity profile may be approximated linearly throughout the thermal boundary layer (Pedley, 1972a). Since our domain is now restricted to a strip of finite height h, the linearization of the velocity profile is valid throughout the complete domain. This approximation requires the Stokes layer thickness δ_S to be much larger than the thermal boundary layer thickness δ_T. In that case the velocity u within the thermal boundary layer can be approximated by ($y = R - r = \delta_T \hat{y}$)

$$u(y,t) = \left.\frac{\partial u}{\partial y}\right|_{y=0} y = S(t)y,$$

with S the shear rate, which is, in a pulsatile tube flow, given by

$$S(t) = S_0 \left[1 + \beta \sin(\omega t)\right],$$

with S_0 the mean, $\omega = 2\pi f$ the angular frequency, and β the amplitude of the shear rate oscillations. This implies that when $\beta > 1$, backflow is involved. Since for coronary flow, the order of magnitude of β will be about one, the dimensionless shear rate $\hat{S}(\hat{t}) = S(t)/S_0$ is an $O(1)$-function of t. Hence, we have

$$u(y,t) = S(t)y = S_0 \delta_T \hat{y} \hat{S}(\hat{t}),$$

yielding

$$V = \delta_T S_0, \qquad \text{and} \qquad \hat{u}(\hat{y},\hat{t}) = \hat{S}(\hat{t})\hat{y}.$$

To find an expression for the thermal boundary layer thickness δ_T, we write (6.5) in terms of $\hat{y}$, $\hat{u}(\hat{y},\hat{t})$, and $\hat{S}(\hat{t})$ as

$$\frac{b}{t_c S_0 \delta_T}\frac{\partial \hat{T}}{\partial \hat{t}} + \hat{S}(\hat{t})\hat{y}\frac{\partial \hat{T}}{\partial \hat{x}} = \frac{\alpha}{b S_0 \delta_T}\frac{\partial^2 \hat{T}}{\partial \hat{x}^2} + \frac{\alpha b}{\delta_T^3 S_0}\frac{\partial^2 \hat{T}}{\partial \hat{y}^2}. \tag{6.6}$$

When advection in x- and conduction in y-direction are the two dominant effects, $\alpha b/S_0\delta_T^3$ must be of $O(1)$, and hence the thermal boundary layer thickness is given by Liepmann and Skinner (1954):

$$\delta_T = (\alpha b/S_0)^{1/3}. \tag{6.7}$$

The linearization of the velocity profile within the thermal boundary layer is allowed if $\delta_T \ll \delta_S$. The Stokes layer thickness in a fully developed pulsatile tube flow is given by Schlichting and Gersten (2000, p. 367)

$$\delta_S = (\nu/\omega)^{1/2},$$

with ν the kinematic viscosity. For a 1 Hz pulsatile water flow we get $\delta_S = 4 \cdot 10^{-4}$ m. The requirement $\delta_T \ll \delta_S$ leads us to an estimate for the admissible shear rate:

$$S_0 \gg \alpha b/\delta_S^3 = 0.3 \text{ s}^{-1}.$$

This requirement is amply satisfied, since our experiments are performed at a mean shear rate of about 115 s^{-1}. Furthermore, δ_T and b are of the same order of magnitude in this range of shear rates, allowing the use of b as length scale in both x- and y-direction. This already indicates that the axial conduction term in (6.6) can certainly not be neglected within the region of interest for our sensor. This is further confirmed by the magnitude of the coefficient of x-conduction; $\alpha/bS_0\delta_T = 0.16$ (see Table 6.1 for the parameter values used).

The magnitude of the dimensionless group in front of the unsteady term in (6.6), the Strouhal number $Sr = b/t_c S_0 \delta_T \approx 1/t_c S_0$, if $b/\delta_T \approx 1$, depends on the choice of the characteristic time scale t_c. The goal of this study is not to analyze start-up processes that occur when switching on the heater, but to describe the periodic variations in the sensor response. Therefore, the oscillation time, $1/\omega$, is used as characteristic time scale; hence

$$Sr = \omega/S_0. \tag{6.8}$$

Eventually, this sensor will be used for coronary flow measurements, where the estimated mean shear rate the sensor experiences when positioned on a guidewire is in the order of magnitude of 1000 s^{-1}. Hence, *Sr* is generally small for our ultimate application (typically $Sr < 0.1$, assuming measurement of the first ten harmonics is sufficient for reconstruction of the coronary flow signal (Milnor, 1989, p. 157)). We therefore assume the fluid temperature distribution to be quasi-steady, thereby neglecting the unsteady term in the thermal energy equation. In the quasi-steady approximation time t represents a parameter rather than a variable. From here on, we therefore omit the explicit dependence on $\hat{t}$ ($\hat{T} = \hat{T}(\hat{x}, \hat{y})$); in fact, the role of $\hat{t}$ is now taken over by the shear rate $\hat{S}$ ($\hat{S} = 1 + \beta \sin(\hat{t})$).

Another simplification is that heat loss through the insulating back of the tube in which the sensor is mounted, is neglected: all heat produced by the heater is assumed to be transferred to the fluid. Capacitive effects, which may cause the heat transfer to the fluid to vary in time, are also neglected. According to Tardu and Pham (2005) this is reasonable, since the thermal diffusivities of the sensor components are two orders of magnitude higher than that of water. Since the exact shape of the heat-flux distribution from the sensor substrate to the fluid depends on the temperature distribution in the fluid, this leads to a conjugate heat-transfer problem, which is hard to solve. We circumvent this coupling of the fluid and substrate temperatures by a much simpler approach: we approximate the shape of the heat-flux distribution

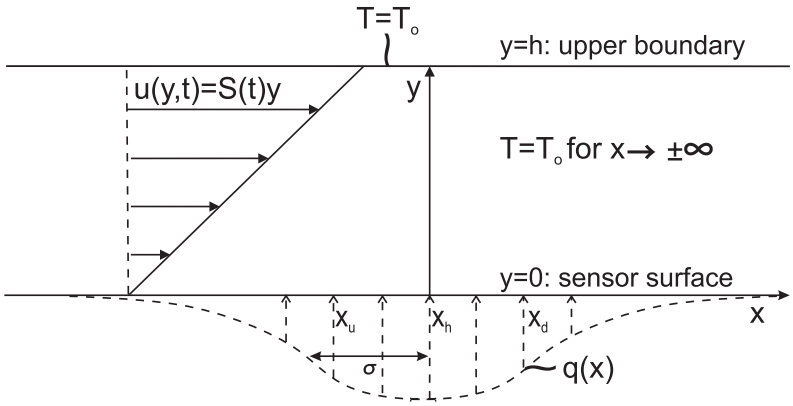

Figure 6.2: *Scheme of the problem geometry.*

from substrate to fluid and use this as a boundary condition for the fluid problem. If all the heat would be transferred from the heater to the fluid directly, i.e. when there is perfect insulation outside the heater compartment, a rectangular-shaped heat-flux boundary condition would be most realistic. For our sensor, however, conduction of heat from the heater towards the other sensor components will smooth the rectangular-shape, leading to a more Gaussian-shaped heat-flux profile, with some deviations due to the asymmetric temperature distribution in the fluid. As a simple approximation of the real heat-flux boundary condition, we therefore use a Gaussian distribution with a standard deviation σ equal to half the heater width, hence $\sigma = b/2$:

$$q(x) = -k\frac{\partial T}{\partial y}\bigg|_{y=0} = \frac{P}{l\sigma\sqrt{2\pi}}e^{-\frac{(x-x_h)^2}{2\sigma^2}}, \tag{6.9}$$

with x_h the position of the heater center, and P/l the total amount of heat transferred from the sensor to the fluid, per unit of length in z-direction (in Wm^{-1}), as given by (6.3).

The resulting dimensional thermal energy equation and boundary conditions describing the quasi-steady problem for the fluid temperature $T = T(x, y)$ within the thermal boundary layer or strip are given by:

$$\begin{gathered} Sy\frac{\partial T}{\partial x} = \alpha\left(\frac{\partial^2 T}{\partial x^2} + \frac{\partial^2 T}{\partial y^2}\right), \qquad x \in \mathbb{R},\ 0 \le y \le h, \\ T(\pm\infty, y) = T_0, \quad \frac{\partial T}{\partial y}(x, 0) = -\frac{P}{kl\sigma\sqrt{2\pi}}e^{-\frac{(x-x_h)^2}{2\sigma^2}}, \quad T(x, h) = T_0. \end{gathered} \tag{6.10}$$

Figure 6.2 shows a schematic view of the resulting problem to be solved. Note that, although we are only interested in the solution close to the heater (for $|x| = O(b)$), we have, for mathematical ease, extended the domain in x-direction to infinity. The outflow boundary condition used, implies that in our model, all heat will eventually escape through the upper boundary $y = h$. Since, for the correct choice of h, this

happens sufficiently far away from the heater, it does not influence the solution in a b-environment of the heater. To ensure this, the upper boundary of the domain has to be located sufficiently far outside the thermal boundary layer for $x = O(b)$. Therefore, h is taken equal to n times the estimated thermal boundary layer thickness, where $n = 1, 2, 3, \ldots$. Further on, it will be shown that for $n \geq 4$ the solution becomes independent of n. Since the thermal boundary layer thickness δ_T depends on the actual shear rate, h depends on S as well. This motivates us to choose h as (note that in the following we use $\sigma\sqrt{2}$ instead of b as characteristic unit of length):

$$h = n\left(\frac{\alpha\sigma\sqrt{2}}{|S|}\right)^{1/3}. \tag{6.11}$$

Hence, in our quasi-steady approximation we solve the problem for each value of S separately, choosing the upper boundary accordingly. The advantage of this S-dependent position of the upper boundary will become clear in the next section. We note that h can become large, i.e. larger than b, for small values of $|S|$, specifically for $|S| < 0.3$ s^{-1}. Then, the thermal energy equation is no longer advection- but diffusion-dominated and in that case δ_T must be taken equal to b. However, for our problem this happens in a very short period of time (less than 0.1% of one period of $S(t)$) and it is therefore not relevant for our solution.

We introduce a new scaling by using the dimensionless variables and parameters:

$$\begin{aligned} \tilde{x} &= \frac{x - x_h}{\sigma\sqrt{2}}, \quad \tilde{y} = \frac{y}{\sigma\sqrt{2}}, \quad \tilde{T}(\tilde{x}, \tilde{y}) = \frac{T(x,y) - T_o}{T_c}, \\ T_c &= \frac{P}{kl\sqrt{\pi}}, \quad \tilde{h} = \frac{h}{\sigma\sqrt{2}}, \quad \tilde{\alpha} = \frac{\alpha}{2\sigma^2 S}, \end{aligned} \tag{6.12}$$

where the temperature scale T_c is based on the heat source term (6.9). We define the Péclet number as

$$Pe = \frac{2\sigma^2 S}{\alpha}, \tag{6.13}$$

hence $\tilde{\alpha}$=1/*Pe*.

Omitting the tildes, the newly scaled system for $T = T(x, y)$ reads

$$\begin{aligned} y\frac{\partial T}{\partial x} &= \alpha\left(\frac{\partial^2 T}{\partial x^2} + \frac{\partial^2 T}{\partial y^2}\right), \quad x \in \mathbb{R},\ 0 \leq y \leq h, \\ T(\pm\infty, y) &= 0, \quad \frac{\partial T}{\partial y}(x, 0) = -e^{-x^2}, \quad T(x, h) = 0, \end{aligned} \tag{6.14}$$

where

$$h = n\alpha^{1/3}, \tag{6.15}$$

with n still to be chosen. Hence, $T(x, y)$ depends on only two parameters, α and n: $T(x, y) = T(x, y; \alpha, n)$. However, if n is taken sufficiently large, i.e. $n \geq 4$, then solution T in a b-environment of the heater becomes independent of n, and α is the only parameter remaining.

6.3 Analytical solution method

To solve the system (6.14) a spectral method is used, which reduces the partial differential equation in (6.14) to a set of ordinary differential equations. To apply this method, we first make the boundary conditions homogeneous, by writing

$$T(x,y) = (h-y)e^{-x^2} + T_1(x,y), \tag{6.16}$$

leaving for T_1 the equation

$$y\frac{\partial T_1}{\partial x} - \alpha\left(\frac{\partial^2 T_1}{\partial x^2} + \frac{\partial^2 T_1}{\partial y^2}\right) = R(x,y)\ , \tag{6.17}$$

with homogeneous boundary conditions and with

$$R(x,y) = (h-y)\,e^{-x^2}\left[2xy + \alpha\left(4x^2-2\right)\right]. \tag{6.18}$$

For the spectral method, we introduce the trial functions $v_k(y)$, given by

$$\frac{\mathrm{d}^2 v_k}{\mathrm{d}y^2} = -\lambda_k^2 v_k, \quad \frac{\mathrm{d}v_k}{\mathrm{d}y}(0) = 0, \quad v_k(h) = 0, \tag{6.19}$$

yielding

$$v_k(y) = \cos(\lambda_k y), \quad \lambda_k = \frac{(2k-1)\pi}{2h}, \quad k = 1, 2, ... \tag{6.20}$$

Here we see the advantage of truncating the infinite half-space to a strip of finite height. Next, we decompose T_1 into a linear combination of the trial functions v_k according to

$$T_1(x,y) = \sum_{k=1}^{\infty} C_k(x)v_k(y) \approx \sum_{k=1}^{K} C_k(x)v_k(y), \tag{6.21}$$

where in the last step we have truncated the series after K terms (as demonstrated in section 6.5, $K = 5$ is more than sufficient for obtaining precise numerical results when the height of the strip is chosen according to the actual shear rate). Substituting (6.16) and (6.21) into (6.14), we obtain

$$\sum_{l=1}^{K}\left[y\frac{\mathrm{d}C_l}{\mathrm{d}x} - \alpha\left(\frac{\mathrm{d}^2 C_l}{\mathrm{d}x^2} - \lambda_l^2 C_l\right)\right] v_l(y) = R(x,y). \tag{6.22}$$

Taking the inner product of (6.22) with functions $v_k(y)$, with the inner product of a function u with v defined as

$$(u,v) \equiv \int_0^h u(y)v(y)\mathrm{d}y,$$

we arrive at an equation for the array $\boldsymbol{C}$, consisting of K elements C_k,

$$h^2\mathbf{W}\frac{\mathrm{d}\boldsymbol{C}}{\mathrm{d}x} - \alpha\frac{h}{2}\left(\frac{\mathrm{d}^2\boldsymbol{C}}{\mathrm{d}x^2} - \mathbf{L}\boldsymbol{C}\right) = \boldsymbol{R}, \tag{6.23}$$

with $\mathbf{W}$ a $K \times K$-matrix with elements W_{kl}, given by (6.24), $\mathbf{L}$ a $K \times K$ diagonal matrix with elements $\Lambda_{kk} = \lambda_k^2$ and $\boldsymbol{R}$ a K-array with elements R_k, given by (6.25):

$$W_{kl} = \frac{1}{h^2}\int_0^h y v_k(y) v_l(y) dy = \int_0^1 \hat{y} v_k(h\hat{y}) v_l(h\hat{y}) d\hat{y}, \tag{6.24}$$

$$R_k(x) = \int_0^h R(x,y) v_k(y) dy. \tag{6.25}$$

We introduce the Fourier transform of $\boldsymbol{C}(x)$ by

$$\boldsymbol{c}(\zeta) = \frac{1}{\sqrt{2\pi}}\int_{-\infty}^{\infty} \boldsymbol{C}(x) e^{-i\zeta x} dx = \mathscr{F}\{\boldsymbol{C};\zeta\}. \tag{6.26}$$

By taking the Fourier transform of (6.23), after dividing it by $\alpha h/2$, we obtain the algebraic equation for $\boldsymbol{c}$:

$$\left(\zeta^2\mathbf{I} + i\zeta\frac{2h}{\alpha}\mathbf{W} + \mathbf{L}\right)\boldsymbol{c}(\zeta) = \mathbf{M}(\zeta)\boldsymbol{c}(\zeta) = \boldsymbol{r}(\zeta), \tag{6.27}$$

with $\mathbf{I}$ the unity $K \times K$-matrix, and

$$\mathbf{M}(\zeta) = \zeta^2\mathbf{I} + i\zeta\frac{2h}{\alpha}\mathbf{W} + \mathbf{L}, \tag{6.28}$$

$$\boldsymbol{r}(\zeta) = \mathscr{F}\{\frac{2}{\alpha h}\boldsymbol{R};\zeta\}. \tag{6.29}$$

We can, using Mathematica 6 (Wolfram Research, Champaign, IL), invert the $K \times K$-matrix $\mathbf{M}$ analytically, by which we find

$$\boldsymbol{c}(\zeta) = \mathbf{M}^{-1}(\zeta)\boldsymbol{r}(\zeta), \tag{6.30}$$

and by taking the inverse Fourier transform of this result, we obtain the solution for the array $\boldsymbol{C}(x)$ as

$$\boldsymbol{C}(x) = \frac{1}{\sqrt{2\pi}}\int_{-\infty}^{\infty} \boldsymbol{c}(\zeta) e^{i\zeta x} d\zeta = \frac{1}{\sqrt{2\pi}}\int_{-\infty}^{\infty} \mathbf{M}^{-1}(\zeta)\boldsymbol{r}(\zeta) e^{i\zeta x} d\zeta\ . \tag{6.31}$$

The latter integral is evaluated numerically using Mathematica 6. The temperature T is now determined by (6.16) and (6.21) with $K = 5$ and $n = 4$.

6.4 Experimental methods

In the experimental set-up, the device was mounted to the inner wall of a tube with an inner diameter of 5 mm (see Figure 6.1 (*b*)). The tube was made of PMMA, which is an insulating material, to prevent heat loss through the back of the device. The device covered about half of the tube perimeter. The polyimide foil including the sensor components has a thickness of only 10 μm (see Figure 6.1 (*a*)), and since the very small step it causes in the tube wall is located about 2 mm away from the actual sensor components (on both sides) this does not significantly disturb the flow pattern near the sensor. In all experiments, the heater was supplied with a power of 80 mW by a voltage source (EST 150, Delta Elektronika, Zierikzee, The Netherlands). Two multimeters (DMM 2000, Keithley Instruments Inc, Cleveland, USA) were used to register the output of the thermopiles that measure T_d-T_u and T_h-T_f.

To ensure fully developed flow over the sensor, the measurement section was located 112 tube diameters from the tube entrance, which is, even at the highest Reynolds number reached (≈ 500), well beyond the laminar entrance region. As test fluid, tap water at room temperature was used. Steady flow through the set-up was generated by a stationary pump (Libel-Project, Alkmaar, The Netherlands). The amount of flow could be adjusted using a clamp. The oscillatory component was added to the mean flow by a piston pump, driven by a computer-controlled motor (ETB32, Parker Hannifin, Offenburg, Germany). Downstream of the sensor, the flow was registered by an ultrasonic flow probe (4PSB, Transonic Systems Inc, Ithaca, NY), which was used as a reference. The signals from the flow probe and the multimeters were recorded simultaneously and transferred to a computer via an acquisition board with a sampling frequency of 20 Hz.

The output voltage of a thermopile is proportional to the temperature difference between its ends via the Seebeck coefficient, which depends on the composition of the thermocouple leads (van Herwaarden et al., 1989). By scaling the stationary sensor response T_h-T_f at $S = 115$ s^{-1} to the analytical value at this shear rate, we found the Seebeck coefficient for the thermocouples in our sensor to be 305 μVK^{-1}. This Seebeck coefficient, which is only a scaling value for the experimental data and does not influence the shape of the responses, is used for all experimental results shown in section 6.5.

Experiments in both steady and unsteady flow conditions were performed. In steady flow, the Péclet number (see (6.13)) was varied from 0 (at zero flow; $S = 0$ s^{-1}) to 34 (at a flow of 368 ml min^{-1}; $S = 500$ s^{-1}). The shear rate at the sensor surface was calculated from the flow measured by the ultrasonic probe assuming a Poiseuille velocity profile.

For the unsteady case the Strouhal number (see (6.8)) was varied from 0.01 to 0.1 by varying the oscillation frequency from 0.2 to 2 Hz, and the amplitude (β) was varied between 0.8 and 1.2 (corresponding to the expected coronary flow regime), keeping the mean shear rate constant at about 115 s^{-1}. In unsteady flow, the shear rate was derived from the flow measurements assuming a Womersley velocity profile (Womersley, 1955).

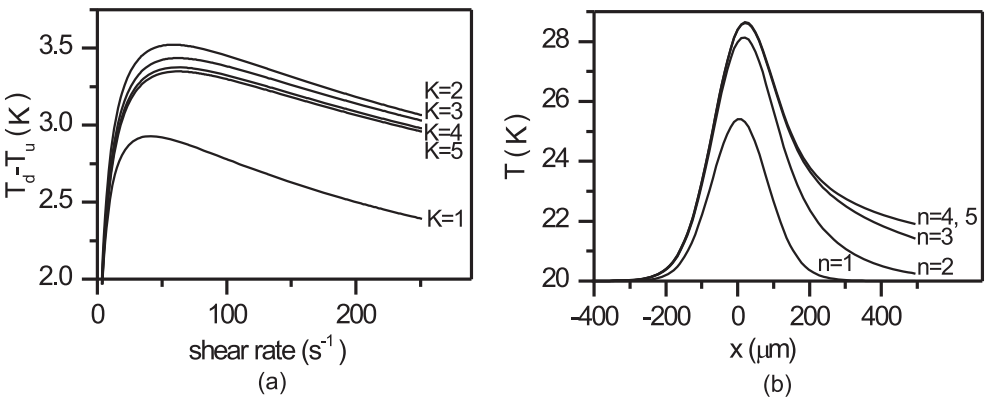

Figure 6.3: *The influence of the number of cosine-terms K on the solution T_d-T_u* ***(a)*** *and parameter n on the solution T at $y = 0$, $S = 100\ s^{-1}$* ***(b)****.*

6.5 Results and discussion

The cosine-series used in (6.21) converged quite rapidly. Only five terms sufficed for an accurate approximation of the solution; see Figure 6.3 (a). The rapid convergence is a consequence of the dependence of h on the actual shear rate S; if h would have been fixed for all S, it could become much larger than the boundary-layer thickness, leading to slow convergence of the cosine series. The parameter n (see (6.15)) was chosen such that the position of the boundary condition did not influence the solution at the sensor surface in a b-environment of the heater; $n = 4$ was found to be large enough to ensure this, as demonstrated in Figure 6.3 (b).

In Figure 6.4 (a), the theoretical temperature profiles over the sensor surface are depicted for different shear rates (hence different *Pe*-values). At low shear rates (low *Pe*), the temperature distribution is more symmetric with respect to the heater center, since in that case conduction is dominating the heat-transfer process. As the shear rate increases the temperature distribution becomes asymmetric, because more heat is advected downstream, while the overall sensor temperature decreases because of the augmented advective cooling.

The experimental data obtained in steady flow are plotted together with the theoretically predicted sensor output in Figure 6.4 (b–d). The results of two separate experiments are shown to give an indication of the data spreading, where each data point represents the average result of 20 s of measurement with a sampling frequency of 20 Hz (i.e. 400 samples). Both the experimental and analytical curves show a steep decline in the relative heater temperature T_h-T_f at low shear rates, and a more gradual one at higher shear rates. Sensor output T_d-T_u is in both model and experiment characterized by a steep increase at low shear rates, followed by a maximum and a decline; see Figure 6.4 (c). These features were also found by Lammerink et al. (1993) and Nguyen and Kiehnscherf (1995). With increasing shear rate, the (T_d-T_u)-temperature difference rises because of augmented advection of heat in downstream direction. At the same time the overall sensor temperature

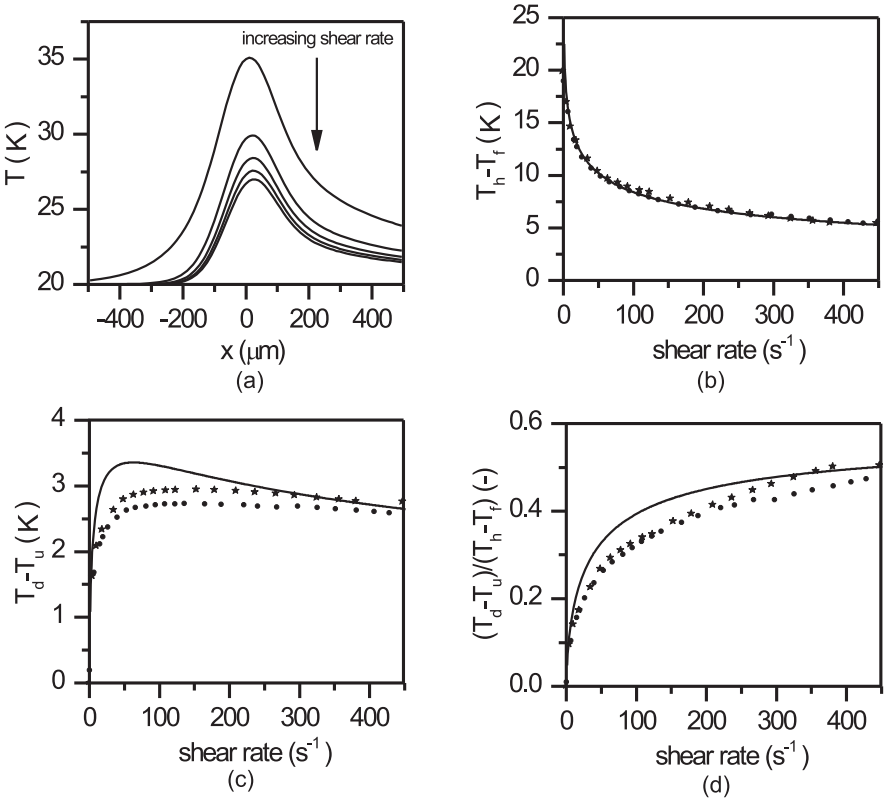

Figure 6.4: *Analytical (—) and experimental (• • •, ⋆ ⋆ ⋆) results in steady flow. The analytical temperature profiles at the sensor surface at S =10, 60, 110, 160, 210 s^{-1}* ***(a)****, the response of the thermopile measuring T_h-T_f* ***(b)*** *and T_d-T_u* ***(c)****, and the ratio of thermopile outputs* ***(d)****.*

decreases (see also Figure 6.4 (a)), hence, a maximum in T_d-T_u is observed. The maximum deviations between model and experiment ranged from 5% for the (T_h-T_f)-signal to 27% for T_d-T_u. Although also measurement inaccuracies may play a role, the discrepancy between theory and experiment is most likely due to the simplified modeling of the substrate: the Gaussian heat-flux distribution is only a rough approximation, since the heat transfer from the substrate to the fluid will be larger upstream than downstream, due to the hot thermal wake. Furthermore, the influence of conduction in the substrate decreases with increasing wall shear rate (Tardu and Pham, 2005). To obtain an invertible relation between the sensor output and the shear rate or Péclet number, the ratio of thermopile outputs, (T_d-T_u)/(T_h-T_f), can be used; see Figure 6.4 (d). Note that this curve is independent of the thermopile calibration, because the Seebeck coefficient is equal for both thermopiles and vanishes when the ratio of outputs is used. From Figure 6.4 it appears that the sensor is most sensitive to lower shear rates. The performance of the sensor at higher shear rates, important for the eventual application of the sensor in coronary

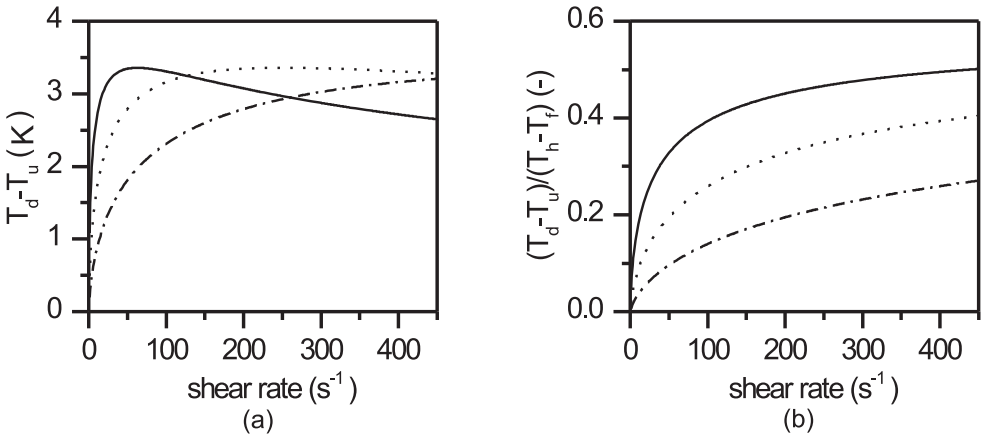

Figure 6.5: *Theoretical results with the original heater width (—), 50% (· · ·), and 25% (- · -) of the original width for T_d-T_u* ***(a)*** *and (T_d-T_u)/(T_h-T_f)* ***(b)****.*

flow, can be improved by decreasing the heater width b, thereby reducing *Pe*. When the heater width $b = 2\sigma$ is decreased, the distance to the heater center of the thermopile measuring T_d-T_u must be reduced by an equal amount, to keep the same relative positions. The theoretical results for decreasing the heater width by 50% and 25% are shown in Figure 6.5. A smaller heater leads to a shift in the maximum temperature difference T_d-T_u, resulting in a more linear relation between the shear rate and the ratio of thermocouple outputs, with a lower sensitivity for lower, and a higher sensitivity for higher shear rates compared to the original response. From Figure 6.5 (*a*) we conclude that the effective heater width has a large influence on the (T_d-T_u)-signal. This could also be an explanation for the discrepancy between theory and experiment shown in Figure 6.4 (*c*); if the effective heater width in the experiment is somewhat smaller than the theoretically used value, this will shift the maximum in the (T_d-T_u)-curve to higher shear rates. The difficulty here is that the effective heater width will depend on the actual shear rate (i.e. the relative influence of conduction in the substrate), making b a function of S. The actual effective heater width can therefore only be obtained by solving the conjugate heat-transfer problem. The sensor response to unsteady flow was investigated experimentally by varying the oscillation frequency, and thereby the Strouhal number, and amplitude in the estimated physiological regime. At each amplitude and frequency, the dynamic sensor response was measured during at least 5 flow cycles; here two periods of each signal are shown. In Figure 6.6 the experimental results for non-reversing shear rates at four *Sr*-values are depicted, together with the quasi-steady analytical solution. The shear rate signals calculated from the flow measurements are aligned, to ensure that the phase differences observed in the thermopile signals are due to thermal unsteady effects, and not to phase differences between the flow and the shear rate. Owing to limitations of the pump, the 2 Hz (*Sr*=0.1) flow signal was not purely sinusoidal, which also shows in the sensor response.

We observe a phase shift and decrease in amplitude with increasing Strouhal

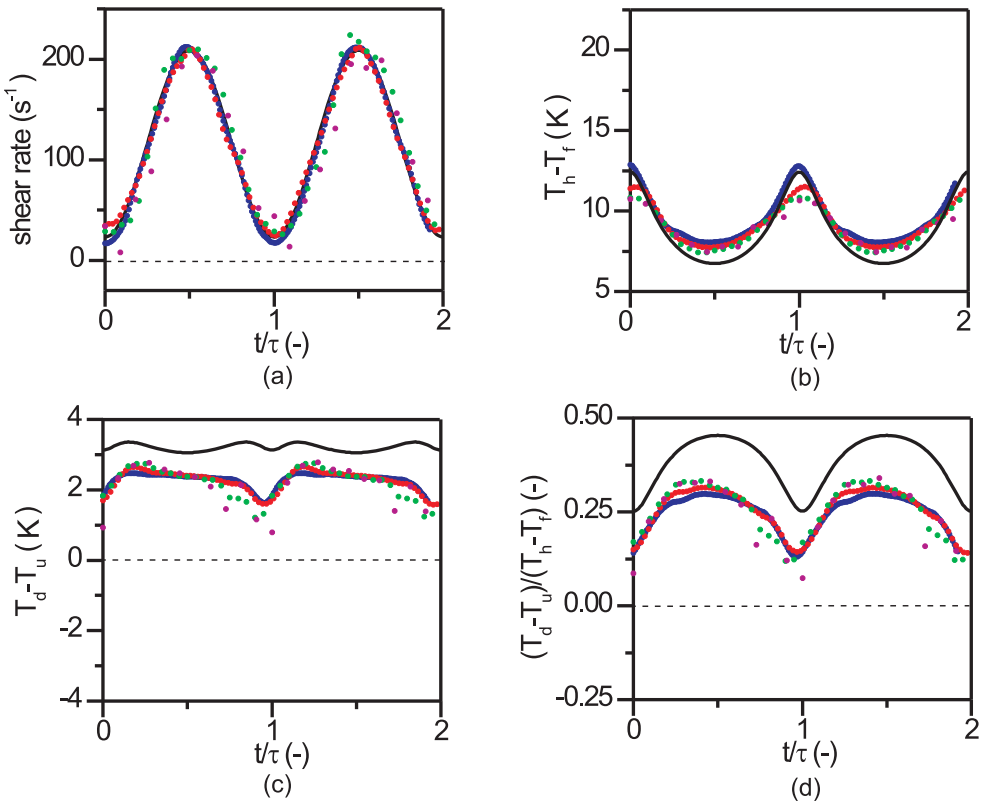

Figure 6.6: *Results in unsteady flow for $\beta = 0.8$, with τ being the period of a flow cycle; analytical (——) and experimental (• • •) curves for Sr=0.01 (**blue**), Sr=0.03 (**red**), Sr=0.06 (**green**), and Sr=0.1 (**magenta**). The shear rate at the sensor surface obtained from the Womersley approximation of the measured flow **(a)**, the response of thermopile measuring T_h-T_f **(b)** and T_d-T_u **(c)**, and the ratio of thermopile outputs **(d)**.*

number in the (T_h-T_f)-signal. The (T_d-T_u)-thermopile output also shows this phase shift, together with a slight change in the signal shape. As *Sr* increases, the shear rate oscillations become too fast for the thermal boundary layer to react instantaneously, and the sensor response starts to deviate from its quasi-steady behaviour, and hence from the analytical solution. The deviation between the signals with $Sr = 0.01$ and $Sr = 0.1$ is larger (17% in T_h-T_f) during minimum shear rate, when unsteady effects are most important, than during maximum shear rate (6%), when advection dominates. Not only during minimum shear rate, but during the complete deceleration phase the spreading between the different *Sr*-curves is somewhat larger. Nevertheless, the quasi-steady analytical solution appears to describe the sensor response quite well in the complete experimental range, up to $Sr = 0.1$, with again larger quantitative differences in the (T_d-T_u)-signal than the (T_h-T_f)-signal. In the coronary flow regime, with Strouhal numbers of about 0.01 for the

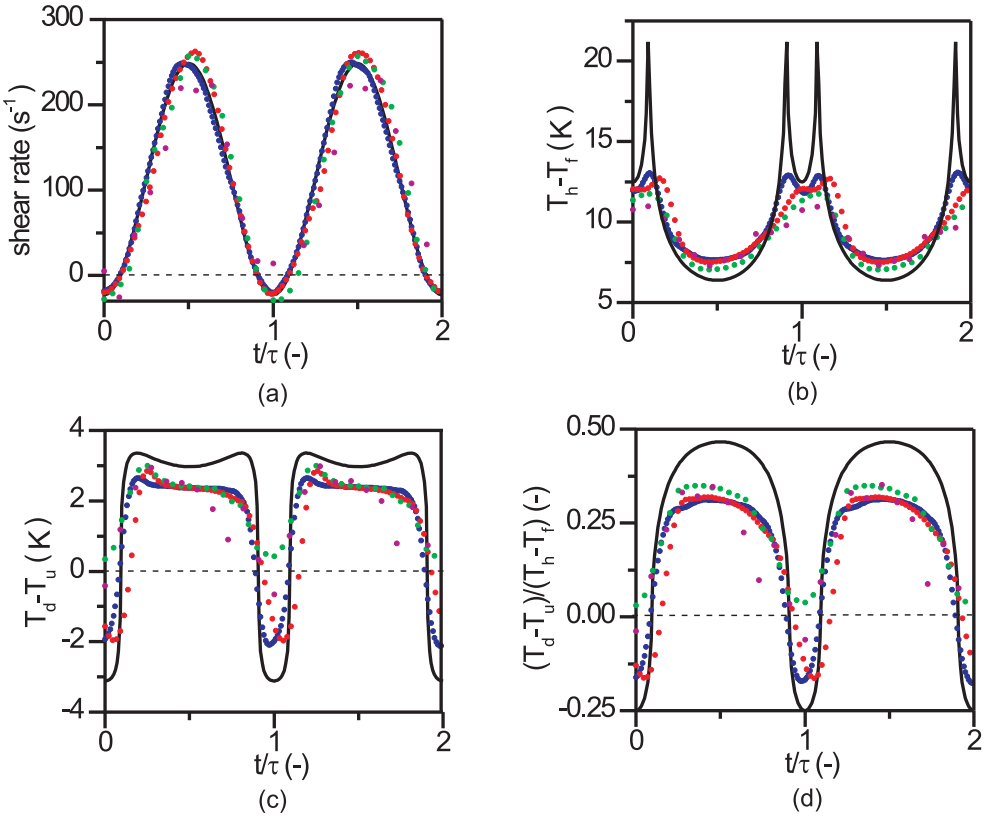

Figure 6.7: *See Figure 6.6, with* $\beta = 1.2$.

first harmonic, a quasi-steady sensor response is therefore expected. In their studies with hot-film anemometers and electrochemical wall-shear probes, respectively, Clark (1974) and Van Steenhoven and van de Beucken (1991) found the quasi-steady regime to hold for *Sr* up to 0.2. For $\beta = 1.2$, larger deviations between the sensor response for *Sr* $= 0.01$ and *Sr* $= 0.1$ have been found during the reversal period and the deceleration phase; see Figure 6.7. A sign change in T_d-T_u, indicating shear rate reversal, was clearly observed for the two lowest *Sr*-values. During the reversal period, hot fluid from the thermal wake is carried back over the sensor, which is not taken into account in the analytical model and leads to further deviations from the quasi-steady response. As the shear rate approaches zero, the heat is carried away from the heater only very slowly, leading to large heater temperatures in the quasi-steady analytical solution, while T_d-T_u, and therefore also $(T_d$-$T_u)/(T_h$-$T_f)$, tend to zero, due to the symmetric influence of conduction. In the experimental data such large relative heater temperatures are never reached because it takes time to heat the fluid, due to its finite thermal diffusivity. Hence, only during the very short period of time where S is close to zero, larger deviations from the quasi-steady solution are observed in the $(T_h$-$T_f)$-signals.

6.6 Conclusion

An analytical model describing the response of a miniature calorimetric sensor to both steady and pulsatile tube flow is developed. In experiments the sensor is subjected to a flow to verify the theoretical predictions. Steady flow analytical and experimental results are in good agreement for the complete range of Péclet numbers studied. Hence, our two-dimensional model with the shear rate at the sensor surface as the only flow parameter is sufficient for examining the steady sensor behaviour. Only a simplified model of the substrate in which the sensor is embedded was taken into account, by means of a heat-flux boundary condition. A conjugate approach will lead to a more accurate quantitative prediction of the temperature differences measured, however, our model has the advantage of a simple representation of the substrate, and still leads to an acceptable description of the sensor response.

The quasi-steady analytical model predicts the sensor behaviour in non-reversing pulsatile flow with Strouhal numbers up to 0.1 quite well. Based on the experimental results, we conclude that the sensor response to coronary flow will be quasi-steady, except during the (short) periods of shear rate reversal. The analytical model can therefore be used to optimize the sensor design for coronary flow measurements, as demonstrated in Figure 6.5.

Author contributions

The research described in this chapter was performed as part of the MSc-project of Hanneke Gelderblom, which was published in *J Fluid Mech*, **666**,428–444,2011 and supervised by the author of this thesis. The development of the analytical model has taken place in close collaboration with Fons van de Ven from the department of Mathematics and Computer Science, Eindhoven University of Technology.

Performed experiments: H. Gelderblom, A.A. van de Ven, A. van der Horst
Data analysis: H. Gelderblom, A.A. van de Ven, A. van der Horst
Interpretation of results: all
Prepared figures: H. Gelderblom, A. van der Horst
Drafted manuscript: H. Gelderblom
Edited and revised manuscript: all
Approved final version of manuscript: all

Chapter 7

Optimization of the design and operation of a miniature thermal sensor for coronary flow assessment

In the previous chapter, a new miniature calorimetric sensor, intended to be used on a guidewire to measure coronary flow, was analytically and experimentally characterized. It consisted of thermocouples to measure temperature differences over a heater, operated at constant power. It was found that the sensor was able to assess the applied non-stationary shear rates, however, the sensitivity at (high) physiological coronary shear rates was limited. In the first part of this chapter, it is investigated whether operating the heater at constant temperature is feasible and whether it improves the response at high shear rates. A numerical model was developed, to compare constant temperature with constant power operation of the heater. To validate the numerical results, experiments were performed where similar devices as presented in chapter 6 were subjected to steady flow. In the second part, the numerical model was used to optimize the sensor response in non-stationary flow, taking into account extra limitations on the design, dictated by the fabrication and mounting process of the devices. From the experiments it was found that the heaters could be operated at constant temperature via a feedback controlled Wheatstone bridge. The results from the numerical model qualitatively agreed with the experiments, indicating that the numerical model can be used to optimize the sensor design. The optimization study indicated that the optimal way of controlling the heater was by keeping the surface temperature constant. Within the imposed limitations, an optimal design was proposed and it was shown that coronary representative shear rates could be assessed by the sensor.

Arjen van der Horst, Dennis D. van der Voort, Marcel C.M. Rutten, and Frans N. van de Vosse, Optimization of the design and operation of a miniature thermal sensor for coronary flow assessment.

7.1 Introduction

Coronary pressure and flow data are necessary for a proper diagnosis of coronary circulatory disease. While pressure assessment via sensor-tipped guidewires is relatively easy, the assessment of flow is complicated due to the radial dependence of the blood velocity. The most common method for coronary flow assessment uses a Doppler-crystal mounted on a guidewire (ComboWireXT, Volcano, San Diego, CA) to measure the blood velocity. However, to determine the flow, a certain velocity profile has to be assumed and the dependence of the signal on the radial location can make it difficult to obtain adequate signals. Another method that enables the assessment of coronary flow, without assuming a certain velocity profile, utilizes the principle of continuous thermodilution (van 't Veer et al., 2009; Aarnoudse et al., 2007). With this technique, however, only the average flow is measured, whereas the dynamic pattern has also been indicated to be valuable (Kern, 1992; Kern et al., 1994; Davies et al., 2006a; Escaned et al., 2009). By combining the thermodilution method with a method that operates a pressure-sensing guidewire as a constant temperature anemometer, the dynamics of coronary representing flows could be measured in an *in-vitro* environment (chapter 5). Drawbacks of this methodology is that a relatively high overheat temperature of 20 K is required to obtain reproducible results and, due to the anemometric approach, local shear rate reversal could not be detected, resulting in poor signals for flows approaching zero.

In chapter 6 (Gelderblom et al., 2011), a new calorimetric sensor, intended to be mounted on a guidewire, was characterized. The sensor was located on a chip embedded in polyimide, to enable it to be bent around a guidewire. It consisted of an aluminium heater, operated at constant power, and two thermopiles to measure flow induced temperature differences. From analytical modeling and experimental characterization it was shown that the device was able to assess non-stationary shear rates, even with shear rate reversal. Using the analytical model, it was shown that the sensor response could be optimized by decreasing the size of the heater, linearizing the relation between the output signal and the shear rate. However, the overall sensitivity of the sensor in the physiological shear rate range was quite limited and, due to the constant power operation, the heater temperature can increase significantly in the case of stagnant flow.

In theory, both drawbacks might be resolved by operating the heater at constant temperature instead of constant power. This prevents high temperatures at very low shear rates, while increasing the sensitivity at high shear rates (Ricolfi and Scholz, 1990). The first aim of this study is therefore to investigate the feasibility of operating the sensor at constant temperature and to compare it to constant power operation. Hereto, a two-dimensional (2D) numerical model, representing the fluid domain and the different device elements is developed, to compare the power supplied to the heater and thermocouple output signals. To investigate the feasibility of operating the sensor at constant temperature and to validate the results obtained from the numerical study, *in-vitro* experiments are performed with similar devices as in chapter 6. A part of a glass wafer with the devices is incorporated into a set-up and subjected to steady flow. The devices are kept on the wafer, instead of being mounted in a

tube (chapter 6), to prevent crack formation in the device components due to the mounting process.

In the second part we take the extra conditions required to mount the flexible device to a guidewire into account. For example, the heater needs to be located at the mechanical neutral line of the sensor, to prevent crack formation during the bending of the device around the thin guidewire (Vieira da Silva et al., 2010). Furthermore, there are restrictions on the axial length of the device and the maximum electrical power that can be supplied. Within these boundary conditions the numerical model is used to investigate the effect of changing the sizes of the individual sensor components as well as different ways of controlling the heater. Based on the results of this study, an optimal sensor design is proposed to be manufactured and tested in further research.

7.2 Materials and methods

A top view of the device available for experimental testing is shown in Figure 7.1a. It consists of two parallel aluminium heaters with a length of 6.3 mm and a width of 50 μm. The space between the two heaters is 40 μm. Temperature differences between downstream (T_d) and upstream (T_u) positions are measured 100 μm from the center of the two heaters, as well as the heater temperature (T_h) with respect to the ambient fluid temperature (T_f), measured 2000 μm upstream. The thermocouples are formed by n- and p-type polysilicon strips, separated by an oxide layer. At the end of the strips contact holes are etched in the oxide and filled with aluminium to make a junction between the two legs of the thermocouple. Six compartments, with each 10 (T_h-T_f)-thermocouples and 20 (T_d-T_u)-thermocouples, are connected in series to increase the signal output.

In the experimental characterization described in chapter 6, it was found that mounting the device into a tube was very difficult. Since we only want to investigate the feasibility of operating the sensor at constant temperature, the sensor was subjected to steady flow, while still on the wafer (flat plate).

7.2.1 Steady flow experiment

Similar to chapters 4 and 5, the control of the temperature of the heater is accomplished via a feed-back controlled Wheatstone bridge (see Fig. 7.1b). Besides the heater (R_H), the electronic circuit consists of a potentiometer (R_T), an operational amplifier, a capacitor C_{B1}=47 nF, and two fixed resistors, which are approximately equal (R_{B1}=R_{B2}=320 Ω). The operational amplifier minimizes the difference between V_T and V_H, which means that R_H is heated until its resistance is equal to R_T. Hence, by setting R_T to the correct value, the temperature of the heater can be controlled. By changing the switch, the heater can also be operated in constant power mode using a voltage source (ES 030-5, Delta Elektronika B.V., Zierikzee, The Netherlands) and a potentiometer R.

The temperature-resistance relation is required, to be able to use the electronic

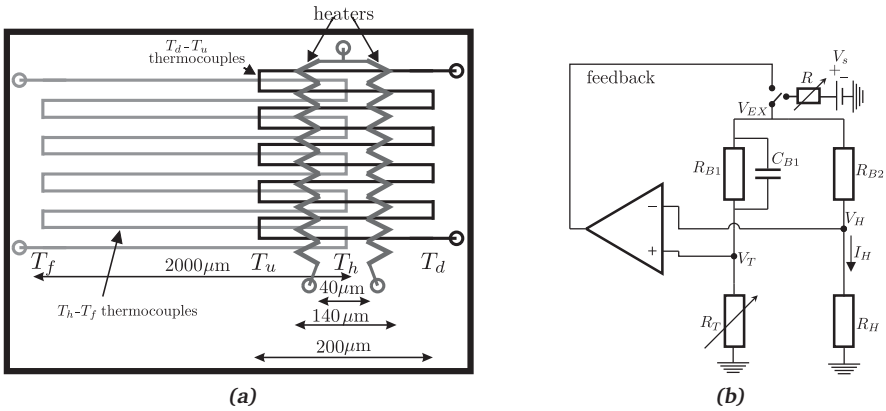

Figure 7.1: ***a)*** *A top view of the different elements of the device. The main flow direction is from left to right.* ***b)*** *A schematic overview of the electronic circuit to control the heater at constant temperature or constant power.*

circuit to heat R_H to the desired temperature. This relation can be approximated by:

$$R(T) = R(T_0)(1 + \alpha(T - T_0)) \ , \tag{7.1}$$

with $R(T_0)$ the resistance at temperature T_0 and α the temperature coefficient, which is a physical property of the material, being 3.9 mK^{-1} for aluminium (Nicholas and White, 2001). Here, it is assumed that α is constant, which is generally not the case. For metals like aluminium, however, this approximation holds for temperatures close to room temperature. To check if the theoretical value of α holds for the heaters, the temperature-resistance relation is characterized using a temperature controlled wafer testing device (490, QuietCHUCK, MDC, Chatsworth, CA).

Once the resistance-temperature relation is known, the sensor response can be tested in the experimental set-up shown in Figure 7.2. A rectangular duct, with a height and width of 0.8 and 10 mm, respectively, is glued onto the glass wafer containing the chips. This forms a channel which enables the application of shear rates to the sensors. Steady flow is attained by using an overflow bath and a pump (VERDER, Vleuten, The Netherlands). The height of the water will remain constant, which gives a steady pressure gradient and therefore a steady flow through the channel, which can be controlled by a clamp located upstream of the sensor. To measure the flow, a measuring cup on a weighing scale catches the fluid coming from the channel. By measuring the rate at which the weight increases the flow is determined. The temperature of the heater is controlled by the electronic control system described above. The voltage difference over the two thermopiles, heater, and R_{B2}, is recorded simultaneously using an acquisition board (PCI-6281 DAQ card, National Instruments, Austin, Texas).

The flow (Q) - shear rate (S) relation at the bottom of a rectangular duct of width b and height h is given by Shah and London (1978):

$$S = KQ \ , \text{ with } K = \frac{C_S}{bhC_Q} \ . \tag{7.2}$$

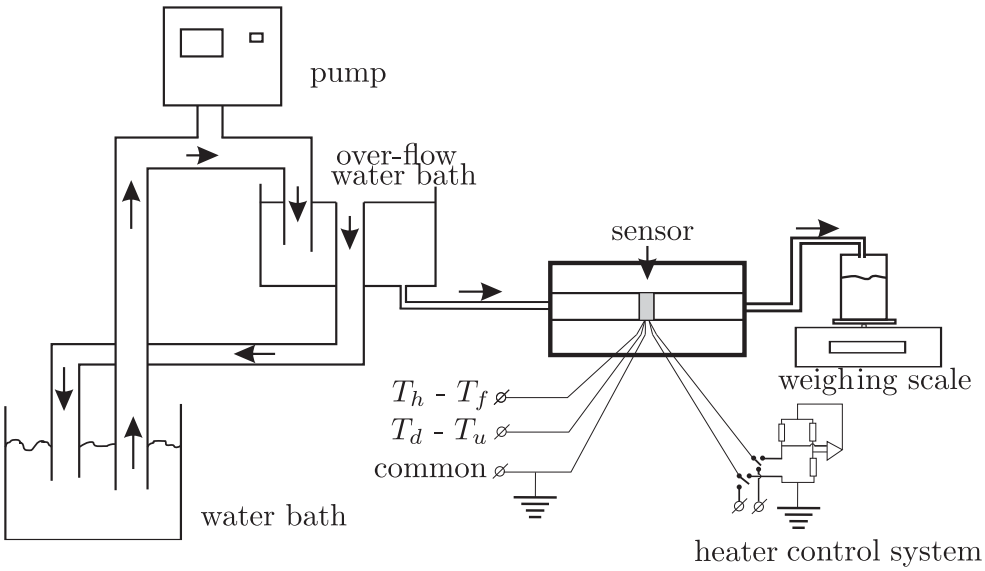

Figure 7.2: *Schematic overview of the experimental set-up used to test the sensor. The sensor is aligned perpendicular to the flow of a rectangular duct channel.*

The constants are defined as:

$$C_Q = \frac{-b^2}{12}\left[1 - \frac{192}{\pi^5}\frac{b}{h}\sum_{n=1,3,..}^{\infty}\frac{1}{n^5}\tanh\left(\frac{n\pi h}{2b}\right)\right] , \tag{7.3}$$

$$C_S = \frac{-4b}{\pi^2}\sum_{n=1,3,..}^{\infty}\frac{1}{n^2}(-1)^{\frac{n-1}{2}}\tanh\left(\frac{n\pi h}{2b}\right) . \tag{7.4}$$

For the dimensions of the channel set-up (b = 10 mm, h = 0.8 mm), the constant K is 1.015 mm^{-3}.

The different experiments performed with this set-up are explained in section 7.2.5.

7.2.2 Computational domain

The computational domain of the 2D finite element model, representing the device that is available for experimental testing, is shown in Figure 7.3. It consists of all important sensor components as well as the glass substrate and the applied water flow. On the boundaries of the domain an insulation boundary condition is prescribed, except for the boundary at the top of the fluid compartment, where the temperature is set to the ambient flow temperature. We chose to include only a simplified representation of the sensor, consisting of only one aluminium heater with dimensions (140×0.5)μm, polysilicon thermopiles with dimensions (2000×0.5)μm

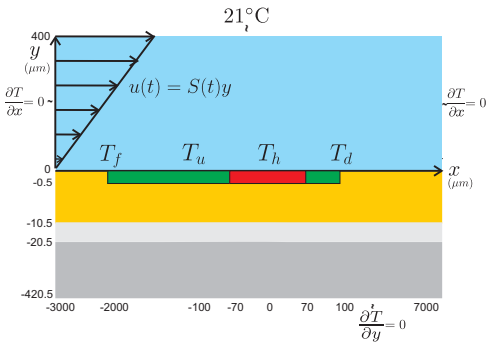

Material	color	k [W/mK]
water	blue	0.61
aluminium	red	237
polysilicon	green	46
polyimide	yellow	0.12
glue	light gray	0.10
glass	gray	1.4

Figure 7.3: *Schematic overview of the computational domain. The arrows represent the flow velocity. The thermal conductivity of the different components are listed in the table.*

and (30×0.5)μm, a 10 μm thick polyimide layer, and a 10 and 400 μm thick layer of glue and glass, respectively. Inclusion of all the other material layers would have resulted in a very complicated mesh, and since these layers are very thin, they are assumed to have a minor influence on the results. The size of the fluid compartment of the computational domain is 10000 μm in x, and 400 μm in y-direction. In the table accompanying Figure 7.3, the thermal conductivities of the different materials are listed. The density and specific heat of water at approximately 20°C are 1000 kg m^{-3} and 4.18 kJ kg^{-1} K^{-1}, respectively. The heater element contains the smallest mesh surface elements (2×0.1)μm. To limited the number of mesh elements, starting at the edge of the heater element, the mesh size is incrementally increased by a factor 1.05, in all directions.

7.2.3 Numerical model

Compared to the analytical model, described in chapter 6, the finite element method allows us to simultaneously solve the equations describing heat balance in both the sensor itself and in the fluid, instead of describing the sensor with a gaussian shaped heat flux. Since this model will also be used in the optimization study, with the sensor subjected to non-stationary shear rates, the equations are derived including time dependency. The equation for the fluid compartment is given by:

$$\frac{\partial T}{\partial t} + S(t)y\frac{\partial T}{\partial x} = \frac{k}{\rho c_p}\nabla^2 T, \tag{7.5}$$

with t the time, T the temperature, k the thermal conductivity, ρ the density, c_p the heat capacity, and the applied shear rate function $S(t)$ is defined as:

$$S(t) = S_0\left(1 + \beta\sin\left(\omega t\right)\right) \ . \tag{7.6}$$

Here, S_0 is the average shear rate, β the relative amplitude, and ω the angular frequency. In the sensor material, heat transfer occurs solely through conduction and

if the heater is operated at constant power, the energy equation reduces to (Incropera et al., 2007, p. 72):

$$\rho c_p \frac{\partial T}{\partial t} = k\nabla^2 T + q''' \ , \tag{7.7}$$

with heat source term q''' being zero everywhere except in the heater compartment. In case the temperature of the heater is controlled, the temperature in the total heater compartment is prescribed and set at a constant temperature.

Discretization

The partial differential equations in (7.5) and (7.7) are spatially discretized according to a standard finite element procedure (Zienkiewicz and Taylor, 1989, chap. 9). Assembling all element contributions into a global set of equations results in:

$$\mathbf{M}\frac{d\underline{T}}{dt} + \mathbf{S}\underline{T} = \underline{f}, \tag{7.8}$$

with $\mathbf{M}$ the mass matrix resulting from the non-stationary term and $\mathbf{S}$ the stiffness matrix resulting from the conduction and advection terms. The matrices are approximated by means of numerical integration, using a Gaussian integration rule (Zienkiewicz and Taylor, 1989, p.171).

For the temporal discretization an Euler implicit scheme is used. This results in

$$\mathbf{M}\frac{\underline{T}_{n+1} - \underline{T}_n}{\Delta t} + \mathbf{S}\underline{T}_{n+1} = \underline{f}_{n+1}, \tag{7.9}$$

or

$$\left(\frac{1}{\Delta t}\mathbf{M} + \mathbf{S}\right)\underline{T}_{n+1} = \underline{f}_{n+1} + \frac{1}{\Delta t}\mathbf{M}\underline{T}_n. \tag{7.10}$$

The final set of equations in (7.10) is solved using a direct profile solver (Segal, 1993), as implemented in the finite element package Sepran (Ingenieursbureau SEPRA, Leidschendam, The Netherlands).

7.2.4 Optimization of the sensor design

The flexible polyimide chip is intended to be bent around a standard guidewire to measure coronary flow (see Fig. 7.4). Because the sensor is only capable of assessing the shear rate at the sensor surface, the sensor output will depend on the radial position of the guidewire inside an artery. To be able to detect this radial position, the chip will contain three sensors, with a length of 250 μm, on the perimeter of the guidewire.

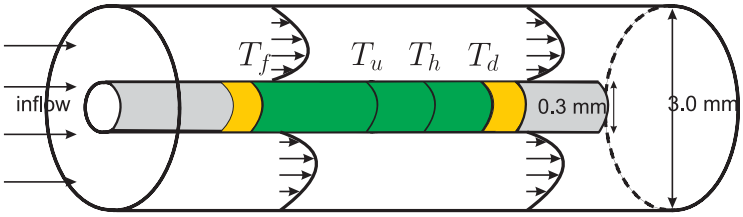

Figure 7.4: *The sensor on a guidewire inside an artery.*

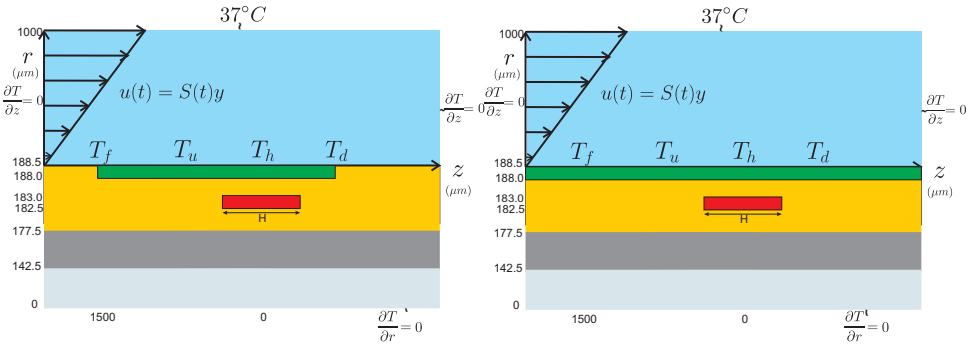

Figure 7.5: ***a)*** *A cross-section of the sensor with the thermocouples (green) at the surface and the heater (red) in the center.* ***b)*** *The mesh used in the numerical problem, with the thermocouple material covering the entire surface. The colors represent the different materials, which are listed in Table 7.1, together with their properties.*

For optimizing the design of the sensor, we have to take several limitations into account. First of all, to prevent the damage to the blood proteins, the surface temperature of the chip may not be much larger than 42°C. Second, to prevent crack formation in the heater during bending, the heater needs to be located in the mechanical neutral line (in this case, the center) of the polyimide layer. Third, to not impair the flexibility of the guidewire, the total length of the sensor may not exceed 1.5 mm in the axial direction. Finally, the total power that can be put into the heater is limited to approximately 12 mW for a single heater with a length of 250 μm.

Within these limitations, the design and control of the sensor is investigated with a 2D axisymmetric numerical model based on the model described in section 7.2.3. The basic design of the computational domain is shown in Figure 7.5a. Compared to Figure 7.3 the heater is now in the center of the chip and the guidewire, represented by a stainless steel tube with air inside, is included. For practical reasons, the simplified representation shown in Figure 7.5b is used in this study. Preliminary research has shown that this simplification does not significantly alter the output signals.

Figure 7.6 shows an example of the shear rate at the sensor surface of a guidewire

in a left anterior descending coronary artery at an average flow rate of 250 ml/min, with the typical periods of negative shear rates during early systole. Since it likely that the sensor will perform better at low frequencies, this shear rate with a relatively high heart rate of 120 beats per minute (BPM) is used as a starting point to test and optimize the design of the sensor.

Table 7.1: *The properties of different materials shown in Figure 7.5.*

Material	color	thermal conductivity [W/mK]	density [kg/m^3]	heat capacity [J/kgK]
blood	blue	0.55	1050	3600
aluminium	red	237	2700	903
polysilicon	green	46	2330	712
polyimide	yellow	0.12	1420	1090
stainless steel	gray	15	782	420
air	light blue	0.027	1	1005

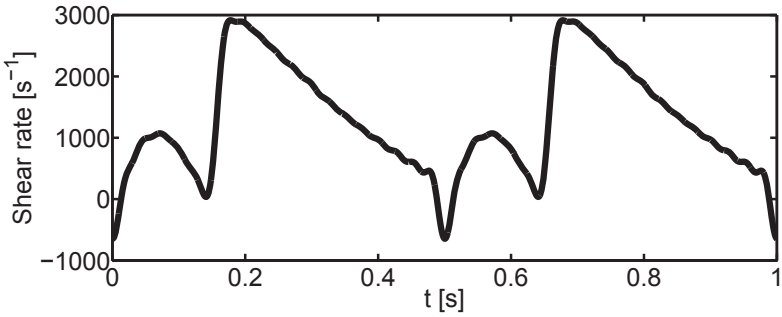

Figure 7.6: *A typical shear rate profile at the guidewire surface in a left anterior descending coronary artery.*

7.2.5 Experiments, simulations, and data analysis

Steady flow experiments

First, the resistance-temperature relation of the heaters was measured with the temperature controlled wafer testing device over a range of 30-70°C. From the slope of this relation the temperature coefficient α was determined using (7.1) and compared to the theoretical value of 3.9 mK^{-1}.

To relate the thermocouple output to temperature differences, the Seebeck coefficient was determined by measuring the (T_h-T_f)-output while controlling the temperature of the heaters over a range of 23-40°C with increments of approximately 2°C. Here, it was assumed that the temperature of the T_h measurement point and the heater temperature were equal. For all measurements, a shear rate of 360 s^{-1} was applied to ensure that the T_f measurement point was equal to the ambient temperature.

Experiments were performed with the heater kept at a constant temperature of 4.2 K above ambient temperature and at a constant power of 80 mW (similar to chapter 6). The steady shear rate was increased from approximately 0 to 2300 s^{-1}. The simulations were performed in the same shear rate range, with quadratically increasing shear rate steps according to:

$$S(i) = \frac{\left(\sum_{i=1}^{N} S_{step}\right)^2}{S_{max}} , \tag{7.11}$$

with, N the number of steps, S_{step} = 50, the average step size, and S_{max} = 2300, the maximum shear rate.

For both the experiments and simulations, the output from the (T_h-T_f)- and (T_d-T_u)-thermocouple, the ratio (T_d-T_u)/(T_h-T_f), and the power supplied were determined and compared.

Optimization of the sensor design

In all simulations, the shear rate profile shown in Figure 7.6 was applied to the sensor with time steps of 2 ms. In the optimization process, first it was determined whether constant power or two types of constant temperature (constant heater temperature and constant surface temperature) operation of the heater is preferable. Hereto, five simulations were performed: **1)** the heater was operated at constant power (5 mW), **2)** the heater was kept at a constant temperature of 42°C, **3)** the same situation as 2 but with a blood temperature of 40°C instead of 37°C, **4)** the thermocouple output T_h-T_f was constant at 5 K, and **5)** the surface temperature at T_h was constant at 42°C. Simulation 3 was performed to test the effect of variations in in ambient temperature. The difference between simulation 4 and 5 represents the effect of heating of the T_f measurement point. The control of the temperature of the heater based on the (T_h-T_f)-signals was performed with a proportional gain (G) controller:

$$dT_{heater} = G(T_h - T_f) , \tag{7.12}$$

with G = 4 and an update frequency of 500 Hz.

Subsequently, for the best way of controlling the heater, the width of the heater was varied from 35 to 280 μm, to investigate its influence on the output signals and to determine the optimal size within the specified limitations. For the appropriate size of the heater, the size of the (T_d-T_u)-thermocouple was varied from 40% to 280% of the heater size. Based on the amplitude of (T_d-T_u)-output signal, the size of the (T_d-T_u)-thermocouple was then chosen.

When the sizes of the different components were determined, a calibration curve based on a power law (similar to ones presented in chapters 4 and 5) was fitted to the data using the Gauss-Newton algorithm as implemented in Matlab (R2010a, The Mathworks, Natick, MA).

The robustness of this calibration relation was then tested by varying the heart rate (12, 60, and 120 BPM) and increasing the shear rate range by a factor of $\frac{1}{3}$ and 3. The correlation between the applied shear rate (S) and the estimated shear rate (S_e)

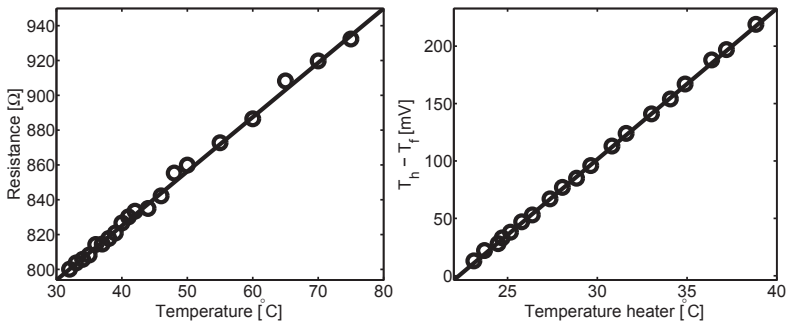

(a) ***(b)***

Figure 7.7: a) *The resistance - temperature relation of the two heaters combined.* ***b)*** *The voltage output - temperature relation of the T_h-T_f thermopile.*

were quantified by determining the correlation coefficient (r), mean absolute error (MAE), and MAE scaled with the absolute shear rate (MAE$_{per}$). MAE and MAE$_{per}$ are defined as:

$$\text{MAE} = \frac{1}{N_s}\sum_{j=1}^{N_s}|S_e(j) - S(j)| \quad , \quad \text{MAE}_{per} = \frac{100}{N_s}\sum_{j=1}^{N_s}\frac{|S_e(j) - S(j)|}{\frac{1}{N_s}\sum_{i=1}^{N_s}|S(i)|} \ , \tag{7.13}$$

with N_s the number of samples.

7.3 Results

7.3.1 Steady flow experiments

Due to the fragility of the sensors, even on a flat surface, successful measurements in the flow channel could be performed on one of the devices only. The Seebeck- and temperature coefficient were also determined on a different device (on the same wafer) as the device tested in the flow channel. Therefore, care should be taken in interpreting the measured power and temperature differences.

Determination of temperature and Seebeck-coefficient

The relation between the temperature and the resistance of the heater was linear over the measured range and is shown in Figure 7.7a. The linear relation described in (7.1), with $R(T_0) = 800\ \Omega$ and $T_0 = 23°$C was fitted to the data, from which a temperature coefficient α of (3.9±0.2) mK^{-1} was found. This is equal to the temperature coefficient found in literature (Nicholas and White, 2001).

Making use of this α, the Seebeck coefficient was determined by electrically heating the heaters. Figure 7.7b shows a linear relation between the output of the (T_h-T_f)-thermocouple and the temperature of the heater. By taking into account that the voltage difference was the result of 60 thermocouples a Seebeck coefficient of (219±3) μVK^{-1} was found.

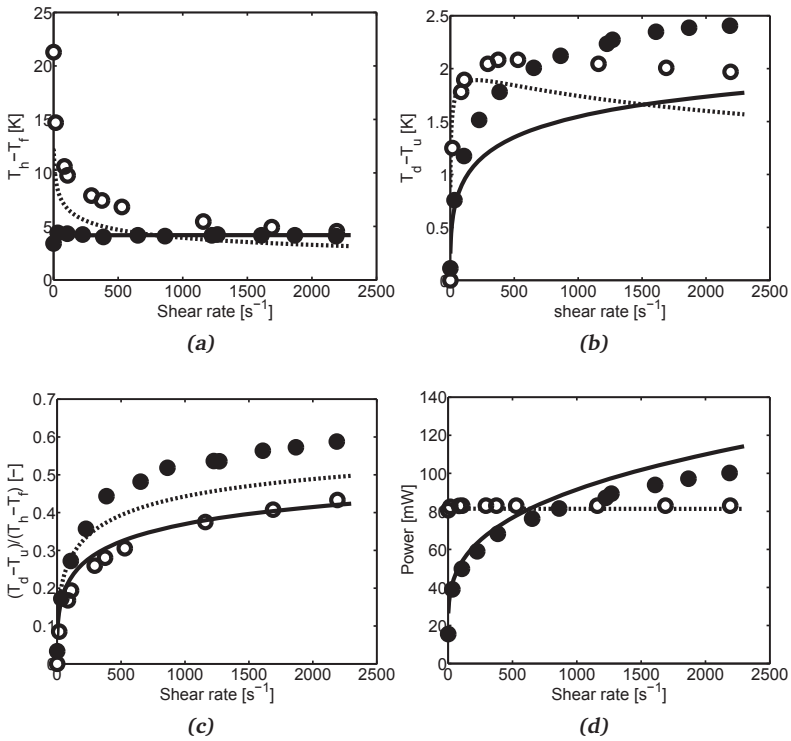

Figure 7.8: *T_h-T_f* ***(a)****, T_d-T_u* ***(b)****, (T_d-T_u)/(T_h-T_f)* ***(c)****, and the power* ***(d)*** *obtained in the experiments and simulations. The constant power experiment and simulation are represented by ∘ and −−, respectively. The constant temperature experiment and simulation are represented by • and −, respectively.*

Comparison between the experiments and numerical model

The temperature and Seebeck coefficient, as determined, were then used to control the heater and measure the temperature differences with the thermocouples. Figure 7.8 shows the results of both the experiments and the numerical model. T_h-T_f was constant at (4.2±0.2) K in the constant temperature mode, indicating that the control system, based on the feedback controlled Wheatstone bridge, performed well (Fig. 7.8a).

When operated at constant power, the (T_h-T_f)-signal obtained with the numerical model, qualitatively agreed with the experiment, except that the absolute temperature was approximately 2 K higher in the experiment. The (T_d-T_u)-signal in the constant power experiment displayed the characteristic behaviour also shown in chapter 6, a fast increase at low shear rates and a slow decrease at high shear rates (Fig. 7.8b). The peak was, however, located at approximately 400 s^{-1}, instead of 150 s^{-1} as shown in Figure 6.4. The (T_d-T_u)-signal from the numerical model showed the same characteristic behaviour with a peak at approximately 200 s^{-1}. When

controlling the sensor at constant temperature, the (T_d-T_u)-signal remains increasing, in both the experiment and simulation. The absolute value of the experiments were, however, again larger than the numerical values. The ratio of the two thermocouple signals also showed qualitatively similar results with the absolute values of the experiments higher than those obtained with the numerical model. Figure 7.8d showed that it was possible to keep the power constant at 82 mW. When the heater was operated at constant temperature, the supplied power in the experiment and numerical model agreed quite well.

7.3.2 Optimization of the sensor design

Control of the heater

Figure 7.9 shows the results for the five different ways of controlling the heater. The (T_h-T_f)-signal of the power controlled heater shows a good correlation with the inverse of the applied shear rate signal level (Fig. 7.9a). For both simulations with the constant heater temperature, the surface temperature also changed significantly with the shear rate. This figure also indicates that the proportional controller of the heater based on the (T_h-T_f)-signal also worked well. As expected, the (T_d-T_u)-signal was not very sensitive to high shear rates, for all three ways of controlling the heater (Fig. 7.9b). The characteristic behaviour with a maximum in the (T_d-T_u)-signal was found in both the power controlled heater and even in the constant temperature controlled heater simulations. Since the surface temperature remained constant in the (T_h-T_f)-controlled simulations, this characteristic behaviour was not found. The ratio (T_d-T_u)/(T_h-T_f) (Fig. 7.9c), improved the sensitivity but was still not very sensitive for high shear rates. As shown in Figure 7.9d, the location of the T_f measuring point is not far enough upstream (1.5 mm) to act as a reference in case of reversing shear rate. However, this does not seem to be significant enough to change the power measured, as indicated by Figure 7.9e, where the difference between T_h-controlled and (T_h-T_f)-controlled heater was negligible. Figure 7.9e also shows that the change of 3 K in blood temperature greatly affected the required power to the heater. This indicates that when controlling the heater at constant temperature, some way of compensating for variations in ambient temperature is required. Compared to the simulations with the heater at constant temperature, the power supplied to the (T_h-T_f)-controlled heater was more than twice as sensitive to changes in the applied shear rate. Considering that the signals from the constant power controlled heater were less sensitive to shear rate changes at high shear rates and that the temperature might become too high at shear rates close to zero, the constant temperature operation seems to be the preferred option. From the two constant temperature control options, controlling T_h-T_f was more sensitive to the applied shear rate, without problems regarding ambient temperature variations. *Hence, it can be concluded that controlling the heater such that T_h-T_f remains constant is the best option and will be used in the rest of this study. Furthermore, to prevent the measured reference temperature to increase further, it is not advised to decrease the size of the (T_h-T_f)-thermopile.*

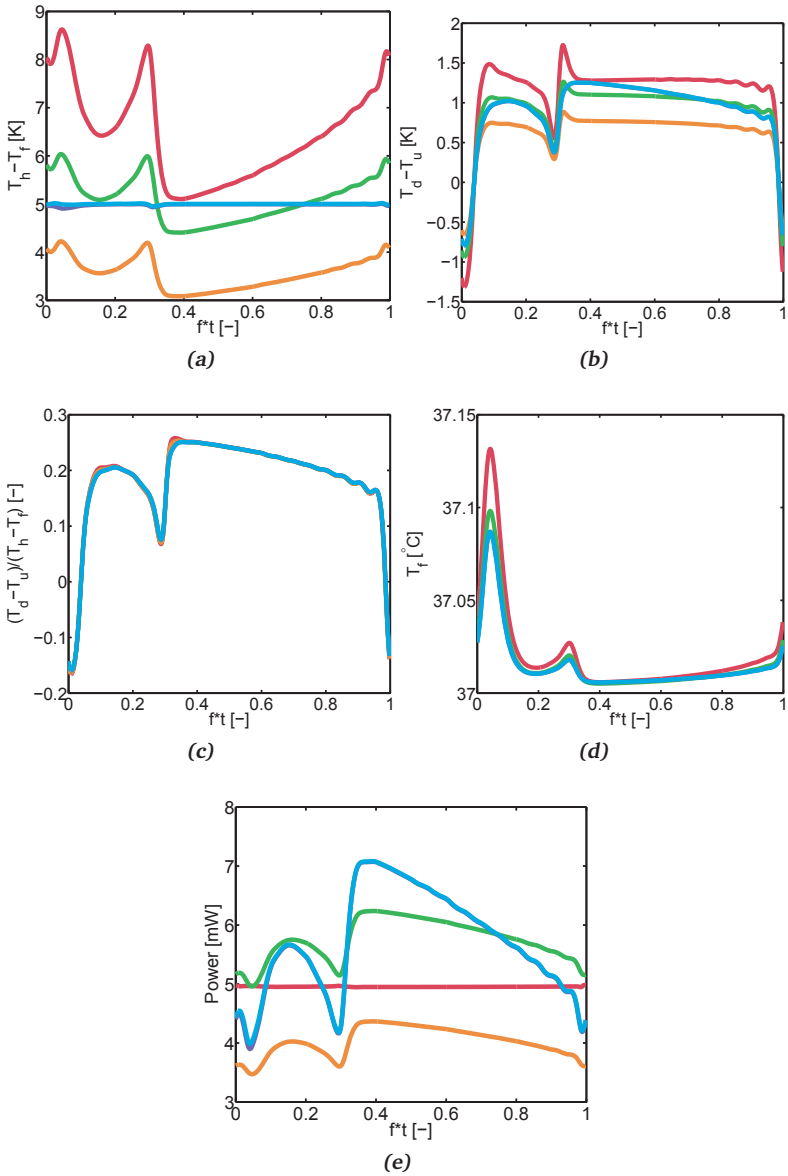

Figure 7.9: *The output signals for the five different simulations for a heater size of 70 μm at a heart rate of 120 BPM. The thermocouple location of T_d and T_u were both directly above the end of each side of the heater. The power was calculated for a heater with a length of 250 μm. The power controlled heater simulation is shown in* ***red****. The constant heater temperature simulations are represented in* ***green*** *and* ***orange*** *for a blood temperature of 37°C and 40°C, respectively. The T_h-controlled heater simulation is shown in* ***purple*** *and the (T_h-T_f)-controlled heater in* ***blue****.*

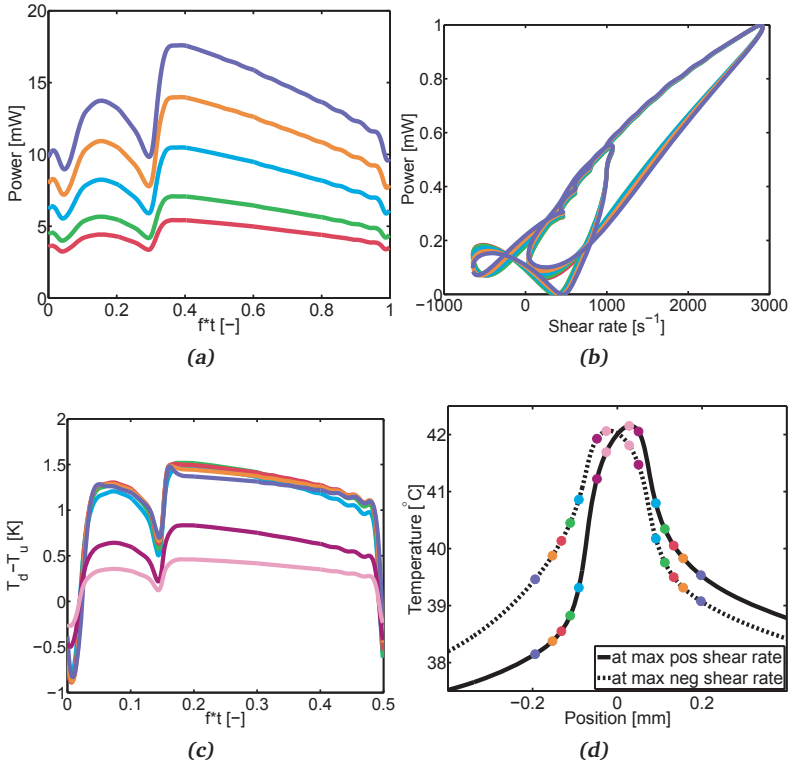

Figure 7.10: ***a)*** *The supplied power to the heater for heater sizes of 35 μm (**red**), 70 μm (**green**), 140 μm (**blue**), 210 μm (**orange**), and 280 μm (**purple**), at a heart rate of 120 BPM. The power is calculated for a heater with a length of 250 μm.* ***b)*** *The normalized power - shear rate relation for the various heater sizes.* ***c)*** *The (T_d-T_u)-thermocouple output for thermocouple positions of 40%(**pink**), 70%(**magenta**), 130%(**blue**), 160%(**green**), 190%(**red**), 220%(**orange**), and 280%(**purple**) of the heater width at a heart rate of 120 BPM and a heater width of 140 μm.* ***d)*** *The temperature distribution at the surface of the chip at positive and negative shear rates, at the different T_d and T_u locations.*

Size of the heater and the (T_d-T_u)-thermocouple

To test the effect of the size of the heater width on the required power, simulations were performed with five different heater sizes, ranging from 35 μm to 280 μm.

In Figure 7.10a the influence of the heater size on the signals is shown. First of all, the power required to keep the heater at a constant temperature was higher when the heater is larger. Figure 7.10b shows that the normalized power signal for all heater sizes was approximately equal. This indicates that time-dependent capacitive effects do not increase significantly for increasing heater length. For our application this means that the size of the heater is only limited by the amount of electrical power that can be supplied. Keeping in mind that the power should not exceed 12 mW, *it*

can be concluded that the width of the heater should not be larger than 150 μm.

As indicated in section 7.2.4, the length of the thermocouple, which measures T_h-T_f, should be as long as possible and was therefore limited by the total size of the chip (1.5 mm). Hence, the only sensor component that needed to be investigated was the size of the (T_d-T_u)-thermocouple. Due to the constant temperature control of the heater, the only function of the (T_d-T_u)-measurement was to distinguish between forward and backward shear rate. Therefore, the only requirement of the (T_d-T_u)-signal was that it changed signs simultaneously with the shear rate with a sufficient signal to noise ratio. Since the amount of noise was unknown we preferred the signal with the largest amplitude.

For the heater width of 140 μm, the size of the thermocouple was varied, ranging from 40% to 280% of the width of the heater. This was equal to 23 μm to 196 μm up- and downstream from the center of the heater. Figure 7.10c indicates a maximum in the (T_d-T_u)-signal between approximately 130% to 190% of the heater width. At those sizes, the measurement points were on the steep part of the curves representing the temperature distribution at the sensor surface (Fig. 7.10d). The time difference between the (T_d-T_u)-signal and the shear rate was approximately 0.04 s. *So, for a heater with a width of 140 μm, the optimal distance between the T_d and T_u measurement point is approximately 200 μm.*

Calibration

To make the conversion from the measured signals to shear rate, a proper calibration curve should be extracted from the data. First, an average time delay of 0.006 s was found between the power and the applied shear rate, using a cross-correlation function. Figure 7.11a shows that this time delay correction mainly affects the large upswing at the start of diastole. For a constant temperature anemometer, the typical relation between power and shear rate can be described with a power law model (similar to one in chapters 4 and 5)

$$P = P_0 + P_1 \left[\frac{S}{S_1} \right]^n . \tag{7.14}$$

In this expression the absolute measured electrical power P is given. P_0 is the absolute power at zero flow; the heat loss due to diffusion. S_1 is a scaling parameter for the shear rate, for which we use the wall shear rate at resting coronary flow (50 ml/min), which is approximately 300 s^{-1}. The parameters of (7.14) could be fitted accurately to the diastolic part of the P-S relation ($P_0 = 4.7$ mW, $P_1 = 2.0$ mW, $n = 0.46$; $R^2 = 0.99$).

The procedure to calculate the shear rate from the power signal was as follows: First, compensate for the (very small) phase delay. Then, calculate the shear rate according to (7.14) and finally compensate for negative shear rates by multiplying with -1 when the (T_d-T_u)-signal is negative. When this calibration relation was used to estimate the shear rate a very good correlation was found, except when the shear rate was negative (see Fig. 7.11b). The error between the applied and calculated shear rate is quantified in the next section.

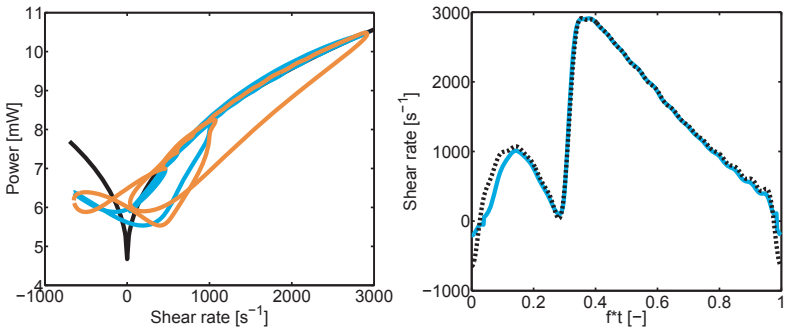

(a) ***(b)***

Figure 7.11: a) *The normalized power-shear rate relation before (**orange**) and after correcting for the phase delay (**blue**). The black solid represents the calibration curve with the fitted parameters.* ***b)*** *The applied shear rate (- -) and the shear rate measured by the sensor (**blue**), making use of the calibration relation.*

Frequency and amplitude response

Coronary flow at a heart rate of 12, 60, and 120 BPM were simulated. The 60 and 120 BPM heart rates are what can be expected during a catheterization procedure and the 12 represents a (quasi-) steady state response. For all three frequencies the calibration curve obtained (7.14) was used to convert the power signal to shear rate.

For negative shear rates, T_f increased significantly, especially at the heart rate of 12 BPM, where the T_f increased with almost 1 K (Fig. 7.12a). For the 60 and 120 BPM heart rates, this increase in T_f was limited to 0.5 K and 0.1 K, respectively. Due to this increase in T_f, the power required to keep the temperature difference T_h-T_f constant also increased, which was clearly shown in the large negative shear rate for the heart rate of 12 BPM (Fig. 7.12b). Although the correlation between the applied and measured shear rate was less at negative shear rates, the overall correlation was good, with $r > 0.99$ for all thee heart rates. The MAE and MAE$_{per}$ were 49 s^{-1} and 4% at 12 BPM, 55 s^{-1} and 4% at 60 BPM, and 72 s^{-1} and 6% at 120 BPM.

The range of the shear rate signal was varied from -500-3000 s^{-1}, to a three times smaller (-170-1000) and three times larger (-1500-9000) shear rate range. As shown in Figure 7.12e, the correlation between the applied and measured shear rate was again good, except for the large upswing of the shear rate with the large range. Here, the proportional controller of the (T_h-T_f)-signal was not fast enough; see Figure 7.12d. For all three shear rate ranges, T_f was not constant for negative shear rates and this effect was exacerbated when the shear rate was more negative. In general the error between the applied and measured shear rate was small. r, MAE, and MAE$_{per}$ were: 0.97, 84 s^{-1}, and 20% for the small range, 0.99, 72 s^{-1}, 6% for the normal range, and 0.99, 306 s^{-1}, 8% for the lange range, respectively. The relatively large errors in the simulation with the low shear range might be related to the relatively larger non-stationary terms, which can result in deviations from the quasi-steady solution.

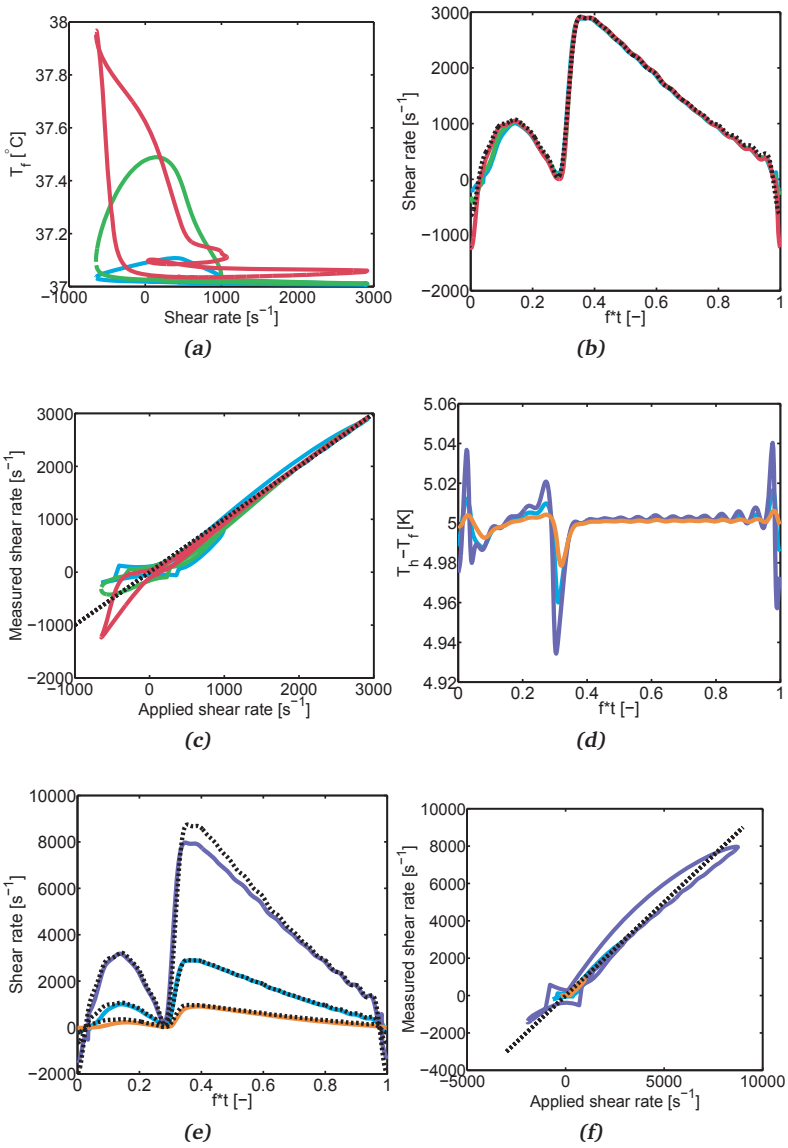

Figure 7.12: a-c) *The output signals measured for applied shear rates representing a heart rate of 12 BPM (**red**), 60 BPM (**green**), and 120 BPM (**blue**).*
d-f) *The output signals measured for applied shear rates ranging from -170-1000 s^{-1} (**orange**), -500-3000 s^{-1} (**blue**), and -1500-9000 s^{-1} (**purple**), at a heart rate of 120 BPM. The dashed (- -) line represents the applied shear rate and the width of the heater and the (T_d-T_u)-thermocouple are 140 μm and 200 μm, respectively. The power is calculated for a heater with a length of 250 μm.*

7.4 Discussion

7.4.1 Steady flow experiments

A 2D numerical model was developed and experiments were performed to investigate the feasibility of operating a miniature thermal sensor at constant temperature. A set-up was developed in which the shear rate over the sensor surface could be controlled accurately. The sensors were inserting into the set-up while they were still on the wafer, to prevent cracking of the sensor elements. This did, however, not resolve the problems regarding the fragility of the sensors and only one complete set of measurements could be performed in the set-up.

In the determination of the temperature coefficient it was found that the aluminium heaters could be described with the literature value of 3.9 mK^{-1}. In the determination of the Seebeck coefficient the heater was controlled by supplying electric current to the heater and simultaneously determining its resistance (and therefore temperature) and the (T_h-T_f)-signal. Here, it was assumed that the nominal value of the two heaters were equal. This might not be the case, resulting in asymmetric heating, which can easily result in a higher heater temperature and therefore a higher (T_h-T_f)-value. Nevertheless, a linear relation between the measured voltage of the T_h-T_f and the heater temperature was found. In chapter 6 the Seebeck coefficient of 305 μVK^{-1} was found, which was acquired from fitting the analytical model to experiments. When comparing that value with Seebeck coefficient found here (219 μVK^{-1}) we see that there is quite a large difference. Maybe the temperature at T_h was not controlled at the correct temperature and/or there was actually an off-set between the (T_h-T_f)-signal obtained with the analytical model and the experiments in chapter 6. It should be noted that, although on the same wafer, the temperature and Seebeck coefficient were determined for a different sensor than the one tested in the flow channel set-up.

The measurements with the constant power controlled heater showed the same characteristic behaviour as was found in chapter 6. The main difference, however, was that the the maximum value of the (T_d-T_u)-signal was found at 400 s^{-1}, whereas in chapter 6 this was 150 s^{-1}. A possible explanation might be found in asymmetric heating of the two heaters. However, T_d-T_u was close to zero at S=0, indicating that the asymmetry in heating is probably limited.

In the constant temperature controlled experiment, it was found that the control system was able to keep the temperature of the heater constant. The (T_d-T_u)-output did not show a maximum, which is an advantage compared to the power controlled experiments. The ratio (T_d-T_u)/(T_h-T_f), however, was similar in both ways of controlling the heater. Another advantage, compared to constant power control, is that the heater temperature does not drop to very low values at high shear rate. Considering that there will be noise on the output signals, this might prove to give a better signal-to-noise ratio at high shear rates. This will only be true if the temperature control of the heater is very accurate. The measured power was also sensitive to the shear rate and can therefore provide extra information for shear rate assessment.

The 2D numerical model is a simplification of the actual device characterized in the experiments. In the numerical model only one heater with a width of 140 μm, was modeled, while in the actual device there were two heaters with a width of 50 μm each. Furthermore, there were several very thin layers, e.g. to insulate the electrical connections, in the actual device that were not modeled. Both simplifications might contribute to the lower temperatures found by the numerical model. Nevertheless, the numerical model was able to qualitatively describe the experimental results.

It can be concluded that controlling the heater at constant temperature is feasible. Compared to the constant power control, it has the advantage that both the sensor temperature cannot increase to temperatures that can damage the blood and the (T_d-T_u)-signal does not decrease at higher shear rates. Furthermore, the required electrical power also provides information regarding the shear rate. Although the absolute values of the measured signals did deviate from the ones obtained with the numerical model, qualitatively they were similar. At least partly, the deviation could be contributed to several uncertain factors in the experiments, e.g,. the Seebeck coefficient and unequal dissipation in the two heaters, and we therefore conclude that the numerical model is suitable to further investigate this type of sensors.

7.4.2 Optimization

To be able to fabricate and mount the flow-sensing devices on a 0.36 mm diameter guidewire without the formation of cracks, the heater element is required to be located at the neutral line of the chip. Compared to the chip with the heater at the surface, this will increase both the effective heater size and capacitive effects due to storage and release of energy in the chip material (polyimide).

Therefore, the design and control of the sensor was investigated using an axisymmetric numerical model. The choice for an axisymmetric model implies that we approximated the coronary vessels as straight with the guidewire located in the center of the vessel. Although the curvature to diameter ratio of coronary arteries is not very large, secondary flows might occur and due to its stiffness, the guidewire will likely prefer a position on the outside of the curve. Consequently, either detailed 3D numerical modeling or experiments are required to determine the actual response of the sensor in different flow conditions.

It was found that the best way to control the heater is by keeping the (T_h-T_f)-thermocouple constant. The power required to keep this signal constant can then be used as a measure for the local shear rate. In this study, the control of the temperature of the heater was performed with a proportional gain controller. Although it was able to keep the (T_h-T_f)-signal nearly constant, in the simulation with the very high shear rate range the (T_h-T_f)-signal deviated significantly. A more sophisticated controller might solve this problem. If in practice the control of the heater based on the (T_h-T_f)-signal proves to be difficult, constant power operation is still an option with the ratio of output of the two thermocouples. However, the sensitivity at higher shear rates is less compared to the measured power in the constant temperature control mode. Additionally, in case of stagnant blood flow, e.g. due to a fully occluded vessel, the surface temperature of the device can become too high, possibly resulting in fibrin

formation and protein dissociation.

Increasing the size of the heater resulted in a better sensitivity to shear rate. While the temperature of T_f did increase with increasing heater size, the effect on the measured power was rather limited. The main limitation for the heater size is the electrical power that can be supplied to the heater. When as indicated, the maximum power is 12 mW, the heater width should not be larger than 140 μm. Since the power is used to measure the shear rate, the (T_d-T_u)-thermocouple is only used to detect shear rate reversal. Although the (T_d-T_u)-signal is not very sensitive to the exact location of measurement, an optimal length of approximately 200 μm was found for a 140 μm heater For the 140 μm heater width and a shear rate signal with a heart rate of 120 BPM, a calibration curve, based on a power law, was fitted to the data. The R^2 was very close to 1, indicating that a power law is appropriate to describe the power-shear rate relation. When applying this relation to the signals obtained from simulations with shear rates with different frequencies and amplitudes, generally a good agreement with the reference signal was found. It must be stressed that a very low frequency and/or a very large negative shear rate will corrupt the reference temperature signal (T_f) and therefore the power signal. In the physiological range, however, this effect seems to be limited. For the small shear rate range the correlation between the applied and measured shear rate was not so good. This might be related to a relatively larger contribution of the non-stationary terms, which results in a deviation from the quasi-steady solution. A transfer function that does take the non-stationary effects into account (e.g. Bellhouse and Rasmussen (1968)) might be helpful to resolve this issue.

7.5 Conclusion

It is possible to control the sensor at constant temperature via a feed-back controlled Wheatstone bridge. Compared to the control at constant power, it provides better sensitivity at high shear rates and is safer at very low shear rates. Although experiments are necessary to validate the non-stationary results of the numerical model, for the next version of sensors to be manufactured, it is recommended that the heater has a width of approximately 140 μm (although the size is mainly limited by the available supply of electrical power) and is (T_h-T_f)-controlled. The optimal size of the (T_d-T_u)-thermocouple for a 140 μm heater is approximately 200 μm.

Author contributions

Performed experiments: A. van der Horst, D.D. van der Voort
Data analysis: A. van der Horst, D.D. van der Voort
Interpretation of results: all
Prepared figures: A. van der Horst, D.D. van der Voort
Drafted manuscript: A. van der Horst
Edited and revised manuscript: all
Approved final version of manuscript: all

Chapter 8

General discussion

The main objective of the research described in this thesis was to develop methods to simultaneously assess the dynamics of coronary pressure and flow with guidewire-mounted sensors. Two different strategies were chosen in the development of these methods. An already clinically used pressure-temperature sensing guidewire was operated as a thermal anemometer to enable flow measurements. The main advantage of this approach is that an existing device is used, which facilitates the process towards clinical application. A clear drawback inherent to this approach is that the device was specifically designed to measure pressure, resulting in suboptimal performance for flow measurements. In the second strategy, a flow sensor embedded into a flexible chip was developed and investigated via analytical, numerical, and experimental characterization. This resulted in a new sensor design to be manufactured and tested in well controlled *in-vitro* and *ex-vivo* experiments.

Since guidewire-mounted sensors can only access the relatively large epicardial arteries, an appropriate model is required to translate potential combinations of arterial, microvascular, and cardiac disease to pressure and flow waves that can be measured in the epicardial arteries. For that purpose, a computational model, consisting of previously developed models, was constructed to simulate the global effect of different types of disease on coronary epicardial hemodynamics.

In this chapter, the main findings described in this thesis are discussed and recommendations for further research are given.

8.1 Computational model of the coronary circulation

Arterial wall mechanics

Knowledge of the patient specific mechanical properties of the coronary arterial wall is required for patient-specific modeling of coronary hemodynamics and can give valuable information regarding the decision-making for the mechanical treatment of arterial disease. To determine these mechanical properties, the parameters of an appropriate constitutive model of the arterial wall need to be fitted to data that

can be obtained *in-vivo*. A challenge in the parameter estimation from clinical data, is that the measurement range is limited to physiological pressures. Furthermore, clinical data do not provide any information regarding the axial strain and the stress-free geometry, which are required to be able to fit a constitutive model. To circumvent this problem, extra modeling constraints can be incorporated into the parameter estimation procedure. In **chapter 2**, such a constraint, concerning the fiber orientation at physiological loading, was derived using a mixed experimental-numerical approach.

The experimental part consisted of inflation-extension experiments on seven healthy porcine and two human left anterior descending coronary arteries and was performed by Van den Broek et al. (2011). The porcine coronary arteries were obtained from a local slaughterhouse, thus avoiding ethical issues regarding laboratory animals. The choice to use porcine arteries as a model system for human coronary arteries was prompted by morphological studies, indicating that porcine coronary arteries resemble human coronary arteries (Crick et al., 1998). A great advantage of the set-up used is that it mimicked the *in-vivo* situation by stretching the arterial segments to the physiological axial stretch and still enabled investigation of the mechanical behaviour over a large pressure range. This physiological axial stretch was determined by stretching the artery until the axial force was relatively insensitive to changes in pressure. While this assumption already has been frequently used to describe the physiological axial stretch (Stålhand and Klarbring, 2005; Humphrey et al., 2009), for each individual porcine coronary artery used, Van den Broek (2010) demonstrated that this assumption is valid by comparing the axial stretch found with measurements with the isolated beating heart set-up (de Hart et al., 2011) described in **chapter 5**.

The numerical model used in this study was the thick-walled, single-layered, fiber reinforced model proposed by Holzapfel et al. (2000). The main advantage of this model is that it has a limited number of material parameters, while the microstructure of the arterial wall is still globally taken into account. As explained in **chapter 1**, the arterial wall consists of three distinct layers, with different constituents and related material parameters. Adopting a model with a more realistic morphology, i.e. more layers, constituents, and fiber distributions, will yield a more accurate description of the mechanics of the arterial wall. However, adding these extra components will also increase the number of parameters that need to be included into the fitting procedure. This will make it improbable that a unique set of parameters can be attained, especially with the quality and limited amount of information available in clinical data. Extra components can be incorporated, but this will require an appropriate generic relation prescribing either the value of this extra parameter or its relation to another parameter.

An estimation procedure was developed to fit the four parameters of the model, by minimizing an objective function defined as the difference between both the modeled and measured pressure-radius data and the pressure-invariant axial force relationship. Residual strains were incorporated via the openings angle method and assuming that the circumferential stress-gradients at physiological loading conditions are minimal. This assumption, together with the pressure-invariant axial force, states

that at physiological loading conditions the arteries are remodeled to an optimal configuration where stresses minimally change during the cardiac cycle. Although this is an idealized representation of the stresses in the arterial wall, several studies (Takamizawa and Hayashi, 1987; Humphrey et al., 2009) demonstrated that the transformation of the typical stress-free geometry to the geometry at physiological loading results in this optimal stress configuration.

It was demonstrated that the parameters of the model could be fitted such that the model described the experimental data accurately. For each individual artery, multiple initial parameter sets converged to the same optimal parameter set, indicating that a global minimum of the objective function was found. The relative variation in the material parameters found was quite large, except for the parameter representing the fiber orientation in the stress-free configuration $(36\pm3)^\circ$. This parameter, however, is the main determinant of the mechanical behaviour at high pressures, where the load is primarily taken by the collagen fibers. Analysis of this fiber orientation at physiological axial stretch and mean arterial pressure revealed that for all arteries the fiber orientation was almost equal $(36.4\pm0.3)^\circ$. This can potentially be explained by a theory described by Hariton et al. (2007), which states that in cardiovascular tissues collagen fibers align in between the principle stress directions with the orientation modulated by their magnitude. Similarly the value of the fiber angle at physiological loading can also possibly explained by netting analysis, which is often used to describe the behaviour of fiber-reinforced composite materials (Gay et al., 2003). The main assumption in netting analysis is that all loads are supported by the fibers only, which approximates the arterial wall in the physiological loading range. An optimal winding fiber angle, of approximately 35° relative to the circumferential direction, exists (Spencer et al., 1974) in which the fibers take all the added load due to the internal pressure. It is important to realize that this theory is only applicable at high pressures were the stress is mainly taken by the stretched collagen fibers. In the modeling of the arterial wall with similar orthotropic models, this fiber orientation at physiological loading can serve as a structural constraint that describes the direct relation between the axial and circumferential stretch and the fiber orientation in the stress-free configuration. It must be stressed that the fiber orientation in these models should not be viewed as the actual fiber morphology in the arterial wall but just as the net result of all fibrous material.

Another point of discussion that is important in the application of optimization constraints to the coronary arteries is the effect of the myocardium. In this study, the arteries were dissected from the hearts and were therefore not constrained by the myocardium. While it has been demonstrated by Liu et al. (2008) that for partially embedded epicardial arteries, as were used in this study, the influence of the myocardium is limited, it is important to realize that for the vessels that are completely embedded into the contracting myocardium different physiological loading conditions apply, which should be included in the optimization rules used. It would be very interesting to perform a similar experimental protocol to determine the mechanical properties of vessels that were embedded into the myocardium.

Although the two human arteries, that have been characterized experimentally, are considered healthy, both arteries showed stiff behaviour in either the axial

or circumferential direction. Although this might be explained by the presence of some degree of arteriosclerosis, in further research more non-diseased human coronary arteries should be experimentally characterized to confidently apply the results obtained to human coronary arteries. Moreover, since mechanical treatment will generally be performed on atherosclerotic arteries, the different components of the plaque should be incorporated into the model and experimentally characterized. The experimental characterization can be performed in a similar set-up and loading protocol as developed by Van den Broek et al. (2011). 3D images are then required to capture the deformation of the non-symmetric composition of the plaque.

Modeling coronary hemodynamics

A computational model was developed that describes coronary pressure and flow waves in health and disease. The model consists of four elements: A heart contraction model, a wave propagation model for the large arteries, a stenosis element compatible with the wave propagation model, and Windkessel elements to model the contribution of all the vessels that are not modeled individually. The combination of these models enables the investigation of the effect of (combinations of) arterial, microvascular, and cardiac disease on the large epicardial arteries, where intracoronary hemodynamical measurements can be performed. In **chapter 3** it was shown that by combining these models, stable solutions were obtained in the normal and disease simulations. The computational cost of these simulations is also relatively low, which makes real-time computation in the catheterization laboratory feasible.

Comparison of the modeled normal systemic and coronary hemodynamics with measurements described in literature demonstrated that the model is suitable for the computation of coronary hemodynamics. A coronary stenosis and left ventricular hypertrophy with an aortic valve stenosis (LVH-AVS) were modeled. The coronary pressure and flow displayed similar characteristic features as found in measurements described in literature. This showed the ability of the model to distinguish between different diseases types. It should be noted that, due to a lack of specific experimental data, the model could only be compared qualitatively to the literature values. For a proper validation of the model, a case study should be performed where the dynamics of coronary arterial and venous pressure and flow, as well as left ventricular pressure and volumes should be measured simultaneously. These measurements should be performed in both diseased and healthy subjects. Alternatively, isolated beating heart experiments (de Hart et al., 2011) might provide a proper platform to perform these measurements under well-controlled conditions. In the validation of the model it is also good to realize that there are a number of simplifications that limit the use of the model for certain disease types. For example, the effect of a myocardial infarction on the ventricular pressure cannot be modeled straight forward with the current contraction model, since it affects only a part of the myocardium.

By using a patient-specific arterial tree, the model can be applied to predict the clinical outcome of mechanical treatment or bypass surgery and can therefore support the cardiologist in evaluating the different treatment strategies. Furthermore, the 1D representation of the coronary arteries can serve as an appropriate boundary condition for a more detailed 3D model. The 1D wave propagation model used in

this study is especially suitable for this application because it is, as most 3D numerical models, time-domain based and approximates the real velocity profile. For this patient-specific application it is paramount to perform a proper sensitivity analysis of the parameters that have to be fitted to the measurements.

Wave intensity analysis (WIA) is a very interesting tool to distinguish between events originating proximal and distal to the measurement site (Parker, 2009). For example, as described by Davies et al. (2006a), WIA is able to detect changes in the compression and suction waves coming from the coronary microvasculature when ventricular hypertrophy is present. An important parameter required in WIA is the pulse wave speed. Several methods were proposed to measure this wave speed (Davies et al., 2006b) but were questioned by Kolyva et al. (2008) for application to coronary arteries. The 1D representation of the coronary arteries of the model developed in this study can provide insight into the validity of these different methods to determine the pulse wave speed in physiological and supra-physiological conditions.

The arterial wall model developed in **chapter 2** was used to describe the compliance of the modeled coronary arteries. From the wall model the parameters of an analytical description (Langewouters et al., 1984) describing the pressure-compliance relation was derived for a range of radii and wall-thicknesses. In relation with coronary hemodynamics, it was shown that the difference between this more realistic wall model and a simple linear elastic model was very limited, even distal to a severe stenosis where the largest differences were expected. It can therefore be concluded that the arterial wall model developed is not a major improvement in the 1D modeling of coronary arteries. Nevertheless, compared to the linear elastic model, the computational cost is not increased and the wall model developed might be more suitable when connecting the 1D model to a more detailed 3D model with a micro-structure based arterial wall.

The model can be improved in several ways. The baroreflex mechanism can be included to regulate the heart rate, as was already incorporated into a similar heart contraction model by Cox et al. (2009). Additionally, by including the coronary autoregulation, the difference between resting and hyperaemic flow can be simulated (Kim et al., 2010). This is valuable since it enables the determination of clinical indices based on the difference between resting and hyperaemic hemodynamics, e.g. CFR (Gould et al., 1990) or DCVR (Krams et al., 2004). This heart contraction model is suitable to include this mechanism, since the work performed by the heart can be used as a parameter in the autoregulation mechanism. Another improvement would be to explicitly model the volumes of the coronary microvessels and not only the volume changes with the constant capacitors. Furthermore, a four element Windkessel model (Stergiopulos et al., 1998) would improve the coupling of the coronary microcirculation to the 1D wave propagation model. Finally, the circulation can be closed by adding the venous and pulmonary system, which has the advantage that the total blood volume is prescribed. The right ventricle can then be modeled similarly as the left ventricle (Cox et al., 2009).

8.2 Thermal anemometry applied to a pressure-sensing guidewire

Pressure-sensing guidewires (pressure wires) are increasingly used to determine the functional significance of coronary arterial stenoses. This is mainly due to the proven clinical importance and ease-of-use of FFR in the catheterization laboratory (Pijls et al., 1996; Tonino et al., 2009). However, to quantify the significance of microvascular disease both pressure and flow measurements are required. The most used device to assess coronary pressure and flow simultaneously is a guidewire combining a pressure sensor and Doppler-crystal to measure blood velocity (ComboWireXT, Volcano, San Diego, CA). Compared to pressure wires, this device is less frequently used in the clinic, since the majority of the patients eligible for catheterization only require evaluation of the severity of a stenosis. Additionally, because the Doppler-crystal is located at the tip of the guidewire, the velocity measurement is influenced by the position and orientation of the guidewire inside the vessel, resulting in a poor signal in 10% to 19% of patients (Kern et al., 2006; Ganz and Hsue, 2009).

In **chapter 4**, a novel way of flow assessment is presented, in which a pressure wire (PressureWire, St. Jude Medical, St. Paul, MN) is operated as a constant temperature anemometer. A relatively simple electrical circuit was devised to keep one of the resistors on a chip near the tip of the guidewire constant. By measuring the power required to keep the resistor at constant temperature, a measure for the flow could be determined. It must be stressed that with this measurement technique the advection of heat is solely determined by the velocity near the sensor surface, which can be represented by the local shear rate. This means that the lumen area and radial position of the sensor are required to convert the measured shear rate to the flow rate.

A calibration curve describing the relation between the average power and shear rate was derived for several overheat temperatures. When considering both the reproducibility and the sensitivity with respect to the shear rate, it was demonstrated that for steady flow the sensor response was optimal at an overheat of approximately 20 K. At this overheat temperature the sensor was subjected to a characteristic coronary flow signal and it was found that CFR could be reliably estimated using the stationary calibration function. Additionally, the phasic nature of the applied flow could be clearly recognized in the measured electrical power signal, indicating that this thermoconvection-based method might also be suitable for dynamic shear rate assessment.

Before this method to assess CFR can be applied in the clinic there are several issues that need to be addressed. First of all, the overheat temperature of 20 K can be argued as a limitation for *in-vivo* application, due to possible blood and vessel damage. Nevertheless, due to the limited time of measurement and the small size of the sensor, it is expected that the amount of damage will be negligible. This issue, however, requires additional research. Another issue is related to the fact that the diffusive heat transfer (P_0) was much larger ($O(10)$) than the convective heat transfer. In itself, this would not be a major problem if P_0 were fairly constant. However,

because the combination of both microcable and sensor resistors is kept constant, slight changes in the temperature of the cable resistors also affect the temperature of the sensor, which has a large effect on P_0. It is therefore very important to measure the cable resistance very accurately before every measurement. From preliminary research it was found that this cable resistance measurement is not easy, since the cable resistance is much smaller ($O(0.01)$) than the sensor resistance.

By combining this thermal anemometric method with the continuous thermodilution method, this issue regarding the cable resistance is circumvented. With the combination of the two methods the absolute volumetric physiological flow dynamics could be determined quite accurately. A calibration function based on a first-order Taylor expansion of the power-law relation, describing the steady relation between power and shear rate, was used to convert the measured electrical power to flow. With this approach, it is paramount to realize that it is based on coarsely simplified relations between the electrical power, heat transfer, shear rate, and flow. While this simple approach has its limitations, it performed surprisingly well for physiological flows. The main drawback of this combined methodology is the inability to detect reversing shear rate, which is theoretically impossible with the anemometric method. This makes this combined methodology mainly suitable for the detection of flow dynamics in diastole, when the flow is typically high. Besides clinically used indices based on the diastolic part of coronary flow (DDT, DPF, IDHVPS), these measurements might provide enough information to make patient-specific modeling possible.

The majority of the measurements is performed in a well controlled *in-vitro* environment. While the set-up used does mimic the coronary epicardial geometry, including a slightly curved vessel, and hemodynamics (Geven et al., 2004), it would be very interesting to characterize the sensors in vessels with different degrees of curvature. Additionally, valuable information can be obtained by performing a proper analysis of the effect of the radial position on the sensor response. This can be done by detailed 3D numerical modeling and/or by developing a set-up for this specific purpose.

Towards clinical application, the thermal anemometric method with the PressureWire has also been evaluated in an *in-vivo* study, in which three Yorkshire swine were instrumented with an epicardial ultrasound flow probe and an occluder to regulated the blood flow (Geven, 2007). With a similar method as described in **chapter 4**, it was demonstrated that the method could also be used in blood and that the calibration curves, describing the relation between electrical power and flow, were similar to the ones found in the *in-vitro* study in **chapter 4**. Furthermore, the single measurement in the isolated beating pig heart platform (de Hart et al., 2011) described in **chapter 5**, also indicated that this methodology is also feasible in blood in genuine physiological conditions. It is clear that more measurements in the isolated beating heart platform need to be performed to investigate this further. By inserting a Doppler guidewire in the same *ex-vivo* measurements, a direct comparison can be made between the accuracy of the Doppler method and the thermal anemometric method.

While in **chapter 4** an electronic circuit was devised for sequential shear rate and pressure measurements, the electronic circuit described in **chapter 5** is capable of

determining the pressure while the resistors on the chip are heated, thus enabling simultaneous pressure and shear rate measurements. The main clinical application of these simultaneous measurements is the assessment of IDHVPS for the detection of microvascular disease (Escaned et al., 2009). The strength of the pressure signal obtained simultaneously with the flow was very low and might be improved by more sophisticated amplification algorithms that are also currently used in the RADI Analyzer (St. Jude Medical, St. Paul, MN). In general, by using more sophisticated electronic circuitry and signal processing methods the Wheatstone bridge-based electronic circuits developed in this thesis can be improved. An important issue in that regard is the shielding of the circuit, which was found to be very important to eliminate outside disturbances.

Finally, to be able to take the method to the clinic, it should be incorporated into a clinically used medical device (RADI Analyzer. St. Jude Medical, St. Paul, MN). This will prevent dis- and reconnecting of the PressureWire to multiple devices and some parts of the protocol, e.g., the setting of the sensor temperature and the calibration of the pressure signal, can then also be automated to shorten the procedure time. The capability of assessing a measure for the flow with a pressure-sensing guidewire will give the cardiologist an extra tool in case pressure measurements alone do not suffice, without having to insert a new guidewire.

8.3 Miniature thermal sensor on a flexible chip

The applicability of a new thermal sensor embedded in a flexible substrate for coronary flow assessment was evaluated with analytical, numerical, and experimental analysis. The starting point in the development of this new sensor was the study performed by Haartsen (2007). This showed that a heating element and thermocouples could be embedded into a flexible polyimide substrate to function as a calorimetric flow sensor. Due to the flexibility of this substrate the chip might be suitable to be bend around a guidewire, serving as a platform for multiple pressure and flow sensors.

The main components of the sensor were a heating element and two thermocouples that measure the temperature difference between the heating element and far upstream (T_h-T_f) and up- and downstream (T_d-T_u) of the heater. Haartsen (2007) demonstrated that by operating the heater at a constant power and by taking the ratio (T_d-T_u)/(T_h-T_f) as output signal an invertible relation with respect to the shear rate was found, which was independent of the Seebeck coefficient. To gain more insight into the applicability of this sensor for coronary flow assessment, experiments were performed and a 2D quasi-steady analytical model was developed (**chapter 6**).

The main advantage of this analytical model is that it includes axial heat conduction in the fluid, while an appropriate simplified representation of the substrate is used. From the dimensionless energy equation, it was found that the sensor response to unsteady flow is influenced by three dimensionless groups, the Strouhal (*Sr*) and Péclet (*Pe*) number and the relative oscillation amplitude (β). In the physiological range the Strouhal number is small ($O(0.01)$-$O(0.1)$), justifying the

quasi-steady approach for the analytical model and indicating that *Pe* determines the sensor response.

The sensors manufactured by Haartsen (2007) were experimentally characterized in steady and pulsatile tube flows. Although there was an off-set indicating that the effective heater size might have been chosen too large, the analytical model agreed well with the experimental results in steady flow. In non-reversing unsteady flow the analytical model predicted the experimentally found sensor behaviour quite well for *Sr* up to 0.1. However, in the short periods of reversing shear rate the sensor response was not quasi-steady anymore, due to the effect of the thermal wake being carried back over the sensor.

While in the unsteady experiments β and *Sr* were within the physiological range, the range of *Pe*, which for a sensor with a specific size is determined by the shear rate, was too low compared to the expected coronary shear rates. When the experimental results are extrapolated to the physiological shear rate range, the performance to detect shear rate changes is rather limited. From the analytical model is became clear that the only parameter that can be varied to optimize the sensor response is the heater width. It was demonstrated that by decreasing the heater width, the maximum in the (T_d-T_u)-signal was shifted to higher shear rate values, resulting in a more linear relation between the shear rate and (T_d-T_u)/(T_h-T_f). Although it is advantageous to linearize the response to shear rate, the increase in performance at high shear rates was still rather limited.

Therefore, it was investigated whether operating the heater at constant temperature could improve this relation at high shear rates (**chapter 7**). A numerical model was developed and steady experiments were performed with the sensors at the bottom of a rectangular channel. The main reason to perform these measurements with sensors on a flat surface, instead of in a tube as used in **chapter 6**, were difficulties mounting and connecting the chips into the tube, often resulting in breaking of the sensor components. From these steady experiments it was demonstrated that controlling the heater at constant temperature is feasible with a feedback controlled Wheatstone bridge. Compared to the constant power control, it has the advantage that both the sensor temperature cannot increase to temperatures that can damage the blood and the (T_d-T_u)-signal does not decrease at higher shear rates. Furthermore, the required electrical power also provides information regarding the shear rate. Although the absolute values of the measured signals did deviate from the ones obtained with the numerical model, qualitatively they were similar. At least partly, the deviation could be contributed to several uncertain factors in the experiments (e.g., the Seebeck coefficient, unequal dissipation in the two heaters) and it was concluded that the numerical model is suitable for further investigating this type of sensors.

After extensive research, Mimoun et al. (2010a) developed a novel technology for the manufacturing of flexible chips with ultra-flexible interconnects. Mimoun et al. (2010b) demonstrated that this technology could be used to mount a flexible chip on a guidewire. To be able to bend these chips to the required bending radii without breaking the sensor components, the components that are circumferentially oriented need to be in the mechanical neutral bending plane, which is approximately at the

center of the thickness of the chip. Compared to the device that was manufactured by Haartsen (2007) where all sensor elements were at the surface, this means that the heater element should be in the center of the flexible foil, whereas the axially oriented thermocouples can be located at the surface.

To optimize the sensor design for coronary flow assessment, a numerical study was performed. This showed again that operating the heater at constant temperature is preferred over constant power operation. Using a very simple proportional gain controller, the temperature of the heater could be controlled to keep the signal from the (T_h-T_f)-thermopile constant. The electrical power required could then be used as a measure for the shear rate and the (T_d-T_u)-signal was used to detect shear rate reversal. With a simple calibration function, this electrical power signal could reliably be used to measure the applied shear rates with different frequencies and shear rate amplitudes. However, at shear rate reversal, due to the thermal wake being carried back (and forth) over the sensor, the response is suboptimal. From the numerical study, taking operational and manufacturing limitations into account, an optimal design of the sensor layout was proposed, which is currently being manufactured.

The flexible chips that are being manufactured consist of a 4$\times$ upscaled chip and the actual chip size required to be mounted on a 1 mm and 0.36 mm diameter guidewire, respectively. These flexible chips are connected to a rigid chip located inside the guidewire with a pressure sensor, enabling simultaneous assessment of the shear rate and pressure. The 4$\times$ scaled chip will contain three individual sensors located on the perimeter of the guidewire to be able to detect the radial position of the guidewire. The number of microcables required to operate and read three flow sensors and one pressure sensor is 18, which should be able to fit the 4$\times$ scaled guidewire. However, no more than three (or maybe four) microcables will fit into the small sized guidewire. Even with one flow sensor and one pressure sensor, this will require on-chip data processing by an application-specific integrated circuit (ASIC). An important limitation of adding more sensors on the tip of the guidewire is the increased complexity of the required ASIC.

In this study, the basic design remained close to the original design of Haartsen (2007). The flexible chip platform might also be suitable for totally different flow sensors. Al-Salaymeh et al. (2004) proposed a method for medical flow assessment based on a pulsed-wire anemometer. With this technique an element is sinusoidally heated at a certain frequency, which is measured by a second element. The phase difference between the heating element and receiving element is then a measure for the local flow velocity. Preliminary research with the numerical model, however, has shown that storage and release of heat into the polyimide sensor material will limit the applicability of time-dependent heating.

The next step in the developmental process of the new sensors based on the design proposed, is the experimental characterization in physiological representative shear rates. Both the large and small sized sensors should be mounted on guidewires to be characterized in appropriate *in-vitro* set-ups, in which they are subjected to unsteady flow, in tubes with different diameters and curvatures, and with the guidewire located at different radial positions. As a follow-up of these *in-vitro* characterization experiments, *ex-vivo* experiments can be performed with the small-size sensors on

guidewires in the isolated beating pig heart platform (de Hart et al., 2011).

Finally, although the work described in this thesis focusses on the development of methods to assess pressure and flow, this flexible-chip on a guidewire can also be used as a platform to add more functionality to the tip of guidewire. Adding imaging tools is especially interesting, since it can support the pressure and local flow measurements with morphological information. Intravascular ultrasound (IVUS), via capacitive micromachined ultrasonic transducers (CMUT), seems particularly promising in this regard.

8.4 Conclusions

In this thesis, methods for simultaneous pressure and flow assessment in the coronary arteries were presented. To support the interpretation of these coronary pressure and/or flow measurements for clinical decision-making, a 1D wave propagation model of the coronary circulation was developed. Although further validation of the model is required, it was demonstrated that the model was able to describe coronary hemodynamics in health and disease.

A method for flow assessment was developed in which an already clinically used pressure-sensing guidewire was operated as a thermal anemometer. It was demonstrated that this technique is promising for CFR assessment and by combining it with a continuous thermodilution technique, the dynamics of coronary pressure and volumetric flow could be determined simultaneously. The advantage of this approach is that the device is already widely used in the clinic, facilitating the process towards clinical application. A drawback inherent to this anemometric method is the inability to distinguish between forward and backward flow velocity at the sensor surface. The main limitation for clinical application, requiring further research, is the potential damage to blood, due to the relatively high sensor temperatures.

To overcome these limitations, a new thermal sensor on a flexible chip was developed, which can be operated at lower temperatures and can detect local velocity reversal. Analytical, numerical, and preliminary experimental characterization indicate that the sensor is suitable for coronary flow assessment. From these characterization studies a new design of the sensor was proposed, which is currently being manufactured to be tested in both *in-vitro* and *ex-vivo* experiments.

References

W. Aarnoudse, W. F. Fearon, G. Manoharan, M. C. F. Geven, F. N. van de Vosse, M. C. M. Rutten, B. De Bruyne, and N. H. J. Pijls. Epicardial stenosis severity does not affect minimal microcirculatory resistance. *Circulation*, 110:2137–2142, 2004a.

W. Aarnoudse, P. van den Berg, F. N. van de Vosse, M. C. F. Geven, M. C. M. Rutten, M. van Turnhout, W. F. Fearon, B. De Bruyne, and N. H. J. Pijls. Myocardial resistance assessed by guidewire-based pressure-temperature measurement: in vitro validation. *Catheter Cardiovasc Interv*, 62:56–63, 2004b.

W. Aarnoudse, M. van't Veer, N. H. J. Pijls, J. ter Woorst, S. Vercauteren, P. Tonino, M. Geven, M. Rutten, E. van Hagen, B. D. Bruyne, and F. van de Vosse. Direct volumetric blood flow measurement in coronary arteries by thermodilution. *J Am Coll Cardiol*, 50:2294–2304, 2007.

R. C. Ackerberg, R. D. Patel, and S. K. Gupta. The heat/mass transfer to a finite strip at small Péclet numbers. *J Fluid Mech*, 86:49–65, 1978.

R. Agah, J. A. Pearce, A. J. Welch, and M. Motamedi. Rate process model for arterial tissue thermal damage: Implications on vessel photocoagulation. *Lasers Surg Med*, 15:176–184, 1994.

A. Al-Salaymeh, J. Jovanović, and F. Durst. Bi-directional flow sensor with a wide dynamic range for medical applications. *Med Eng Phys*, 26:623–637, 2004.

D. Algranati, G. Kassab, and Y. Lanir. Why is the subendocardium more vulnerable to ischemia? a new paradigm. *Am J Physiol-Heart Circ Phys*, 300:H1090–H1100, 2011.

T. Arts, P. H. M. Bovendeerd, F. W. Prinzen, and R. S. Reneman. Relation between left-ventricular cavity pressure and volume and systolic fiber stress and strain in the wall. *Biophys J*, 59:93–102, 1991.

F. Baaijens, C. Bouten, and N. Driessen. Modeling collagen remodeling. *J Biomech*, 43:166–175, 2010.

E. Barbato, W. Aarnoudse, W. R. Aengevaeren, G. Werner, V. Klauss, W. Bojara, I. Herzfeld, K. G. Oldroyd, N. H. J. Pijls, and B. D. Bruyne. Validation of coronary flow reserve measurements by thermodilution in clinical practice. *Eur Heart J*, 25: 219–223, 2004.

B. J. Bellhouse and C. G. Rasmussen. Low-frequency characteristics of hot-film anemometers. *DISA information*, 6:3–10, 1968.

D. Bessems. *On the propagation of pressure and flow waves through the patient-specific arterial system*. Thesis/dissertation, Eindhoven University of Technology, 2007.

D. Bessems, M. Rutten, and F. van de Vosse. A wave propagation model of blood flow in large vessels using an approximate velocity profile function. *J Fluid Mech*, 580: 145–168, 2007.

J. M. Bland and D. G. Altman. Statistical methods for assessing agreement between two methods of clinical measurement. *Lancet*, 327:307–310, 1986.

P. H. Bovendeerd, P. Borsje, T. Arts, and F. N. van de Vosse. Dependence of intramyocardial pressure and coronary flow on ventricular loading and contractility: a model study. *Ann Biomed Eng*, 34:1833–1845, 2006.

P. Bruinsma, T. Arts, J. Dankelman, and J. Spaan. Model of the coronary circulation based on pressure dependence of coronary resistance and compliance. *Basic Res Cardiol*, 83:510–524, 1988.

H. H. Bruun. Hot-film anemometry in liquid flows. *Meas Sci Technol*, 7:1301–1312, 1996.

B. D. Bruyne, J. Bartunek, S. U. Sys, N. H. J. Pijls, G. R. Heyndrickx, and W. Wijns. Simultaneous coronary pressure and flow velocity measurements in humans - feasibility, reproducibility, and hemodynamic dependence of coronary flow velocity reserve, hyperemic flow versus pressure slope index, and fractional flow reserve. *Circulation*, 94:1842–1849, 1996.

B. D. Bruyne, N. H. J. Pijls, L. Smith, M. Wievegg, and G. R. Heyndrickx. Coronary thermodilution to assess flow reserve - experimental validation. *Circulation*, 104: 2003–2006, 2001.

M. Carboni, G. W. Desch, and H. W. Weizsäcker. Passive mechanical properties of porcine left circumflex artery and its mathematical description. *Med Eng Phys*, 29: 8–16, 2007.

J. S. Choy, O. Mathieu-Costello, and G. S. Kassab. The effect of fixation and histological preparation on coronary artery dimensions. *Ann Biomed Eng*, 33:1027–1033, 2005.

C. J. Chuong and Y. C. Fung. On residual stresses in arteries. *J Biomech Eng*, 108: 189–192, 1986.

T. Claessens, P. Verwilst, C. Missant, P. Claus, P. Verdonck, P. Wouters, and P. Segers. In vitro, in vivo and numerical assessment of the working principle of the TruCCOMS™ continuous cardiac output catheter system. *Med Eng Phys*, 31:1299–1306, 2009.

C. Clark. Thin-film gauge for fluctuating velocity measurements in blood. *J Phys E Sci Instrum*, 7:548–556, 1974.

J. M. Clark and S. Glagov. Transmural organization of the arterial media. The lamellar unit revisited. *Arteriosclerosis*, 5:19–34, 1985.

K. D. Cole. Flush-mounted steady-periodic heated film with application to shear-stress measurement. *Trans ASME C: J Heat Transfer*, 130:1116011–11160110, 2008.

L. Cox, S. Loerakker, M. Rutten, B. de Mol, and F. van de Vosse. A mathematical model to evaluate control strategies for mechanical circulatory support. *Artif Organs*, 33: 593–603, 2009.

S. Crick, M. Sheppard, S. Ho, L. Gebstein, and R. Anderson. Anatomy of the pig heart: comparisons with normal human cardiac structure. *J Anat*, 193:105–119, 1998.

J. E. Davies, Z. I. Whinnett, D. P. Francis, C. H. Manisty, J. Aguado-Sierra, K. Willson, R. A. Foale, I. S. Malik, A. D. Hughes, K. H. Parker, and J. Mayet. Evidence of a dominant backward-propagating ”suction” wave responsible for diastolic coronary filling in humans, attenuated in left ventricular hypertrophy. *Circulation*, 113:1768–1778, 2006a.

J. E. Davies, Z. I. Whinnett, D. P. Francis, K. Willson, R. A. Foale, I. S. Malik, A. D. Hughes, K. H. Parker, and J. Mayet. Use of simultaneous pressure and velocity measurements to estimate arterial wave speed at a single site in humans. *Am J Physiol Heart Circ Physiol*, 290:H878–h885, 2006b.

J. de Hart, A. de Weger, S. van Tuijl, J. M. A. Stijnen, C. N. van den Broek, M. C. M. Rutten, and B. A. J. M. de Mol. An ex vivo platform to simulate cardiac physiology: a new dimension for therapy development and assessment. *Int J Artif Organs*, 34: 495–505, 2011.

R. Dekker, M. Dümling, J. Fock, O. Gourhant, C. Jonvill, T. Michielsen, H. Pohlmann, W. Schnitt, A. Tombeur, and T. Zoumpoulidis. A 10 μm thick rf-id tag for chip-in-paper applications. In *Proc. Bipolar/BiCMOS Circuits and Technology meeting (BCTM)*, pages 18–21, 2005.

J. M. Downey and E. S. Kirk. Inhibition of coronary blood-flow by a vascular waterfall mechanism. *Circ Res*, 36:753–760, 1975.

N. J. B. Driessen, C. V. C. Bouten, and F. P. T. Baaijens. A structural constitutive model for collagenous cardiovascular tissues incorporating the angular fiber distribution. *J Biomech Eng*, 127:494–503, 2005.

M. Elwenspoek. Thermal flow micro sensors. In *Proc IEEE Semiconductor Conf*, pages 423–435, 1999.

J. Escaned, A. Flores, P. Garcia-Pavia, J. Segovia, J. Jimenez, P. Aragoncillo, C. Salas, F. Alfonso, R. Hernandez, D. J. Angiolillo, P. Jimenez-Quevedo, C. Banuelos, L. onso Pulpon, and C. Macaya. Assessment of microcirculatory remodeling with intracoronary flow velocity and pressure measurements validation with endomyocardial sampling in cardiac allografts. *Circulation*, 120:1561–1568, 2009.

W. F. Fearon, L. B. Balsam, H. M. Farouque, A. D. Caffarelli, R. C. Robbins, P. J. Fitzgerald, P. G. Yock, and A. C. Yeung. Novel index for invasively assessing the coronary microcirculation. *Circulation*, 107:3129–3132, 2003.

W. F. Fearon, W. Aarnoudse, N. H. J. Pijls, B. de Bruyne, L. B. Balsam, D. T. Cooke, R. C. Robbins, P. J. Fitzgerald, A. C. Yeung, and P. G. Yock. Microvascular resistance is not influenced by epicardial coronary artery stenosis severity: experimental validation. *Circulation*, 109:2269–2272, 2004.

L. Formaggia, D. Lamponi, M. Tuveri, and A. Veneziani. Numerical modeling of 1d arterial networks coupled with a lumped parameters description of the heart. *Comput Methods Biomech Biomed Engin*, 9:273–288, 2006.

Y. C. Fung, K. Fronek, and P. Patitucci. Pseudoelasticity of arteries and the choice of its mathematical expression. *Am J Physiol-Heart Circ Phys*, 237:H620–H631, 1979.

P. Ganz and P. Y. Hsue. Assessment of structural disease in the coronary microvasculature. *Circulation*, 120:1555–1557, 2009.

T. C. Gasser, R. W. Ogden, and G. A. Holzapfel. Hyperelastic modelling of arterial layers with distributed collagen fibre orientations. *J Royal Soc Interface*, 3:15–35, 2006.

D. Gay, S. V. Hoa, and S. W. Tsai. *Composite materials: design and applications*. CRC Press, Boca Raton, 4th edition, 2003.

H. Gelderblom, A. van der Horst, J. R. Haartsen, M. C. M. Rutten, A. A. F. van de Ven, and F. N. van de Vosse. Analytical and experimental characterization of a miniature calorimetric sensor in a pulsatile flow. *J Fluid Mech*, 666:428–444, 2011.

M. C. F. Geven. *Methods to assess the coronary circulation by guidewire-mounted sensors*. Phd thesis, Eindhoven University of Technology, 2007.

M. C. F. Geven, V. N. Bohte, W. H. Aarnoudse, P. M. J. van den Berg, M. C. M. Rutten, N. H. J. Pijls, and F. N. van de Vosse. A physiologically representative in vitro model of the coronary circulation. *Physiol Meas*, 25:891–904, 2004.

K. L. Gould, R. L. Kirkeeide, and M. Buchi. Coronary flow reserve as a physiologic measure of stenosis severity. *J Am Coll Cardiol*, 15:459–474, 1990.

D. Gregg and H. Green. Registration and interpretation of normal phasic inflow into a left coronary artery by an improved differential manometric method. *Am J Physiol*, 130:114–125, 1940.

X. Guo and G. S. Kassab. Distribution of stress and strain along the porcine aorta and coronary arterial tree. *Am J Physiol-Heart Circ Phys*, 286:H2361–H2368, 2004.

J. Haartsen. Development of thermoelectric biosensors with silicon transfer technology. Msc thesis, Eindhoven University of Technology, 2007.

N. Hadjiloizou, J. E. Davies, I. S. Malik, J. Aguado-Sierra, K. Willson, R. A. Foale, K. H. Parker, A. D. Hughes, D. P. Francis, and J. Mayet. Differences in cardiac microcirculatory wave patterns between the proximal left mainstem and proximal right coronary artery. *Am J Physiol Heart Circ Physiol*, 295:H1198–H1205, 2008.

F. Hansen, P. Mangell, B. Sonesson, and T. Lnne. Diameter and compliance in the human common carotid-artery - variations with age and sex. *Ultrasound Med Biol*, 21:1–9, 1995.

I. Hariton, G. Debotton, T. C. Gasser, and G. A. Holzapfel. Stress-driven collagen fiber remodeling in arterial walls. *Biomech Model Mechanobiol*, 6:163–175, 2007.

K. Hayashi and T. Naiki. Adaptation and remodeling of vascular wall; biomechanical response to hypertension. *J Mech Behavior Biomed Mat*, 2:3–19, 2009.

A. Hirsch, R. Nijveldt, J. D. Haeck, A. M. Beek, K. T. Koch, J. P. Henriques, R. J. van der Schaaf, M. M. Vis, J. J. Baan, R. J. de Winter, J. G. Tijssen, A. C. van Rossum, and J. J. Piek. Relation between the assessment of microvascular injury by cardiovascular magnetic resonance and coronary doppler flow velocity measurements in patients with acute anterior wall myocardial infarction. *J Am Coll Cardiol*, 51:2230–2238, 2008.

G. A. Holzapfel, T. C. Gasser, and R. W. Ogden. A new constitutive framework for arterial wall mechanics and a comparative study of material models. *J Elast*, 61: 1–48, 2000.

G. A. Holzapfel, T. C. Gasser, and M. Stadler. A structural model for the viscoelastic behavior of arterial walls: Continuum formulation and finite element analysis. *Europ J Mech A-Solids*, 21:441–463, 2002.

G. A. Holzapfel, G. Sommer, M. Auer, P. Regitnig, and R. W. Ogden. Layer-specific 3d residual deformations of human aortas with non-atherosclerotic intimal thickening. *Ann Biomed Eng*, 35:530–545, 2007.

T. Hozumi, Y. Kanzaki, Y. Ueda, A. Yamamuro, T. Takagi, T. Akasaka, S. Homma, K. Yoshida, and J. Yoshikawa. Coronary flow velocity analysis during short term follow up after coronary reperfusion: use of transthoracic doppler echocardiography to predict regional wall motion recovery in patients with acute myocardial infarction. *Heart*, 89:1163–1168, 2003.

T. Hughes and J. Lubliner. On the one-dimensional theory of blood flow in the large vessels. *Math Bioscie*, 18:161–170, 1973.

J. D. Humphrey, J. F. Eberth, W. W. Dye, and R. L. Gleason. Fundamental role of axial stress in compensatory adaptations by arteries. *J Biomech*, 42:1–8, 2009.

Y. L. Huo and G. S. Kassab. A hybrid one-dimensional/womersley model of pulsatile blood flow in the entire coronary arterial tree. *Am J Physiol Heart Circ Physiol*, 292: H2623–H2633, 2007.

F. P. Incropera, D. P. DeWitt, T. L. Bergman, and A. S. Lavine. *Introduction to heat transfer*. John Wiley & Sons, 5th edition, 2007. ISBN 987-0-471-45727-5.

J. M. Isner, J. Kishel, K. M. Kent, J. A. Ronan, A. M. Ross, and W. C. Roberts. Accuracy of angiographic determination of left main coronary arterial narrowing - angiographic-histologic correlative analysis in 28 patients. *Circulation*, 63:1056–1064, 1981.

G. S. Kassab, H. Gregersen, S. L. Nielsen, X. Lu, L. B. Tanko, and E. Falk. Remodelling of the left anterior descending artery in a porcine model of supravalvular aortic stenosis. *J Hypertens*, 20:2429–2437, 2002.

R. C. P. Kerckhoffs, P. H. Bovendeerd, J. C. S. Kotte, F. W. Prinzen, K. Smits, and T. Arts. Homogeneity of cardiac contraction despite physiological asynchrony of depolarization: A model study. *Ann Biomed Eng*, 31:536–547, 2003.

M. J. Kern. Interpretation of cardiac pathophysiology from pressure waveform analysis: Coronary hemodynamics. part ii: Patterns of coronary flow velocity. *Cathet Cardiovasc Diagn*, 25:154–160, 1992.

M. J. Kern, F. V. Aguirre, T. J. Donohue, R. G. Bach, E. A. Caracciolo, M. S. Flynn, T. Wolford, and J. A. Moore. Continuous coronary flow velocity monitoring during coronary interventions: Velocity trend patterns associated with adverse events. *Am Heart J*, 128:426–434, 1994.

M. J. Kern, B. B. De, and N. H. J. Pijls. From research to clinical practice: Current role of intracoronary physiologically based decision making in the cardiac catheterization laboratory. *J Am Coll Cardiol*, 30:613–620, 1997.

M. J. Kern, A. Lerman, J. W. Bech, B. D. Bruyne, E. Eeckhout, W. F. Fearon, S. T. Higano, M. J. Lim, M. Meuwissen, J. J. Piek, N. H. J. Pijls, M. Siebes, and J. A. E. Spaan. Physiological assessment of coronary artery disease in the cardiac catheterization laboratory - a scientific statement from the american heart association committee on diagnostic and interventional cardiac catheterization, council on clinical cardiology. *Circulation*, 114:1321–1341, 2006.

H. Kim, K. Jansen, and C. Taylor. Incorporating autoregulatory mechanisms of the cardiovascular system in three-dimensional finite element models of arterial blood flow. *Ann Biomed Eng*, 38:2314–2330, 2010.

H. Kitabata, T. Imanishi, T. Kubo, S. Takarada, M. Kashiwagi, H. Matsumoto, H. Tsujioka, H. Ikejima, Y. Arita, K. Okochi, A. Kuroi, S. Ueno, H. Kataiwa, T. Tanimoto, T. Yamano, K. Hirata, N. Nakamura, A. Tanaka, M. Mizukoshi, and T. Akasaka. Coronary microvascular resistance index immediately after primary percutaneous coronary intervention as a predictor of the transmural extent of infarction in patients with st-segment elevation anterior acute myocardial infarction. *J Am Coll Cardiol Img*, 2:263–272, 2009.

C. Kolyva, J.A.E.Spaan, J. Piek, and M. Siebes. Windkesselness of coronary arteries hampers assessment of human coronary wave speed by single-point technique. *Am J Physiol Heart Circ Physiol*, 295:H482–H490, 2008.

R. Krams, P. Sipkema, and N. Westerhof. Varying elastance concept may explain coronary systolic flow impediment. *Am J Physiol*, 257:H1471–H1479, 1989.

R. Krams, F. J. ten Cate, S. G. Carlier, A. F. W. van der Steen, and P. W. Serruys. Diastolic coronary vascular reserve: A new index to detect changes in the coronary microcirculation in hypertrophic cardiomyopathy. *J Am Coll Cardiol*, 43:670–677, 2004.

J. Kroon, W. Huberts, E. Bosboom, and F. van de Vosse. A 1d algorithm of reduced complexity for simulation of vascular hemodynamics. *Int J Num Meth Bio Eng*, submitted:–, 2012.

T. S. J. Lammerink, N. R. Tas, M. Elwenspoek, and J. H. J. Fluitman. Micro-liquid flow sensor. *Sens Actuators A*, 37–38:45–50, 1993.

G. J. Langewouters, K. H. Wesseling, and W. J. A. Goedhard. The static elastic properties of 45 human thoracic and 20 abdominal aortas invitro and the parameters of a new model. *J Biomech*, 17:425–435, 1984.

Y. Lanir. A structural theory for the homogeneous biaxial stress-strain relationships in flat collagenous tissues. *J Biomech*, 12:423–436, 1979.

H. A. Leather, A. Vuylsteke, C. Bert, W. M'Fam, P. Segers, P. Sergeant, E. Vandermeersch, and P. F. Wouters. Evaluation of a new continuous cardiac output monitor in off-pump coronary artery surgery. *Anaesthesia*, 59:385–389, 2004.

H. W. Liepmann and G. T. Skinner. Shearing-stress measurements by use of a heated element. *NACA Tech Note*, 3268, 1954.

T. Liu, B. T. Campbell, and J. P. Sullivan. Surface temperature of a hot film on a wall in shear flow. *Int J Heat Mass Transfer*, 37:2809–2814, 1994.

Y. Liu, W. Zhang, and G. Kassab. Effects of myocardial constraint on the passive mechanical behaviors of the coronary vessel wall. *Am J Physiol Heart Circ Physiol*, 294:H514–H523, 2008.

S. W. Ma and F. M. Gerner. Forced convection heat transfer from microstructures. *Trans ASME C: J Heat Transfer*, 115:872–880, 1993.

G. B. J. Mancini, M. J. Mcgillem, S. F. Deboe, and K. P. Gallagher. The diastolic hyperemic flow versus pressure relation - a new index of coronary stenosis severity and flow reserve. *Circulation*, 80:941–950, 1989.

I. Masson, P. Boutouyrie, S. Laurent, J. D. Humphrey, and M. Zidi. Characterization of arterial wall mechanical behavior and stresses from human clinical data. *J Biomech*, 41:2618–2627, 2008.

C. Di Mario, R. Krams, R. Gil, and P. Serruys. Slope of the instantateous hyperemic diastolic coronary flow velocity-pressure relation. a new index for assesment of the physiological significance of coronary stenosis in humans. *Circulation*, 90:1215–1224, 1994.

D. Hildick-Smith and L. Shapiro. Coronary flow reserve improves aftr aortic valve replacement for aortic stenosis: An adenosine transthoracic echocardiography study. *J Am Coll Cardiol*, 36:1889–1896, 2000.

A. Vieira da Silva, B. Mimoun, and R. Dekker. Fless: a matlab based graphical user interface for stress strain analytical modeling of multilayered structures with applied bending. In *SAFE*, pages 175–179, 2010.

A. N. Menendez and B. R. Ramaprian. The use of flush-mounted hot-film gauges to measure skin friction in unsteady boundary layers. *J Fluid Mech*, 161:139–159, 1985.

M. Meuwissen, M. Siebes, S. Chamuleau, B. van Eck-Smit, K. Koch, R. de Winter, J. Tijssen, J. Spaan, and J. Piek. Hyperemic stenosis resistance index for evaluation of functional coronary lesion severity. *Circulation*, 106:441–446, 2002a.

M. Meuwissen, M. Siebes, J. A. E. Spaan, and J. J. Piek. Rationale of combined intracoronary pressure and flow velocity measurements. *Z Kardiol*, 91:III108–III112, 2002b.

W. R. Milnor. *Hemodynamics*. Williams & Wilkins, 2th edition, 1989.

B. Mimoun, V. Henneken, and R. Dekker. Flex-to-Rigid (f2r): A novel ultra-flexible technology for smart invasive medical instruments. In *Mater Res Soc Symp Proc*, pages JJ05–09, 2010a.

B. Mimoun, V. Henneken, and R. Dekker. Release and mounting of partially flexible devices inside and around tubes for smart invasive medical applications. In *EPTC*, pages 7–12, 2010b.

C. D. Murray. The physiological principle of minimum work applied to the angle of branching of arteries. *J Gen Physiol*, 9:835–841, 1926.

J. P. Mynard and P. Nithiarasu. A 1d arterial blood flow model incorporating ventricular pressure, aortic valve and regional coronary flow using the locally conservative galerkin (lcg) method. *Comm Num Meth Eng*, 24:367–417, 2008.

R. M. Nerem, J. J. A. Rumberger, D. R. Gross, W. W. Muir, and G. L. Geiger. Hot film coronary artery velocity measurements in horses. *Cardiovasc Res*, 10:301–313, 1976.

N. T. Nguyen and R. Kiehnscherf. Low-cost silicon sensors for mass flow measurement of liquids and gases. *Sens Actuators A*, 49:17–20, 1995.

J. V. Nicholas and D. R. White. *Traceable temperatures: an introduction to temperature measurement and calibration*. John Wiley & Sons, 2nd edition, 2001.

I. Okcular, M. Sezer, E. Aslanger, A. Cimen, B. Umman, Y. Nisanci, and S. Umman. The accuracy of deceleration time of diastolic coronary flow measured by transthoracic echocardiography in predicting long-term left ventricular infarct size and function after reperfused myocardial infarction. *Eur J Echocardiogr*, 11:823–828, 2010.

T. Olsson, J. Stålhand, and A. Klarbring. Modeling initial strain distribution in soft tissues with application to arteries. *Biomech Model Mechanobiol*, 5:27–38, 2006.

K. H. Parker. An introduction to wave intensity analysis. *Med Biol Eng Comput*, 47: 175–188, 2009.

K. H. Parker and C. J. Jones. Forward and backward running waves in the arteries: analysis using the method of characteristics. *J Biomech Eng*, 112:322–326, 1990.

P. K. Paulsen. The hot-film anemometer - a method for blood velocity determination. i. invitro comparison with the electromagnetic blood flowmeter. *Eur Surg Res*, 12: 140–148, 1980a.

P. K. Paulsen. The hot-film anemometer - a method for blood velocity determination. ii. invivo comparison with the electromagnetic blood flowmeter. *Eur Surg Res*, 12: 149–158, 1980b.

T. J. Pedley. On the forced heat-transfer from a hot film embedded in wall in two-dimensional unsteady flow. *J Fluid Mech*, 55:329–357, 1972a.

T. J. Pedley. Two-dimensional boundary-layers in a free stream which oscillates without reversing. *J Fluid Mech*, 55:359–383, 1972b.

T. J. Pedley. Viscous boundary layers in reversing flow. *J Fluid Mech*, 74:59–79, 1976a.

T. J. Pedley. Heat transfer from a hot film in reversing shear flow. *J. Fluid Mech.*, 78: 513–534, 1976b.

T. J. Pfefer, B. Choi, G. Vargas, K. M. McNally, and A. J. Welch. Pulsed laser-induced thermal damage in whole blood. *J Biomech Eng*, 122:196–202, 2000.

P. Pfeifer and K. Schubert. Hot wire anemometry for experimental determination of flow distribution in multilayer microreactors. *Chem Eng J*, 135:S173–S178, 2008.

N. H. J. Pijls, B. de Bruyne, K. Peels, P. H. van der Voort, H. J. Bonnier, J. K. J. Bartunek, and J. J. Koolen. Measurement of fractional flow reserve to assess the functional severity of coronary-artery stenoses. *N Engl J Med*, 334:1703–1708, 1996.

N. H. J. Pijls, B. B. De, L. Smith, W. Aarnoudse, E. Barbato, J. Bartunek, G. J. W. Bech, and F. van de Vosse. Coronary thermodilution to assess flow reserve: Validation in humans. *Circulation*, 105:2482–2486, 2002.

W. T. Porter. The influence of the heart-beat on the flow of blood through the wall of the heart. *Am J Physiol*, 1:145–163, 1898.

A. Rachev and S. E. Greenwald. Residual strains in conduit arteries. *J Biomech*, 36: 661–670, 2003.

M. Rebay, J. Padet, and S. Kakaç. Forced convection from a microstructure on a flat plate. *Heat Mass Transfer*, 43:309–317, 2007.

P. Reymond, F. Merenda, F. Perren, D. Rufenacht, and N. Stergiopulos. Validation of a one-dimensional model of the systemic arterial tree. *Am J Physiol Heart Circ Physiol*, 297:H208–H222, 2009.

R. Rezakhaniha and N. Stergiopulos. A structural model of the venous wall considering elastin anisotropy. *J Biomech Eng*, 130:031017, 2008.

J. A. G. Rhodin. Handbook of physiology: The cardiovascular system. *A*rchitecture of the vessel wall. Chapter 1, pages 1–31. American Physiology Society, 2nd edition, 1980.

T. Ricolfi and J. Scholz. *Thermal sensors*, volume 4. Weinhein, 1990.

M. R. Roach and A. C. Burton. The reason for the shape of the distensibility curves of arteries. *Can J Biochem Phys*, 35:681–690, 1957.

H. Schlichting and K. Gersten. *Boundary-Layer Theory*. Springer-Verlag, Berlin, 8th edition, 2000.

C. A. J. Schulze-Bauer and G. A. Holzapfel. Determination of constitutive equations for human arteries from clinical data. *J Biomech*, 36:165–169, 2003.

W. A. Seed and N. B. Wood. Use of a hot-film velocity probe for cardiovascular studies. *J Phys E Sci Instrum*, 3:377–384, 1970a.

W. A. Seed and N. B. Wood. Development and evaluation of a hot-film velocity probe for cardiovascular studies. *Cardiovasc Res*, 4:253–263, 1970b.

W. A. Seed and N. B. Wood. Application of constant temperature anemometry in measurement of intra-arterial blood flow velocity. *Int J Eng Sci*, 10:1009–1021, 1972.

A. Segal. *Sepran User Manual*. Ingenieursbureau SEPRA, Leidschendam, 1993.

P. Segers, S. Vanderberghe, J. Decryenaere, J. Poelaert, P. Wouters, F. Colardyn, and P. Verdonck. Hydraulic bench testing of the truccath™/trucomm™ continuous cardiac output monitor. *Cardiovascular Engineering*, 3:93–102, 2003.

R. Shah and A. London. *Laminar flow forced convection in ducts: a source book for compact heat exchanger analytical data*. London: Academic Press, 1978.

S. Shanmugavelayudam, D. Rubenstein, and W. Yin. Effect of geometrical assumptions on numerical modeling of coronary blood flow under normal and disease conditions. *J Biomech Eng*, 132:061004, 2010.

M. Siebes, B. J. Verhoeff, M. Meuwissen, R. J. de Winter, J. A. E. Spaan, and J. J. Piek. Single-wire pressure and flow velocity measurement to quantify coronary stenosis hemodynamics and effects of percutaneous interventions. *Circulation*, 109:756–762, 2004.

M. Siebes, C. Kolyva, B. J. Verhoeff, J. J. Piek, and J. A. Spaan. Potential and limitations of wave intensity analysis in coronary arteries. *Med Biol Eng Comput*, 47:233–239, 2009.

C. Slager, J. Wentzel, F. Gijsen, A. Thury, A. van der Wal, J. Schaar, and P. Serruys. The role of shear stress in the destabilization of vulnerable plaques and related therapeutic implications. *Nat Clin Pract Cardiovasc Med*, 2:456–464, 2005.

N. P. Smith, A. J. Pullan, and P. J. Hunter. An anatomically based model of transient coronary blood flow in the heart. *SIAM J Appl Math*, 62:990–1018, 2002.

F. Sones and E. Shirey. Cine coronary arteriography. *Med Concepts Cardiovasc Dis*, 31: 735–738, 1962.

J. A. E. Spaan. Coronary diastolic pressure-flow relation and zero flow pressure explained on the basis of intramyocardial compliance. *Circulation Research*, 56: 293–309, 1985.

J. A. E. Spaan, N. P. W. Breuls, and J. D. Laird. Diastolic-systolic coronary flow differences are caused by intramyocardial pump action in the anesthetized dog. *Circ Res*, 49:584–593, 1981.

J. A. E. Spaan, J. J. Piek, J. I. E. Hoffman, and M. Siebes. Physiological basis of clinically used coronary hemodynamic indices. *Circulation*, 113:446–455, 2006.

A. J. M. Spencer, T. G. rogers, and R. L. moss. An optimal angle of winding for pressurized fibre-reinforeced cylinders. *Mech Res Comm*, 1:27–32, 1974.

S. G. Springer. The solution of heat transfer problems by the Wiener-Hopf technique. II. Trailing edge of a hot film. *Proc R Soc Lond A*, 337:395–412, 1974.

S. G. Springer and T. J. Pedley. The solution of heat transfer problems by the Wiener-Hopf technique. I. Leading edge of a hot film. *Proc R Soc Lond A*, 333:347–362, 1973.

J. Stålhand. Determination of human arterial wall parameters from clinical data. *Biomech Model Mechanobiol*, 8:141–148, 2009.

J. Stålhand and A. Klarbring. Aorta in vivo parameter identification using an axial force constraint. *Biomech Model Mechanobiol*, 3:191–199, 2005.

J. Stålhand, A. Klarbring, and M. Karlsson. Towards in vivo aorta material identification and stress estimation. *Biomech Model Mechanobiol*, 2:169–186, 2004.

C. F. Stein, P. Johansson, J. Bergh, L. Löfdahl, M. Sen, and M. Gad-el-Hak. An analytical asymptotic solution to a conjugate heat transfer problem. *Int J Heat Mass Transfer*, 45:2485–2500, 2002.

N. Stergiopulos, D. Young, and T. Rogge. Computer simulation of arterial flow with application to arterial and aortic stenoses. *J Biomech*, 25:1477–1488, 1992.

N. Stergiopulos, B. Westerhof, and N. Westerhof. Total arterial inertance as the fourth element of the windkessel model. *Am J Physiol-Heart Circ Phys*, 276:H81–H88, 1998.

H. Suga, K. Sagawa, and A. A. Shoukas. Load independence of instantaneous pressure-volume ratio of canine left ventricle and effects of epinephrine and heart-rate on ratio. *Circ Res*, 32:314–322, 1973.

Y. H. Sun, T. J. Anderson, K. H. Parker, and J. V. Tyberg. Wave-intensity analysis: a new approach to coronary hemodynamics. *J Appl Physiol*, 89:1636–1644, 2000.

L. A. Taber and D. W. Eggers. Theoretical study of stress-modulated growth in the aorta. *J Theor Biol*, 180:343–357, 1996.

K. Takamizawa and K. Hayashi. Strain energy density function and uniform strain hypothesis for arterial mechanics. *J Biomech*, 20:7–17, 1987.

F. S. Tardu and C. T. Pham. Response of wall hot-film gages with longitudinal diffusion and heat conduction to the substrate. *Trans ASME C: J Heat Transfer*, 127:812–819, 2005.

P. A. L. Tonino, B. D. Bruyne, N. H. J. Pijls, U. Siebert, F. Ikeno, M. van 't Veer, V. Klauss, G. Manoharan, T. Engstrom, K. G. Oldroyd, P. N. V. Lee, P. A. MacCarthy, and W. F. Fearon. Fractional flow reserve versus angiography for guiding percutaneous coronary intervention. *N Eng J Med*, 360:213–224, 2009.

S. Tsangaris. Oscillatory flow of an incompressible, viscous-fluid in a straight annular pipe. *J Mec Theor Appl*, 3:467–478, 1984.

H. Uchiyama and M. Ide. Development of a hot-film anemometer calibrator for water flow measurement. *Flow Meas Instrum*, 20:75–80, 2009.

R. Vaishnav, J. Young, and D. Patel. Distribution of stresses and of strainenergy density through the wall thickness in a canine aortic segment. *Circ Res*, 32:577–583, 1973.

J. Valenta, J. Svoboda, D. Valerianova, and K. Vitek. Residual strain in human atherosclerotic coronary arteries and age related geometrical changes. *Bio-Med Mat Eng*, 9:311–317, 1999.

F. N. van de Vosse and N. Stergiopulos. Pulse wave propagation in the arterial tree. *Annu Rev Fluid Mech*, 43:467–499, 2011.

C. N. van den Broek. *Mechanical characterization and constitutive modeling of the coronary artery*. PhD thesis, Eindhoven University of Technology, 2010.

C. N. van den Broek, A. van der Horst, M. C. M. Rutten, and F. N. van de Vosse. A generic constitutive model for the passive porcine coronary artery. *Biomech Model Mechanobiol*, 10:249–258, 2011.

A. van der Horst, M. C. F. Geven, M. C. M. Rutten, N. H. J. Pijls, and F. N. van de Vosse. Thermal anemometric assessment of coronary flow reserve with a pressure-sensing guide wire: An in vitro evaluation. *Med Eng Phys*, 33:684–691, 2011.

A. van der Horst, C. N. van den Broek, F. N. van de Vosse, and M. C. M. Rutten. The fiber orientation in the coronary arterial wall at physiological loading evaluated with a two-fiber constitutive model. *Biomech Mod Mechanobiol*, 11:533–542, 2012.

A. W. van Herwaarden, D. C. van Duyn, B. W. van Oudheusden, and P. M. Sarro. Integrated thermopile sensors. *Sens Actuators A*, 21–23:621–630, 1989.

P. van Loon. Length-force and volume-pressure relationships of arteries. *Biorheology*, 14:181–201, 1977.

C. H. G. A. van Oijen. *Mechanics and Design of fiber-reinforced vascular prostheses*. Phd thesis, Eindhoven University of Technology, 2003.

B. W. van Oudheusden. The thermal modelling of a flow sensor based on differential convective heat transfer. *Sens Actuators A*, 29:93–106, 1991.

B. W. van Oudheusden and J. W. Huijsing. Integrated silicon flow-direction sensor. *Sens Actuators*, 16:109–119, 1989.

A. A. van Steenhoven and F. J. H. M. van de Beucken. Dynamical analysis of electrochemical wall shear rate measurements. *J Fluid Mech*, 231:599–614, 1991.

M. van 't Veer. *Hemodynamic measurements in coronary, valvular and peripheral vascular disease. The role of the medical engineer in a cardiovascular departement of a non-academic heartcenter*. Phd thesis, Eindhoven University of Technology, 2008.

M. van 't Veer, M. C. F. Geven, M. C. M. Rutten, A. van der Horst, W. H. Aarnoudse, N. H. J. Pijls, and F. N. van de Vosse. Continuous infusion thermodilution for assessment of coronary flow: Theoretical background and in vitro validation. *Med Eng Phys*, 31:688–694, 2009.

T. J. VanDyke and A. Hoger. A new method for predicting the opening angle for soft tissues. *J Biomech Eng*, 124:347–354, 2002.

M. Vavuranakis, C. Stefanadis, E. Triandaphyllidi, K. Toutouzas, and P. Toutouzas. Coronary artery distensibility in diabetic patients with simultaneous measurements of luminal area and intracoronary pressure - evidence of impaired reactivity to nitroglycerin. *J Am Coll Cardiol*, 34:1075–1081, 1999.

B. J. Verhoeff, M. Siebes, M. Meuwissen, B. Atasever, M. Voskuil, R. J. de Winter, K. T. Koch, J. G. P. Tijssen, J. A. E. Spaan, and J. J. Piek. Influence of percutaneous coronary intervention on coronary microvascular resistance index. *Circulation*, 111: 76–82, 2005.

C. Wang, M. Garcia, X. Lu, Y. Lanir, and G. S. Kassab. Three-dimensional mechanical properties of porcine coronary arteries: a validated two-layer model. *Am J Physiol-Heart Circ Phys*, 291:H1200–H1209, 2006.

R. Y. Wang and R. L. Gleason. A mechanical analysis of conduit arteries accounting for longitudinal residual strains. *Ann Biomed Eng*, 38:1377–1387, 2010.

S. L. Waters, J. Alastruey, D. A. Beard, P. H. M. Bovendeerd, P. F. Davies, G. Jayaraman, O. E. Jensen, J. Lee, K. H. Parker, A. S. Popel, T. W. Secomb, M. Siebes, S. J. Sherwin, R. J. Shipley, N. P. Smith, and F. N. van de Vosse. Theoretical models for coronary vascular biomechanics: Progress & challenges. *Prog Biophys Mol Biol*, 104:49–76, 2011.

H. W. Weizsäcker, H. Lambert, and K. Pascale. Analysis of the passive mechanical properties of rat carotid arteries. *J Biomech*, 16:703–715, 1983.

N. Westerhof, F. Bosman, and N. A. De Vries CJ. Analog studies of the human systemic arterial tree. *J Biomech*, 2:121–143, 1969.

P. M. Wild and G. W. Vickers. Analysis of filament-wound cylindrical shells under combined centrifugal, pressure and axial loading. *Compos Part A-Appl Sc Manu*, 28: 47–55, 1997.

J. R. Womersley. Method for the calculation of velocity, rate of flow and viscous drag in arteries when the pressure gradient is known. *J Physiol*, 127:553–563, 1955.

J. R. Womersley. An elastic tube theory of pulse transmission and oscillatory flow in mammalian arteries. Technical report, WADC, 1957.

M. Xia, K. Kemmochi, and H. Takayanagi. Analysis of filament-wound fiber-reinforced sandwich pipe under combined internal pressure and thermomechanical loading. *Compos Struct*, 51:273–283, 2001.

D. Young and F. Tsai. Flow characteristics in models of arterial stenoses. i. steady flow. *J. Biomech*, 6:395–410, 1973a.

D. Young and F. Tsai. Flow characteristics in models of arterial stenoses. ii. unsteady flow. *J. Biomech*, 6:547–559, 1973b.

O. Zienkiewicz and R. Taylor. *The Finite Element Method*, volume 1. London : Arnold, 4th edition, 1989. ISBN 0-7506-5049-4.

D. Zinemanas, R. Beyar, and S. Sideman. Effects of myocardial-contraction on coronary blood-flow - an integrated model. *Ann Biomed Eng*, 22:638–652, 1994.

M. A. Zulliger, P. Fridez, K. Hayashi, and N. Stergiopulos. A strain energy function for arteries accounting for wall composition and structure. *J Biomech*, 37:989–1000, 2004a.

M. A. Zulliger, A. Rachev, and N. Stergiopulos. A constitutive formulation of arterial mechanics including vascular smooth muscle tone. *Am J Physiol-Heart Circ Phys*, 287:H1335–H1343, 2004b.

Samenvatting

Het bloedvatenstelsel dat de hartspier van bloed voorziet, de coronaire circulatie, is gevoelig voor arteriosclerose. Deze ziekte kan leiden tot vernauwingen, waardoor de bloedstroom naar bepaalde delen van de hartspier belemmerd kan worden. De meest gebruikelijke manier om de ernst van deze vernauwingen te bepalen is coronaire angiografie. Het nadeel van deze methode is dat het alleen inzicht geeft in de morfologie van de kransslagaders en niet in de extra weerstand tegen bloedstroming. Om deze weerstand te bepalen zijn voerdraden met sensoren ontwikkeld, die de druk en snelheid van het bloed kunnen meten. Op basis van het tijdsgemiddelde van deze grootheden zijn verschillende indices ontwikkeld die gebruikt worden om de ernst van vernauwingen te kwantificeren. Echter, de interpretatie van deze tijdsgemiddelde grootheden wordt bemoeilijkt doordat de coronaire circulatie is ingebed in de samentrekkende hartspier en kan worden verbeterd door gelijktijdig de dynamiek van de bloedstroom en -druk te bepalen. Het onderzoek dat wordt beschreven in dit proefschrift richt zich derhalve enerzijds op de ontwikkeling van sensoren die gelijktijdig de dynamiek van coronaire druk en bloedstroom kunnen meten en anderzijds op het modelleren van het hart en de kransslagaders om deze dynamische metingen beter te kunnen interpreteren.

In de ontwikkeling van de sensor die zowel bloeddruk als bloedstroom kan meten zijn twee verschillende strategieën gehanteerd: Het op een andere wijze gebruiken van een bestaande druksensor waardoor ook bloedstroming gemeten kan worden en de ontwikkeling van een geheel nieuwe sensor specifiek geschikt voor het meten van coronaire bloedstroming. Als onderdeel van de eerste strategie is een methode ontwikkeld om een voerdraad met een druksensor (drukdraad) die in de kliniek wordt gebruikt om druk te meten in de kransslagaders, zo aan te sturen dat hij gebruikt kan worden als thermische anemometer. Met deze methode is het elektrisch vermogen, dat nodig is om de sensor te verwarmen tot een bepaalde temperatuur, een maat voor de afschuifsnelheid van het bloed op het oppervlak van de sensor. Deze methode is getest in een *in-vitro* opstelling en bleek geschikt om de klinische index CFR te bepalen. Er is ook aangetoond dat, door de methode iets aan te passen en te combineren met een continue thermodilutie methode, de dynamiek van coronaire druk en volumestroom simultaan gemeten kon worden in een *in-vitro* en *ex-vivo* opstelling. De voornaamste nadelen van deze methode zijn de relatief hoge sensortemperatuur en het niet kunnen bepalen van de richting van de bloedstroom.

In de tweede strategie is een nieuwe sensor ontwikkeld. De sensor is ingebed

in een flexibele polyimide chip die ontwikkeld is om gemonteerd te worden op een voerdraad. De sensor bestaat uit een verwarmingselement, dat aangestuurd wordt op constant vermogen, en twee thermozuilen die temperatuurverschillen meten stroomopwaarts en -afwaarts van het verwarmingselement. Om beter inzicht te krijgen in de ontwerpparameters is een analytisch model ontwikkeld en zijn experimenten uitgevoerd waarin de sensoren werden blootgesteld aan stationaire en instationaire stromingen. De experimentele resultaten kwamen redelijk overeen met het analytisch model, maar de gevoeligheid bij fysiologische afschuifsnelheden was beperkt. Met *in-vitro* experimenten en een numeriek model is er aangetoond dat deze gevoeligheid verbeterd kan worden door het verwarmingselement op constante temperatuur te houden. De dynamiek van de fysiologische afschuifsnelheden, inclusief terugstroming, kon nauwkeurig worden bepaald bij een sensortemperatuur van maar 5 K boven de lichaamstemperatuur. Gebaseerd op de karakterisering met het numerieke model is een verbeterd ontwerp voorgesteld dat gefabriceerd zal worden voor testen in *in-vitro* en *ex-vivo* opstellingen.

Om de dynamische bloeddruk- en bloedstroommetingen met de verschillende sensoren beter te kunnen interpreteren is een model van het hart en coronaire circulatie ontwikkeld. Het model is gebaseerd op de koppeling van vier bestaande modellen: Een model van het linker ventrikel, een 1D golfvoortplantingsmodel voor de grote epicardiale kransslagaders, een element dat het effect van een vernauwing simuleert en Windkessel-elementen om de microcirculatie te beschrijven. De resultaten die verkregen zijn met het gecombineerde model zijn vergeleken met experimentele waarnemingen die beschreven zijn in de literatuur. Hieruit kan worden geconcludeerd dat het model in staat is om het effect van verschillende ziekten op epicardiale hemodynamica te simuleren. Na verdere validatie van het model kan het gebruikt worden om het effect van combinaties van epicardiale en/of microcirculatie ziekten op de epicardiale druk en stroming te bestuderen.

Voor zowel de mechanische behandeling van vernauwingen als het modelleren van de hemodynamica in de kransslagaders zijn de mechanische eigenschappen van de wand van de kransslagaders nodig. Om deze mechanische eigenschappen te bepalen is een constitutief model gefit op resultaten die verkregen zijn met *in-situ* extensie-inflatie experimenten met humane en varkenskransslagaders. De verkregen resultaten laten zien dat het gebruikte constitutieve model de experimentele data goed kan beschrijven. Verdere analyse van de parameter die de oriëntatie van de collageenvezels beschrijft laat zien dat voor alle gemeten vaten deze oriëntatie bij fysiologische belasting hetzelfde is. In vervolgonderzoeken kan dit gegeven gebruikt worden om problemen met betrekking tot over-parameterisatie te voorkomen, in het bijzonder wanneer soortgelijke modellen gefit worden op data verkregen in een klinische setting.

In dit proefschrift is een model van de coronaire circulatie gepresenteerd en zijn methoden voor het gelijktijdig meten van bloeddruk en bloedstroming geïntroduceerd. Door een reeds klinisch gebruikte drukdraad te gebruiken als thermische anemometer, is een methode ontwikkeld die nu gemakkelijk in de kliniek toegepast kan worden, terwijl een nieuwe sensor is ontworpen om in de toekomst nauwkeurigere metingen te verrichten onder verschillende omstandigheden.

Dankwoord

Hoewel alleen mijn eigen naam op de kaft staat zijn er veel mensen betrokken geweest bij de totstandkoming van dit proefschrift die ik in dit dankwoord graag wil benoemen.

Allereerst wil ik mijn (co-)promotoren bedanken. Frans, jij hebt mij de kans en het vertrouwen gegeven om dit onderzoek te verrichten. Ik heb veel geleerd van jouw kritische en analytische blik, die onmisbaar zijn om gedegen onderzoek uit te voeren. Ik was na elk overleg weer verbaasd dat je, ondanks dat je niet altijd de exacte details kende, precies de goede vragen kon stellen. Nico, bedankt dat je mij een inkijk hebt gegeven in de werkelijkheid van hemodynamische metingen in de kliniek. Je bijdrage via de vele coronairoverleggen is zeer waardevol geweest. Beste Marcel, jij bent de (niet zo) stille motor achter dit onderzoek. Met zowel inhoudelijke als praktische problemen kon ik altijd bij jou terecht. Daarnaast waren de vele niet werkgerelateerde gesprekken erg gezellig en vaak ook nog leerzaam.

I would like to thank Magnus Samuelsson, Ton van der Steen, Ronald Dekker, Anton van Steenhoven, and Peter Hilbers for the careful evaluation of this thesis and for taking place in my defense committee.

Ronald, zonder de prettige samenwerking met jou zou dit onderzoek een stuk minder veelzijdig zijn geweest. Bedankt dat je me de kans hebt gegeven om nog een jaar binnen het project te werken. Benjamin, I really enjoyed working together. Thanks for giving me an insight into the amazing world of designing and manufacturing chips. I am looking forward to our cooperation in the experimental testing of the flexible sensors.

The valuable input and interest from our collaborators at Philips Research and St. Jude Medical; Jaap Haartsen, Vincent Henneken, Jeannet van Rens, Pär Gustafsson, Magnus Samuelsson, and Stefan Tiensuu, is very much appreciated.

Marcel V, jij bent het bewijs dat een ingenieur onmisbaar is een ziekenhuis! Bedankt voor de vele gezellige uren samen in het lab en de tijd die je gestoken hebt in het grondig doornemen van dit proefschrift. Chantal, onze samenwerking is het bewijs dat het geheel vaak meer is dan de som der delen. Maartje, bedankt voor de begeleiding tijdens mijn afstudeerproject dat de opmaat is geweest tot dit onderzoek. Ik wil ook graag Sjoerd en Marco van HemoLab bedanken voor alle adviezen in het lab en de ondersteuning bij de kloppende hart experimenten.

De afgelopen jaren heb ik de nodige studenten mogen begeleiden die ook allen direct of indirect een bijdrage hebben geleverd aan dit onderzoek. Hanneke, door

jouw inzet heeft het project een vliegende start gekregen. Hoofdstuk 6 zou er zonder jou heel anders uit hebben gezien. Robin, door jouw toewijding en praktische skills kunnen we nu simultaan druk en afschuifsnelheid kunnen meten. Frits, hoewel het onderzoek niet altijd even vlot verlopen is vormt jouw werk wel de basis van het model in hoofdstuk 3. Dennis, bedankt voor je bijdrage aan hoofdstuk 7. Ik vind het erg leuk dat we de nieuwe sensoren nog samen gaan testen. Job, Martin en Steven, alhoewel jullie werk niet direct terug te vinden is in dit proefschrift, heeft het toch nieuwe inzichten gegeven die erg belangrijk zijn geweest bij het analyseren van de verschillende onderzoeksresultaten.

I would like to thank all my roommates for all the interesting discussions and nice working atmosphere. Chantal en Jasper, ik kijk met veel plezier terug op de vele kilometers die we samen afgelegd hebben om vanuit WH-4.115 koffie te halen.

Om hard te kunnen werken heb je natuurlijk ook ontspanning nodig. Beste mannen van BC Bal Door 'T Netje, ook al zijn de wedstrijdjes op vrijdagavond (gelukkig) juist niet altijd even ontspannend, vormen ze altijd een erg goed begin van het weekend. Tom, bedankt voor je vriendschap, onze vele gesprekken tijdens onze lange fietstochten doen me altijd goed. Sander, vanaf het eerste jaar van de BMT-opleiding klikte het al tussen ons. Ik kijk met veel plezier terug op de tijd samen in het studentenhuis, de korte vakanties, de uren in het sportcentrum en de vele stapavonden. Ik vind het een eer dat je mijn paranimf bent.

Kirsten, bedankt dat je altijd zo'n leuke en lieve zus bent. Ik vind het heel speciaal dat je mijn paranimf wil zijn. Pap en mam, ik heb erg veel geluk dat ik zulke lieve ouders heb. Zonder jullie aandacht en onvoorwaardelijke steun zou ik niet in staat zijn geweest om dit boekje te produceren. Lieve Anne, dankjewel dat je er altijd voor me bent. Ik kijk erg uit naar onze toekomst samen!

Arjen, maart 2012

Curriculum Vitae

Arjen van der Horst werd geboren op 9 september 1982 te Tilburg. In 2000 behaalde hij zijn VWO-diploma aan het Paulus lyceum te Tilburg. Aansluitend studeerde hij Biomedische Technologie aan de Technische Universiteit Eindhoven. Als onderdeel van deze studie liep hij stage aan Imperial College London in het Verenigd Koninkrijk. Hier deed hij onderzoek naar de akoestische eigenschappen van een axiale hartpomp. Zijn afstudeerwerk deed hij in de vakgroep Cardiovasculaire Biomechanica van de Technische Universiteit Eindhoven en richtte zich op de ontwikkeling van een methode om een drukdraad te gebruiken als thermische anemometer voor het meten van bloedstroming in kransslagaders. Na zijn afstuderen in 2007 werd vervolg gegeven aan dit werk in de vorm van een promotie-onderzoek, resulterend in dit proefschrift.